UNIVERSITY OF SOUTHAMPTON

Faculty of Engineering and Physical Sciences
School of Chemistry

Electrochemical Dynamics Investigated by Small Angle Scattering

by

Gilles Ernest Heinrich Karl Möhl
MSc
ORCiD: https://orcid.org/0000-0003-4910-3601

A thesis for the degree of
Doctor of Philosophy

September 2021

University of Southampton

Abstract

Faculty of Engineering and Physical Sciences
School of Chemistry

Doctor of Philosophy

Electrochemical Dynamics Investigated by Small Angle Scattering

by Gilles Ernest Heinrich Karl Möhl

Electrodeposition has been proven a viable tool for the making of nanostructures (template electrodeposition), which are most promising in achieving novel properties through nanoscale effects. In this work, Small angle X-ray and neutron scattering is applied to study the structural properties of electrodeposited materials due to its suitability for *operando* electrochemistry experiments. Firstly, Grazing Incidence Small Angle X-ray Scattering (GISAXS) is used to investigate the arrangement of electrodeposited Au particles on a bare TiN electrode. This system represents a simplification of the configuration needed for template electrodeposition of nanomaterials and it is used to explore the arrangement of the deposits without the constraints of a physical template, showing their non-random arrangement. The understanding gained from this first study is then applied to the non-aqueous electrodeposition of bismuth telluride from dichloromethane, which is observed through *in situ* Grazing Incidence Neutron Scattering (GISANS). Neutrons are chosen in order to decouple the observations from processes happening within the electrolyte solution, but require a suitable electrochemical cell with unusually large electrodes. No evidence for the individual deposition of Bi and Te is found for deposition times longer than 1 s. Another route undergone in this work is the investigation of Electrochemically Assisted Surfactant Assembly (EASA) using *operando* GISAXS. EASA represents a reliable technique for the making of vertically aligned mesoporous silica films, which in turn are applicable to template electrodeposition. Its limitations in applicability arise from the unwanted formation of surface aggregates and the narrow range of available pore sizes. The *operando* experiments give the first time-resolved insight into the EASA process, showing film and aggregate formation under real conditions. A novel route for reduced aggregates using an electrolyte-free sol is presented. Lastly, nanostructured HPd pH sensors are made and used to monitor the hydroxide concentration in the vicinity of a TiN electrode under electric potential, showing that hydrogen, water and oxygen reduction dominate the formation of the gradient, and that its relaxation time widely exceeds typical deposition times.

Contents

List of Figures

List of Tables

List of Additional Material

Dataset: ”Dataset for: Electrochemical Dynamics Investigated by Small Angle Scattering”; DOI:10.5258/SOTON/D1966

Dataset: ”Using GISAXS to detect correlations between the locations of gold particles electrodeposited from aqueous solution”; DOI:10.5258/SOTON/D1312

Dataset: ”In situ GISANS study on the electrodeposition of bismuth telluride on titanium nitride from non-aqueous solution”; DOI:10.5291/ill-data.1-04-145

Dataset: ”Understanding the size limits of silica pore formation by in situ grazing incidence small angle X-ray scattering”; DOI:10.5258/SOTON/D1967

Declaration of Authorship

I declare that this thesis and the work presented in it is my own and has been generated by me as the result of my own original research.

I confirm that:

1. This work was done wholly or mainly while in candidature for a research degree at this University;
2. Where any part of this thesis has previously been submitted for a degree or any other qualification at this University or any other institution, this has been clearly stated;
3. Where I have consulted the published work of others, this is always clearly attributed;
4. Where I have quoted from the work of others, the source is always given. With the exception of such quotations, this thesis is entirely my own work;
5. I have acknowledged all main sources of help;
6. Where the thesis is based on work done by myself jointly with others, I have made clear exactly what was done by others and what I have contributed myself;
7. Parts of this work have been published as: Moehl, Gilles E and Bartlett, Philip N and Hector, Andrew L, *Langmuir*, 2020, **36**, 4432-4438.

Signed:..... Date:.....

Acknowledgements

Firstly, I would like to thank my supervisor, Professor Andrew Hector for trusting a physicist and offering me a position in the first place. I am very grateful to him for providing me with an environment in which I could work freely on the research for my PhD, and for always being ready to discuss anything or to be a member of a beam time team. I would also like to thank Prof. Phil Bartlett, who always had a useful question to ask during project presentations and was always available for discussions if needed. For the funding of my research I would like to thank EPSRC with the ADEPT programme grant (EP/N035437/1) as well as the National Productivity Investment Fund. I would like to thank the people who stood by my side during various beam times, which include Prof. Andrew Hector, Dr. Sam Fitch, Li Shao, Jonathan Allen and Nabil Mohamed. Beam times are always an adventure and a good team can make them so much easier.Special thanks to Prof. Guy Denuault for his continuous help regarding the pH experiments showing in chapter 4. I would like to thank Dr. Ana Perdomo Marin for teaching me how to make microelectrodes, and for Jiasheng Yi for letting me use his bench and micropositioner setup countless times during lockdown labtime. I would also like to thank the Hector group with its past and present members, but especially Dr. Samantha Soule, Dr. Hang Cheng, Dr. Joshua Wittham, Dr. Min Zhang, and Sidrah Hussein. I would like to thank the mechanical workshop and especially Alan Glass for always going with my strict demands on the fabrication of PEEK cells. I would also like to thank the glassblowers for their very nice work, whether it was the making of cells, microelectrode housings or cutting 5 mm thick Si wafers. My fellow chemists, Panashe and Wilma. I would also like to thank my island friends: Ben, Bernard, Tom, Will, Zach, George, Basil, Aaron, Ellie, Darcy and Kira. Playing music and hanging out with you guys has been the most fun experience and I hope we can continue doing so even when I am back on the mainland. Pour ma maman, merci de m'avoir envoyé le lien pour ce projèt il y a quatre ans et de m'avoir encouragé d'y aller et d'y rester. Merci de toujours être là pour moi et les autres petits. Charles und Ninon, Ihr seid meine besten Schwestern und ich danke Euch fuer Eure Unterstuetzung waehrend ich so weit weg war. Liebe Esthis, ohne Dich waehre diese Arbeit sehr doof gewesen. Danke, dass Du immer fuer mich da bist und Dir meine wilden Theorien anhoerst.

To Esther.

Abbreviations

AAO	Anodic Alumina
AC	Alternating Current
ALS	Advanced Light Source
CA	Chronoamperometry
CE	Counter Electrode
CMC	Critical Micelle Concentration
CTAB	Cetyltrimethylammonium Bromide
DC	Direct Current
DCM	Dichloromethane
DLS	Diamond Light Source
DWBA	Distorted Wave Born Approximation
EASA	Electrochemically Assisted Surfactant Assembly
EISA	Evaporation Induced Self Assembly
GISANS	Grazing Incidence Small Angle Neutron Scattering
GISAXS	Grazing Incidence Small Angle X-ray Scattering
ILL	Institut Laue-Langevin
ITO	Indium-tin Oxide
MDE	Micro-disk Electrode
OCP	Open Circuit Potential
OTAB	Octadecylrimethylammonium Bromide
PMMA	Poly(Methyl Methacrylate)
PVD	Physical Vapour Deposition
REF	Reference Electrode
SANS	Small Angle Neutron Scattering
SAXS	Small Angle X-ray Scattering
SDD	Sample Detector Distance
SEM	Scanning Electron Microscopy
SLD	Scattering Length Density
TEOS	Tetraethyl Orthosilicate
WE	Working Electrode

Chapter 1

Introduction

Electrodeposition is an effective way to modify a surface by depositing a layer of a new material, which is then chemically bound to that surface and hence results in very well-adhered coatings. The technique, which has been in use for over 200 years, plays a major role in the making of protective or decorative coatings, ranging from gold coating jewellery to nickel-plated strings for electric guitars up to chrome plated car parts. The beauty of the process lies within the high deposition rates and the possibility to coat "around corners", as well as being of lower cost than classic coating procedures which require vacuum/high temperature conditions.[1–4]

Nowadays, interest has grown around the use of electrodeposition to form nanoparticles, where the size and number density of the nuclei depend on the chosen experimental parameters. The study of nucleation in electrodeposition has a long history with significant advances being made in the 1950s.[5] Much of the fundamental description of electrochemical nucleation was established in the 1980s and 1990s,[6–13] nevertheless there still remain areas of disagreement and continued development.[14–16] Scharifker and Mostany were the first to report a general theoretical description of the current transients obtained during three-dimensional electrochemical nucleation on a finite number of active sites, taking into account the overlap of growth centres during diffusion limited growth.[12,13] This model was refined by Sluyters and Rehbach,[7] and further by Heerman and Tarrallo.[8] The essential element within the theoretical considerations is the concept of planar diffusion zones and their overlap, using so-called nucleation exclusion zones around the nuclei. Scharifker *et al.* later described the spatial distribution of nucleation rates around growing spherical nuclei in which zones of reduced nucleation are the result of calculating the realistic rate distribution around nuclei. Their explanation includes the broadening of size distributions from overlapping diffusion fields, which were then demonstrated experimentally by Liu *et al.* using conditions of decoupled growth in order to achieve narrower size distributions.[10,11,17,18] They showed through simulations that the nearest neighbour distances for the 1st, 2nd and 3rd neighbours differ from random nucleation. For Pb, Ag and

Cu this was later shown experimentally using electron microscopy, where the nearest neighbour distance followed a geometrical progression.[19,20] From a theoretical viewpoint, this mechanism was recently described analytically by Tomellini, who elucidated how the nearest neighbour distribution of particles evolves from Poissonian to non-random pair correlations during progressive nucleation.[21]

Further detailed advances were made in 2013 with Ustarroz *et al.*, proposing a generalised aggregative growth mechanism for electrochemical deposition.[22] The model was derived from TEM experiments performed on carbon coated TEM grids, on which Ag and Pt were electrodeposited respectively on a time scale ranging from 1 ms to 1000 s. It states, that instead of classical Volmer-Weber dynamics, an aggregative growth mechanism governs the deposition. Nucleation of nanoclusters takes place initially, which then grow until reaching a critical size at which they remain stable versus redissolving. Consecutively, surface diffusion driven by electrochemical potential leads to the aggregation of clusters, where the extent of partial or full coalescence dictates the occurrence of further growth by direct attachment. The study shows that the critical size reached by stable nanoclusters does not depend on potential or time of the deposition, but on the employed materials. Their morphology however depends on the nucleation rate and surface mobility, which both react to the applied overpotential. Similarly, the coalescence kinetics are potential dependent and hence determine whether a structure evolves in a dendritic fashion (low coalescence) with small particles, high porosity and surface coverage or to full recrystallisation with island-like particles of less number.

In a later study, this model was implemented into finite element simulation of the electrochemical process by Mamme *et al.*, which focuses on the influence of overpotential and surface mobility.[23] Using a random walk algorithm for modelling, the study shows that the surface mobility of nanoclusters has greater influence on the deposition nature than the applied overpotential. By showing that nucleation kinetics alone are not sufficient to describe the evolution of the number of clusters over time, the model was modified to take cluster aggregation into account. This leads to the emergence of two regimes, in which either nucleation or aggregation dominate the process, which corresponds to the findings of the study mentioned previously.[22] In the same year, Macpherson *et al.* undertook similar work aimed at the tracking of single atoms evolving to crystalline nanoparticles during electrodeposition, showing the movement of atomic Au-clusters on the surface of a boron-doped diamond electrode and their transition to crystalline nanoparticles.[15] Even surface-mediated Ostwald ripening was observed, were atoms are exchanged between sufficiently close ordered nanoparticles and disordered atomic clusters, with atoms travelling from the atomic cluster to the nanoparticle, a process during which the initially ordered nanoparticle becomes disordered, only to recrystallize once the process is nearly finished.

These studies have added important considerations to the classical electrochemical model and show the importance of experiments targeting the structural properties of electroplated materials. This in turn requires further development of experimental

techniques within the field, allowing for deeper analysis of the underlying processes.

This introductory chapter contains general background information on theory and methods relevant to this work. Not everything described was practically used for this thesis, but it is required to build the general context.

1.1 Classical electrochemical theory

The first equation one encounters when approaching electrodeposition or electrochemistry, is the general charge transfer reaction (Eq. 1.1), where species O are reduced to species R by receiving a number of n electrons or species R are oxidised to species O by giving away n electrons:

$$O(aq) + n \cdot e^{-}(m) \Longleftrightarrow R(aq). \tag{1.1}$$

Nernst showed that the potential at an electrode in a standard electrochemical system is given by (Eq. 1.2):

$$E_e = E^{\Phi} + \frac{RT}{nF} ln(\frac{a_O}{a_R}) \tag{1.2}$$

where the Equilibrium potential E_e depends on the standard electrode potential E^{Φ} and the activities of a_O and a_R at the electrode surface (R denote ideal gas constant, T the temperature, F the Faraday constant, and n the number of electrons). For the case of depositing a metal Me on any substrate S, the overpotential η_c (the difference between electrode potential and reaction potential) needed for the metal to crystallize on the surface can be written as[24]

$$\eta_c = E - E_{Me/Me^{z+}} = -\frac{RT}{zF} ln(\frac{a_{Me_{ads}}}{a_{0,Me_{ads}}}), \tag{1.3}$$

with $a_{Me_{ads}}$ and $a_{0,Me_{ads}}$ denoting the activities of Me_{ads} when E does not correspond to the Nernst equilibrium potential (z: oxidation state according to $Me \rightarrow Me^{z+} + z\, e^{-}$). This departure from equilibrium conditions. This definition requires that all contributions involved in the process are sufficiently fast to be treated as being in thermodynamic equilibrium. Deposition of the metal Me happens whenever $\eta_c < 0$ or $\Delta\mu > 0$ (cathodic region, supersaturation), stripping occurs when $\eta_c > 0$ or $\Delta\mu < 0$ (anodic region, undersaturation). The difference in chemical potential $\Delta\mu$, which describes the amount of energy to be released/absorbed by a given species through a change in their concentration, can be used to rewrite Equation 1.3. Using the chemical potential $\mu_i = \mu_i^0 + (RT) ln(a_i)$, we obtain the equation:

$$\Delta\mu = \mu_{Me_{ads}} - \mu_{Me_{0,ads}} = zF(E - E_{Me/Me^{z+}}), \tag{1.4}$$

with the standard chemical potential μ_i^0 for component i. While the dissolution of Me can happen wherever atoms are more loosely bound to the crystal, the deposition happens mostly at so-called "kink" sites, which are for example defects on the surface. Budevski *et al.*[24] describe all of this in detail, including the fact that depending on the cluster morphology (2D/3D), under- and overpotential deposition can occur.

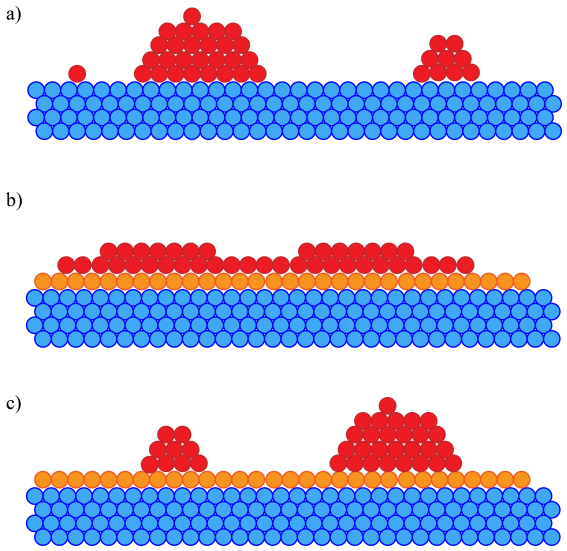

FIGURE 1.1: a) Volmer-Weber island growth b) Frank-van der Merwe layer-by-layer growth and c) Stranski-Krastanov (island growth on strained layers).Redrawn.[24]

They also distinguish between different mechanisms for the deposition of metals on a substrate, depending on the binding energy of atoms on "foreign" or "native substrates": if the binding energy Ψ of the deposited atom is lower to the substrate than to its own kind, deposition occurs according to the "Volmer-Weber" (3D island growth) model, independently of the crystallographic misfit between substrate and deposit. If the binding energy Ψ is higher to the substrate than to its own kind, "Frank-van der Merwe" (2D layer-by-layer) growth happens for combinations with small crystallographic mismatch (hetereoepitaxial growth), whilst "Stranski-Krastanov" growth dominates when the mismatch is large, resulting in the initial growth of strained layers with island growth on top of them (3D on 2D). Figure 1.1 illustrates the mentioned growth mechanisms. All three rely on the initial formation of clusters/particles on the surface, driven by the deposition potential. Any particle that exceeds a certain dimension will begin to grow, having undergone so-called nucleation before. As shown by the *Gibbs energy of cluster formation* (Eq. 1.5)

$$\Delta G(N) = -Nze|\eta| + \Phi(N), \tag{1.5}$$

every electron transfer induced by the formation of a nucleus (N atoms) decreases the Gibbs energy of the system, but at the same time some of the energy has to be invested into the formation of new interfaces, represented by $\Phi(N)$. Equation 1.5 shows that, depending on the energy needed to create the interfaces of formed nuclei, the process might be spontaneous or not, regardless of the presence of any overpotential η: for small nuclei, the second term of the equation dominates, resulting in a positive $\Delta G(N)$. Therefore, the formation of small nuclei can in this case only occur within a fluctuation of energy only. For sufficiently large nuclei, the first term dominates and a negative $\Delta G(N)$ is achieved to form a particle, which does not dissolve again. The critical change

in Gibbs energy needed for the formation of a spherical nucleus is given by:

$$\Delta G_{crit} = \frac{\sigma A_{crit}}{3} = \frac{N_{crit} z e |\eta|}{2}, \tag{1.6}$$

with the surface energy σ and the critical surface A_{crit}, which illustrates why at higher overpotentials, less atoms are needed to nucleate a particle. From the previous equation, the rate of nucleation r can be written as:

$$r = A \cdot exp(-\frac{\Delta G_{crit}}{kT}), \tag{1.7}$$

which is the Volmer-Weber equation (1926) (with the rate constant k and the pre-exponential factor A).

One of the major advantages of electrodeposition compared to chemical or physical vapour deposition is the possibility of using the electrical response of a system in order to follow its behaviour. The recording of the system's potential or current resulting from any applied electric signal can be used to determine important properties. For the special case of nucleation, chronoamperometry has been extensively used and several articles include models describing the current transients resulting from the application of a potential step to an electrochemical system.[24–33] As discussed previously, the applied potential does not only affect the rate of nucleation and therefore the occurrence of instantaneous or progressive nucleation but also the size of the deposited nuclei, their number density on the surface and equally importantly, the driving of secondary reactions that might affect deposition (water splitting/electrolyte decomposition). Whilst there have been many articles dealing with theory behind diffusion-controlled growth during electrodeposition, a coherent model for both short and long times[12,34] was derived only in 1999 by Heerman and Tarallo.[8] They cleared up the discrepancies that had arisen from two articles prior to theirs, where models for short and long times had been presented individually. The essential element to be extracted from their article is the dimensionless equation (Eq. 1.8) for the current density J during diffusion-limited deposition (with the constant $k = (2\pi)^{3/2} D (Mc/\rho)^{1/2} (N_0/r)$, describing the growth rate of diffusion zones, where D denote diffusion coefficient, M molar mass of the deposit, c concentration, ρ density and N_0 the density of active nucleation sites):

$$J(rt) = \frac{1}{(rt)^{1/2}} \frac{\Phi}{\theta} (1 - exp(-krt\theta)). \tag{1.8}$$

Here, θ is the fractional coverage, Φ a function related to a Dawson's integral (tabulated). For high values of rt, $\Phi \rightarrow 1$ and instantaneous nucleation occurs. For small values of rt, $\Phi \rightarrow \frac{2}{3} rt$ and we deal with the case of progressive nucleation. A very common technique to graphically distinguish between instantaneous and progressive nucleation is to plot the current transients in a dimensionless form t/t_m vs I/I_m altogether with the theoretical curves of both limiting cases in order to see which one has

the higher resemblance to the data.[12] Heerman and Tarallo have also proposed a technique including non-linear regression of the current transients and an iterative fitting procedure using the Levenberg-Marquardt algorithm.[35] This is used for the extraction of nucleation rate constant and site density from experimental data, but brings a number of issues to the table as to its validity, as discussed in the following section.

1.2 Current understanding of electrochemical nucleation dynamics

In recent years it was found, that the current and particle number from experimental surface analysis systematically deviate from the values expected from current transient analysis. Classical models for electrochemical phase formation lack the inclusion of dynamic (time/space) nucleation rates, as well as the effect of surface movement and aggregation of nuclei, and the dynamic nature of nucleation sites. One has to bear in mind that the measurable current is a convolution of several electrochemical processes, which can lead to similar transients even with fundamentally different mechanisms governing individual reactions. This underlines the importance of a combined analysis of electrochemical data as well as a detailed surface analysis in order to resolve classical and non-classical effects occurring. In 2018, Ustarroz. *et al.* proposed the a new approach to determine the temporal evolution of cluster number, including especially the effect of cluster surface mobility and comparing numerical simulations with experimental data. The number of clusters versus time after the application of a step potential is given by:[23]

$$N(t) = N_0[1 - exp(-A_0 \cdot (t - t_{ind}))], \tag{1.9}$$

with N_0 being the nucleation saturation number density, A_0 the nucleation rate constant and t_{ind} the induction time, which takes into account processes happening before the formation of stable nuclei. Equation 1.9 relies on the assumption that a stable nucleus remains immobile on the electrode surface following its successful formation. When including the aggregation of nuclei, their number can be described as (Eq. 1.10)

$$N_{Nuclei}(t) = N_{inf} \cdot (1 - exp[-A_{Nuclei} \cdot (t - t_{ind})]), \tag{1.10}$$

which in turn allows for the number of clusters on the surface $N_{Clusters}(t)$ to be expressed by (Eq. 1.11):

$$N_{Cluster}(t) = N_{Nuclei}(t) \cdot B \cdot (1 + exp[-A_{AGG} \cdot (t - t_{ind})]). \tag{1.11}$$

N_{inf} is the nucleation number density at saturation, A_{Nuclei} the real nucleation constant, B (0¡B¡0.5) a correction factor limiting the saturation number density of bigger clusters, A_{AGG} the aggregation rate constant which depends on the surface diffusion coefficient

$$D = D_0 \cdot N_{adatoms}^{\alpha}, \tag{1.12}$$

of a cluster (D_0: surface diffusion coefficient of an adatom, $N_{adatoms}$: number of adatoms in a cluster, α : relative surface mobility factor). As shown in Figure 1.2 (top), the equation not taking aggregation into account (yellow curve) is only valid for ”longer” times,

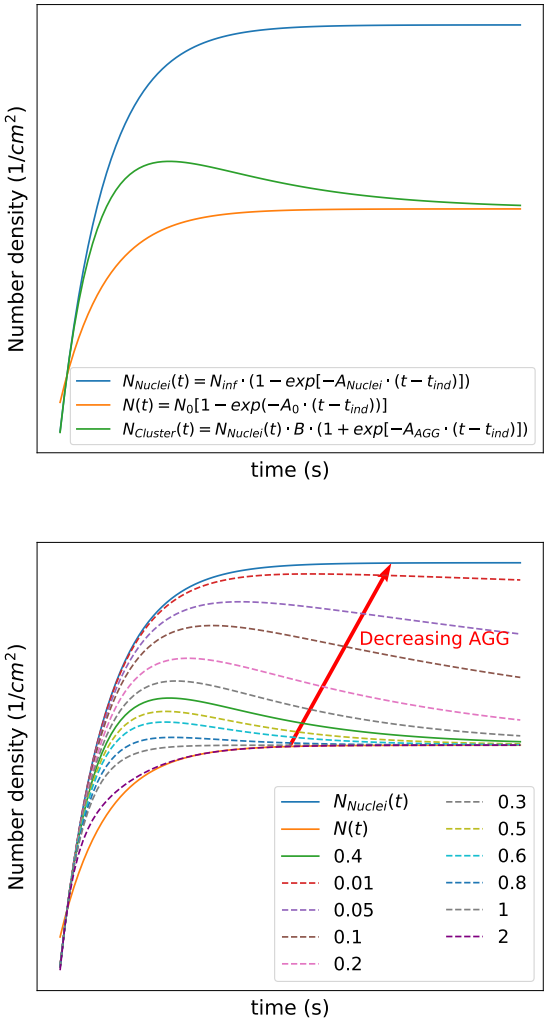

FIGURE 1.2: (top) Visualisation of different N(t): (amber) the total number of nuclei, (green) the number of clusters including aggregation and (blue) the number of nuclei when omitting aggregation. (bottom) Plotting $N_{Clusters}(t)$ for a variation of A_{AGG} using a fixed nucleation rate . Redrawn.[23]

which however can reside in the millisecond range depending on the applied conditions. It can be seen, that even without considering nucleation itself from an energetic point of view, the surface mobility of cluster does significantly influence their number density. Figure 1.2 (bottom) shows that, for a fixed A_{Nuclei} the effect is not significant for slow surface mobility compared to the formation of new nuclei.

The general influence of mobile aggregates on the process of phase formation can be summarised as follows: A high overpotential η leads to larger clusters with large size distribution if the surface mobility is high (low α), whereas a low surface mobility generally leads to a higher number of clusters of smaller size and narrower distribution. Figure 1.3 shows an illustration of the phenomenon for the combinations of high and low values of η and α.

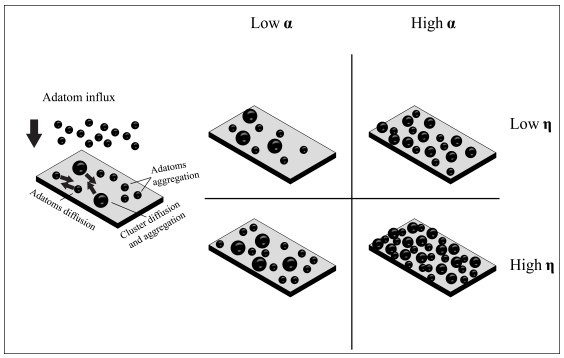

FIGURE 1.3: Schematic drawing of adatom deposition and aggregation during electrodeposition and the effect of overpotential (η) and relative surface mobility factor (α) on the distribution of nanoclusters. Redrawn.[23]

1.3 Gold electrodeposition

One of the earliest electroplating experiments to be reported, was the deposition of gold onto silver coins done by Brugnatelli in 1803.[36,37] Nowadays, electrolytic deposition of gold is a fairly well established method for the making of gold coatings in various fields of interest, *e.g.* electronics, cars, telecommunication, biomedical processes, etc. due to the material's outstanding corrosion resistance and electrical conductivity. Gold is ideal for the making of contacts, bonds and other high reliability conductors. In the field of catalysis and optoelectronics, an appreciation of the size-dependent properties of gold nanoparticles has increased over recent years.[38–41] Gold nanoparticles can be produced in a variety of shapes using self-assembling surfactants,[42] or *e.g.* by electrodeposition.[43–48]

Gold deposition can be done using $K(AuCl)_4$ as the source of gold ions in a chloride bath, as done in this work. KCl, HCl or KNO_3 are typical supporting electrolytes. The reactions have been established as the following:[49–52]

$$[AuCl_4]^- + 3e^- \rightleftarrows Au^0 + 4[Cl]^-. E_0 = 802\,mV \ vs\ Ag/AgCl \tag{1.13}$$

$$[AuCl_4]^- + 2e^- \rightleftarrows [AuCl_2]^- + 2[Cl]^-. E_0 = 726\,mV \ vs\ Ag/AgCl \tag{1.14}$$

$$[AuCl_2]^- + e^- \rightleftarrows Au + 2[Cl]^-. E_0 = 951\,mV \ vs\ Ag/AgCl \tag{1.15}$$

The electrochemical nucleation and growth of gold has been the focus of multiple studies, using a variety of deposition baths and substrates. Oskam *et al.* used scanning transmission electron microscopy and electrochemical analysis to show that the deposition of gold on silicon substrates follows three-dimensional island growth.[53] Concerning the observation of non-classical effects, Dudin *et al.* reported a systematic decrease of particle number over time when studying the nucleation and growth of gold on single walled carbon nanotubes.[50] Very recently, McPherson *et al.* investigated the nucleation and growth of Au at an atomic lengthscale, describing the dynamics as a

combination of surface movements and structural changes of clusters and nuclei depending on their surroundings.[15] These studies show that even a system as widely and sucessfully used as the electrodeposition of gold, still has unknown aspects to be discovered.

1.4 Bismuth Telluride electrodeposition

Thermoelectric materials allow for the conversion of electricity into heat or *vice versa*. Big effort was and is still put into finding materials with a high figure of merit value ZT, which is defined as (Eq. 1.16):

$$ZT = \frac{S^2 \sigma T}{\kappa}, \tag{1.16}$$

with the Seebeck coefficient S, the electrical conductivity σ, the absolute Temperature T, and thermal conductivity κ.[54] The ideal material would hence have a high Seebeck coefficient and electrical conductivity, while conducting heat poorly: Goldsmid calculated the ratio of electrical and thermal conductivity in an article published 1954,[55] using the relationship for electronic mobility previously described by Shockley and Bardeen,[56] and thermal conductivity elucidated by Peierls.[57] Further applying the theory led to the identification of Bi_2Te_3 as the best candidate for thermoelectric refrigeration, as it is a semiconductor with high mean atomic weight and reasonably simple preparation routes.[58] A variety of classic methods (metallurgy, vapour deposition, ...) have been used to synthesise this compound,[59–64] but an especially cost-effective route for synthesising Bi_2Te_3 films is electrodeposition, allowing for the controlled formation of the material at room temperature.[65–68] Magri *et al.* used an aqueous electrolyte solution made from a mixture of Bi^{3+} and $[HTeO_2]^+$ solutions, where the deposition reaction consisted of the electroreduction of Te ions in the presence of a Bi salt:[65]

$$3HTeO_2^+ + 9H^+ + 12e^- \rightarrow 3Te + 6H_2O \tag{1.17}$$

$$3Te^{4+} + 2Bi^{3+} + 18e^- \rightarrow Bi_2Te_3. \tag{1.18}$$

With electrodeposition being recognised by the thermoelectric community, deeply investigating the deposition processes has become even more essential in order to achieve perfect control.[69–73] This is especially important regarding the intrinsic flexibility of the technique regarding composition and morphology of deposits under various conditions. Therefore, efforts were made to further optimise the system. For example, dimethyl sulfoxide (DMSO) can be used as a solvent instead of water,[74] as this increases the solubility of Bi and Te and also the electrochemical window, which allows for deposition at lower potentials before encountering the decomposition of the electrolyte. Another alternative was recently reported by our colleagues Meng *et al.*, who described

the deposition of Bi_2Te_3 in the weakly coordinating solvent dichloromethane (DCM).[75] Using this kind of solvent can facilitate the electrodepositon into nanotemplates, especially when their dimensions reside below 10 nm.[76,77] This shows the great general interest around gaining a better understanding of the electrodepositon of not only Bi_2Te_3 but chalcogenides as a whole, for a wide range of electronic applications.[78–83]

Bismuth Telluride nanowires Bi_2Te_3 compounds are commercially available thermoelectric materials with their figure of merit ZT typically approaching a value of 1 at room temperature, limiting their application to specialised needs of power generation in laboratory equipment or space missions.[84,85] The material could be a much more promising candidate for thermoelectrics when made as a nanomaterial, where strongly enhanced properties have been predicted.[86–89] Again, a multitude of ways exists to fabricate nanowires: *e.g.* solvothermal approaches[90] or the, in this context more relevant, electrodeposition into nanostructured templates,[91] *e.g.* using anodic alumina (AAO) templates[92–95] or track etched PMMA membranes.[96] Sander *et al.* describe the deposition into AAO templates with a pore size of 25, 50 and 75 nm.[97] Used is an aqueous electrolyte made of 0.075 M Bi and 0.1 M Te in 1 M HNO_3. This electrolyte system, which bases on the electrochemical reduction of Bi^{3+} and $HTeO_2^+$ in acidic solution has been successfully used for the fabrication of Bi_2Te_3 nanowires and films.[98–103] A recent review on Bi_2Te_3 nanowire fabrication came to the conclusion, that the figure of merit ZT increases from 0.58 to 1.16 through the use of nanoscale morphologies, which however had its focus on techniques other than electrodeposition.[104] Decicated studies on electrodeposited Bi_2Te_3 nanowires have shown, that *e.g.* the filling ratio of the template, which strongly influences the electronic conductivity, plays a strong role regarding the performance of such nanowire arrays.[105] Mavrokefalos *et al.* reported, that another very important factor is precisely controlling the chemical composition, as contaminations of the deposition environment can lead to dramatically lowered ZT values of nanowires compared to their bulk counterparts, as impurities can result in parasitic doping, which decreases the thermoelectric performance.[95]

1.5 Template electrodeposition

A promising technique for the making of nanostructured materials, is the so-called "template electrodeposition".[106] Briefly summarised, the technique comprises the application of a non-conductive but nanostructured material on the target electrode, much like a structured resist would be used for lithography. A variety of materials is used as such, ranging from oxide based materials,[107–111] track etched polymer membranes,[112–114] surfactant/polymer templates,[115–117] spherical particles in the micron/nano range,[118–120] and even dynamic templates such as of gas bubbles forming layers on an electrode during deposition.[121–124] After filling the pores with the material of choice, the template is

removed by etching/calcination in order to obtain the target nanomaterial.
The electrolyte solution aside, template electrodeposition requires specialised tuning of the applied conditions in order to achieve uniform growth throughout the whole template regarding filling of pores and desired composition. A common method used is pulsed electrodeposition, where the "on" and "off" time are tuned to achieve the required growth behaviour.[125–128] Other approaches focus on radically changing the physicochemical environment, *e.g.* using a supercritical fluid in order to minimise surface tension and enhance precursor diffusion into the template,[76,129,130] or a deep eutectic solvent.[131] Despite the variety of available techniques, template electrodeposition remains a challenge for every set of electrode/electrolyte system and is hence a promising candidate for deeper investigations, especially involving time resolved experiments.[132,133]

1.6 Electrochemically Assisted Surfactant Assembly (EASA)

The making of structured materials through template surfactant assembly is a nowadays widely used technique, because it allows for the fabrication of materials with specifically tailored properties.[134] Films, powders and fibres can be made this way in order to match their specific application. A major field of interest lies within structured thin films, which have use in the realms of optics, electronics, electrochemistry and as sensing devices. Evaporation induced surfactant assembly (EISA) relies on the formation of a structured film through the self-assembly of a surfactant/precursor (silica) network during solvent evaporation.[135,136] This sol-gel based process can be carried out using spincoating, dipcoating and inkjet printing and has led to significant advances in the field of mesoporous nanostructures. A caveat of the technique however is, the restriction to flat surfaces when used with spin coating or dipcoating. Additionally, there is no selectivity as the entire substrate will be covered with the film except when using printing. The most prominent issue however is that apart from 3D structures (cubic), the most common structure found in 2D-hexagonal silica films are pores which are aligned parallel to the substrate, which inhibit the transport of material. Pore alignment and morphology remain the most challenging tasks within this practically simple technique.

In 2007 Walcarius *et al.* reported on a process which enables the formation of vertically aligned mesoporous silica structures through electrochemistry.[110] This so-called Electrochemically Assisted Surfactant Assembly (EASA) uses the application of a potential difference (potentiostatic) between two electrodes to induce the self assembly of a cationic surfactant on a conductive substrate. The current flow during deposition results in a local change of pH from acidic to alkaline which catalysis the condensation of silica species to form a mesostructured gel. The fundamental difference of EASA silica deposition to EISA methods and other techniques using cathodic metal deposition around polymeric templates is the controlled growth of a sol-gel network from the surface and the fact that the species generated at the electrode are not incorporated into the film.[137] Walcarius *et al.* showed the applicability of the procedure on a variety of conductive substrates such as indium-tin oxide (ITO), gold, carbon, platinum and even on non-conductive substrates using high electric fields.[138] For the deposition, a pre-aged solution of tetraethyl orthosilicate (TEOS) and cetyltrimethylammonium bromide (CTAB) in 1:1 ethanol/water at pH=3 is used. A sufficiently negative potential applied to the working electrode is then needed to induce film formation through the local increase of pH at the electrode surface. The locally increased pH leads to the polycondensation of the silica sol and hence yields a surfactant templated film. Depending on the substrate material the optimized potential value can be different.

The proposed mechanism for EASA is shown in Figure 1.4. As soon as the cathodic potential is applied, hemispherical micelles form on the electrode surface.[139–141] Due to the use of an ethanol/water mixture as medium, the hydrocarbon chains of the CTAB

assemble inside the hemimicelles leaving the TEOS on their outside. With increasing time the micelles grow vertically to channels. Following deposition, the surfactant is removed by calcination or Soxhlet extraction, leaving a mesoporous film with vertically aligned pore channels. The argument given as proof that only the applied potential leads to micelle formation is the reported critical micelle concentration (CMC) of 30 mM [CTAB] in 1:1 water/ethanol with[142] as reference, although the article does not obviously contain that information and a value of 22 mM was reported by Li *et al.*[143] Interestingly, below and above the CMC, vertically aligned structures can be obtained. This was reported by Goux *et al.*, who investigated the effect of sol composition on the obtained structure.[137] The dramatic effect of the sol composition and especially the CTAB/TEOS ratio is known for EISA (different mesophases, orientations). For EASA, this effect is limited to either forming vertically aligned hexagonal structures, or barely any structure at all. Ordered silica structures can be obtained over a wide range of surfactant concentrations where especially its ratio to the TEOS is important for successful film fabrication. An optimized ratio of CTAB/TEOS is 0.32, which still depends on the total concentration of TEOS and cannot be chosen arbitrarily.[137] The lattice parameter of CTAB derived silica structures resides around 3.8 nm for C_{14}TAB up to 4.6 nm for C_{18}TAB, where the structure expands when made with a longer surfactant. One problem arising when using EASA is the formation of unwanted aggregates on the film. Their presence can be attributed to the quickly expanding hydroxide diffusion layer, reaching dimensions much larger than the actual film thickness. This way, the change in pH does not only drive polycondensation of silica at the electrode surface, but also in the bulk solution above. This effect was shown to be increasing with deposition time, but is also related to the use choice of counterion as well as sol ageing time.[144,145] With increasing CTAB/TEOS concentrations it has been found that more surface aggregates are formed due to the enhanced gelification speed. Taking all of these factors in mind, optimized values for EASA deposition of mesoporous silica films can be summarized as the following:[137]

- Short deposition times (10-20 s)
- $[\text{TEOS}] < 125\,\text{mM}$
- $[\text{CTAB}]/[\text{TEOS}] = 0.32$

Silica films can be made through EASA under potentiostatic as well as galvanostatic conditions. The film thickness is limited by the enhanced formation of surface aggregates with increasing depositions time.
Further investigating the mechanism behind EASA is a very interesting field. The fact that the quickly growing diffusion layer leads to the formation of ordered films in the first couple hundreds of nm, while nucleating (porous) aggregates above it at

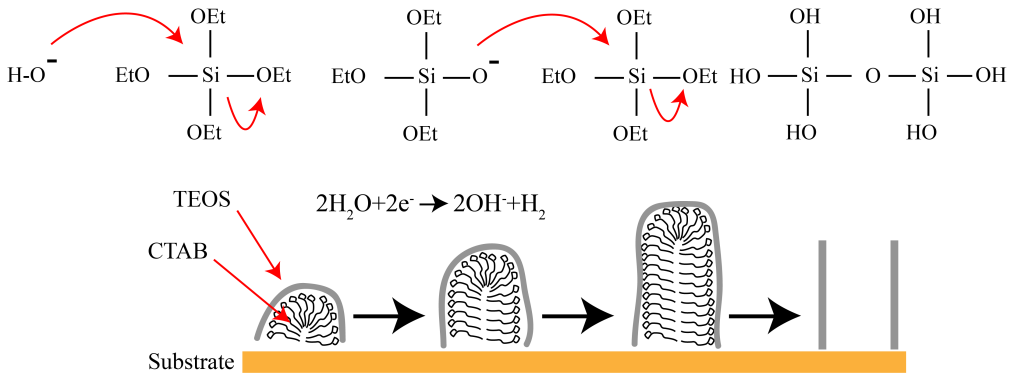

FIGURE 1.4: Schematic drawing of the proposed mechanism behind the EASA method used to fabricate vertically ordered mesoporous silica films. Adapted from.[138]

conditions both above and below the CMC leads to many open questions. The vertical alignment should require surface effects in addition to the electrochemical process (surface CMC[140]), but it doesn't explain why the ordered film formation in vertical direction would stop in favour of aggregates. Another possibility could be that secondary products of the polycondensation reaction inhibit the continuous deposition of aligned pores, an effect that would increase in magnitude with deposition time. Understanding the exact conditions at which vertically aligned silica pores are formed should enable the precise tuning of the deposition conditions to ones where it is possible to deposit thick films with no aggregates.

Chapter 2

Instrumental methods

This chapter contains details on all experiments done for this thesis. All reagents were used as received unless stated otherwise. Table 2.1 lists the reagents used for the experiments shown in this work. Whenever aqueous solutions were made, deionised water (resistivity$>18\,\mathrm{M\Omega\,cm}$) from a Suez Select Fusion was used.

TABLE 2.1: Reagents used for the experiments.

Name	Chemical Formula	Manufacturer	Use
Ammonia solution (35w%)	$NH_3(aq)$	Fisher	Silica sol
Ammonium tetrachloropalladate	12%wt. $(NH_4)_2PdCl_4$	Sigma	pH sensor
Dichloromethane (DCM)	CH_2Cl_2	Fisher	Bi_2Te_3 deposition
Dichloromethane(deuterated)	CD_2Cl_2	Eurisotope	Bi_2Te_3 deposition
Ditetrabutylammonium tellurium hexachloride	$[^nBu_4N]_2[TeCl_6]$	Reid Group	Bi_2Te_3 deposition
Ethanol	C_2H_5OH	Fisher	Silica Sol
Heptane	2%wt. C_7H_{16}	Sigma	pH sensor
Hexaamine ruthenium chloride	$Ru(NH_3)_6Cl_3$	Sigma	Redox probe solution
Hexadecyltrimethylammonium bromide	$[(C_{16}H_{33})N(CH_3)_3]Br$	Sigma	Silica sol
Hydrochloric acid	HCl	Fisher	silica sol/pH experiments
Mesitylene	C_9H_{12}	Sigma	Silica sol
Nitrogen	N_2	BOC	Solution degassing
Octadecyltrimethylammonium bromide	$[(C_{18}H_{33})N(CH_3)_3]Br$	Sigma	Silica sol
Octaethylene glycol monohexadecyl ether	$C_{16}EO_8$	Sigma	pH sensor
Potassium chloride	KCl	Fisher	Supporting electrolyte
Potassium hexacyanidoferrate	$K_4[Fe(CN)_6]$	Sigma	REF calibration
Potassium hexacyanoferrate	$K_3[Fe(CN)_6]$	Sigma	REF calibration
Potassium tetrachloroaureate	$K(AuCl_4)$	Sigma	Au deposition
Tetrabutylammonium chloride	$[^nBu_4N]$	Sigma	Bi_2Te_3 deposition
Tetrabutylammonium bismuth tetrachloride	$[^nBu_4N][BiCl_4]$	Reid Group	Bi_2Te_3 deposition
Tetraethyl orthosilicate	$Si(OC_2H_5)_4$	Sigma	Silica sol
Sodium hypochlorite	NaClO	Fisher	REF fabrication
Sodium nitrate	$NaNO_3$	Timstar	Silica Sol
Sulphuric acid	H_2SO_4	Fisher	pH sensor

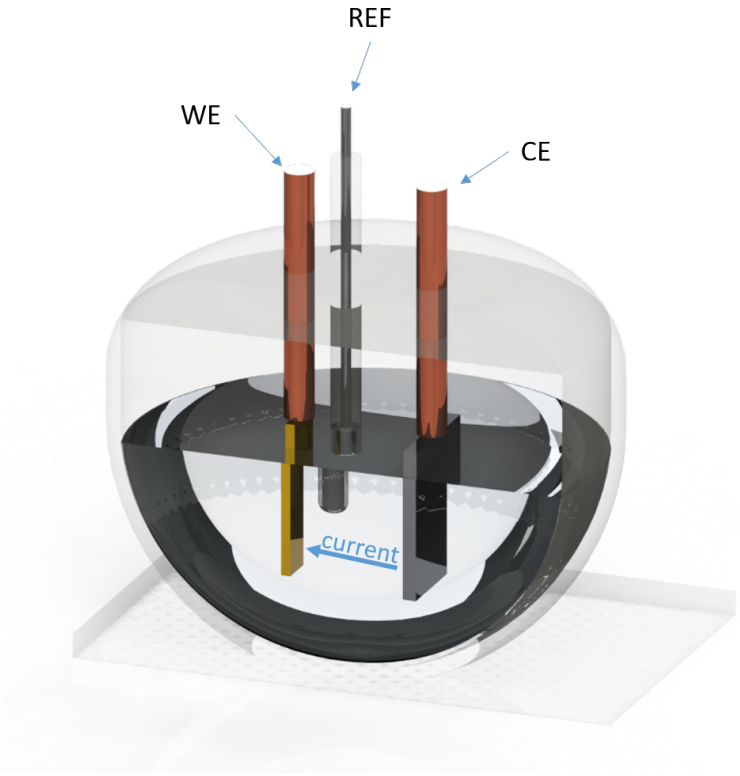

FIGURE 2.1: Schematic drawing of the three-electrode deposition setup, including counter (CE), Working (WE)and reference (REF) electrodes.

2.1 Electrochemical setup

For all electrochemistry experiments, a standard three electrode geometry (see Figure 2.1) consisting of working (WE), counter (CE) and reference electrode (REF) was used. Micro-disk electrodes (MDE) were additionally used for pH profiling experiments, as shown later in this chapter. The following potentiostats were used to drive the electrochemical reactions: Biologic SP-150 and VSP, MetrOhm Autolab.

2.1.1 Working electrodes (WE)

All working electrodes used in this work are essentially sputtered thin film electrodes, with silicon wafer as the substrate. The production was fully done by fellow researchers in Electronics and Computer science.

TiN thin film

The TiN electrodes were made by sputtering 200 nm of TiN onto a 700 μm thick Silicon wafer (Buehler Helios, rate: 0.135 nm/s), which results in surfaces with a roughness of 1 nm (H=0.349, lateral correlation length=20.72 nm. The measurements are consistent

with data from Kirchner *et al.*[146] Standard substrate sizes are 8x20 mm and 5x30 mm, depending on the application. For the neutron experiment, a custom made wafer with 5 mm thickness (Si-Mat) was used to make substrates of 54x10 mm, coated with 200 nm of TiN.

2.1.2 Counter electrodes (CE) & Reference electrodes (REF)

Pt gauze/thin film

Pt gauze was used as counter electrode material, with a typical area of 10x20 mm. For the neutron experiment, a thin film Pt electrode was used, which consisted of 200 nm Pt on Si wafer (10x54 mm). Prior to any experiment, the gauze electrodes were cleaned by flame.

Ag/AgCl&silver rod pseudoreference

The standard reference electrode used in this work was [Ag]/[AgCl] in 4 M KCl. The silver wire was prepared by leaving it in sodium hypochlorite over night. When a DCM electrolyte was used, the reference electrolyte solution was changed to 0.1 M $[^{n}Bu_4N]$ in DCM.
For the EASA experiments, just the silver wire part of the electrode was used in order to avoid the potential blockage of the electrode frit (pseudo-reference).

2.2 Potentiometric pH measurements

Nowadays, glass electrode pH-meters are part of a standard laboratory inventory.[147] The earliest use of the glass electrode was reported more than 100 years ago by Fritz Haber and Zygmunt Klemensiewicz,[148] just after the conceptual introduction of the pH scale by S.P.L. Sörensen in 1909. While this type of pH meter has proven its utility for common everyday scientific routines, there is a multitude of PH sensors available today. These range from pH responsive polymers to ion sensitive field effect transistors and optical method based sensors.[149,150] The different approaches allow for specific characteristics as *e.g.* scaling down sensor dimensions, or very fast response times. A particularly interesting procedure reported by Bartlett et al.[151] and later applied for time resolved pH measurements by Serrapede et al.[152,153] is the use of nanostructured Pd films on a microelectrode as potentiometric sensor.

2.2.1 Properties of nanostructured Palladium hydride

The discovery of its ability to take up significant amounts of hydrogen in the 1860s[154] has put palladium very much within the scope of research.[155] When subjected to hydrogen, palladium forms α, β and a transition phase of α + β. During the latter, the open circuit potential (OCP) of the electrode is merely dependent on the ambient pH, making it a pH sensor.[156,157] This stage only lasts until the palladium hydride compositions reverts to only the α-phase being present and it necessitates the prior "loading" of the material with hydrogen. This is typically done in solution by either potentiostatic or galvanostatic means of electrolysis, were the latter does not require any knowledge of the ambient pH in the first place. This is done until the phase transition from the α + β, to the β-phase is observed. After that, the sensor is left to stabilise in its "plateau region", during which it can be used as a sensor. The "life time" of the sensor depends on its volume (area x thickness of the Pd film), the degree of loading, and most importantly on the chemical environment it is put into, as *e.g.* the presence of air/oxygen increases the loading time, while decreasing its life time. It has been shown that this kind of sensor can be applied in conditions at which glass electrodes fail to work (ph>12), and its fabrication as a microelectrode allows for very local and also time resolved measurements.[153]

2.2.2 pH sensor fabrication

The pH sensors used in this work consist of a Pt-microdisk electrode (Pt-MDE) coated with a nanostructured Pd layer, which is galvanostatically loaded with hydrogen until

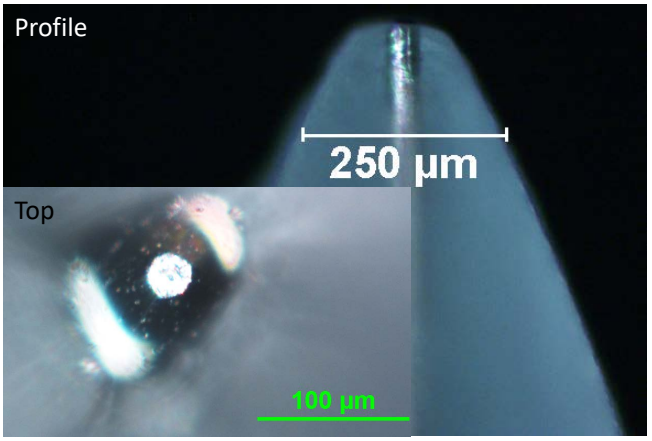

FIGURE 2.2: Profile and top view optical microscopy of a home made Pt-MDE in soda glass enclosure with 25 µm Pt wire. $R_{glass}/R_{wire} < 4$

reaching a composition at which the open circuit potential of the sensor depends on the ambient pH only.

Pt microdisk electrodes Pt-MDEs were fabricated in house through the following method: Pt wire of desired diameter 25 µm was cut to a few cm length and inserted into the tip of a soda glass pipette. After flame-sealing the wire into the glass tip, a homemade heating/suction setup was used to further seal the glass around the wire along a length of roughly 1 cm. Attention was paid to obtaining a bubble free enclosing of the wire. Abrasive paper of increasing grit (P80-P1200) was then used to shape and flatten the electrode tip to minimise the amount of glass body around the wire at the most shallow angle possible. Figure 2.2 shows microscopy images of profile and top view of such an electrode were the fraction of the radius of glass body and Pt wire lie below 4 (R_{glass}/R_{wire}). Once successfully shaped, the Pt-MDE was wet-polished using alumina powders of 1, 0.3 and 0.05 µm size for 1, 2, and 4 minutes respectively. After that, cyclic voltammetry in 1 M H_2SO_4 was performed using Pt gauze as counter and a saturated mercurous sulphate electrode (SMSE) as reference until a stable voltammogram was achieved.

Pd plating procedure The procedure for the making of nanoporous Pd films requires a plating mixture. In preceding work done by Bartlett et al., the following composition was used: 12%wt. $(NH_4)_2PdCl_4$, 39%wt. H_2O, 47%wt. $C_{16}EO_8$, and 2%wt. C_7H_{16},[151] which was adopted for this work. In practise, 1 g of mixture was prepared at once, meaning that the amounts given can be read in units of g. $(NH_4)_2PdCl_4$ was firstly dissolved in H_2O, yielding a dark brown liquid. Next, $C_{16}EO_8$ was added while stirring with a spatula, as the high amount of added $C_{16}EO_8$ leads to a mixture with high viscosity. Following the addition of C_7H_{16}, the mixture was heated to 40°C using oil or sand bath for 30 min and then cooled down in an ice bath for 3 min (beaker sealed

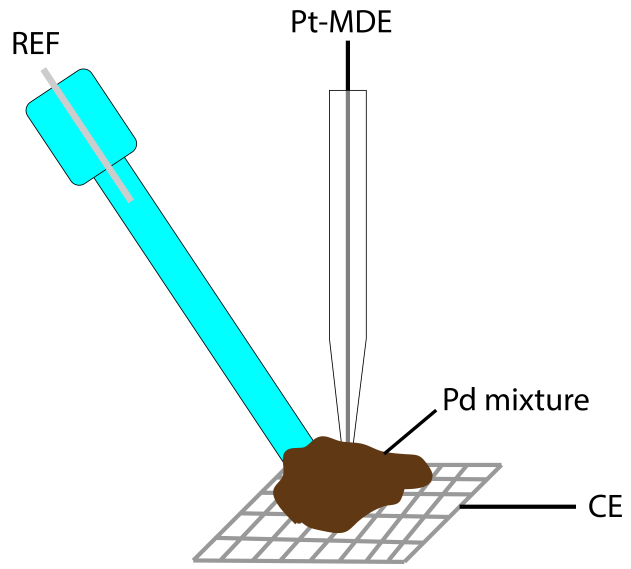

FIGURE 2.3: Illustration of the Pd plating setup, showing the Pt-MDE working and the reference electrode sunk into a small amount of Pd mixture, which in turn rests on the Pt gauze counter electrode.

with parafilm). The heating and cooling cycle was then repeated twice more, whereby the mixture was stirred using a spatula after each cooling period. This process, called "annealing", is necessary for the formation of the desired hexagonal phase within the mixture, which is needed as the template for subsequent deposition of nanoporous palladium.[151]

Pd deposition was done using a three electrode setup consisting of the Pt-MDE as working, Pt gauze as counter and Ag/AgCl as reference electrode, as shown in Figure 2.3. For the assembly, one spatula of Pd mixture was placed on the flat-laid Pt gauze. Both reference electrode and Pt-MDE were immersed in the mixture from above, whereby it was made sure that the reference electrode tip was free from any droplets of storage electrolyte. As described by Serrapede et al.,[153] the Pd deposition procedure was performed by applying 0.4 V (potential in double layer region) vs Ag/AgCl for 5 s, followed by 0.1 V until reaching a charge passed of 10 µC, corresponding to 2 mC/cm^2. Figure 2.4 a) shows a cyclic voltammogram (3 rounds) of a Pt-MDE in Pd plating mixture at 2 mV/s between 0.05 V and 0.4 V vs Ag/AgCl (setup as shown in Figure 2.3), while Figure 2.4 b) shows the previously mentioned plating procedure. During the initial 5 s in the double layer region, virtually no current is recorded, whereas when switching to 0.1 V a clear current transient corresponding to the deposition of Pd can be seen. As the nanoporous Pd film still contains the organic template at this stage, the Pd-MDE was put in water over night.

Characterisation and calibration of PdH sensors After washing out the organic template from within the Pd film using deionised water, the electrode needed to be electrochemically activated. This was done once again by cyclic voltammetry in 1 M H_2SO_4

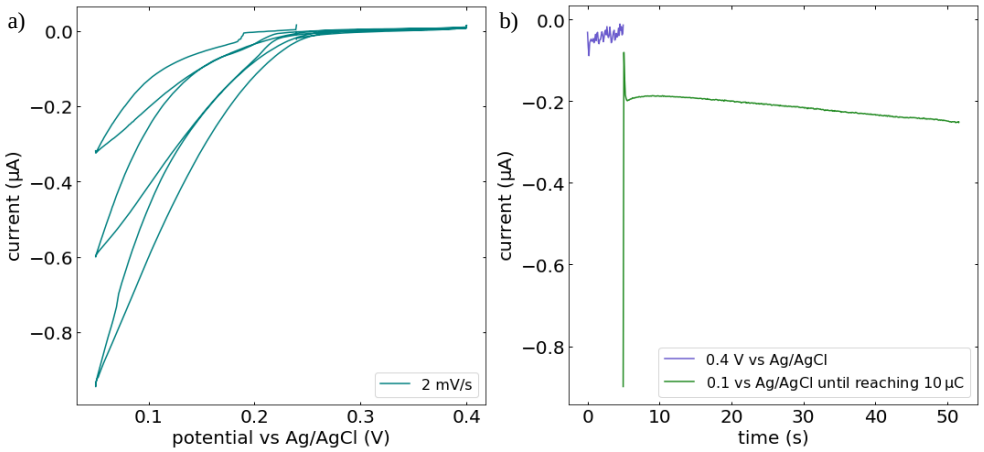

FIGURE 2.4: a) Cyclic voltammogram (3 rounds) of a Pt-MDE in Pd plating mixture at 2 mV/s between 0.05 V and 0.4 V vs Ag/AgCl. b) Potentiometric electroplating of Pd on Pt-MDE, consisting of 5 s at 0.4 V, followed by applying 0.1 V until reaching 10 µC or 2 mC/cm^2.

(SMSE reference and Pt gauze counter electrodes) at 100 mV/s. During the experiment, it was clearly visible that there was still some amount of organic template left within the Pd film, as the electrochemical response gradually increased until reaching the classic shape of palladium (roughly 10 cycles needed). This observation is in clear agreement with the ones made by Serrapede *et al.*[153] Figure 2.5 a) shows a comparison of both, Pt- (blue) and Pd-MDE (green) at 100 mV/s vs SMSE and with Pt gauze counter electrode. The current of the blue line was multiplied by 10 in order to make the shape visible on the same scale as the green line. As expected, the nanoporous Pd film leads to a great increase in electrochemical area, a larger current and hence better visibility of the voltammetric features (which have been described to great length in previous work[153]). Figure 2.5 b) shows the same Pd-MDE cycled at 10 mV/s, exhibiting the signature features of Pd in the cathodic region which are the result of the adsorption/desorption of hydrogen (i,vi), its insertion/extraction from the α-phase (ii,v) and β-phase of HPd (iii,iv). This step typically concluded the pH sensor preparation process and the electrodes were stored in deionised water until used.

Calibration According to Serrapede's work, the palladium hydride sensors exhibit Nernstian behaviour when used in oxygen free solutions (argon purged), and that the calibration curve (pH *vs* OCP) becomes more shallow the higher the amount of oxygen in the system. As means of comparison, calibration measurements were performed for the Pd-MDE. These were done in aqueous buffer solutions (Fisher Scientific, used as received), as shown in Figure 2.6 for Pd-MDEs 5 and 6 which were used in experiments that will be described later in this work. Both sensors were calibrated by galvanostatic loading at -18 nA in a pH buffer with a value of 4, 7, 10, and 13 until fully loaded. The buffer solutions were not deareated as this would not be possible with an actual

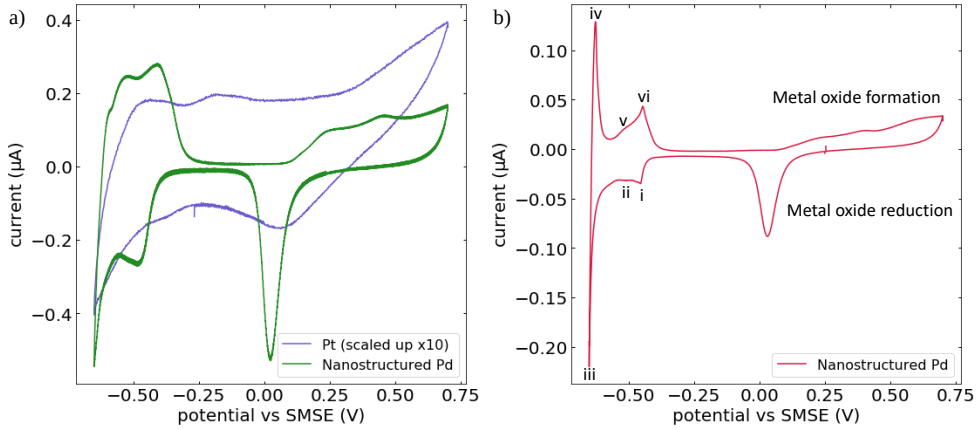

FIGURE 2.5: a) Comparison of both, Pt-(purple) and Pd-MDE (green) at 100 mV/s vs SMSE and with Pt gauze counter electrode. b) Pd-MDE cycled at 10 mV/s using the same setup as in a). Roman numbers depict: (i,vi) adsorption/desorption of hydrogen, (ii,v) insertion/extraction from the α-phase (iii,iv) and β-phase of HPd.

silica sol (foaming of the surfactant) and would hence decrease the comparability of measurements dramatically. Open circuit potential (OCP) was measured until the sensor returned to its initial potential. The measurements were repeated at least thrice for each electrode per respective buffer solution, of which the observed plateau regions potentials were averaged. Pd-MDE5 had a slope of -46.35 mV/Ph, while Pd-MDE6 had -38.56 mV/pH. These values are in agreement with the results in Serrapede's work on the influence of air in solution on the sensors. The discrepancy between the two values might be the result of the slightly different electrode geometries and "work age" of both sensors, as Pd-MDE5 was calibrated before and Pd-MDE6 after a series of measurements. The slopes were calculated using a custom Python script using the Scipy package for linear fitting of the data. The life time of the sensors during calibration was typically in the range of 2-3 minutes, as the solution was not degassed beforehand and the oxygen present shortened the plateau phase would be a lot longer under oxygen-free conditions.[152,153,157]

***Operando* pH setup** Drawings of the *operando* pH setup used in this work are shown in Figure 2.7. Front, side and top view of pH sensor (grey), TiN working electrode (WE, amber), reference (green) and counter electrode (CE, silver) are depicted. As shown in the front view, the pH sensor was tilted away from the TiN WE in order to minimise their distance by physical contact between the two (glass body on TiN). The sensor was aligned this way so that the alkaline wave generated during the experiments could migrate past it with minimal disturbance.

The dynamic pH measurements were done using a Biologic VSP two channel potentiostat, where one of the channels was used as the "driving channel" connected to a TiN working electrode and the second one to the Pd-MDE. Both channels shared the same Ag/AgCl reference electrode. The counter electrode (Pt gauze) was connected to only

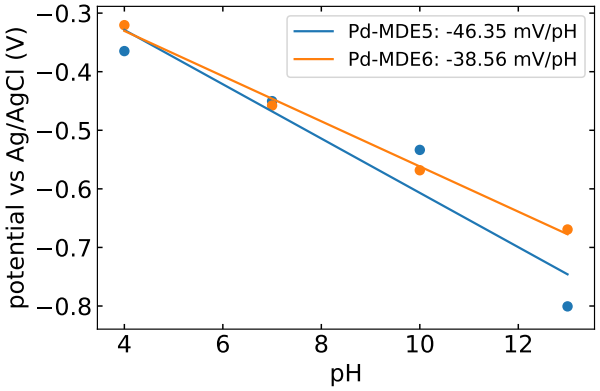

FIGURE 2.6: Calibration curves of Pd-MDE5 and 6 in aqueous buffer solutions at pH values of 4, 7, 10, and 13. The sensors were loaded galvanostatically prior to the recording of the open circuit plateau regions. Data points were averaged over at least 3 measurements. Slopes calculated using a custom Python script (Scipy package).

one of the channels due to inconsistencies when shared, which made a switching procedure necessary during the actual measurements. Figure 2.8 shows the connections used for the experiments: the reference electrode was always connected to both channels, and the counter electrode remained connected to channel 1 only. During the galvanostatic loading of the MDE, channel one was connected to the MDE (orange line). At this stage, the TiN WE was left not connected, and channel two remained idle. During the main experiment (red lines), the TiN working electrode was connected to channel 1, and the MDE to channel 2. Channel 1 would then be used to run the chronoamperometry experiment, while channel 2 recorded the OCP of the MDE. A vital detail in this endeavour was the synchronisation of both channels prior to the experiment, and the use of "pause" commands that would make the programme wait for a click by the operator.

A micropositioner made up from three micropositioner stages (Physik Instrumente, M605-01DD) assembled in an x-y-z configuration was used for precise movement of the MDE during the experiments. The stages were controlled by micro controllers (Physik Instrumente Mercury) and individually referenced before each use. A calibration image was taken ahead of each experimental run using a mobile USB microscope, for which the MDE was driven as close as possible to the electrode of interest up to achieving slight contact between the two. ImageJ[158] was then used to estimate the distance between MDE tip and working electrode surface.

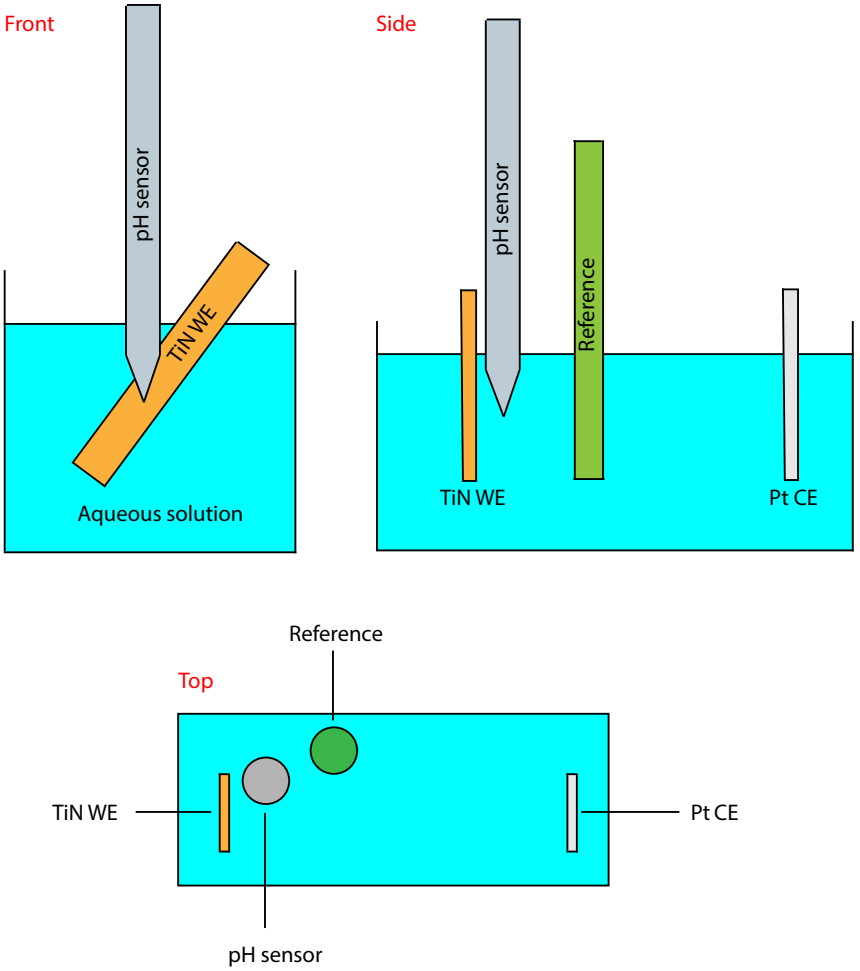

FIGURE 2.7: Schematic drawing of the electrode configuration for the dynamic pH measurements. pH sensor (grey), TiN working electrode (WE, amber), reference (green) and counter electrode (CE, silver) shown in front, side and top view. The TiN WE was tilted away from the pH sensor to minimise their distance by making physical contact between glass body and TiN WE.

2.3 Scanning electron microscopy (SEM)

Electron microscopy becomes useful when the structures to be resolved reside beyond the resolution limit of optical microscopy. Instead of photons, electrons are used in this technique as they have a much smaller wavelength, which is crucial for attaining the demanded high resolution. The wavelength λ is given by the de-Broglie equation:[159]

$$\lambda = \frac{h}{p}, \tag{2.1}$$

where h is Planck's constant and p the relativistic momentum of the electron. High electrostatic fields induce the emission of free electrons, which are accelerated by a high voltage (several kV) in direction of the sample surface. A condenser lens focuses them onto a very small spot, which scans the surface of interest line by line, emitting

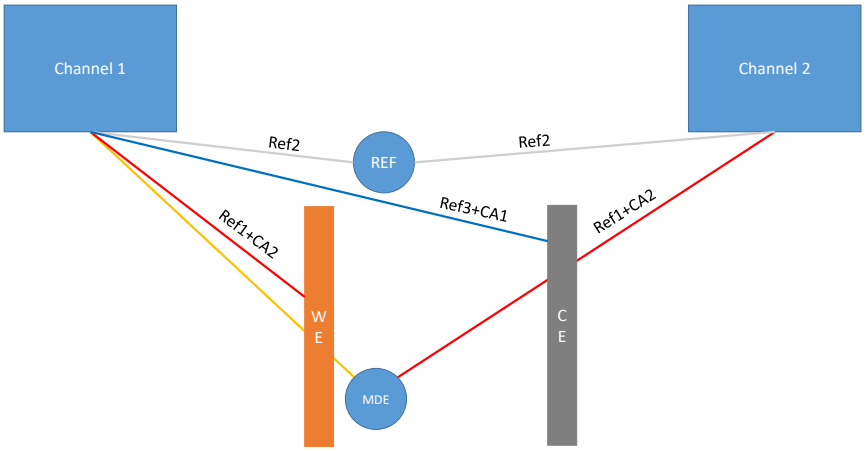

FIGURE 2.8: In situ pH connection diagram. Grey and blue connections remained intact throughout the whole experiment. The orange connection was only used for galvanostatic loading of the MDE, while the red lines show the connections which were used in the main experiment. The Biologic VSP twin channel potentiostat was used with synchronised channels.

secondary electrons. These are then recorded on a closely located detector. While the resolution mainly depends on the beam size, the contrast is determined by the conductivity and topography of the surface, which is why non-conductive samples have to be coated with a conductive coating beforehand in order to minimize surface charging effects.[160]

The SEM images in this work were taken on a JEOL JSM-6500F electron microscope with field emission electrode. The samples were always imaged as prepared with no additional coating applied. For metallic samples such as gold and bismuth telluride 15 kV acceleration voltage was used, while for silica based samples, 10 kV was used.

2.4 Small Angle Scattering

Small angle scattering using either X-rays or neutrons is a frequently used technique for the investigation of soft matter systems, *e.g.* polymers or even biological systems.[161–168] Many experiments allow for the use of a transmission geometry, as *e.g.* when looking at solutions or melts. When dealing with thin films however, a grazing incidence geometry presents multiple advantages which include the dramatic increase of probed surface area and statistical relevance of the data. In the following, the theory of X-ray and neutron scattering will be explained, as well as the effect of using a grazing incidence geometry versus one of transmission.

2.4.1 X-ray Scattering

When used in scattering experiments, X-rays probe the real-space electron-density, as they mainly interact with the electron shell of atoms. Figure 2.9 visualizes a basic scattering experiment. Monochromatic radiation with wavelength λ and intensity I_0 is used as incident beam, which scatters at the sample surface. The intensity I of the scattered beam is recorded by a detector D at a distance A, the so-called sample detector distance (SDD). The scattering vector $\vec{q}$ is defined by the the difference of the wavevectors (Eq. 2.2):[169]

$$\vec{q} = \vec{k_f} - \vec{k_i}. \tag{2.2}$$

The typical result of a scattering experiment is the distribution of the intensity in reciprocal q-space, $I(\vec{q})$.

where $|\vec{q}|$ is defined by the Bragg equation (Eq. 2.3):[170]

$$|\vec{q}| = \frac{4\pi}{\lambda} \sin\theta_B \tag{2.3}$$

with the Bragg angle θ_B which is half of the angle enclosed by $\vec{k_i}$ and $\vec{k_f}$. The interference function $S(\vec{q})$ (Eq. 2.4) describes the scattering properties for equal particles, where N_m stands for the total number of particles (monomers) in the sample and I_m the individual scattering intensity produced by each particle residing in the incident beam:[171]

$$S(\vec{q}) = \frac{I(\vec{q})}{I_m N_m}. \tag{2.4}$$

$S(\vec{q})$ is the ratio between the measured intensity and the one that would be measured if the particles scattered incoherently, that is often also referred to as structure factor. The scattering intensity $I(\vec{q})$ is usually divided into two contributions: Form factor $P(\vec{q})$ and the already mentioned structure factor $S(\vec{q})$ (eq. 2.5):[172,173]

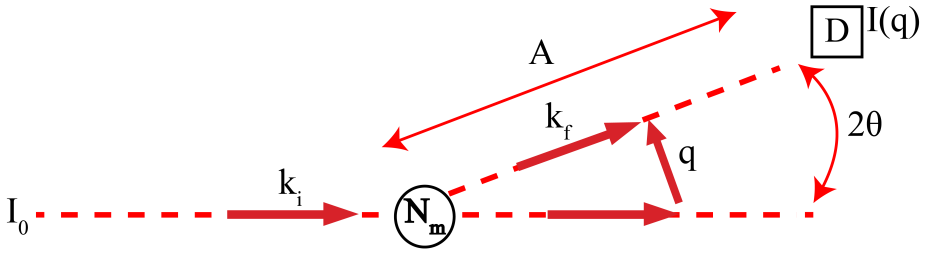

FIGURE 2.9: General setup of a scattering experiment. I_0 is the intensity of the incident beam with wavevector $\vec{k_i}$ that hits a sample consisting of N_m scattering entities. The scattered wave with intensity $I(\vec{q})$ and wavevector $\vec{k_f}$ is recorded using a detector D at a distance A. The Bragg scattering angle θ_B has half of the value of the angle enclosed by the intial and final wavevectors $\vec{k_i}$ and $\vec{k_f}$. Redrawn.[171]

$$I(\vec{q}) \propto S(\vec{q})P(\vec{q}). \tag{2.5}$$

$P(\vec{q})$ takes then into account the shape of the scattering objects, while $S(\vec{q})$ describes their structural organization within the system. The difficulty after acquiring a scattering spectrum is then to distinguish between the two contributions which is in many cases not of trivial matter.

2.4.2 Neutron Scattering

For neutrons, the interaction with matter during scattering does not happen at the electron shell (as it does for X-rays), but with the protons and neutrons in the nuclei of atoms. The wavelength of a neutron is given by the de Broglie wavelength (see equation 2.1). The Scattering Length Density (SLD) can be computed by summing the contributions from scattering lengths b_i (tabulated values[174]) arising from the presence of N atoms within a unit cell, as shown in the following equation (Eq. 2.6):

$$SLD = \frac{\sum_{i=1}^{N} b_i}{V_m}. \tag{2.6}$$

The neutron scattering lengths, which correspond to the strength of interaction between a nucleus and a neutron, do not follow any predictable trend. The values are almost randomly changing with atomic number, which can lead to significant differences even when comparing just two isotopes of the same element. Contrast matching by isotope exchange becomes hereby possible, which is used especially to minimise incoherent scattering from *e.g.* hydrogen by exchanging it to deuterium when looking at organic systems. This is very useful for specialized experiments, because whilst most heavy elements are practically opaque to X-rays (metals, semiconductors), neutrons can easily penetrate Al, Si,... which allows for the performance of experiments inside large

enclosures needed for *e.g.* high temperature/pressure without the need to include X-ray transparent windows. When it's needed to detect light elements, neutrons have an advantage because the scattering does not increase with atomic number Z, making it possible to have good contrast even for low Z elements. This means in general that a combination of both X-ray and neutron scattering enables the investigation of all kinds of contrast environments.

2.4.3 Grazing Incidence Small Angle Scattering

For thin films, a grazing incidence geometry is beneficial because it maximises the probed area due to the projection of the beam on the sample surface (see Figure 2.10). The technique is therefore called Grazing Incidence Small Angle (X-ray/Neutron) Scattering (GISAXS/GISANS), which makes it possible to probe a surface in its vertical and horizontal direction. As opposed to regular small angle scattering data, the image is the result of diffraction and reflection processes (processes schematically illustrated in Figure 2.11).[175] The regular Born approximation (BA) can hence not be used as the theoretical base for the process; the so-called distorted wave Born approximation (DWBA)[176] has to be used. Detailed calculations of the scattering patterns using DWBA exist, for example by Rauscher et al., who start from a planar surface which has a certain roughness and density fluctuations and calculate the specular and off-specular intensities resulting from various different geometries.[176] For the case of GISAXS/GISANS, the definition of the scattering vector $\vec{q}$ can be written as:[169]

$$\vec{q} = \vec{k_f} - \vec{k_i} = \frac{2\pi}{\lambda} \begin{Bmatrix} cos(\psi_f)cos(\alpha_f) - cos(\alpha_i) \\ sin(\psi_f)cos(\alpha_f) \\ sin(\alpha_i) + sin(\alpha_f) \end{Bmatrix}, \tag{2.7}$$

with incident angle angle α_i, reflection angle α_f in the xz-plane and ψ_f, the reflection angle in the xy-plane. Looking back at Figure 2.10, one can see a bright red spot in the detector image, which corresponds to the specular reflection of the beam. Beneath that, in z-direction, another local maximum in intensity can be found, which is called the Yoneda-peak.[177] Its location in $\vec{q_z}$ depends on the optical density of the probed material/interface and critical angle α_c which is given by the following ensemble of equations:

$$\alpha_c = \sqrt{2\delta}, \tag{2.8}$$

$$n = 1 - \delta + i\beta, \tag{2.9}$$

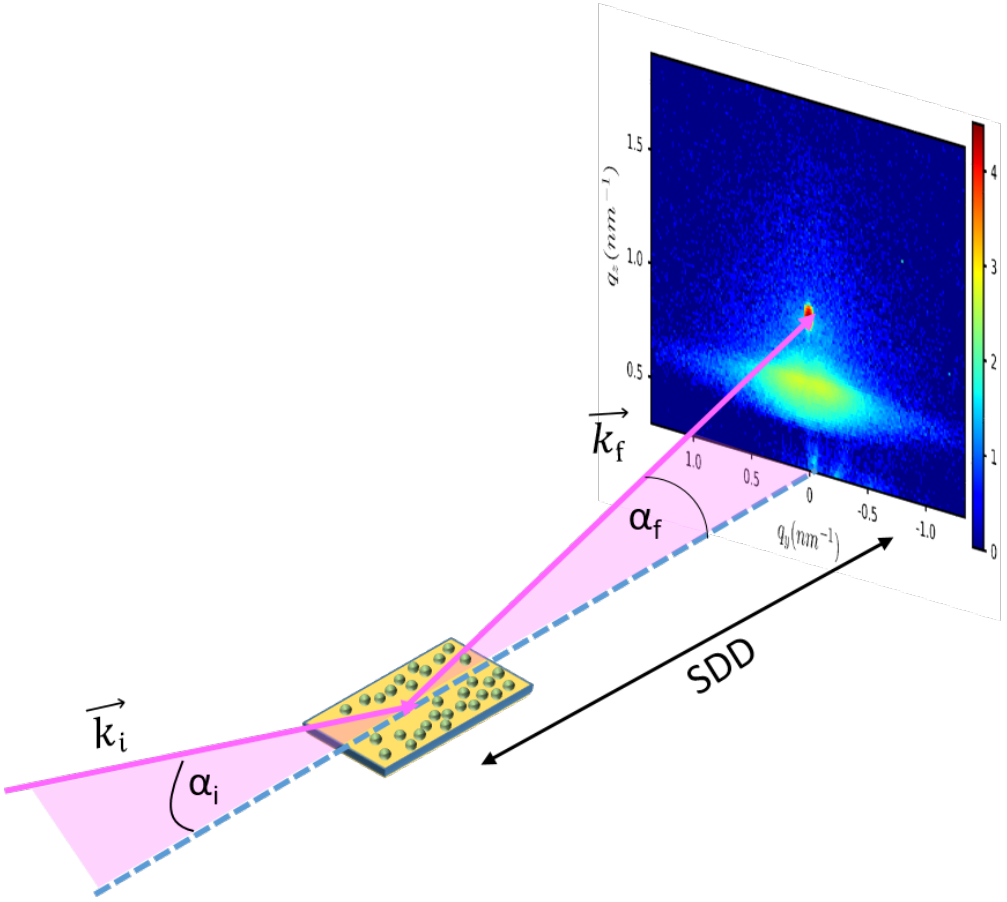

FIGURE 2.10: Schematic drawing of a GISAXS setup. The X-ray beam (pink) impinges on the sample surface under a very shallow angle α_i at exiting at an angle α_f. The scattering pattern is recorded on a two dimensional detector at a sample detector distance (SDD) of typically a few meters.

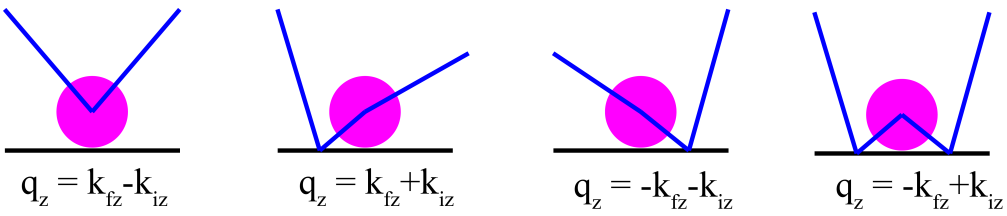

FIGURE 2.11: Illustration of the terms contributing to the full scattering cross-section calculated in the Distorted wave born approximation. Indices i and f denote in- and out coming beam respectively.

α_c relates to the complex refractive index n with its refractive part δ and the absorbent part β.[169] When using neutrons, usually the scattering length density SLD is used instead of δ and β, which converts *via*:[178]

$$\alpha_c = arcsin(\frac{\lambda\sqrt{16\pi SLD}}{4\pi}), \tag{2.10}$$

Information about form and structure factor can be extracted by analysing scattering data, which is typically done by integrating intensities along one direction ($\vec{q}_y/\vec{q}_z$) of the detector image. The best known software for GISAXS data treatment was presented by Lazzary et al.,[175] which provides a framework for fitting and simulating GISAXS data for a variety of different form and structure factors. They demonstrate the agreement between experimental data of a thin sputtered gold layer and a simulation of the 2D scattering image using truncated spheres as the particles, which are distributed over a 1D paracrystal. A more recently developed software for that purpose is BornAgain.[179] GISAXS has been used in combination with high resolution microscopy for the investigation of *e.g.* sputtering processes on silicon or polymer substrates by Schwartzkopf et al. and others in order to derive detailed atomistic models.[180,181] For electrochemical systems Ruge et al. developed a dedicated and very complex electrochemical cell, which was used to study the deposition of Gold on a Au(001) surface,[182] and in later work the structural reorganization of a Pt(111) surface whilst cycling in perchloric acid.[183,184] Hillman et al. in turn used *in situ* neutron reflectivity to study the deposition and dissolution of single and bi-component metal layers in real time.[185] X-ray diffraction has been used to investigate electrochemical interfaces in the context of *e.g.* single crystal surfaces[186,187] and catalysts.[188] This shows the variety of applications of scattering experiments on electrochemical systems, which in combination with real space methods can provide significant insights into the fundamentals of electrochemistry.

2.5 X-ray experiments

2.5.1 *Ex situ* experiments

In house

X-ray experiments were carried out on a Rigaku Smartlab with copper X-ray source, which provides a beam with an energy of 8 keV. GISAXS images were recorded for 1h unless stated otherwise at a sample detector distance of 301.5 mm. The incident angle for Au samples was set to $\alpha_i = 0.7°$, for Bi_2Te_3 to $\alpha_i = 0.37°$ and for mesoporous silica $\alpha_i = 0.3°$.

Warwick SAXS

One batch of samples was characterised at the University of Warwick using their dedicated SAXS instrument (Xenocs XEUSS 2.0), using a beam with an energy of 8 keV and a sample detector distance of 2480 mm. The incident angle was set to $\alpha_i = 0.7°$ with a collection time of 1 hour.

Advanced Light Source

Selected samples were measured at beamline 7.3.3 SAXSWAXS at Advanced Light Source, Berkeley, USA. For this, a beam energy of 10 keV was used at an angle of $\alpha_i = 0.567°$ and an SDD of 3529 mm on a Dectris Pilatus 2M detector.

2.5.2 *Operando* GISAXS cell v2

After a commissioning experiment (see Appendix A.1), a newly designed cell was made in order to improve sample changing and most importantly accelerate the alignment procedure through better reproducibility. Figure 2.12, shows a) an illustration of the setup and b) a schematic of the cross section indicating the location of all electrodes/contacts as well as the beam path (pink). As cell material, polyether ether ketone (PEEK) was used due to its great chemical resistance versus a large range of substances. A planar geometry of working and counter electrode was chosen to ensure even deposition across the whole area of 5x10 mm^2. A silver rod pseudo-reference was used for the silica experiments, but the cell enables the use of a regular Ag/AgCl electrode if needed. The first actual *operando* experiment was carried out from March 6-8, 2019 using v2 of the cell on DLS I07, with 2007.52 mm SDD and a beam energy of 12.25 keV (1.012 Å). The Dectris Pilatus 2M was in this case set to record 700 images in

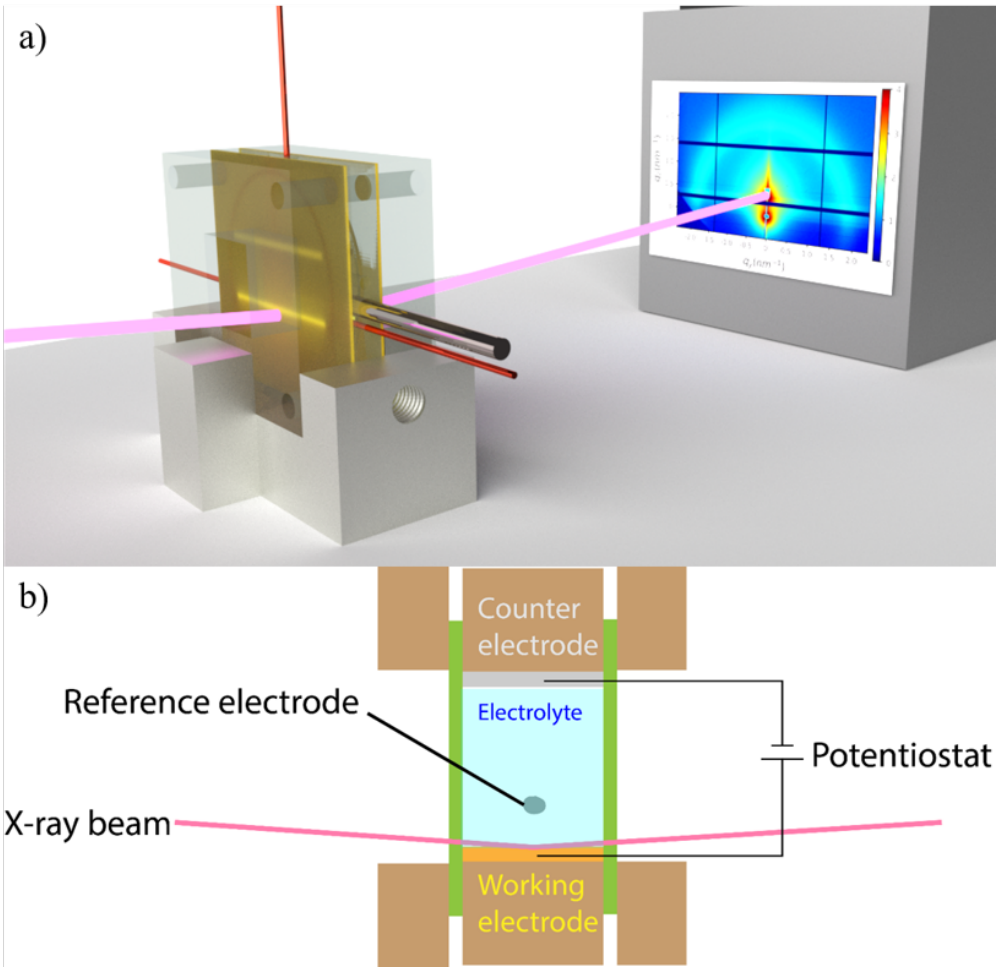

FIGURE 2.12: a) Illustration of the cell with the beam (pink) reflected at the substrate surface before reaching the detector. b) Schematic of the cell cross section, indicating the location of all electrodes/connections as well as the beam path.

one run with 100 ms exposure time and 20 ms readout time between images. An incident angle of $\alpha_i = 0.2°$ just below the critical angle of the TiN substrate was used in order to probe the entire film.

2.6 Neutron experiment

From October 10th to 17th 2018 at ILL in Grenoble, France, an *in situ* GISANS experiment during the electrodeposition of bismuth telluride in a DCM(d) electrolyte was performed. A cell made from polyether ether ketone (PEEK) was used on the D33 beamline, with TiN working, Pt counter and Ag/AgCl reference electrodes in a planar geometry. The beamline was set to a wavelength of 7 Å with a main detector distance of 6.7 m. Cells were filled in an argon-filled glovebox. The electrolyte used for all the experiments were prepared by dissolving 2.5 mM $[^{n}Bu_4N][BiCl_4]$, 3 mM $[^{n}Bu_4N]_2[Te_2Cl_6]$ and 0.1 M $[^{n}Bu_4N]$ in deuterated DCM. A deuterated solvent was used to minimize incoherent scattering from hydrogen atoms in the solvent and to enhance the scattering length density. Calculated values for each layer in the setup and the experimental setup itself can be seen in Figure 2.13. The advantage of this method is the investigation of the electrode surface whilst avoiding absorption effects from the electrolyte. During the experiment, a potential of -2 V was applied for 1, 2, 10,70,... s after which scattering images were recorded for the duration of 1 h each. The incident angle was chosen at 0.5° in order to sufficiently penetrate the TiN layer.

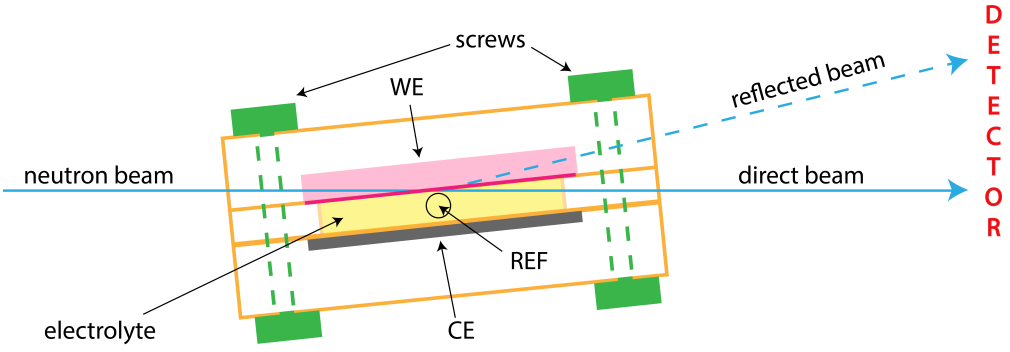

FIGURE 2.13: GISANS setup where neutron beam (blue) reflects on the DCM/TiN interface (red) during the electrodeposition of Bi_2Te_3.

Chapter 3

Structural dynamics during electrodeposition of metals and semiconductors

This chapter contains results related to the fundamentals of electrodeposited metals and semiconductors. It is divided into individual sections regarding the deposition of gold and bismuth telluride onto titanium nitride working electrodes. As mentioned in the introduction (Chapt.1), research on the nucleation and growth of metals onto foreign substrates had its origin decades ago. Nevertheless, there is still research in this field done today, where the most cutting edge techniques available nowadays are used to describe the deposition process from the first atom or particle nucleating on the surface to particles coalescing into a continuous film.
Particularly interesting is the still scarcely answered question on the mobility of electrodeposited particles: significant work in this field was done in recent years, using transmission electron microscopy to follow the nucleation and growth of individual particles along deposition. This approach relies heavily on available computing resources needed to identify particles one by one in consecutive images and following their morphological evolution in relation to their surroundings. This is where the use of a scattering based technique can be beneficial, as all information is averaged over the whole investigated area. While this of course takes away the detail of each singular aspect of the process, it is possible to see collective effects and trends, which motivated the use of GISAXS/GISANS in this work.

3.1 Gold deposition on TiN

In this work, the deposition of Au onto TiN was used as a model system of which the deposition conditions are well known and the reagents needed are readily available and not very hazardous. In the following subsections, the results obtained from this study will be shown, starting from the electrochemical characterisation of the system and going on to further studies of the structure of nano particles deposited at various conditions.

3.1.1 Gold chloride bath

Gold was deposited from aqueous solution onto flat TiN substrates. The electrolyte consisted of 1 mM $K[AuCl_4]$ in 0.1 M KCl supporting electrolyte. Preparation was typically done using the following quantities:

- 10 ml Milli-Q water
- 3.8 mg $K[AuCl_4]$
- 75.45 mg KCl

Prior to any deposition, the electrolyte solution was degassed using dry nitrogen gas for a minimum time of 15 minutes. The electrochemical system was characterised using cyclic voltammetry at a scan rate of 50 mV/s starting from open circuit potential (0.7 V vs. Ag/AgCl) to -1.0 V, then to 1.2 V and back, as shown in Figure 3.1. The reduction peak at 0.2 V during the first cathodic scan can be attributed to the initial deposition of gold on the TiN substrate. In aqueous chloride solutions containing $[AuCl_4]^-$ there are three possible anodic redox couples with the reactions (see Section 1.3 for details). A nucleation loop is observed below -0.5 V in this first scan. In subsequent scans, the gold reduction peak shifts to more positive potentials, which indicates that the deposition of Au on Au is favoured versus TiN. The transition from just one to two reduction peaks in scans 2 and 3 indicates the presence of both Au(III) and Au(I) complexes, both of which can be reduced to Au(0) during deposition. The corresponding oxidation (stripping) peak is seen just above 1.0 V which is in agreement with previous work on this system.[50–52,189]

3.1.2 Chronoamperometric studies

Current transients Gold was deposited onto TiN for different potentials and times. Figure 3.2 shows the different transients during 5 s of constant deposition from 200 mV

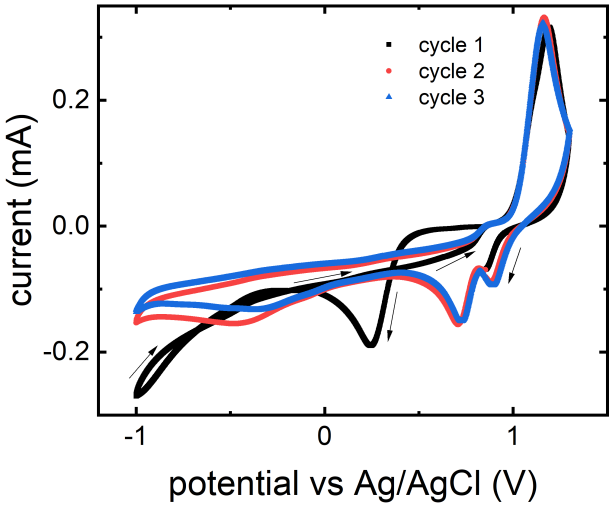

FIGURE 3.1: Cyclic voltammetry of a TiN working electrode in 1 mM $K[AuCl_4]$ in a 0.1 M KCl supporting electrolyte with Pt counter and Ag/AgCl counter electrode. Scan rate: 50 mV/s; cycle numbers colour coded. Potential sweep starting from open circuit potential (≈0.7 V) going to -1.0 V and then to 1.2 V on the backwards scan.

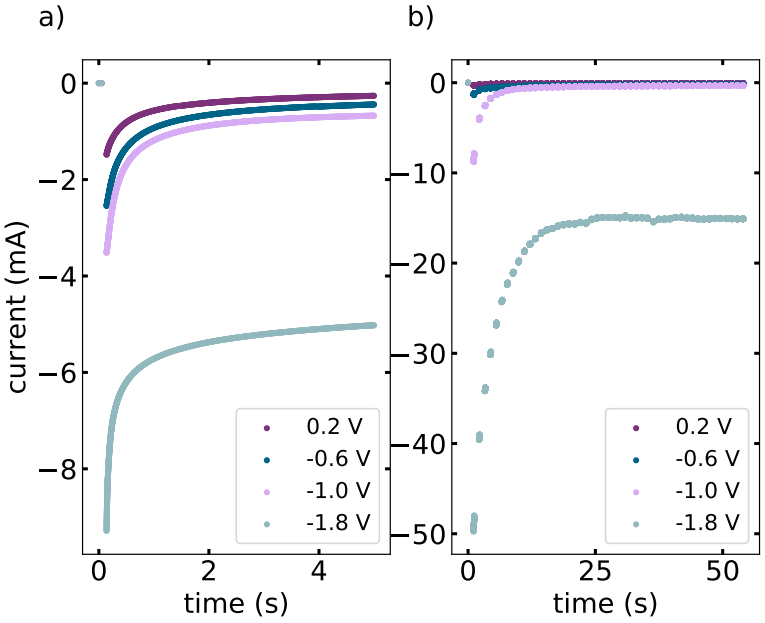

FIGURE 3.2: Current transients of gold deposited onto TiN in 1 mM $K[AuCl_4]$ in 0.1 M KCl supporting electrolyte with Pt counter and Ag/AgCl counter electrode for different a) constant potentials 0.2, -0.6, -1.0, and -1.8 V for 5 s and b) pulsed potentials of 0.2, -0.6, -1.0, and -1.8 V for 50x0.1 s with 1 s rest in between pulses.

to -1.8 mV (a)) and three corresponding curves for pulsed deposition (b)). The first noticeable feature of these curves is the fact that the current increases generally with higher overpotential, which matches general expectations.

Scanning electron microscopy SEM images of selected samples can be found in Figure 3.3. At the lowest overpotentials, very few large nuclei can be seen in the surface, and these seem to decrease in size with higher overpotentials. Generally, the number of nuclei increases significantly with higher overpotentials. This corresponds to the behaviour one would expect from equation 1.5. A low overpotential requires a large number of atoms to cross the energetic barrier of cluster formation. At higher overpotentials, less atoms are needed and hence smaller nuclei form in larger numbers on the surface due to the increased probability of exceeding the limit of cluster formation.
The same potentials were then used to do an experiment with pulsed potential, where the potential was pulsed for the same total time as before but with an increment of 0.1 s, with 1 s rest in between pulses. The corresponding SEM images can be seen in Figure 3.4. Again, with higher overpotentials, smaller nuclei are produced in higher numbers, but more interestingly, the density of nuclei can be dramatically increased through pulsing at lower overpotentials compared to constant potential deposition. This is due to the resting periods the system has between pulses, during which the local concentration near the electrode surface (which is initially depleted during application of the potential because ions from the solution are converted to adsorbed atoms on the electrode surface) can equilibrate itself and resume with a higher local concentration of ions available for deposition.

Particle radii From the SEM images, a mean value for the particle radii can be extracted, which was done in this work using the software ImageJ.[190] This required individual tuning of the image's contrast and sharpness to ultimately convert it to a binary image, where the particles would be black dots on a white surface. From this state, ImageJ is able to calculate the number of particles and their average area, which in turn can be converted to a particle radius whereby they were all approximated as perfectly spherical using $R = \sqrt{A/\pi}$. The resulting radii for constant and pulsed deposition of gold for 5 s/50x0.1 s at different potentials can be seen in Figure 3.5. The plots show what was expected from looking at the images: the particle radius decreases with higher overpotential, namely from a few hundreds of nm to tens of nm for constant potential, and from around 70 ± 10 nm to 40 ± 20 nm during pulsed deposition, except for the highest overpotential were the size distribution increases significantly. This could be due to particles going into coalescence (as can be seen in Picture 3.4), which increases the error for the particle detection algorithm dramatically, as in this case all particles are assumed to be perfectly spherical projections. For lower overpotentials the

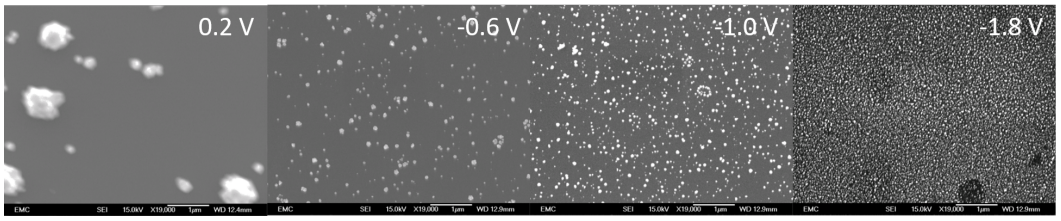

FIGURE 3.3: SEM images of gold deposited on TiN in 1 mM $K(AuCl_4)$ in a 0.1 M KCl supporting electrolyte with Pt counter and Ag/AgCl counter electrode for 5 s at different potentials (0.2, -0.6,-1.0,-1.8 V). Magnification: x19000

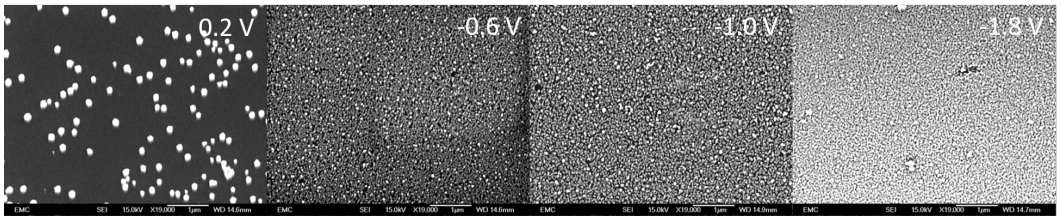

FIGURE 3.4: SEM images of gold deposited on TiN in 1 mM $K(AuCl_4)$ in a 0.1 M KCl supporting electrolyte with Pt counter and Ag/AgCl counter electrode for 50 x 0.1 s at different potentials (0.2, -0.6,-1.0,-1.8 V). Magnification: x19000

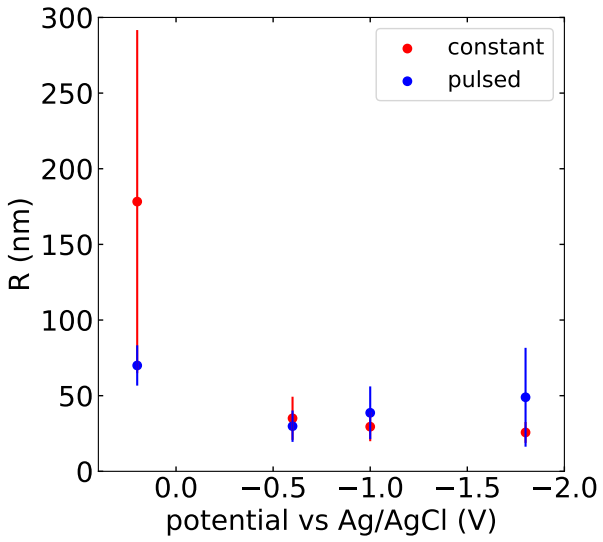

FIGURE 3.5: Particle radii extracted from the SEM images from Figure 3.3 (red) and 3.4 (blue) using the image processing software ImageJ.[190] Radii calculated from images converted to binary, where the average area and number of particles is extracted from the contrast and then using $R = \sqrt{A/\pi}$ (particles approximated as spherical).

pulsed deposition protocol gives smaller particles than constant deposition, especially at *e.g.* 0.2 V, were the size decreased by a factor of 2. When using higher overpotentials, the difference between both protocols seems to be less important, as similar radii are obtained.

GISAXS The focus of this study lies on how deposition potential and use of constant/pulsed deposition affects the nuclear density and in particular the inter-particle distance. Figure 3.6 shows the GISAXS images corresponding to the SEM images shown in Figure 3.3 and 3.4. The images show the raw data from the two-dimensional detector. The red spot which stays at the same position for every image is the specular reflection of the beam which impinges onto the substrate surface with an angle of $\alpha_i = 0.7°$, SDD of 301.5 mm, and exposure time of 30 min. Just below the reflection, another intensity maximum can be seen which is the previously mentioned Yoneda peak (see Section 2.4.1 for details). The vertical position of this peak directly leads to the scattering length density and hence electron density of the material probed, namely the optical contrast between the particles on the surface, the air around them and the substrate itself. At a beam energy of 8 keV, the Yoneda peak of gold, which corresponds to the critical angle has a value of $q_z = 0.79\,nm^{-1}$, which fits well to the feature seen in Figure 3.6. The relatively high incident angle of 0.7° was chosen so that the Yoneda peak and the reflection were separated locally on the detector at this short SDD. When examining the GISAXS images qualitatively by eye, one can see that with increasing overpotential, the general shape of the diffuse scattering cloud moves from a very narrow and vertically elongated signal to one spread out in horizontal direction. This effect increases when using the pulsed potential method, except for -1.8 V. Revisiting the SEM images of those samples shown in Figures 3.3 and 3.4, it seems that the GISAXS images with stronger horizontally spread out signals correspond to samples with higher density of smaller particles. This makes sense as a higher number of particles leaves fewer space on the surface for each individual, which means their distances to each other are smaller. In reciprocal space, this leads to signals with higher q values and hence to the horizontal spreading of the patterns. The fact that larger distances show a decreased scattering signal can be attributed to the fact that the small SDD on the in-house instrument can not resolve those, otherwise similar shapes should be visible on a detector placed further away from the sample. It is possible to roughly distinguish particle densities and sizes from their 2D scattering patterns, but more information can be obtained from integrating those images along one axis, as shown in the following.

Horizontal cuts In order to investigate the lateral arrangement of the particles, horizontal cuts are performed along q_y at the Yoneda peak. The plots are depicted in Figure 3.7 and were shifted vertically for better visualisation. The top row shows horizontal cuts for deposition times of 0.1, 1 and 5 s and the respective potentials are colour coded going from lower (black) to higher overpotentials (red). Similarly, the bottom row shows the results for the corresponding pulsed depositions of 1, 10 and 50 times 0.1 s which corresponds to the same total time. First of all, it is visible that with increased deposition time/number of pulses, the statistics of the profiles improve a lot, which is due to the increased number of particles/their size and hence more scattered

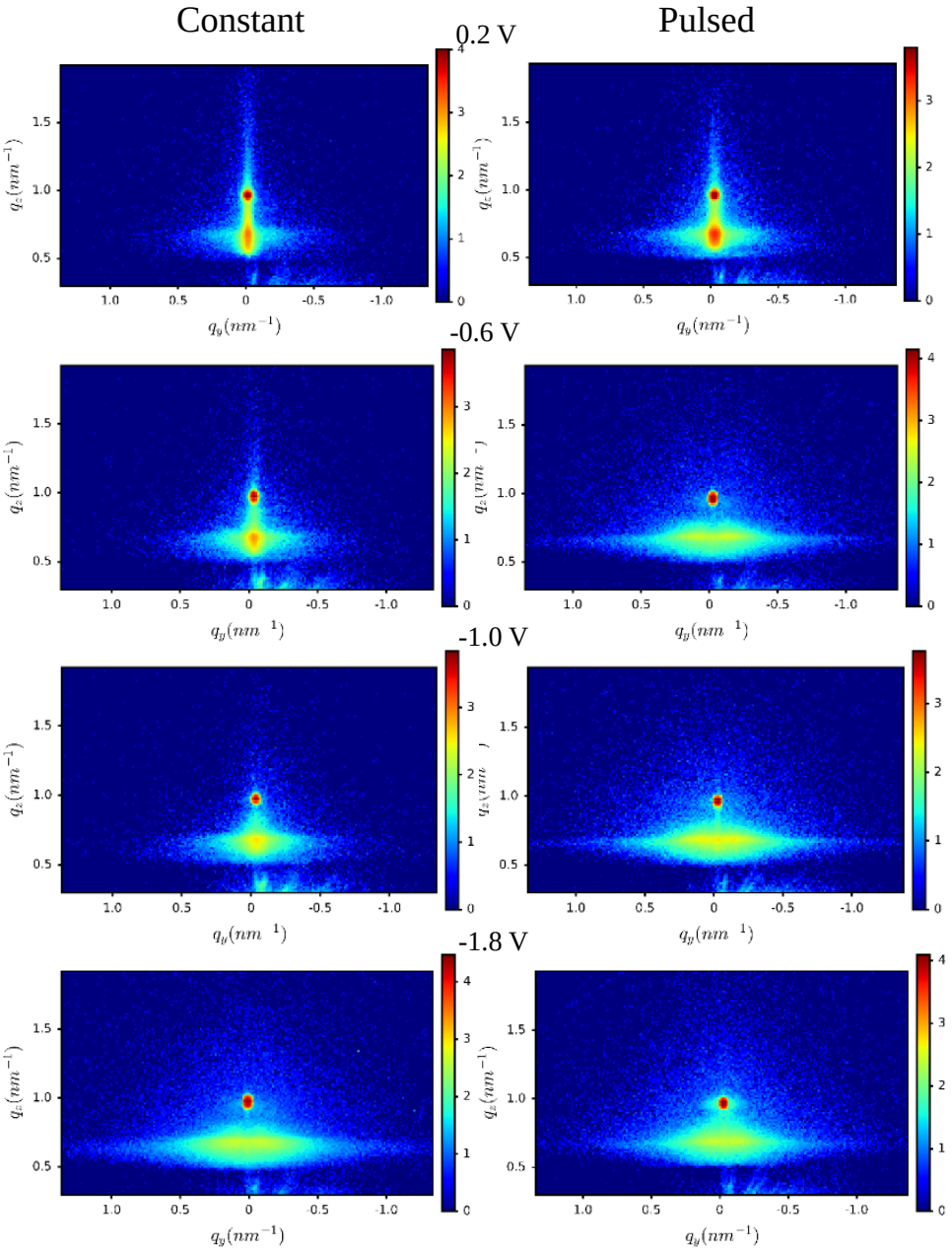

FIGURE 3.6: GISAXS images of gold on TiN at different potentials for constant/pulsed deposition (5 s/50*0.1 s). Incident angle: $\alpha_i = 0.7°$, SDD=301.5 mm, exposure time: 30 min. The colour bar indicates intensity from low (dark blue) to high (red).

signal on the detector. Higher deposition overpotentials generally lead to more pronounced shoulders in the pattern, whereas the curves of the particles deposited at 0.2 V show only a very weak signal. Regarding the effect of pulsed potential, the curves in the bottom row (especially for 10 and 50 pulses) do not exhibit the same low q decline of intensity as seen in the corresponding constant potential equivalents above, which indicates their increased number or particles on the surface. As the shoulders in this data are generally very broad it is not suitable to fit any peak function to them in order to further extract particle distances. Furthermore, the use of time as a general normalisation for the depositions seems not to be ideal when comparing particle number and size of different potentials, as with the energetic changes induced by changing the potential, the deposition rate varies too. This is why it was next considered of benefit to repeat a similar experiment at which the passed charge per area would be used as the scale to quantify changes of particle size and number. This also gives the opportunity to change the range of deposition potentials to a region spanning more of the conditions at which slight changes induce larger effects, as it seemed that the number of particles saturated already around -1.0 V, which can be explained by the increased influence of water electrolysis at the electrode versus regular deposition of the material.

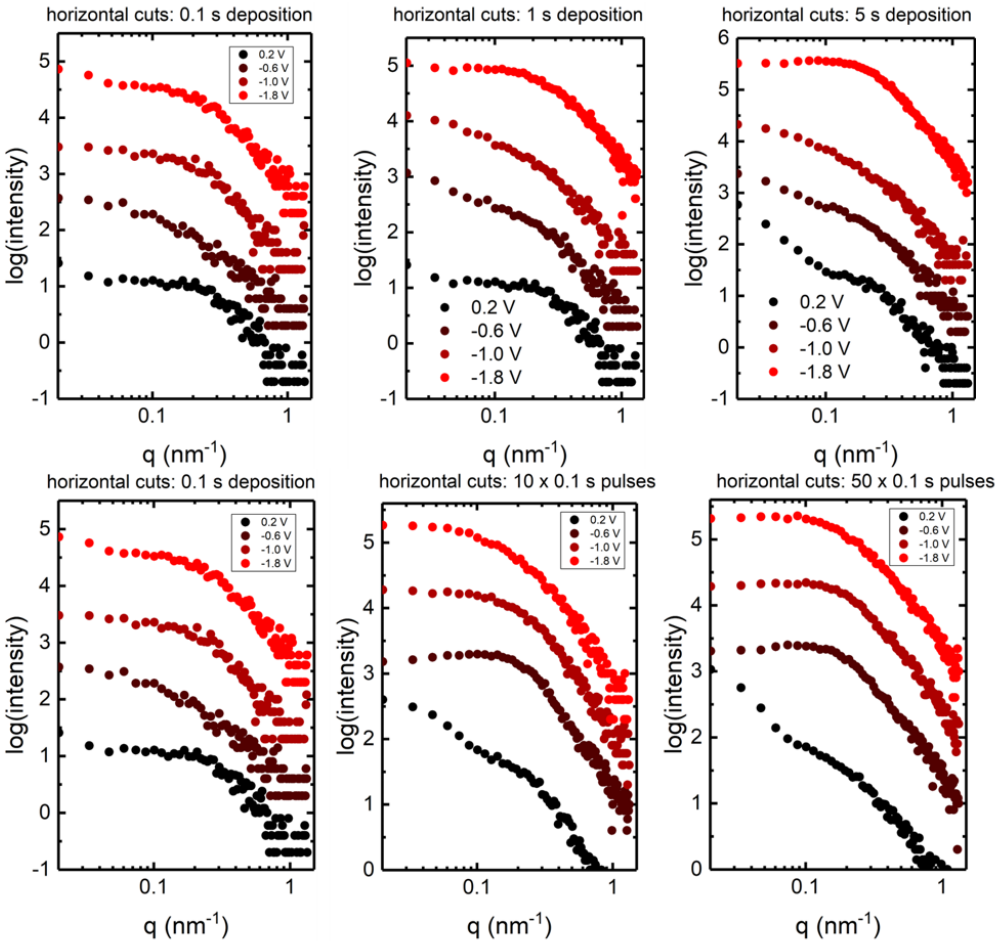

FIGURE 3.7: GISAXS images of gold on TiN at different potentials for constant/pulsed deposition (0.1, 1, 5 s/ 1, 10, 50*0.1 s). Plots are shifted vertically for clarity.

3.1.3 Charge-normalized chronoamperometry

As mentioned in the previous paragraph, the normalisation of depositions to their respective times results in a distortion of particle numbers and sizes due to the current dependence on the potential leading to more charge passed at higher overpotentials. This was the rationale for the upcoming part, where deposition experiments with the same charge passed at different potentials will be discussed.
This means that the number of passed electrons is the same for each sample per defined surface area. As the deposition rate (current) depends on the applied potential, the respective times will not be the same for each sample (increasing time with lower overpotentials).

Electrochemical data Figure 3.8 shows a summary of the electrochemical data for the experiments. From the cyclic voltammetry in Figure 3.1 it appears that a minimum

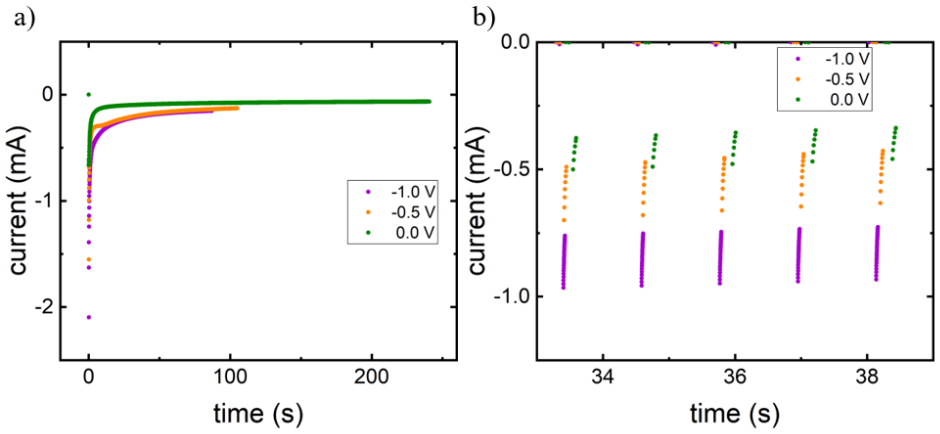

FIGURE 3.8: a) Constant current transients Au deposited on TiN in 1 mM $K(AuCl_4)$ in 0.1 M KCl supporting electrolyte with Pt counter and Ag/AgCl reference electrode at 0 V, -0.5 V and -1 V until reaching a charge density of 0.444 mC/mm^2 c) Pulsed transients shown for the three potentials in b) for 33-39 s deposition. Only small part shown as example due to the high number of very short pulses.

contribution of the hydrogen evolution reaction can be assumed when limiting the potential to being above -1 V. This is why the potentials for this experiment were revised to values at which it is expected that only the nucleation rate is changed directly by the potential, excluding secondary reactions like the reduction of hydrogen. The values 0 V, -0.5 V and -1 V were chosen as the potential window. Figure 3.8 a) shows the constant current transients obtained for the denoted potentials for a charge of 0.444 mC/mm^2. As expected, the transients for lower overpotentials are longer in time. In Figure 3.8 b) the respective pulses are shown for the different potentials (zoomed in for better visibility), which show the same dependency. The pulse length was 0.44 $\mu C/mm^2$ with 1 s relaxation time in between.

Scanning electron microscopy As done before, SEM images were taken for each of the samples. Apart from the three different potentials, three different amounts of charge (0.022 mC/mm^2, 0.111 mC/mm^2 and 0.444 mC/mm^2) were used for constant as well as pulsed deposition (50, 250 and 1000 times 0.44 $\mu C/mm^2$), giving rise to 3x3x2 samples. Those images can be seen in Figure 3.9 a),b) and c) for 0, -0.5 and -1.0 V and charge densities of i) 0.022 mC/mm^2, ii) 0.111 mC/mm^2 and iii) 0.444 mC/mm^2 respectively, where the colour indicates whether a constant (blue) or pulsed potential (green) was used. Figure 3.9 d) summarises the corresponding particle radii, which were extracted directly from these images using ImageJ.[190] As seen previously when increasing overpotential, the particle size decreases, whilst it generally augments for increased charge. As for the effect of pulsing, it appears that the particles from pulsed deposition have larger radii than the ones from constant deposition. That suggests that with the use of short pulses, the growth of particles is generally favoured compared to

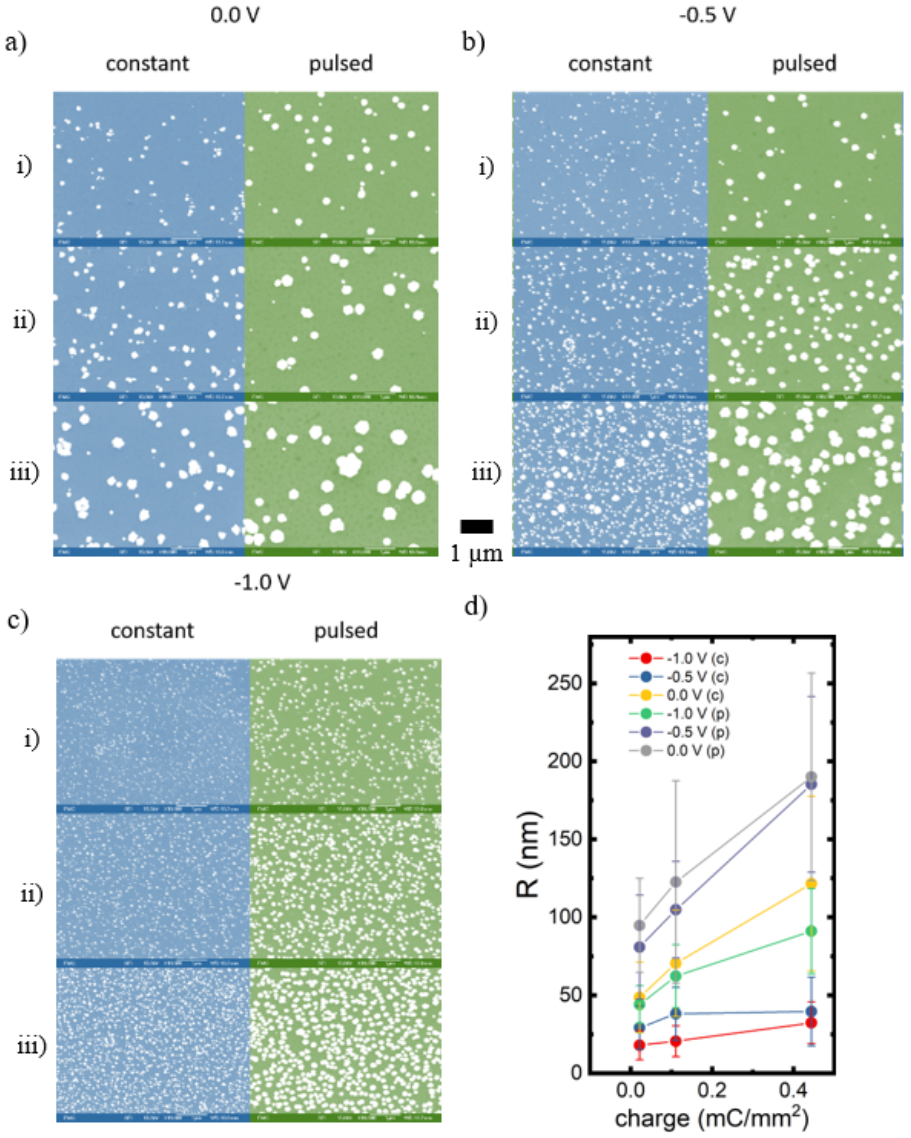

FIGURE 3.9: SEM images of gold particles deposited on TiN in 1 mM $K(AuCl_4)$ in a 0.1 M KCl supporting electrolyte with Pt counter and Ag/AgCl counter electrode at a) 0 V, b) -0.5 V and c) -1.0V for i) 0.022 mC/mm^2, ii) 0.111 mC/mm^2 and iii) 0.444 mC/mm^2 for constant deposition (blue) and 50, 250 and 1000 x 0.44 µC/mm^2 for pulsed deposition (green). d) Particle radii extracted from the images shown in a), b) and c) using ImageJ.[190]

the nucleation of new particles, or that due to the shortness of the pulse only larger particles reached a stable point allowing them to stay on the surface. Generally the range of potentials seems to portray well the change from low nucleation rate with growth of larger particles to the growth of mainly small particles at high number density. Interestingly, -0.5 V seems to be a point at which an intermediate condition between both is reached, where larger particles are deposited amongst mainly smaller ones.

GISAXS To further characterise the samples, GISAXS images were again recorded for each sample using the dedicated SAXS instrument at the University of Warwick (see Section 2.5.1 for details). Horizontal cuts at the Yoneda position of gold were made and are shown in Figure 3.10 a)-f). When looking at the horizontal GISAXS profiles, we can see that no strong peaks can be seen which would indicate a high degree of lateral ordering. Similarly to patterns shown in previous sections, the low q intensity increases with charge regardless of the potential value when using a constant potential, whereas the opposite happens in the pulsed regime. This shows that the number of particles steadily increases at constant potential deposition (especially at higher overpotentials), while it decreases when the pulsed protocol is used. The latter can only mean that particles have coalesced into larger particles either through *e.g.* Ostwald ripening or surface movement.

Unified fit Further analysis of the data can only be done by fitting a model to the horizontal scattering profiles. For this reason, a unified fit model for weakly correlated particles was applied to the data in order to extract correlation distances from each profile. This was done using the Irena package for Igor Pro.[191,192] The model calculates the scattering profile from the size of particles and also their correlation length, if assumed that they are correlated. Up to two correlation lengths can be included in one set of fit parameters. This was done successfully only for the set of samples made with constant potential because the length scales in this particular pulsed regime were too large for the resolution of the instrument and made it impossible to properly fit the data. In Figure 3.10 g), the resulting nearest neighbour distances (*nnd*) from the SEM images as well as correlation distances are displayed. One can see that the distance between particles decreases with increasing overpotential. This fits with the increased rate of nucleation with higher overpotentials, which leads to a higher surface density of particles and a smaller distance between them. For increased amounts of charge, we see an increased distance for deposition at 0 V and -1 V, and a decrease for -0.5 V. A decrease of correlation distance indicates progressive nucleation, while an increase shows that the experimental settings favour particle growth and coalescence rather than nucleation. In all cases, the nearest neighbour distance extracted from SEM and the values obtained from the unified model fit of the GISAXS data are in good agreement - which is mainly due to the flexibility of the model and the little features in the data. Improvements could be achieved by performing the scattering experiments at a dedicated facility like a synchrotron, where the increased dynamic range and resolution should give better insight into the surface arrangement of the particles.

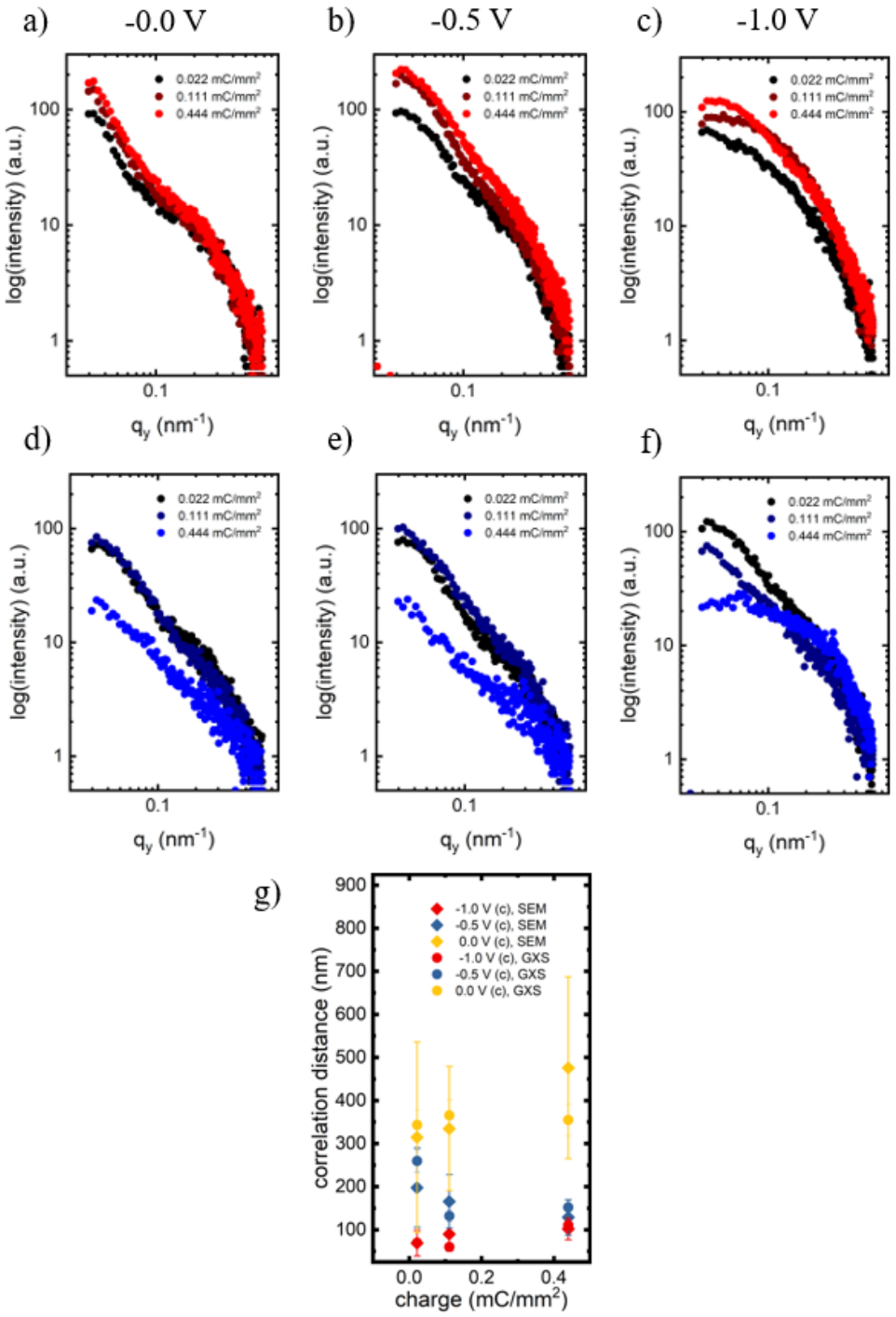

FIGURE 3.10: Horizontal profiles for samples deposited at the following conditions: constant potential of a) 0 V, b) -0.5 V and c) -1.0 V; pulsed potential of d) 0 V, e) -0.5 V and f)-1 V; g) correlation distances extracted from SEM and GISAXS data (a,b,c) respectively from constant deposition for increasing amounts of charge.

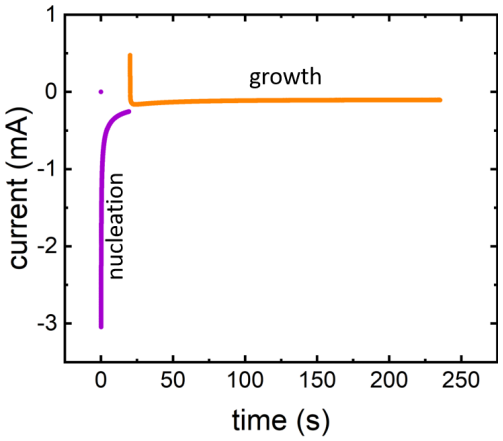

FIGURE 3.11: a) Current transients of deposition at a nucleation potential of -1.0 V and growth potential of 0.0 V.

3.1.4 Twin potential step

Another variation of Au deposition experiments of interest for this work is the application of a high nucleation overpotential, followed by a low overpotential growth step. The aim of this procedure was to maximise the number of nuclei on the surface during the nucleation potential, and to homogeneously increase particle size in the growth phase. The results of this study were published in ACS Langmuir.[193]

Current transients Figure 3.11 shows the current transients obtained during deposition of Au using a high nucleation overpotential at -1.0 V for 0.056 mC/mm^2 followed by growth at 0 V until reaching a total surface charge density of 0.222 mC/mm^2. Depositions were carried out with fixed charge densities using -1.0 V and -2.0 V as nucleation potentials (0.056 mC/mm^2) and 0, -0.4 and -0.8 V as growth potentials respectively (0.222 mC/mm^2).

SEM Every sample was then analysed by scanning electron microscopy (SEM); images are shown in Figure 3.12 for nucleation at -1 V and -2.0 V and growth at either ii/vi) 0.0 V, iii/vii) -0.4 V or iv/viii) -0.8 V respectively. From the SEM images, the radii of the particles were extracted using ImageJ[158] and plotted in 3.13. Distributions of the corresponding particle radii are shown in Figure 3.14. One can see that for higher nucleation overpotential, or shorter growth periods, the particle size distributions migrate towards smaller values. This corresponds to expectations, as the critical size a nucleus needs to exceed for successful nucleation decreases with greater driving force (overpotential).[194]

GISAXS at ALS This time the GISAXS experiments were carried out as part of the GISAS summer school in Bayreuth Germany, which meant that selected samples were

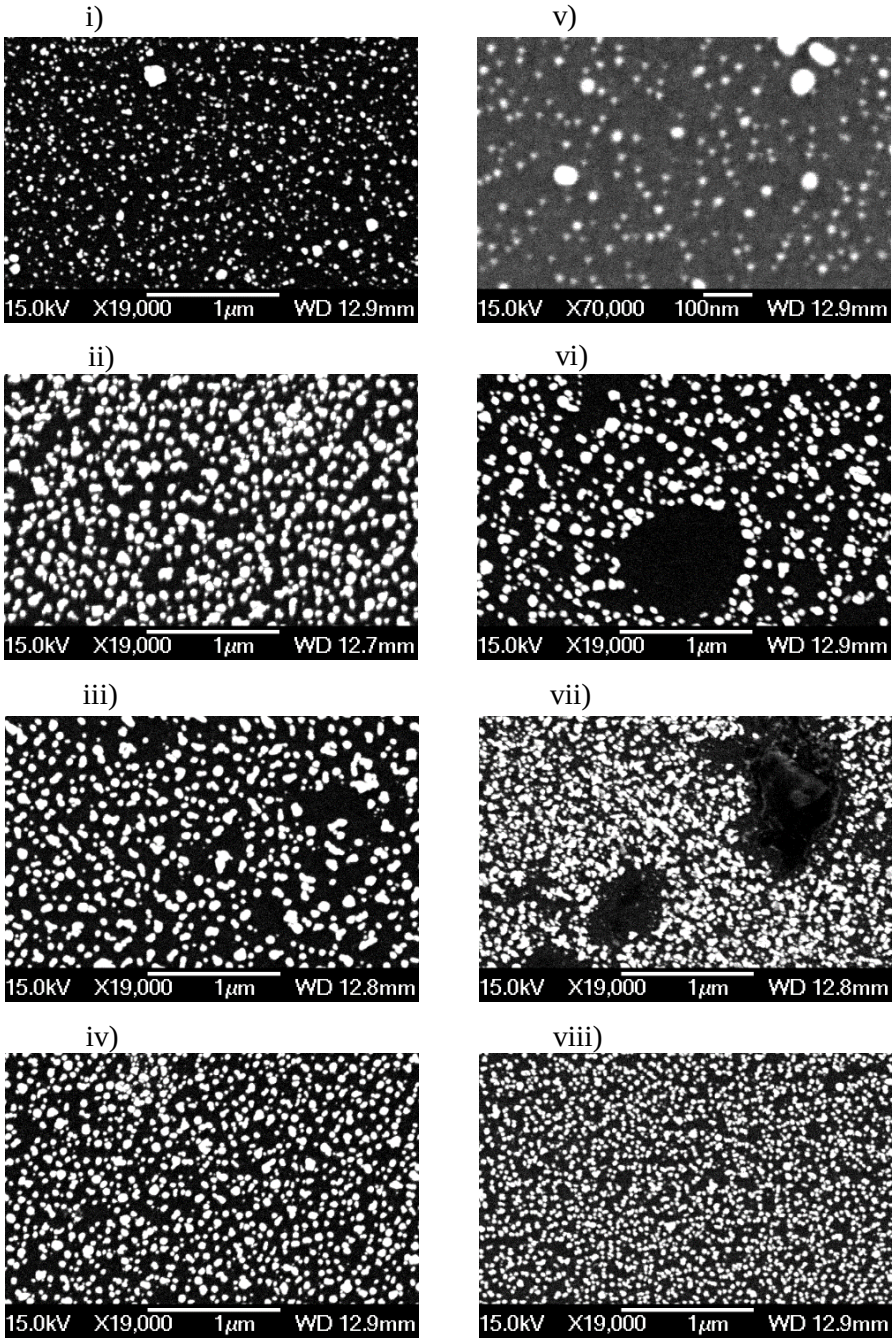

FIGURE 3.12: SEM images of particles formed after a nucleation pulse at i)-iv) -1.0 V or v)-viii) -2.0 V with consecutive growth steps at either 0.0, -0.4 or -0.8 V, ii-iv) and vi-viii) respectively.

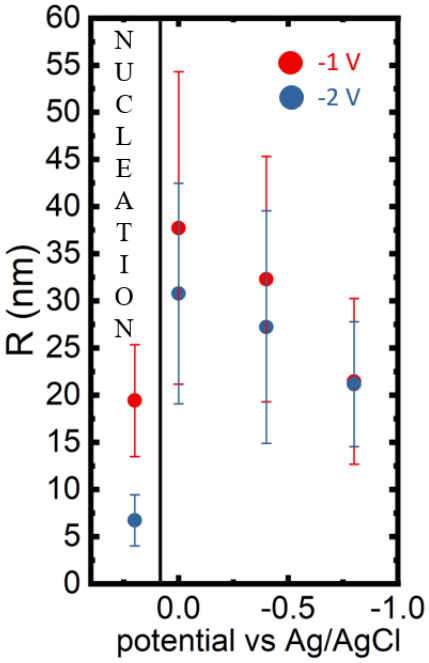

FIGURE 3.13: Particle radii extracted from SEM data. Particle radii after applied nucleation potentials of -1 V (red) and -2 V (blue).

characterised at beam line 7.3.3 SAXSWAXS at Advanced Light Source (see 2.5.1 for details). The two-dimensional detector images are shown in Figure 3.15. One can observe the occasional occurrence of deposition-less areas in the SEM images, which are attributed to pre-deposition contamination. Due to their micron scale size, these areas are not visible in the GISAXS data, as they are outside the detectable range of length scales of the experiment. Horizontal line profiles were extracted from the raw data using the DPDAK[195] software package by projecting the intensity at the Yoneda position onto the q_y axis; these which are shown in Figure 3.16 a) for -1.0 V and -2.0 V nucleation potentials respectively. The profiles show a broad peak for both potentials, where the lower potential peak has a higher q value, which means that the correlation distance d (see inset Figure 3.16 a)) for the particles deposited at higher nucleation overpotential (-2.0 V) is shorter than that for the particles deposited at lower nucleation overpotential. The same procedure was applied to the images taken after the respective growth periods, in Figure 3.16 b) and Figure 3.16 c). The values for the correlation distances do not strongly depend on the growth potential but rather on the nucleation potential. For -1.0 V nucleation, distances around 120 nm are observed, while for -2.0 V nucleation potential, the d values are smaller (average below 100 nm). The GISAXS correlation distances (d) are contrasted with the nearest neighbour distance extracted from SEM data (nnd) in the insets of Figure 3.16 b) and c). The distances obtained from the GISAXS data are significantly larger in all cases. Generally, using a larger nucleation overpotential results in a smaller distance between particles as more particles nucleate.[194]

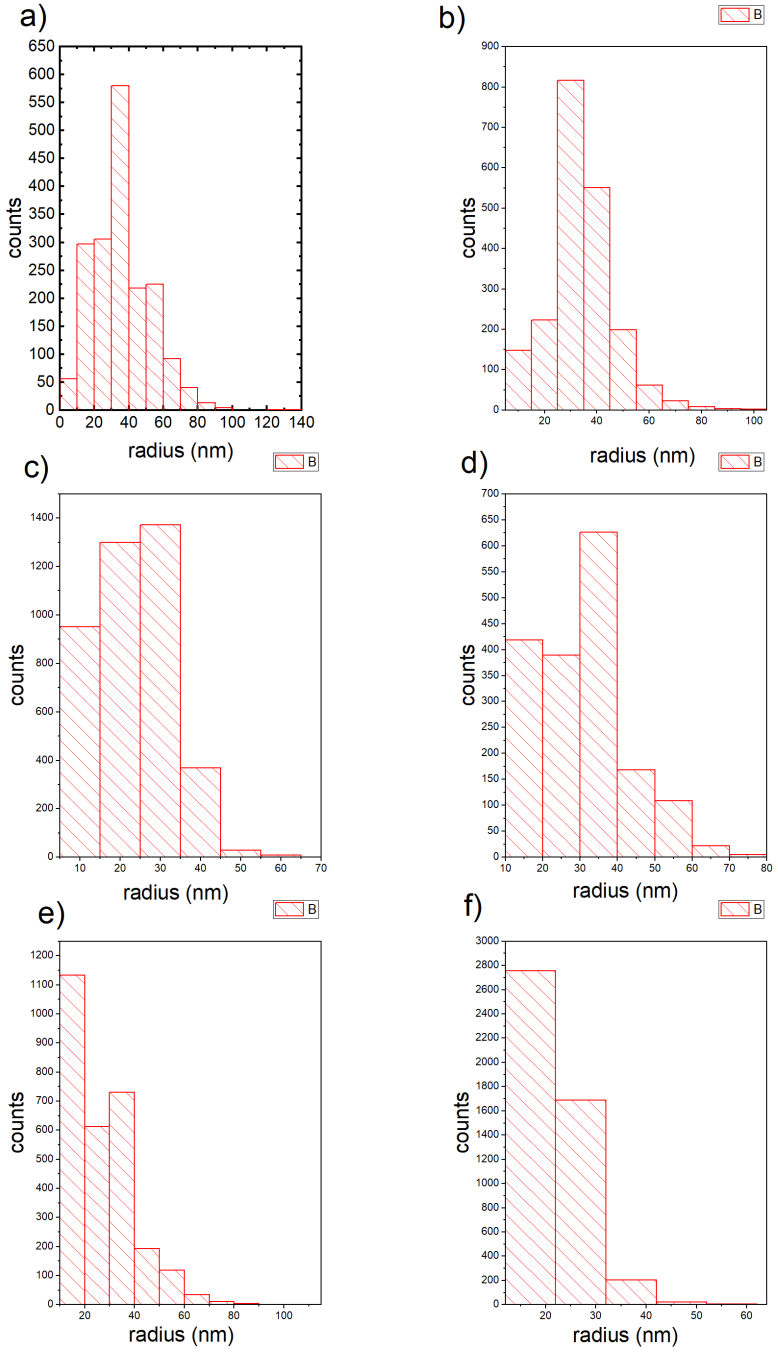

FIGURE 3.14: Distribution of radii for particles deposited at -1 V nucleation potential and a) 0 V, b) -0.4 V, c) -0.8 V growth potential and -2 V nucleation potential d) 0 V, e) -0.4 V, f) -0.8 V growth potential respectively.

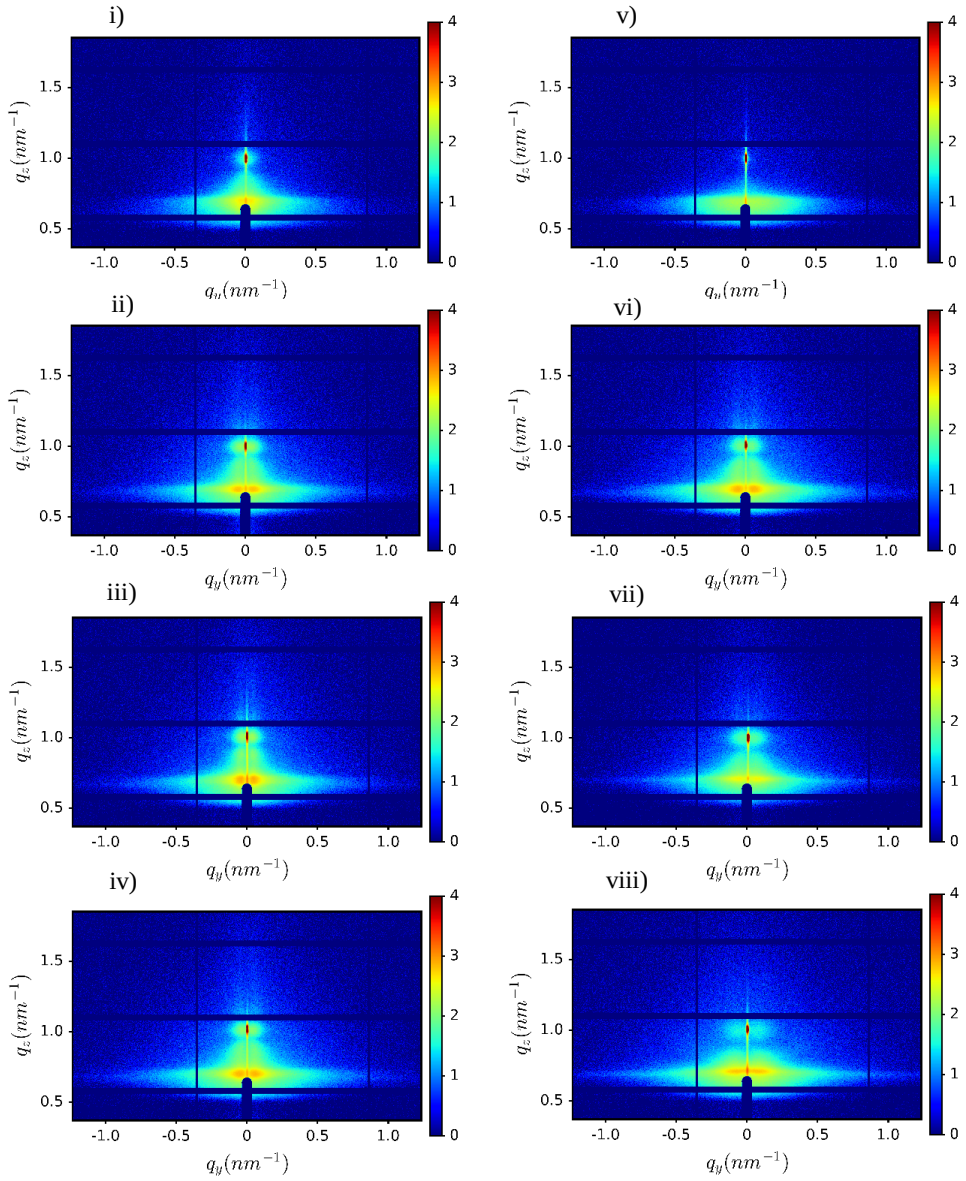

FIGURE 3.15: GISAXS images of particles formed after a nucleation pulse at i)-vi) -1.0 V and v)-viii) -2.0 V with consecutive growth steps at either ii)/vi) 0.0 V, iii)/vii) -0.4 V or iv)/viii) -0.8 V respectively.

Nearest neighbour distance In order to understand why the correlation distances obtained from GISAXS (d) are larger than the apparent nearest neighbour distance (nnd), the SEM images from Figure 3.12 were revisited. The larger correlation lengths indicate the possibility that not all particles present contribute to the correlation distance observed in the GISAXS data, but rather that the contributing particles possess a higher degree of ordering than the whole distribution. To verify this, subsets of the particle distribution were analysed for their nearest neighbour distance and particle density. The threshold for the smallest particles to be included into the $nnd*$ calculations was increased from zero to the largest value at which particles were still counted. A visualisation of the method is shown in Figure 3.17, for a sample deposited at -1 V nucleation

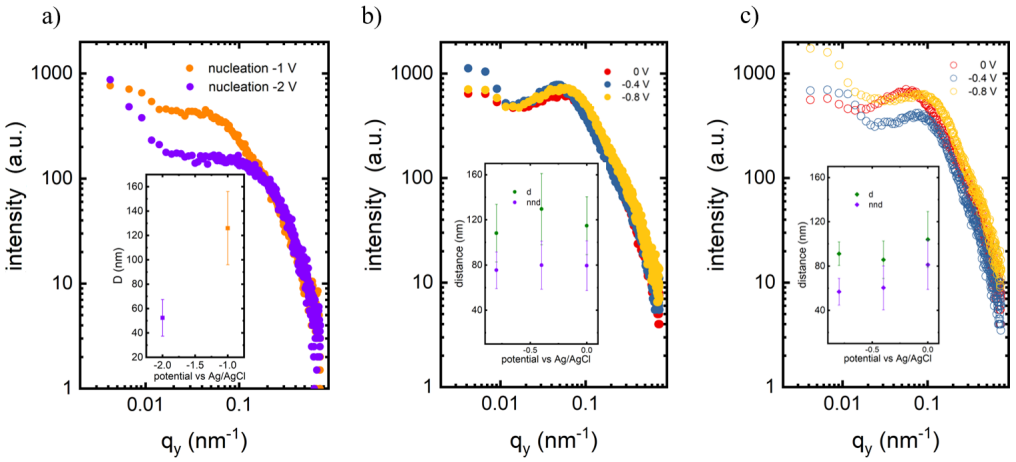

FIGURE 3.16: a) Horizontal cuts of GISAXS data from particles nucleated at -1.0 V and -2.0 V respectively. Inset: correlation distances d extracted from curves in a). b) Horizontal GISAXS profiles of particles deposited at -1.0 V nucleation potentials and 0, -0.4, -0.8 V respectively. Inset: d, and nnd corresponding to data in (a). c) Horizontal GISAXS profiles of particles deposited at -2.0 V nucleation potentials and 0, -0.4, -0.8 V respectively. Inset: d, and nnd corresponding to data in (c).

potential and 0 V. This means that particles were filtered out from the bottom end of the distribution of radii. For each increment, $nnd*$, the reduced number density, $N*$, of the particles was evaluated. The corresponding graphs are shown in Figure 3.18 a) for -1 V nucleation and b) -2 V nucleation potential. When increasing the lower particle radius threshold, the nearest neighbour distance $nnd*$ at first increases slowly but then diverges rapidly for the higher values. From these graphs the lower particle radius threshold corresponding to the $nnd*$ value equal to the distance obtained from GISAXS, is extracted. In turn this yields a value for the number of particles which are placed at that distance to each other. If the particles were randomly distributed on the substrate, their distance d could be calculated from their number density N by $d_{uni} = 1/2N^{-1/2}$. For a square array, the distance would be $d_{sq} = N^{-1/2}$ and for hexagonally packed particles $d_{hex} = 1.0746\text{x}N^{-1/2}$.[20] This means that the resulting number densities can be compared to the ones calculated from the d values to show which arrangement fits best. The number density N_{sq} and N_{uni}, calculated from the correlation distance obtained in GISAXS as well as the reduced number density $N*$, calculated from the number of particles remaining after filtering out smaller particles as explained above are summarized in Figure 3.19 a) and b) for -1 V and -2 V nucleation potential respectively. It can be seen that the reduced number density $N*$ consistently takes a value higher than would be expected for disordered particles, which indicates that this particular part of the distribution is not randomly distributed, but possesses some ordering.

This effect can also be evaluated by looking at the nearest neighbour index $I_{NN} = nnd/d_{uni}$, which indicates ordering of dispersed particles for values greater than 1 and particle clustering for values lower than 1. A corresponding plot for particles deposited

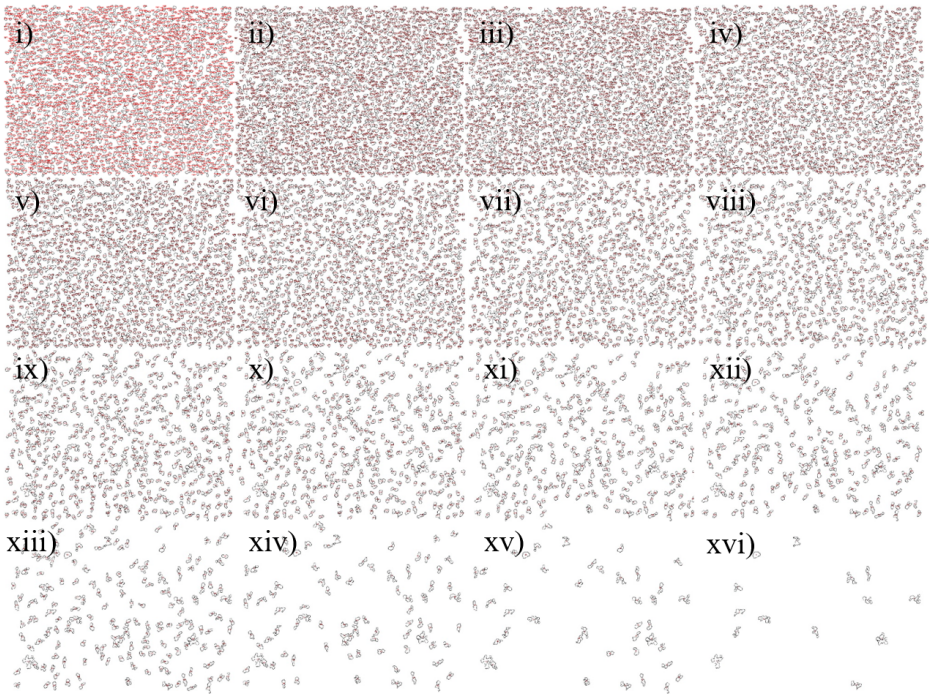

FIGURE 3.17: Images of particles filtered out with increasing lower size threshold.

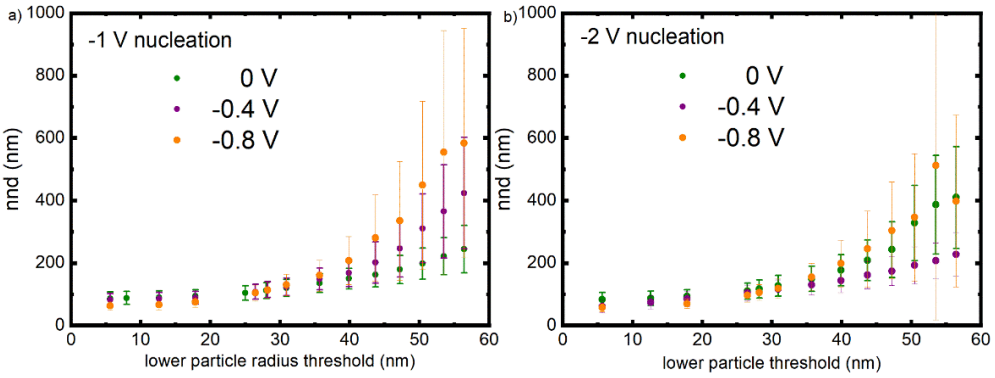

FIGURE 3.18: : $nnd*$ values for increasing lower particle radius threshold for a) -1 V and b) -2 V nucleation potential.

at -1 V nucleation and 0 V growth can be seen in Figure 3.19 c). It shows a maximum of I_{NN} when increasing the lower particle threshold, followed by a rapid decay of the curve to values below 1. The increasing values at the beginning of the curve indicate that the larger particles are better ordered than the smaller ones, while the decay towards the largest particle sizes indicates that these are not actual spherical particles of that size, but clusters that were falsely identified during data treatment. This explains why the nearest neighbour distance from the microscopy does not quite fit to the GISAXS data, as the increased ordering of the larger particles leads to a stronger scattering signal.

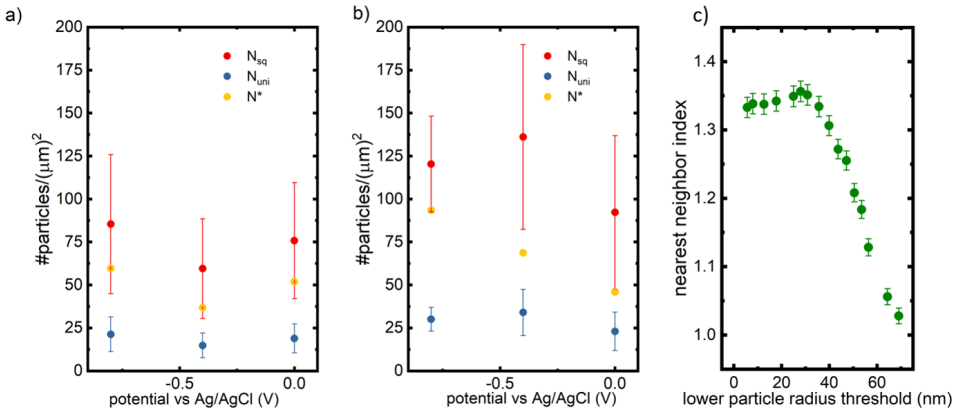

FIGURE 3.19: The number density N_{sq} and N_{uni}, calculated from the correlation distance obtained in GISAXS as well as the reduced number density $N*$ calculated from the particles remaining in the distribution with a value of $nnd*$ corresponding to d are plotted in a) for -1.0 V and b) -2.0 V nucleation. c) Nearest neighbour index $I_{NN} = nnd/d_{uni}$ of particles deposited at -1 V nucleation and 0 V growth for different values of the lower particle size threshold.

DWBA simulations of GISAXS patterns To further investigate the validity of the assumptions made, simulations of the system within the Distorted Wave Born Approximation (DWBA) were done using the dedicated software BornAgain.[179] It allows the user to fully reconstruct any desired sample and instrument environment within the realms of small angle X-ray or neutron scattering. Figure 3.20 shows a screen shot of the BornAgain user interface: for the instrument used in the simulation, the properties of the SAXSWAXS beamline 7.3.3 at ALS were recreated entirely ($\lambda = 1.24$ Å, SDD=3529 mm, pixel size=172 μm^2, incident angle=0.567°). The sample was constructed as a bottom layer of Si ($\delta = 4.8889 \times 10^{-6}$ Å^{-2}, $\beta = 7.3544 \times 10^{-8}$ Å^{-2}) with a 200 nm thick TiN layer ($\delta = 1.0657 \times 10^{-5}$ Å^{-2}, $\beta = 4.66555 \times 10^{-7}$ Å^{-2}) on it and an air layer on top. Spherical Au particles with Gaussian particle size distribution ($\delta = 2.9912 \times 10^{-5}$ Å^{-2}, $\beta = 2.2073 \times 10^{-6}$ Å^{-2}) were introduced into the air layer in an arrangement on a radial paracrystal. As parameters, values from the previously analysed SEM and GISAXS data were used as inputs. The TiN layer was assigned a basic roughness corresponding to the measurements done in our group, while the specular reflection was not simulated. The results from these simulations are compared to the raw data in Figure 3.21 and 3.22, showing that our assumptions fit the raw data reasonably well regarding the shape of the diffuse scattering clouds and their intensity. Discrepancies between real data and simulation result from the use of a simplistic model. In reality, the particles are not perfectly spherical and most probably have a variety of form factors around a spheroidal shape or even a hybrid between a cuboid and spheroid. The particles do of course sit on a surface which means their contact angle will not be perfectly 180°, which is also not taken into account when using the form factor of a full sphere. This simplification of the form factor leads to slight differences in the shape of the scattering signal in the simulation, but the overall good agreement

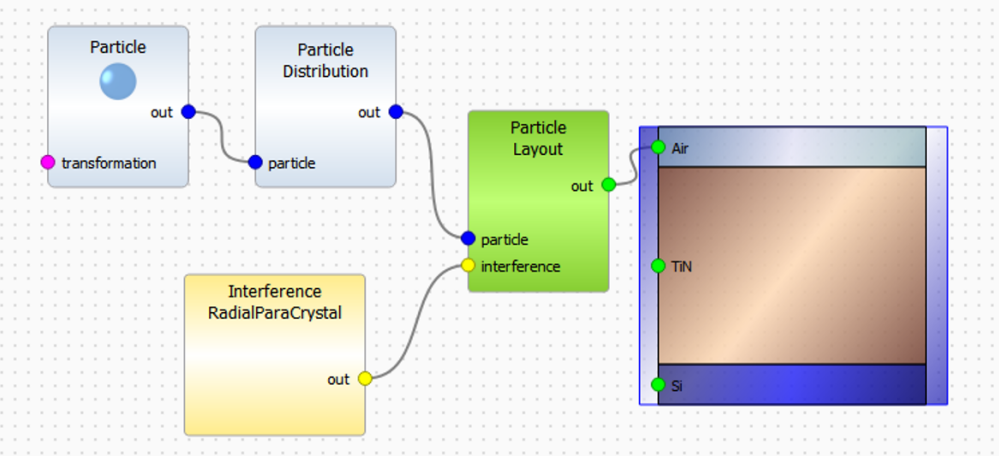

FIGURE 3.20: Screenshot of the BornAgain user interface showing the model employed for the GISAXS simulations. Sample: bottom layer of Si ($\delta = 4.8889\,\mathrm{x}\,10^{-6}$ Å^{-2}, $\beta = 7.3544\,\mathrm{x}\,10^{-8}$ Å^{-2}) with a 200 nm thick TiN layer ($\delta = 1.0657\,\mathrm{x}\,10^{-5}$ Å^{-2}, $\beta = 4.66555\,\mathrm{x}\,10^{-7}$ Å^{-2}) on it and an air layer on top. Instrument: Recreation of the SAXSWAXS beamline 7.3.3 at ALS ($\lambda = 1.24$ Å, SDD=3529 mm, pixelsize=172 μm^2, incident angle=0.567°)

shows that this assumption is not too far from reality. This is because a distribution of particles of cubiodal/spheroidal shape will average out to a sphere-like shape when taking into account the signals of all shapes and orientations involved. The aspect that does not average out is the contact angle, which means that the apparent form factor should be closest to a truncated sphere. The use of this form factor however leads to a significantly increased computation time due to a not analytically solvable integral in the mathematical description, and since the focus of this work lies more on the structural arrangement of the particles than their actual shape, the "faster" computation option was chosen. For additional comparison, GISAXS data of a blank TiN substrate are shown in Figure 3.23 where no strong structural features are prominent as the TiN electrodes are notoriously flat surfaces.

Limited nucleation sites The first step in the experiment was the application of a high overpotential nucleation pulse leading to rapid initial deposition of small nuclei due to the high nucleation rate. This is expected from theoretical predictions[24] and confirmed by electron microscopy (see Figure 3.12). With a diffusion coefficient of $D = 10^{-5}\,\mathrm{cm}^2/\mathrm{s}$,50 the diffusion layer $\delta = \sqrt{\pi D t}$ expands beyond 100 nm in less than 5 µs. The fast overlap of diffusion zones quickly enlarges the areas of reduced nucleation and thus modulates the favoured surface for nucleation, meaning that zones of enhanced and reduced nucleation alternate across the electrode surface. As a consequence, during nucleation particles do not randomly distribute on the surface but nucleate with similar distances to each other as the ones corresponding to a square/hexagonal array (close packed), and their distance depends on the nucleation rate (higher

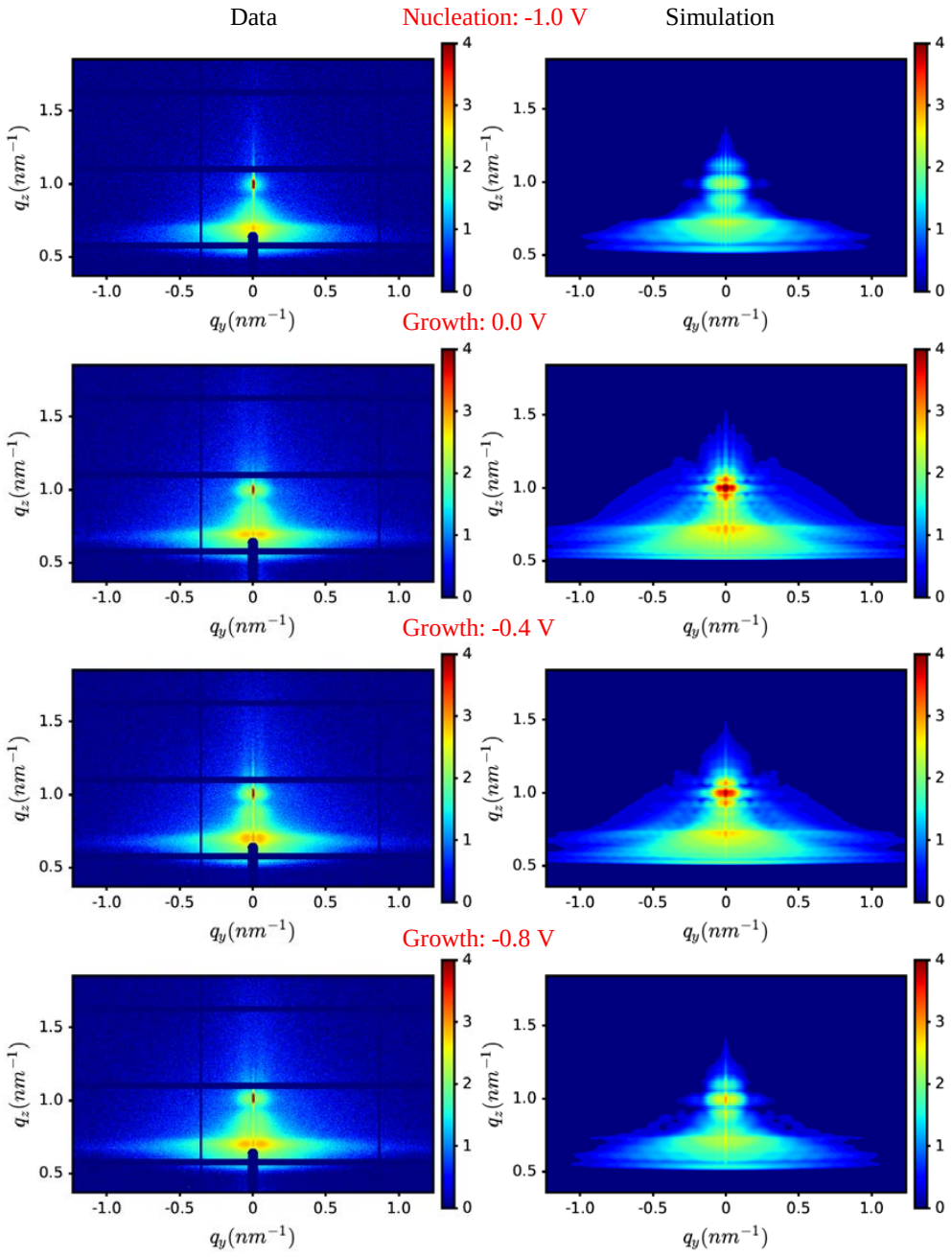

FIGURE 3.21: Comparison of the raw GISAXS data with DWBA simulations produced using BornAgain for particles formed after a nucleation pulse at -1.0 V with consecutive growth steps at either 0.0, -0.4 or -0.8 V. Simulation details shown in Figure 3.20.

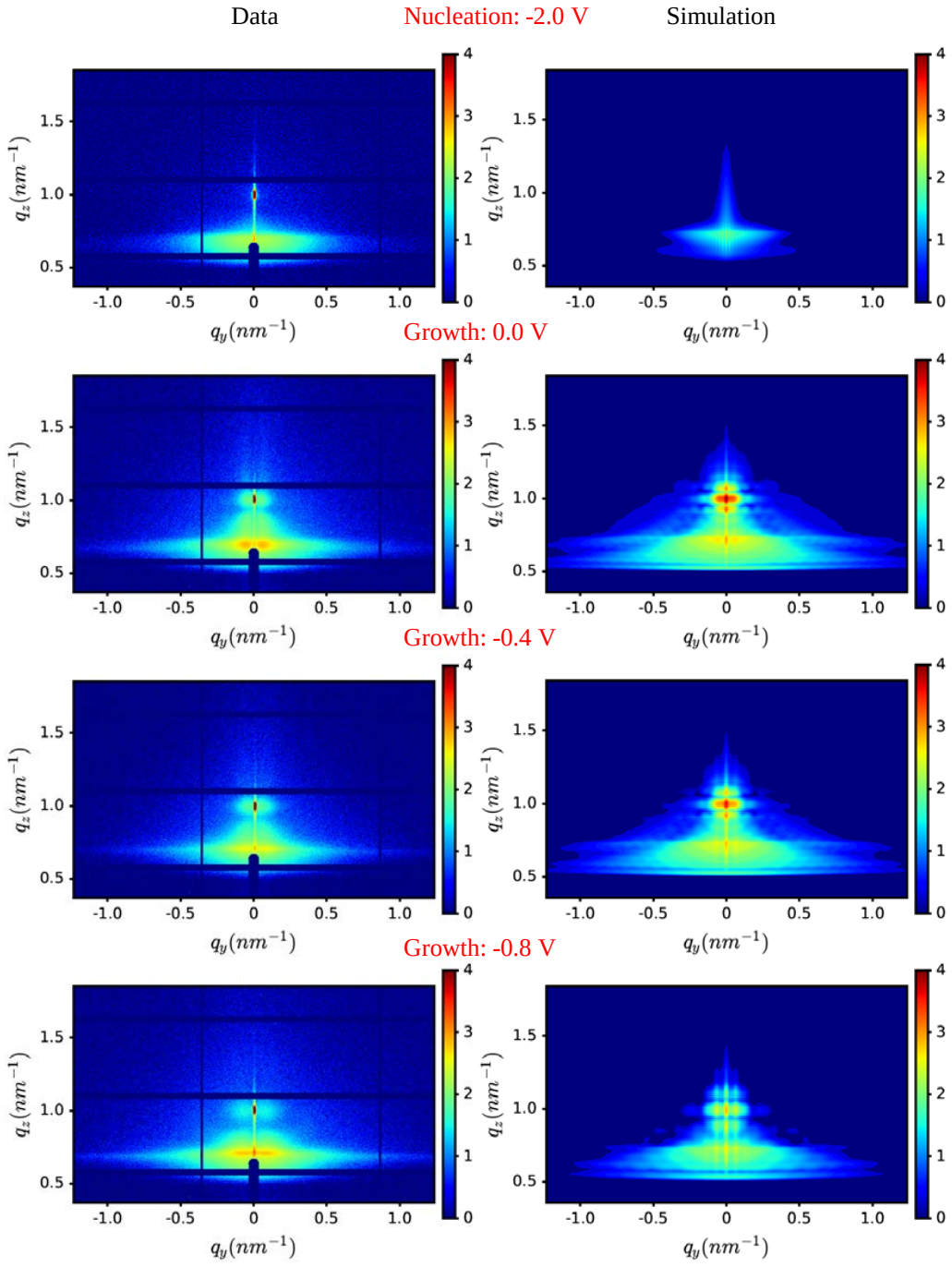

FIGURE 3.22: Raw GISAXS data as well as DWBA simulations produced using BornAgain for particles formed after a nucleation pulse at -2.0 V with consecutive growth steps at either 0.0, -0.4 or -0.8 V. Simulation details shown in Figure 3.20.

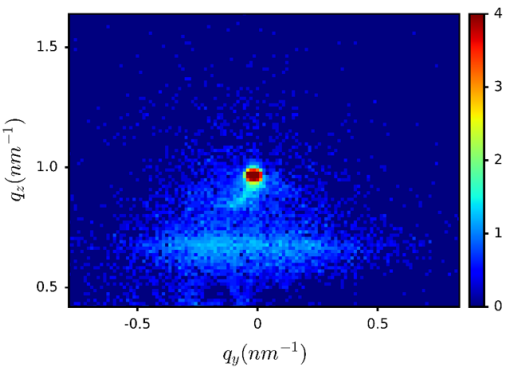

FIGURE 3.23: GISAXS data of a blank TiN substrate measured on our in house SAXS system (Rigaku Smartlab). Incident angle= 0.7 deg, SDD = 301.5 mm, λ = 1.54 Å, collimator: 100 μm, exposure time = 30 min.

rate, smaller distances). Following this, the remaining space is filled with particles in a less ordered manner during the growth period. The consecutive change of potential when going from the high nucleation overpotential to the lower growth overpotential reduces the nucleation rate and thus the current magnitude significantly, depending on the choice of growth potential (see Figure 3.11 a)). From our experiment, we know that within the error bars, the mean correlation distance detected in the GISAXS data does not differ significantly for the respective growth potentials 0 V, -0.4 V and -0.8 V. At the same time, the mean particle radii decrease with decreasing growth potential, which shows that through lowering the nucleation rate the growth of particles is increasingly favoured. This in turn means that in the growth phase, particles generated during the nucleation pulse are more likely to expand in size at the expense of further nucleation, leading to the formation of two size regimes. This explains why a longer distance than the nearest neighbour distance is obtained from the GISAXS data, since the technique probes the film on a very large scale in which the larger particles seem to be dominating the scattering pattern because they have a higher degree of ordering.

Summary In this Section we have shown that GISAXS is a valuable technique to reveal structural properties of nanoparticle films that cannot be directly detected by microscopy. In the present case GISAXS demonstrates the presence of zones with reduced nucleation, which would not only need enormous amounts of measurement time to be observed by electron microscopy but also a large amount of computing power to reveal information with similar quality. The combined use of electron microscopy and scattering enables the elucidation of nucleation mechanisms that are otherwise difficult to observe. For the electrodeposition of gold on TiN using GISAXS we have shown that the spatial arrangement of electrodeposited gold nanoparticles has a non-random distribution. The surface itself should not impose any geometrical constraints on the process since the surface is not patterned and extremely flat (roughness of 1 nm)), even

though it has been shown that TiN made by PVD grows in a columnar fashion[196] (with much smaller dimensions than the structures observed in this work). This kind of insight is especially significant for the use of nanostructured electrodes, as it indicates possible limitations of the electrodeposition when using, for example, a nanoporous template on top of an electrode, where the packing could be so dense that the pore distance is of similar distance to the diffusion layers around each pore.[76] In such a case, a non-homogeneous filling of the template would occur if pores happen to reside in a zone of reduced nucleation, i.e. the ones around a pore that had already been successfully filled. Simulations of nanoelectrode arrays have shown that with increasing pore density and decreasing aspect ratio, the nanoelectrode array behaves more and more like a non-structured electrode of equivalent surface area.[197,198] This does of course not take into account the actual diffusion process inside the nanopores, which will differ strongly from classical models, especially when the dimensions approach the size of the electrochemical species. Future investigations of electrodeposition into porous templates will be needed in order to properly understand the process.

3.2 Bismuth telluride deposition on TiN

In this Section, studies on the non-aqueous deposition of Bi_2Te_3 are presented. The compound was chosen because it is of interest for the thermoelectric component of the ADEPT project, of which a key aspect is the deposition of *e.g.* a thermoelectric material into a porous template. Being a binary material, Bi_2Te_3 can be electrodeposited from a non-aqueous solvent (DCM) in a wide potential range, as shown by our colleagues Meng *et al.*[75] The solvent was chosen for the exact purpose of facilitating the target procedure of template deposition, where sufficient diffusion of the precursor anions is required. In the frame of this thesis it is an example of a realistic application, involving the same setup and electrode materials as in the previously studied model system. The main focus of the investigation is hence the deposition of Bi_2Te_3 on TiN, without the use of a mesoporous silica template. Questions around the structural evolution of Bi_2Te_3 deposits in time are discussed.

3.2.1 *Ex situ* studies

Electrochemistry Bismuth telluride deposition was carried out using a three-electrode standard setup as shown in the previous chapter. The non-aqueous solution consisted of 2.5 mM $[^nBu_4N][BiCl_4]$, 3 mM $[^nBu_4N]_2[TeCl_6]$ and 0.1 M $[^nBu_4N]Cl$ in DCM. 10 ml of solution were prepared as follows:

- 10 ml dry DCM
- 14.7 mg $[^nBu_4N][BiCl_4]$
- 24.8 mg $[^nBu_4N]_2[TeCl_6]$
- 278.9 mg $[^nBu_4N]Cl$

As the Bi and Te reagents are moisture sensitive, all Bi_2Te_3 experiments were carried out in a nitrogen filled Belle glovebox. These custom made precursors were synthesised by members of Prof. Gill Reid's group.
A cyclic voltammogramm of the system is shown in Figure 3.24 a), featuring a reduction peak on the forward scan around -0.8 V and a second bump around -1.5 V. Previous studies on this system done by members of the group indicate that Bi_2Te_3 is deposited from -0.6 V to -2.0 V with consistent composition.[75] As the deposition mechanism, they suggest the deposition of bismuth on previously reduced tellurium, which they concluded from individual voltammograms of the precursors. 3.24 b) shows current transients recorded at -1.0, -1.6 and -2.0 V for the duration of 1 s. The current magnitude increased significantly with decreasing potential. For samples deposited at -2.0 V, a dark film was noticeable even at only 1 s deposition time, suggesting a very high deposition rate at that potential.

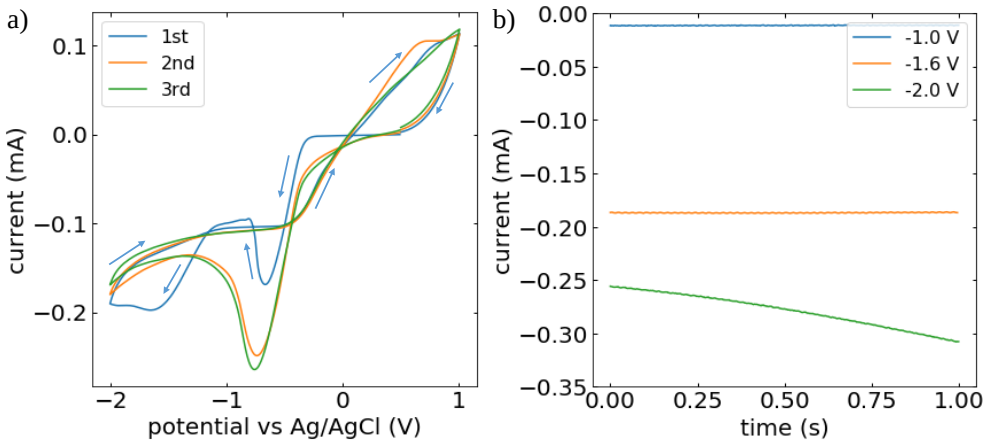

FIGURE 3.24: a) Cyclic voltammetry of a TiN electrode in 2.5 mM $[^nBu_4N][BiCl_4]$, 3 mM $[^nBu_4N]_2[TeCl_6]$ and 0.1 M $[^nBu_4N]Cl$ in DCM between -2.5 V and 1.0 V. b) Chronoamperometry for the duration of 1 s done at -1.0, -1.6 and -2.0 V vs Ag/AgCl respectively.

SEM Due to the features in the previously shown voltammogram, -1.6 and -2.0 V were chosen for further experiments. The deposition time was reduced as much as possible, as very high rates were expected with this electrolyte. SEM images of samples made at -1.6 and -2.0 V at 10 and 20 ms can be seen in Figure 3.25. Judging by eye, the number of particles increases when going from -1.6 V to -2.0 V, using the same deposition time. The particle size as well as their mean distance appears to be smallest for -2.0 V, which is why this potential was chosen for the scattering study (according to the limitations of the in house GISAXS system). Figure 3.26 displays further SEM data of depositions done at -2.0 V for i) 100 ms, ii) 200 ms, iii) 500 ms, and iv) 1000 ms. The further elongation of the deposition time expectedly leads to an increase in particle size and number. Average particle radii as well distances to their nearest neighbour were extracted from the SEM images using the software ImageJ. The results are compiled in Figure 3.27 a) and b) respectively. The average radii increases from 13 nm to 25 nm when increasing the deposition time from 10 to 200 ms. For longer times, the radial values seem to saturate, although the variance becomes so large that an actual trend can no longer be distinguished. This can be attributed to the simultaneous nucleation of small particles and the aggregation and growth of previously formed ones. A similar trend can be seen for the nearest neighbour distance, which increases at first and then seemingly saturates.

GISAXS GISAXS measurements of the samples deposited at -2.0 V for deposition times between 10 and 1000 ms were done on our in-house instrument, using an incident angle of 0.3°, and an SDD of 300.5 mm for a duration of 1800 s (beam size: 0.3 mm). The incident angle was chosen slightly below the critical angle of TiN (0.33° @8 keV) for total reflection of the beam on the substrate. At the same time, any of the deposited material would be penetrated and give good contrast in the images, even though the

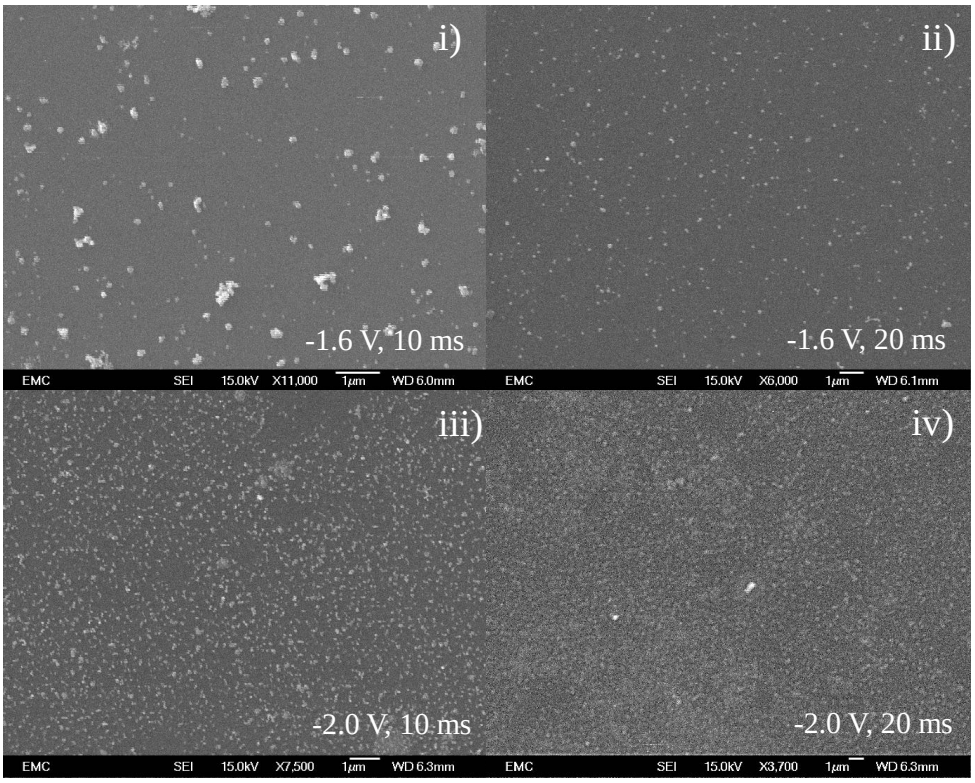

FIGURE 3.25: SEM of Bismuth telluride deposited from 2.5 mM $[^nBu_4N][BiCl_4]$, 3 mM $[^nBu_4N]_2[TeCl_6]$ and 0.1 M $[^nBu_4N]Cl$ in DCM. i) -1.6 V, 10 ms, ii) -1.6 V, 20 ms, iii) -2.0 V, 10 ms, iv) -2.0 V, 20 ms.

optical densities of Bi, Te, Bi_2Te_3 and TiN are relatively close together. The highest scattering contrast in this system lies at any interface between Bi and TiN (excluding the TiN/air interface) with a q_z value of 0.32 nm^{-1}, just below the specular reflection. The interface TiN/Te has the lowest contrast and would not be visible in this setup (q_z=0.08 nm^{-1}), and TiN/Bi_2Te_3 lies between the two (q_z=0.22 nm^{-1}). Figure 3.28 a) shows horizontal scattering profiles taken a) below and b) above the specular reflection, for Bi_2Te_3 deposited at -2.0 V for times between 10 and 1000 ms. The profiles are similar in their overall shape, consisting of a continuous decay in intensity towards higher q_y values with a slight shoulder at around 0.3 nm^{-1}. This could be attributed to a correlation distance of the particles of around 20 nm, but due to the broadness of the peak (shoulder) a broad variance can be expected. The low q_y intensity (above 0.07 nm^{-1}) decays significantly for deposition times above 100 ms, indicating a decrease in the number of particles. This is the result of coalescence of smaller to larger particles with increased deposition time. In summary, the data suggests that small particles are formed throughout the deposition, while the ones already present grow in size. As the shoulder remains visible even at longer deposition times, it can be deduced that small particles are continuously formed while the larger ones are generated through surface aggregation. Their distance does not change significantly even though the previously shown SEM images indicate an increase in particle distance and its variance

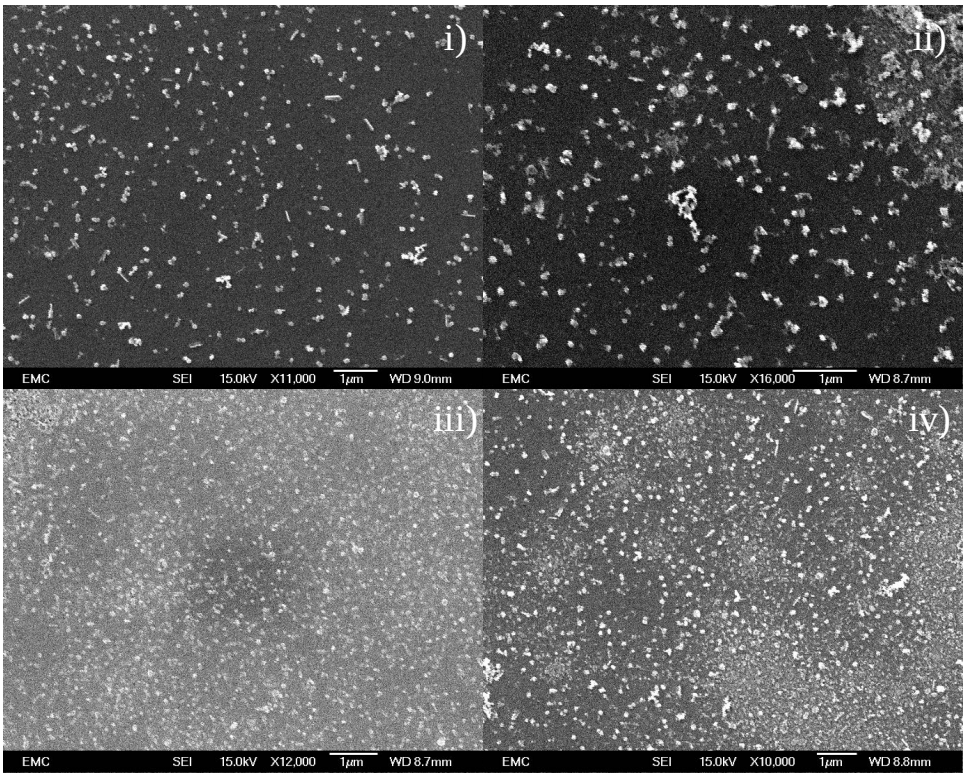

FIGURE 3.26: SEM of Bismuth telluride deposited at -2.0 V from 2.5 mM $[^{n}Bu_4N][BiCl_4]$, 3 mM $[^{n}Bu_4N]_2[TeCl_6]$ and 0.1 M $[^{n}Bu_4N]Cl$ in DCM. i) 100 ms, ii) 200 ms, iii) 500 ms, and iv) 1000 ms.

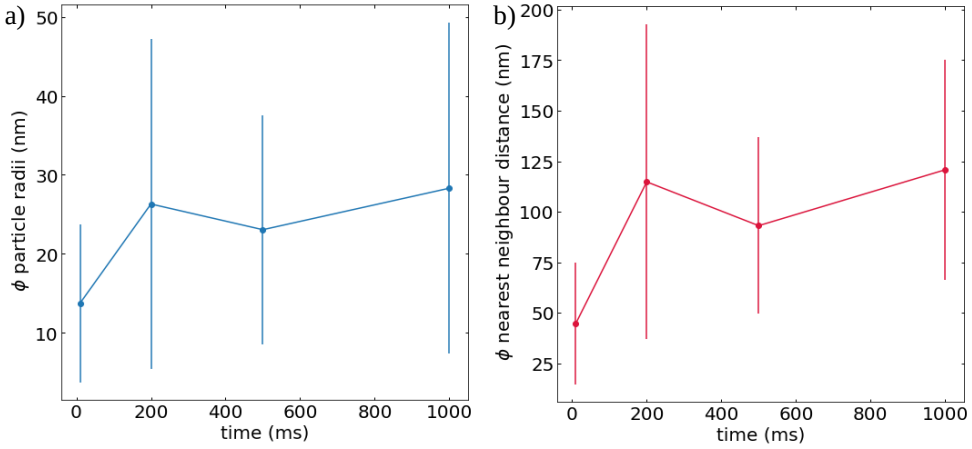

FIGURE 3.27: a) Average particle radii and b) nearest neighbour distances extracted from SEM images of samples made at -2 V and 10, 200, 500, and 1000 ms deposition time.

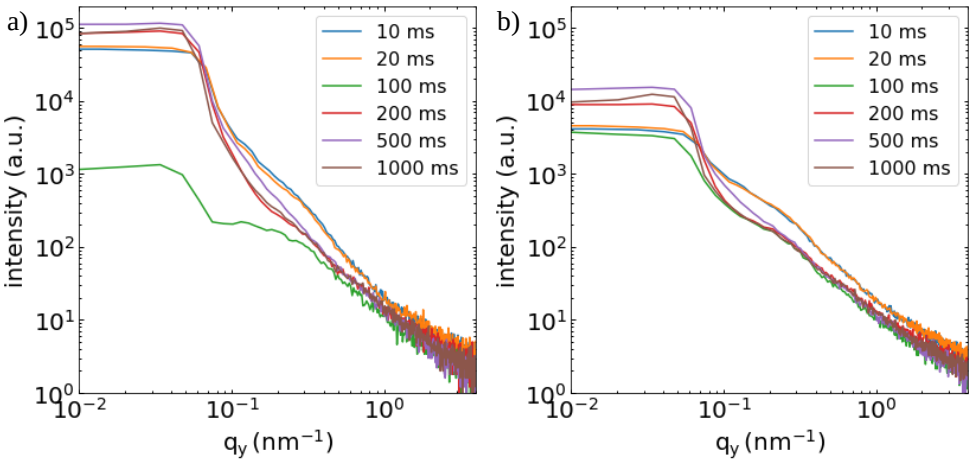

FIGURE 3.28: Horizontal scattering profiles of Bi_2Te_3 deposited at -2.0 V for times between 10 and 1000 ms in a) below and b) above the specular reflection.

with increasing deposition time (see Figure 3.27). With that in mind, one might gracefully postulate that the electrode surface and its structural condition would not at all impact the nucleation of new particles. Instead, merely the limitations in solution imposed by the availability of electrochemically available species dictate their reduction at any physically suitable location. With a more extensive measurement range, one would therefore expect to find multiple correlation lengths in the patterns, of which one would remain constant and relate to the smaller and newly formed particles, while the other one would increase in magnitude with deposition time. Another possibility could be, that the constantly appearing correlation length corresponds to the average distance of kinks/surface defects on a TiN electrode. No similar distance was observed during the deposition of Au on TiN, which means that either Au and Bi_2Te_3 have different "affinities" to nucleation sites or that DCM completely alters their distribution as compared to water.

Figure 3.29 summarises vertical projections of the measured scattering intensity for the same samples. The strong peak around $q_z = 0.42\,nm^{-1}$ identifies as the specular reflection of the incoming beam. There are slight variations in the recorded intensity, namely a small increase above the specular reflection, but no significant change indicating the transition of a binary particle composition to a singular one. This might be better revealed with enhanced contrast and measurement range, or with a vastly different approach tailored directly to the analysis of the spatial chemical composition.

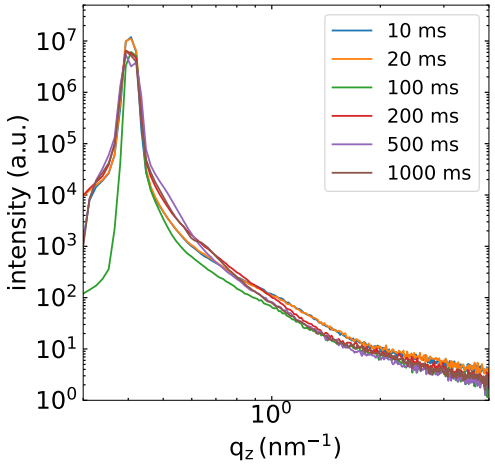

FIGURE 3.29: Vertical scattering profiles of Bi_2Te_3 deposited at -2.0 V for times between 10 and 1000 ms.

3.2.2 *In situ* GISANS

In order to better understand the electrodeposition process of Bi_2Te_3 from non-aqueous solution, an *in situ* GISANS experiment was performed at ILL/D33.[199] This had the advantage that the system could be investigated without disturbing the electrochemical environment, as would a very high energy X-ray beam needed to obtain sufficient transmission through DCM, which can lead to the unwanted introduction of electrons through the beam itself. The neutron beam penetrated the sample through the side of the wafer (Si, 5 mm thick) (Si-Mat, custom ordered 6" wafers) in order to probe the electrode surface (TiN, 200 nm) on which Bi_2Te_3 was deposited (as shown in the previous chapter in Figure 2.13). This means that the plane of reflection resided entirely within the substrate itself. Deuterated DCM (Eurisotope, used as received) was used as the solvent in order to minimise incoherent scattering from hydrogen atoms. Otherwise, the electrolyte solution was prepared as described in Section 3.2.1 within a Mbraun glovebox in Ar atmosphere (ILL support lab). A potential of -2 V *versus* Ag/AgCl was used for electrodeposition, which was applied for 1 s (#1), 2 s (#2), 10 s (#3), 70 s (#4), 300 s (#5), 600 s (#6), 1200 s (#7), 1800 s (#8), 3000 s (#9) after which SANS collections of 1 h were done at a wavelength of 7 $\AA$ and sample detector distance of 7.5 m. The corresponding current transients are shown in Figure 3.30. The incident angle was chosen as 0.5°, in order to maximize the beam footprint on the sample and hence the overall scattering signal. Due to the combination of materials used inside the cell, there was no usable critical edge at the electrolyte/electrode interface, so the incident angle was set high enough to not overlap with the two Yoneda peaks in the pattern.

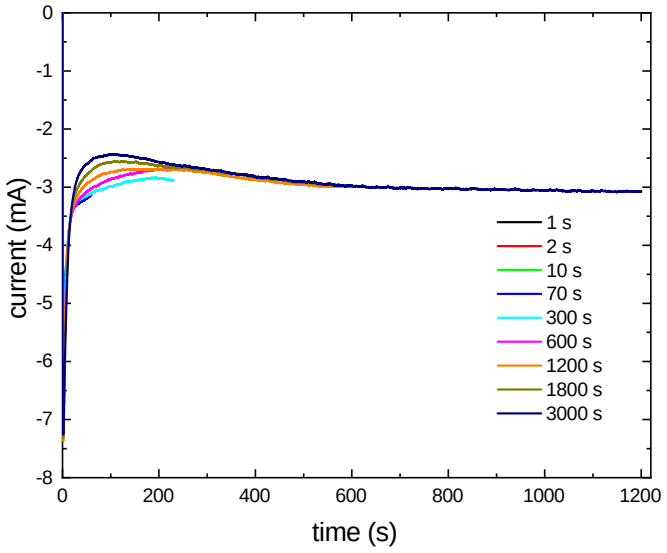

FIGURE 3.30: Current transients of the consecutively applied potential of -2 V during bismuth telluride deposition.

3.2.2.1 Neutron contrast

The foundation of small angle scattering is contrast, which is essentially the difference in scattering length density of the scattering particle and its surroundings. The radiation $I(q)$ scattered by N non-interacting particles of volume V in solution depends on the difference in scattering length density (SLD) $\Delta\rho = \rho_{particle} - \rho_{solvent}$ following the relation:

$$I(q) = N(\Delta\rho V)^2 P(q), \tag{3.1}$$

where the form factor $P(q)$ takes the variation of intensity with varying momentum transfer into account.[200,201] Table 3.1 shows the physical and scattering length densities, and molecular weights M_w of the employed materials. It can be seen that, the largest contrast resides between the deuterated solvent and Bi_2Te_3, followed by the Si/TiN interface. The difference between TiN/DCM(d) is lower than the one between Si/TiN, which is why critical reflection conditions could not be used. The deposition of Bi_2Te_3 slightly increases the contrast at the TiN surface, which is beneficial to the experiment. Of course, the considerations so far do not include the presence of the precursors/supporting electrolyte in the solution, which could move the setting either way. This is why the actual SLD of the electrolyte solution needed to be calculated. This was done using the neutron scattering and activation calculator from the National Institute of Standards and Technology (https://www.ncnr.nist.gov/resources/activation/), which allows for the calculation of SLD values and neutron contrast based on the atomic composition of a material. Deuterated DCM has a physical density of $1.35\,g/cm^3$ (according to supplier), which was chosen as the global value for the calculation as the precursors were dissolved. Using the respective mass fraction of each precursor and the supporting electrolyte, the SLD of plating

TABLE 3.1: Physical and scattering length densities (SLD) of the materials used in the neutron experiment. Values calculated using the "Neutron activation and scattering calculator" from the National Institute of Standards and Technology (https://www.ncnr.nist.gov/resources/activation/).

Material	Density (g/cm^3)	SLD(Re) ($10^{-6}Å^{-2}$)	M_w (g/mol)
Si	2.3290 [202]	2.073	28.085
TiN	5.21 [202]	3.037	61.874
Bi_2Te_3	7.74 [202]	1.985	800.761
CD_2Cl_2	1.35 [203]	3.661	84.93
Bi	9.79 [202]	2.407	208.981
Te	6.24 [202]	1.673	127.60
Deposition solution	1.35	3.570	n/a

solution was calculated as $\rho_{solution} = 3.570x10^{-6}$ Å^{-2}, which results in a contrast of $\rho_{electrode/solution} = 0.527x10^{-6}$ Å^{-2}.

3.2.2.2 Reflective signal/Yoneda peaks

Figure 3.31 shows a raw GISANS image taken *in situ* after the deposition of Bi_2Te_3 (after step #8). The cell was set up vertically on the beamline, which is why the usual vertical scattering direction (q_z) is shown as q_x in the image. The GISANS data features two Yoneda peaks in the q_z direction, which are shown in the one dimensional projections in Figure 3.32 a). The intensity of the specular reflection decreases within the first five deposition steps and increases again after that, which is underlined in the graph of their corresponding intensities shown in Figure 3.32 b), where the profile obtained from measuring the blank substrate in the cell was subtracted from each consecutive scattering profile. This graph also shows that the Yoneda peak around 0.04 nm^{-1} continuously loses intensity, while the one around 0.13 nm^{-1} gains intensity with each deposition step. Figure 3.32 c) shows the specular reflection intensity, which displays the previously mentioned trend.
A closer look at the Yoneda peaks is important, as they do correspond to different interfaces in the system which might be of interest to the experiment. Figure 3.33 a) shows a zoomed in region of the vertical profiles around the the lower Yoneda peak, where the increasing number of electrodeposition steps is indicated by the colour of the curves transitioning from blue to purple. These profiles were fitted using a combined Gaussian and linear function, of which the resulting peak positions and their corresponding SLD values are shown in Figure 3.33 b). The graphs show that the peak moves from 0.0425 nm^{-1} to 0.0435 nm^{-1} during the 9 steps of electrodeposition, which corresponds to a shift in SLD from 0.36 x 10^{-6} $Å^{-2}$ to 0.38 x 10^{-6} $Å^{-2}$. The contrast at the electrode/-solution in interface was calculated previously as $\rho_{electrode/solution} = 0.527 \times 10^{-6}$ $Å^{-2}$, which is a close value to the one found here at the beginning of the experiment with

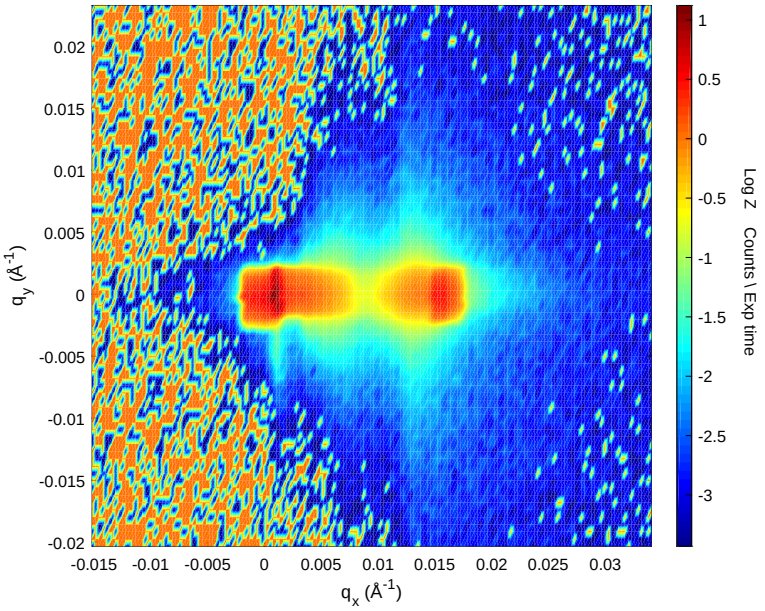

FIGURE 3.31: Raw GISANS data recorded during electrodeposition of Bi_2Te_3. Wavelength 7 Å, Incident angle 0.5°, exposure time 1 h. Cell set up vertically on the beamline - usual vertical scattering direction (q_z) shown as q_x.

the substrate blank (step 0) and can hence be attributed to this interface. The discrepancy within the values could have a multitude of reasons, as for example a possible contamination of the system with water, which would lower the contrast at this interface. Although efforts were made to keep this possibility at a minimum, we cannot exclude it from consideration. The increase of contrast at this interface with increased number of deposition steps indicates the deposition of a material, which increases the contrast at that interface. This is for true for Bi_2Te_3 as well as Bi and Te individually, as can be seen from Table 3.1. The fact that there is only one peak in this region visible as opposed to multiple ones indicates that the deposition of Bi_2Te_3 does not happen separately to Bi and Te nucleating on the surface. Otherwise, a transition of multiple peaks to a singular one would be expected, as the resulting films are known to be mainly Bi_2Te_3. Of course, with the shortest deposition time used in this work being 1 second long, a process of individual nucleation might have happened at much shorter times (ms). This process could also be happening so fast that it would not be visible in the scattering images obtained over 1 hour of averaging.

Regarding the higher Yoneda peak, the same method was used to extract peak positions and SLD values, as shown in Figure 3.34. One can see in Figure 3.34 c), that the peak position stays constant over time. Its corresponding SLD values of over 4.0×10^{-6} $\AA^{-2}$ is higher than any of the other interfaces and almost 10 times higher than the interface between electrode and electrolyte, so it's not exactly obvious where this peak originates from. The most compelling explanation for this peak is being the product of the refracted beam going through the entire plating solution in order to be

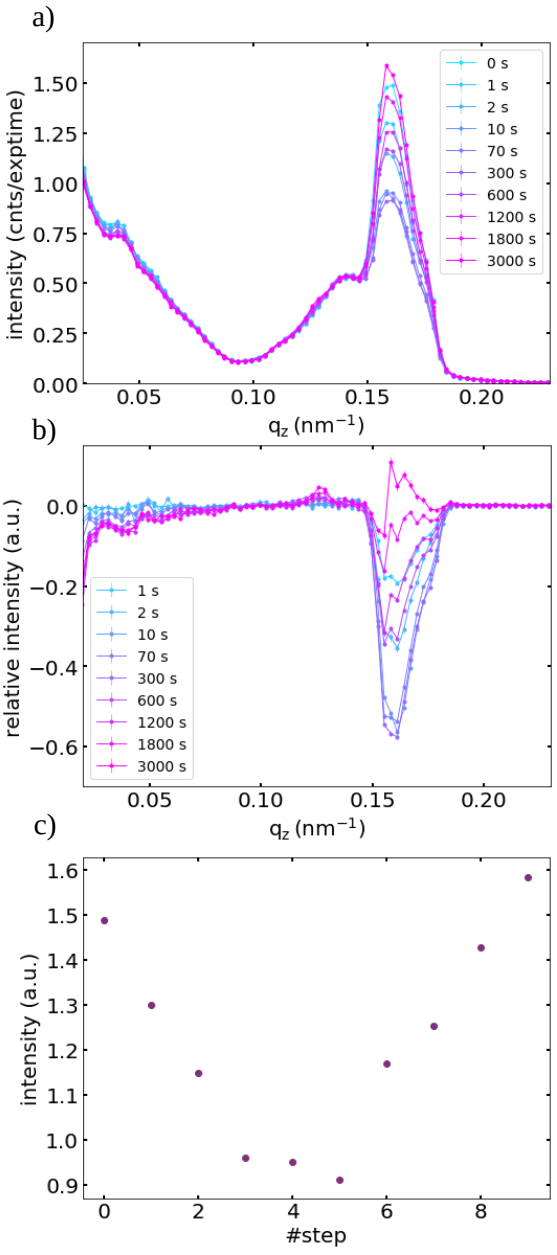

FIGURE 3.32: a) Vertical scattering profiles during the electrodepositon of Bi_2Te_3. b) Relative intensities (signal of blank substrate subtracted) of the profiles shown in a). c) Reflection intensity plotted versus its respective deposition step.

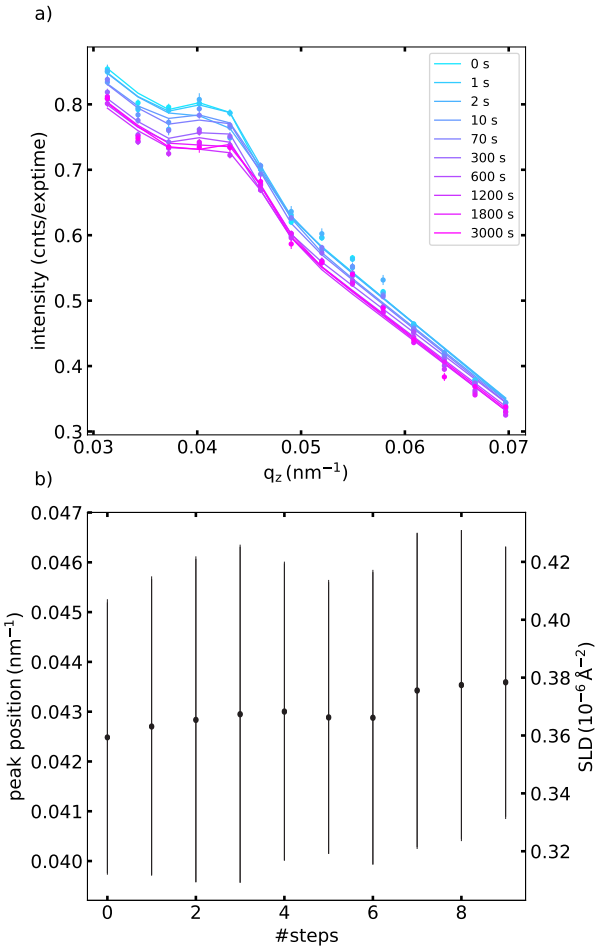

FIGURE 3.33: a) Vertical scattering profiles during the electrodepositon of Bi_2Te_3 around the lower Yoneda peak. b) Peak positions and corresponding SLD values calculated using equation 2.10. Peak positions were extracted by fitting a combined Gaussian and linear function to the profiles.

reflected at the Pt counter electrode. Pt has an SLD of 6.357×10^{-6} $\mathring{A}^{-2}$, which in contrast to the plating bath would result in a high q_z value. This would mean that this peak corresponds to processes happening at the counter electrode side of the experiment. However, there is a smaller bump emerging on its left, which was investigated as well.

The results are shown in Figure 3.35. It can be seen that a peak appears around 0.1271 nm^{-1} towards deposition steps 8 and 9. As the contrast value of over 3.2×10^{-6} Å^{-2} corresponding to this peak is far higher than the electrode/solution interface, it is presumably the effect of an air bubble forming inside the cell during the experiment, as the value is close to the contrast between TiN and air. This is another hint at the possible contamination of the system through water, although the introduction of the air bubble would mainly have happened after the cell being on the line for more than 8 hours, at which point the o-rings might have started to fail due to their continuous exposure to DCM. Considering the main peak in this region to be the reflection at the counter

electrode, the side peak could also indicate the deposition of a material on the counter electrode.

3.2.2.3 Off-specular signal/ Lateral structure

While the reflective part of the scattering image gives information about the chemical composition of the sample, the surface structure of an interface can be investigated by integrating the intensity along the horizon of reflection at the height of the material specific peak of interest. Figure 3.36 a) shows the corresponding Yoneda cuts from the SANS images, at the position of the Yoneda at $0.042\,\mathrm{nm}^{-1}$. Firstly, it can be seen that Bi_2Te_3 deposits in a layer-by-layer fashion as opposed to island growth, as no lateral peaks are visible which would indicate a correlation distance between growing islands. The increasing intensity in the high q-range is most probably related to increasing roughness of the film as it becomes thicker. The corresponding relative intensities are shown in Figure 3.36 b), where a decrease in low q intensity is the most prominent feature, which could indicate the decrease of particle numbers as they grow and coalesce into larger aggregates. In an attempt to better understand the scattering profiles, they were fitted using the Guinier-Porod model:[204]

$$I(q) = G * exp(\frac{-q^2 Rg^2}{3}) \; for \; q \leq q_1, \tag{3.2}$$

$$I(q) = \frac{D}{q^d} \; for \; q \geq q_1, \tag{3.3}$$

which include the Guinier parameter G, the Porod parameter D, the Porod exponent (fractal dimension) d and the radius of gyration Rg. In practise, the following relations are used to calculate the parameters:

$$q_1 = \frac{1}{Rg}(\frac{3d}{2})^{1/2}, \tag{3.4}$$

$$D = G * exp(\frac{-q_1^2 Rg^2}{3}) q_1^d. \tag{3.5}$$

The model, which is most commonly applied to polymer solutions, can be used to determine the dimensionality and size of scattering objects. Size is determined through the radius of gyration Rg, and dimensionality by the fractal dimension d (slope of the high q scattering). The Guinier and Porod parameters G and D are scaling factors for their respective regions. The resulting curves (converging, minimal chi-square) are shown in 3.36 c). The obtained parameters of these fits are presented in Figure 3.37. In this dataset, the full Guinier-Porod model was not suitable to fit, which is why only the decaying part (Porod region) was fitted in order to obtain the exponents at which the curves decay. The results of this can be contemplated in Figure 3.37, showing a very

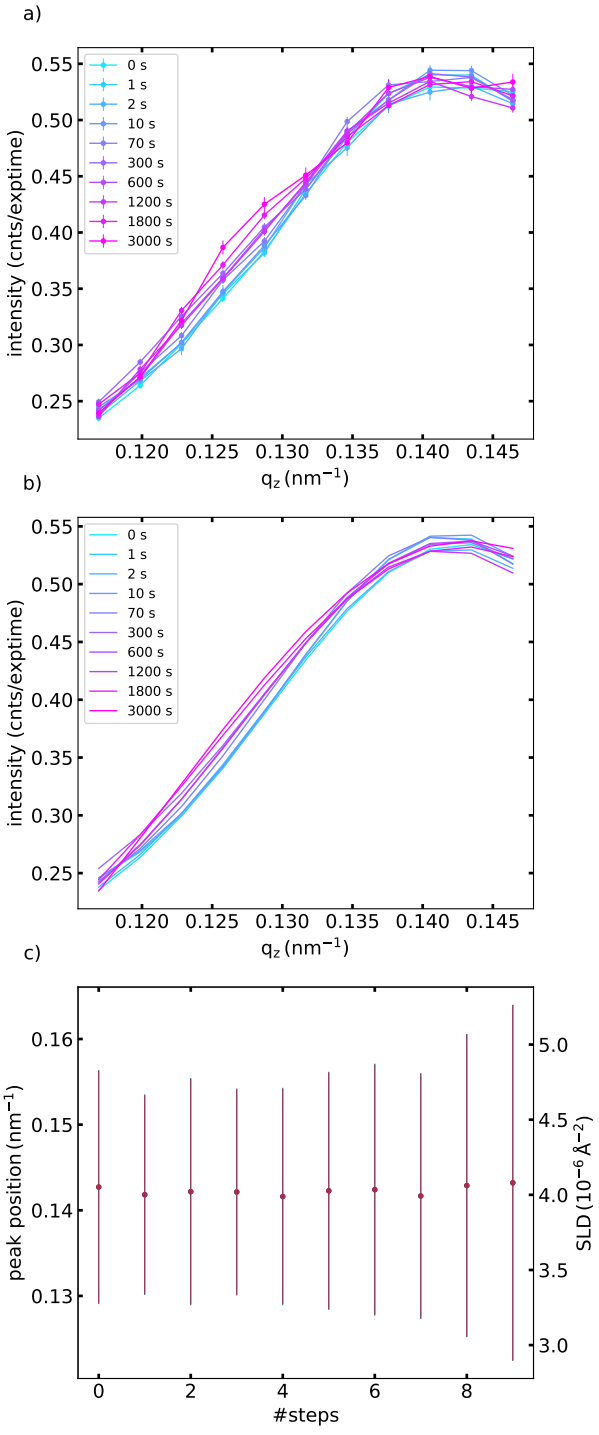

FIGURE 3.34: a) Vertical scattering profiles during the electrodepositon of Bi_2Te_3 limited to the region around the higher Yoneda peak. b) Fit lines of combined Gaussian and linear function to the profiles to extract the peak positions. c) Peak positions and corresponding SLD values calculated using equation 2.10.

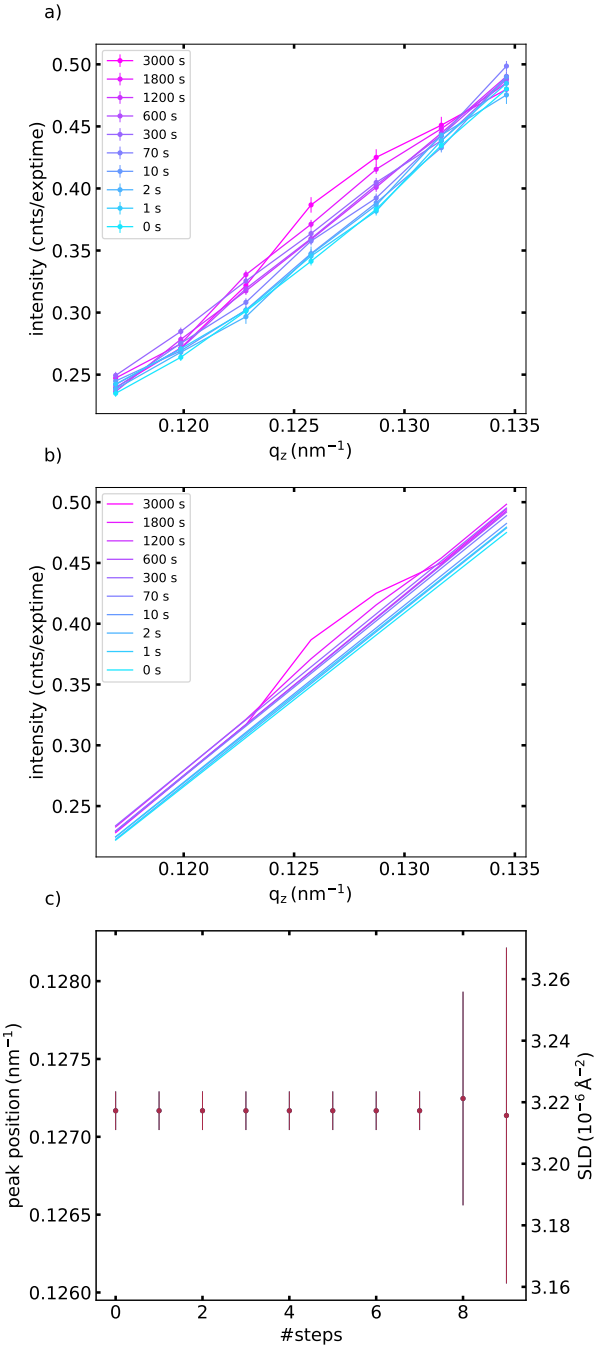

FIGURE 3.35: a) Zoom of scattering profiles during the electrodepositon of Bi_2Te_3 at values just below the higher Yoneda peak shon in Figure 3.34. b) Fit lines of combined Gaussian and linear function to the profiles to extract the peak positions. c) Peak positions and corresponding SLD values calculated using equation 2.10.

slight increase of the Porod parameter D with a simultaneous decay of the fractal dimension d. For values between 3 and 4, the fractal dimension indicates a surface fractal type of structure, which in this case seems to be moving towards the region of mass fractals ($d < 3$).[204] This indicates the disordered structure of the film moving from a surface fractal to a mass fractal with increasing film thickness.

The above procedure was then applied to the Yoneda peak at $0.13\,\mathrm{nm}^{-1}$. Integrations along q_y, relative intensities as well as the fit curves are on display in Figure 3.38 a), b) and c) respectively. This time the full Guinier-Porod model suited the data very well and the fit results shown in Figure 3.39 indicate that while G and Rg stay mostly constant during the course of deposition, d once again decreases from its initial value of roughly 2.9 down to 2.7. This trend shows once again the migration of the film towards the mass fractal regime. The absence of strong lateral features in the Yoneda cuts from this peak speak against the possibility of this being related to the counter electrode surface, as in practise it was seen that sputtered Pt films possess a rather strong diffuse signal, which should be visible here unless it was blocked by the cell walls, as this electrode was 5 mm below the main reflection plane. In this case these the features could only be part of the reflected refracted beam going through the film in reverse order, which would make it a parasitic SANS signal. Totally excluded in these considerations is the possibility of parts of the film de-wetting from the surface floating around in the plating bath, which is likely to happen with increased measurement time and film thickness.

Summary As a conclusion to this experiment, it can be said that there is no evidence from this data of Bi_2Te_3 growing on TiN in the typical island growth fashion as seen in previous experiments with gold. In addition, the absence of multiple peaks in the reflective part of the data indicates that the overall deposition process does not involve large particles made from the individual elements, which later combine to form Bi_2Te_3. This fits well with the fact that no lateral features were seen, which would have been the case for separate deposition. This does of course not exclude the reduction of Bi, Te and Bi_2Te_3 on a length scale much smaller than observable in this experiment, or simple at deposition times shorter than the ones probed in this study.

For future experiments around this system it would probably be worthwhile to divide it into one part looking at the chemical composition of the layers, while the other one focuses on the structural evolution. This could be realised by combining data from a neutron reflectivity experiment with a SANS experiment, giving information about the chemical composition in vertical direction (neutron reflectivity) and structure of the deposits (SANS). This would enable getting more precise information in both domains without compromising on either of them.

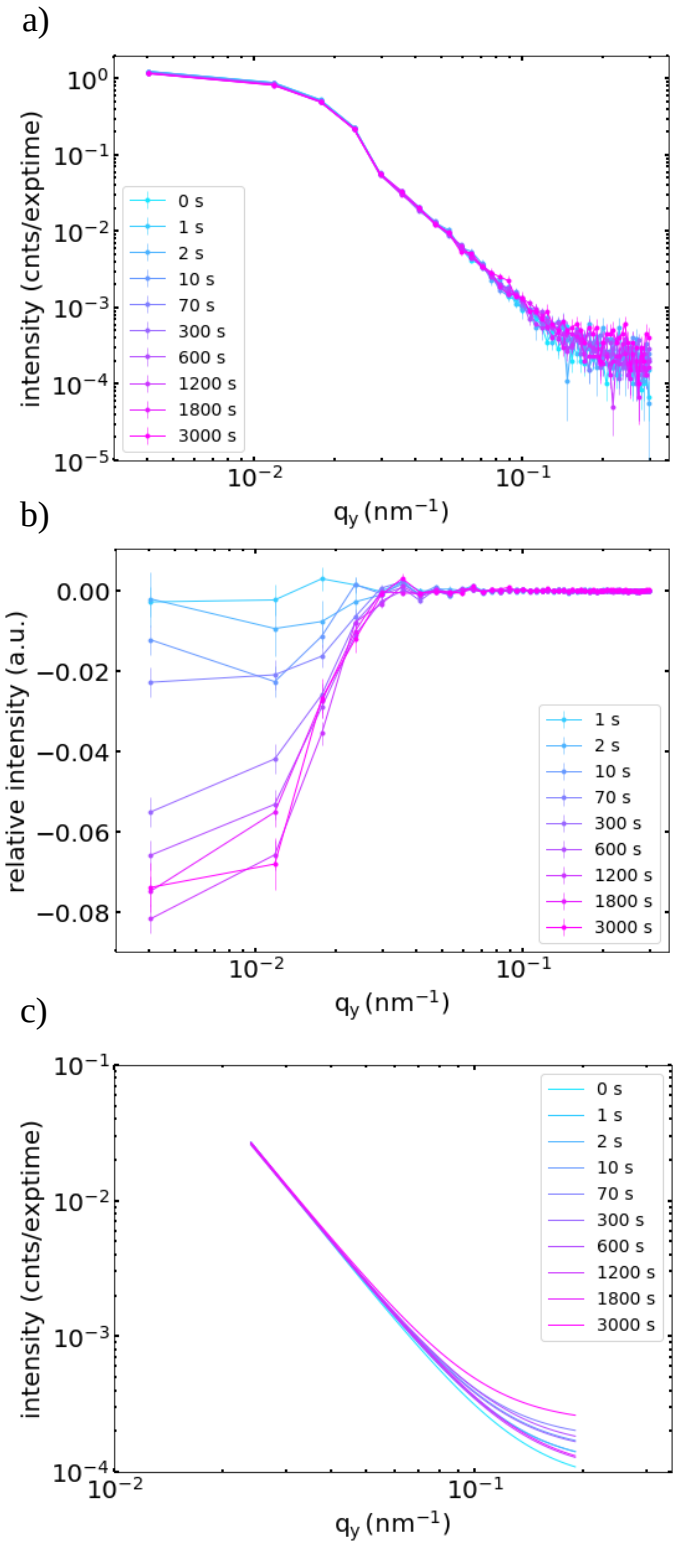

FIGURE 3.36: a) Integrated horizontal profiles at the Yoneda position of 0.042 nm^{-1}. b) Relative intensities of the data shown in a). c) Guinier-Porod fits of the data shown in a).

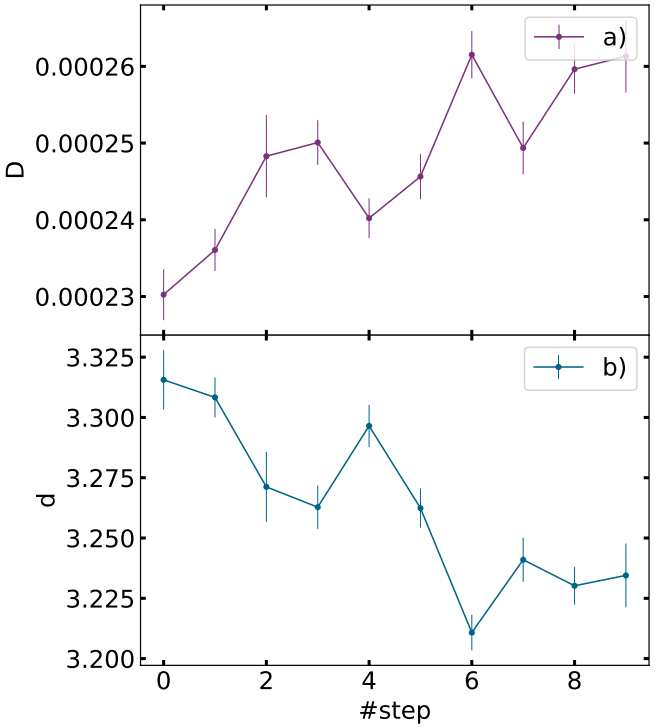

FIGURE 3.37: a) Porod parameter D and b) fractal dimension d obtained from the Porod fits shown in Figure 3.36.

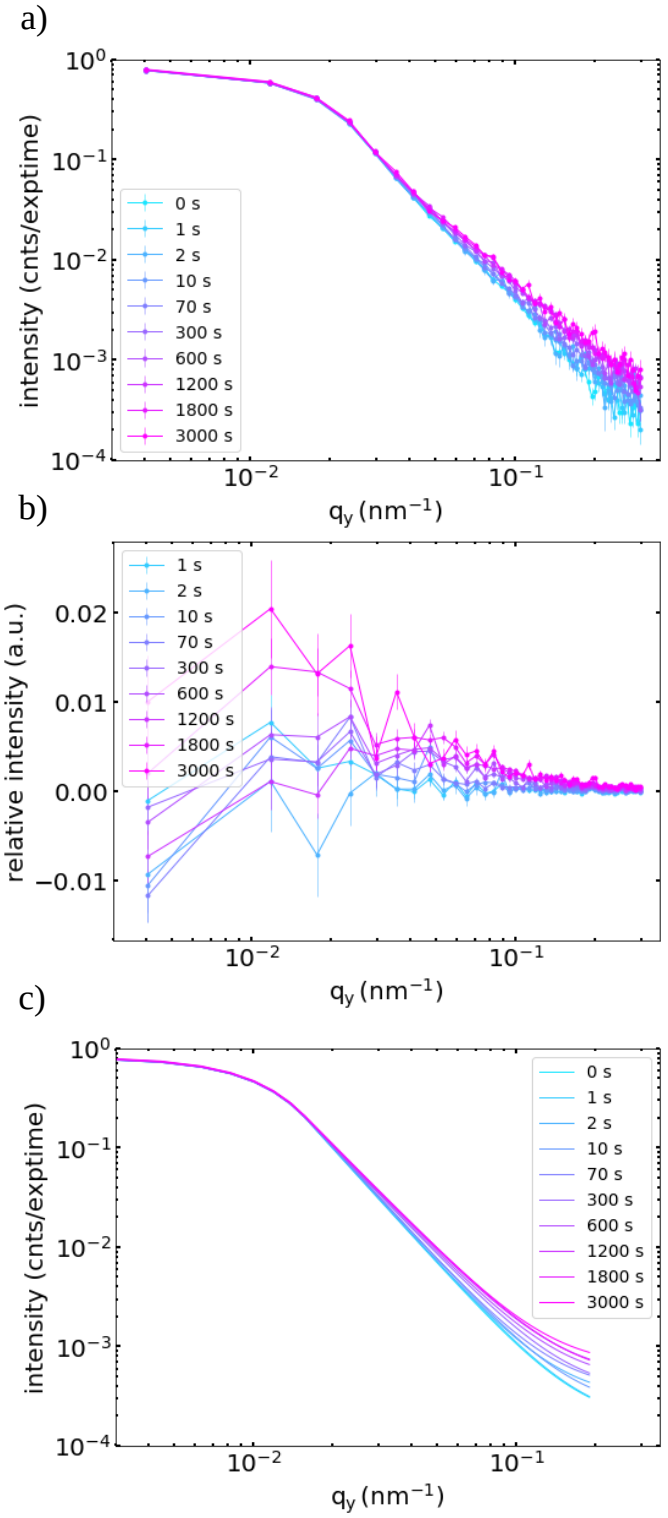

FIGURE 3.38: a) Corresponding horizontal profiles at the Yoneda position of 0.13 nm^{-1}. b) Relative intensities of the data shown in a). c) Guinier-Porod fits of the data shown in a).

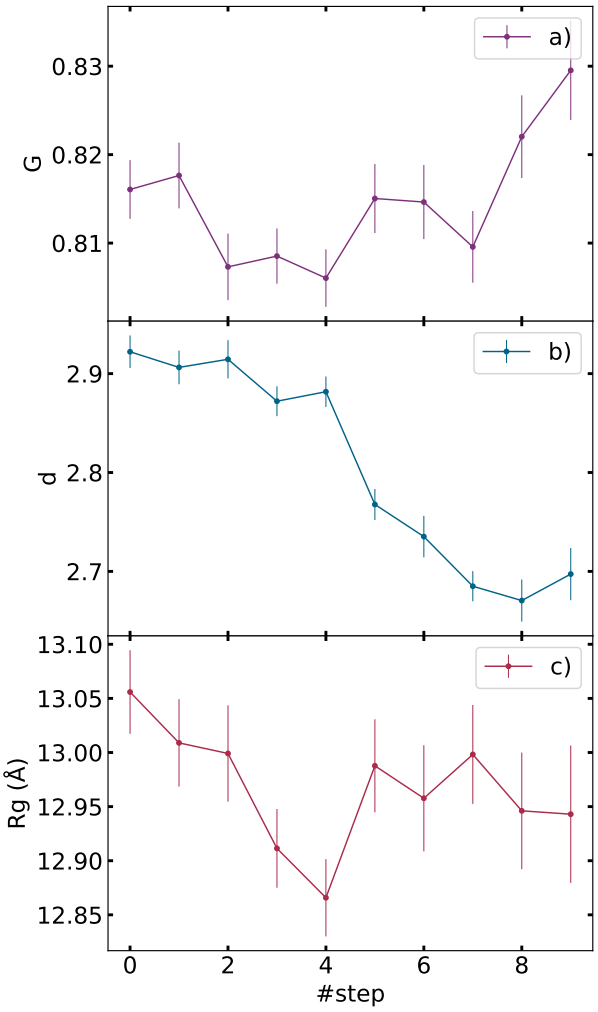

FIGURE 3.39: a) Guinier parameter G b) fractal dimension d and c) radius of gyration Rg obtained from the Guinier-Porod fits shown in Figure 3.38.

Chapter 4

Time resolved studies of EASA

This chapter summarises results obtained from studies on the Electrochemically Assisted Surfactant Assembly (EASA) of silica. The first section comprises a study on the electrochemically assisted deposition of silica structures on bare TiN substrates, while simultaneously performing GISAXS measurements. As mentioned in the introduction of this work (see 1.6), EASA is a useful technique for the making of mesoporous silica structures with pore channels aligned vertically to the substrate surface. It has however not been precisely revealed, what the exact mechanism behind the deposition process is, especially regarding the formation of spherical particles on top of the film, and the limits of pore dilation using a swelling agent. This was the rationale behind driving this fundamental time-resolved investigation around the structural evolution during film formation, using GISAXS as the monitoring technique. In addition, *ex situ* control measurements are carried out. Finally, a revised version of the mechanism is formulated as the result of this detailed multimodal study.
In the second section, the effect of applying a sinusoidal potential to an electrode during EASA is elucidated. The intention was to reduce the number of surface aggregates and increase film thickness of EASA-generated silica films by a reduction of the hydroxide diffusion layer thickness.
Finally, the evolution of local pH near a TiN electrode at cathodic potential is shown, measured in real time using a HPd microelectrode as pH-sensor.

4.1 EASA on TiN: An *operando* GISAXS study

This section contains the experimental results obtained from an *operando* study of the EASA process on a TiN substrate. A substrate placed inside a full electrochemical cell acted as the reflective surface for an X-ray beam used to monitor the formation of silica structures through the application of a constant cathodic potential. The majority of the results consists of time resolved GISAXS measurements, which were carried out at Diamond Light Source, beamline I07 (see Section 2.5.2). A dedicated electrochemical cell was used, which can be seen in Section 2.5.2, Figure 2.12. Additional GISAXS experiments were done either *ex situ* at the DLS/I07 beamline, or in-house on our Rigaku Smartlab diffractometer (c.f. Section 2.5.1).

4.1.1 Experimental setup and conditions of the *operando* GISAXS study

Silica sol compositions A variety of different solutions was used during the *operando* GISAXS-EASA experiment, as shown in table 4.1. All solutions consisted of 20 ml 0.1 M $NaNO_3$ and 20 ml ethanol at pH=3 (using 0.2 M HCl). Either hexadecyltrimethylammonium bromide (CTAB) or octadecyltrimethylammonium bromide (OTAB) were then used as surfactant and different amounts of mesytylene were used as swelling agent to increase the poresize of the network. Table 4.1 shows the different compositions of the solutions used with their shortnames.

Sample alignment After the complete assembly of the cell, the respective solution was pumped through the cell using a peristaltic pump (Ismatec) in order to fill it up and the flow was maintained throughout the alignment and measurement. It was then mounted onto the beamline's hexapod with a custom made cell holder. Sample alignment was done using a standard procedure: at first the height would be scanned using the direct beam and then adjusted to half-cut conditions. Then, the incident angle was

TABLE 4.1: Compositions of the silica sol used during the *in operando* GISAXS experiment at DLS/I07.

Solution	CTAB (mg)	OTAB (mg)	Mesitylene (µl)	Mesitylene:CTAB
A1	480	0	0	0:1
A2	480	0	17.9	0.1:1
A3	480	0	90	0.5:1
A4	480	0	179	1:1
B1	0	480	0	0:1
B2	0	480	90	0.5:1
B3	0	480	179	1:1
B4	0	480	358	2:1

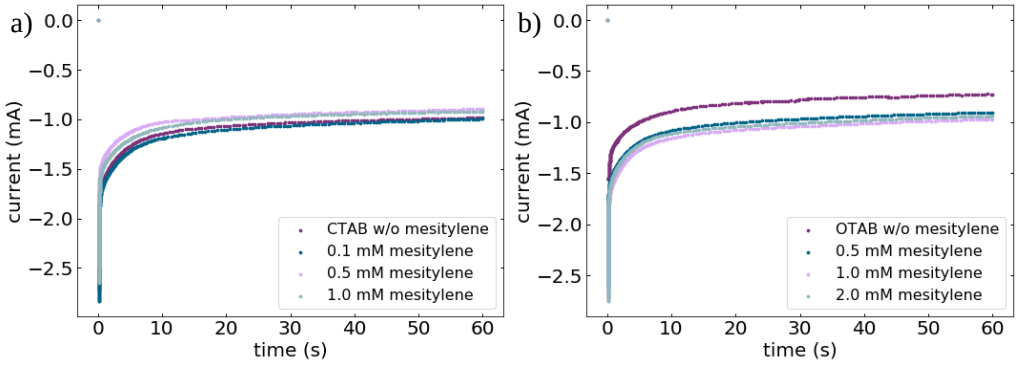

FIGURE 4.1: Chronoamperometry of silica films deposited using different solution a) A1-A4 and b) B1-B4. The potential was kept constant at -2 V for 60 s for all depositions.

scanned until a reflection from the sample surface was obtained. From the pixel position of the reflections on the detector, the zero position was extrapolated by a linear fit of angle vs specular intensity. The whole procedure was repeated once in order to ensure precise alignment conditions. The critical angle of TiN at 12.25 keV has a value of 0.21°, which determined the use of 0.20° as incident angle for the experiments in order to probe the whole film above the substrate, as the TiN surface is totally reflecting in this setting. The sample detector distance was set in a way that the first order peak of the silica structure which resides typically around 1.6 nm^{-1} would be at the centre of the q_y range, giving enough probed q-space on both sides to enable detection of smaller as well as much larger structures.

Electrochemistry Every deposition was carried out at a potential of -2.0 V *vs* Ag/AgCl for 60 s, as this potential was determined as optimal for TiN substrates in work done in this group previously.[196] The deposition time was increased beyond optimised parameters in order to follow the process for a longer time period. Prior to any deposition, the TiN electrodes were rinsed with ethanol. The current transients recorded during deposition are shown in Figure 4.1. With the exception of Sample B1_1, the transients show almost identical profiles, all asymptotically approaching a value of roughly -1 mA. The current transients show the indirect nature of the deposition process, in which the current is only used for inducing the required local change in pH. This is why no features appear in the electrochemistry which could be related to the formation of the film.

Control experiments In order to make sure the *operando* GISAXS cell would provide adequate electrochemical conditions for the EASA of silica, control experiments were done in house, using the exact same electrochemical setup. The scattering image was then recorded in house on our Rigaku Smartlab system. Deposition times were kept in the range of seconds only in order to minimize the formation of surface aggregates so that the presence of vertically aligned channels could be confirmed. Figure 4.2 a)

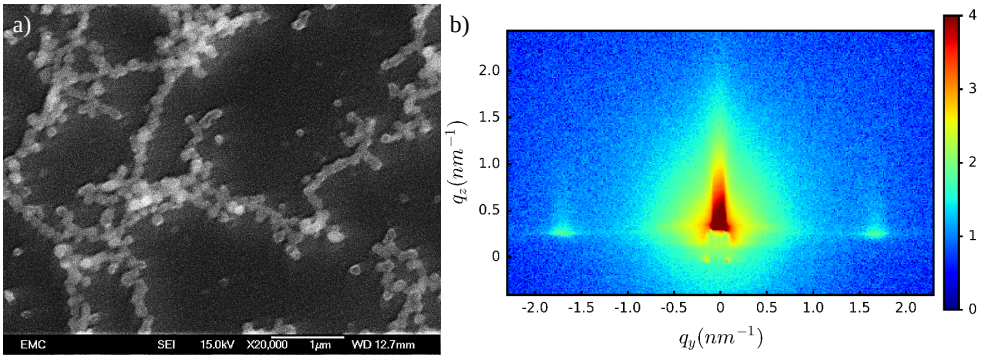

FIGURE 4.2: a) SEM and b) GISAXS image of a silica deposited onto TiN using a potential of -2.0 V for 2 s. GISAXS measurement done in house on Rigaku Smartlab.

shows the corresponding SEM and b) GISAXS image of a silica deposited onto TiN using a potential of -2.0 V for the duration of 2 s. Only a small number of aggregates can be seen in the microscopy, and the GISAXS clearly shows two spots in horizontal direction, corresponding to vertically aligned pore channels. A very slight ring can be seen too, due to the presence of a few surface aggregates.

4.1.2 Silica EASA using CTAB

In order to better quantify the process, the experiments will be dealt with separately. The first system to be discussed is silica EASA with CTAB and no swelling agent.

Scattering images During the deposition of silica, scattering images were recorded with 100 ms exposure time and 20 ms readout. In total, 700 images were recorded for each experiment, leading to a total time of 84 s. The potential was switched off 60 s after the start of scattering data acquisition, so that GISAXS images could be recorded until 24 s after this point. Silver behenate (AgBh) was used to accurately measure the sample detector distance of 2007.52 mm using the calibration tool in the software DPDAK.[195] At first, a look at full detector images from different times is useful. Figure 4.3 shows two dimensional images taken right at a) 0 s, b) after finishing the whole experiment but with the sample still inside the full cell and c) after ageing the sample at 130 °C overnight. It can be seen, that before applying the potential, no scattering features apart from the direct beam (blocked by beamstop), the specular reflection and a small amount of diffuse signal around the Yoneda position can be seen (Figure 4.3 a)). After completing the deposition (Figure 4.3 b)), a strong ring became visible at a position above $q_y = 1.5\,\mathrm{nm}^{-1}$. When measuring the same sample *ex situ* after its removal from the cell (Figure 4.3 c)), lateral features become visible alongside the ring which where not distinguishable right after deposition due to dominance of the aggregate signal. This indicates, that apart from the film forming with vertical pore channels, a similar structure with no preferred orientation was formed.

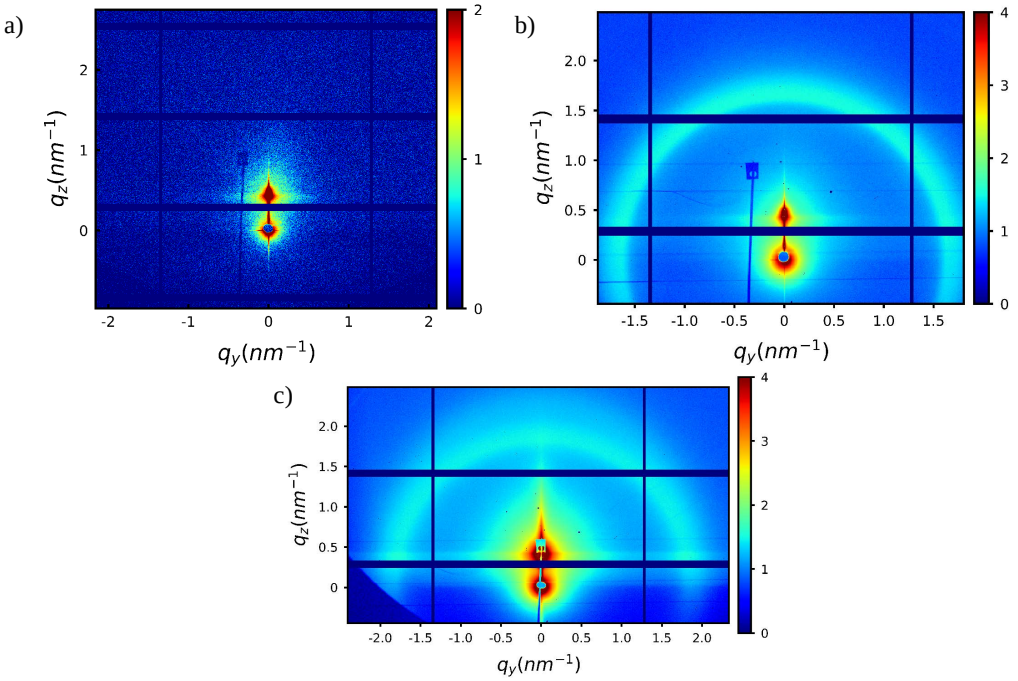

FIGURE 4.3: Scattering images for a) 0 s, b) after deposition and c) after ageing of the samples. Exposure times: 0.1 s, 5 s and 60 s respectively. Incident angle: 0.2°.

Lateral peak positions As the next step, the position of the scattering features was analysed from horizontal integrations of the detector images once again using DPDAK software package for Python.[195] The first frame in which a peak can be distinguished from the background noise (by eye) is frame 25, which corresponds to a deposition time of $25 * 0.12\,s = 3\,s$. This peak is shown in Figure 4.4 a), alongside with the position of the peak after finishing the deposition(b)) as well as after aging (c)). The first scattering feature appears to only consist of horizontal spots, with the ring emerging only a few frames later. The spots correspond to the vertically aligned compact film on the electrode, while the ring results from spherical porous particles on top of the silica film. The compact film seems to be forming before the spherical particles, which makes sense as the hydroxide is generated from the electrode surface. Liu *et al.* reported the time until the start of silica gelation for EASA with TEOS from their simulation results as 1.3 ± 0.3 s,[205] which fits roughly to the emergence of the scattering feature.

A simple Lorentzian peak function was used to fit the peaks, yielding positions shown in Table 4.2. The position where calculated using $d = 2\pi/q$ and $\Delta d = 2\pi\Delta q/q^2$. The distance d corresponds to the pore spacing in this case and the values fit well with values reported in the literature,[110,137,196] lying in the range of roughly 3-4 nm, with uniformly distributed alignment. The ageing of the sample led to a decrease of the pore spacing of roughly 0.3 nm, which can be attributed to the full evaporation of remaining solvents during the process.

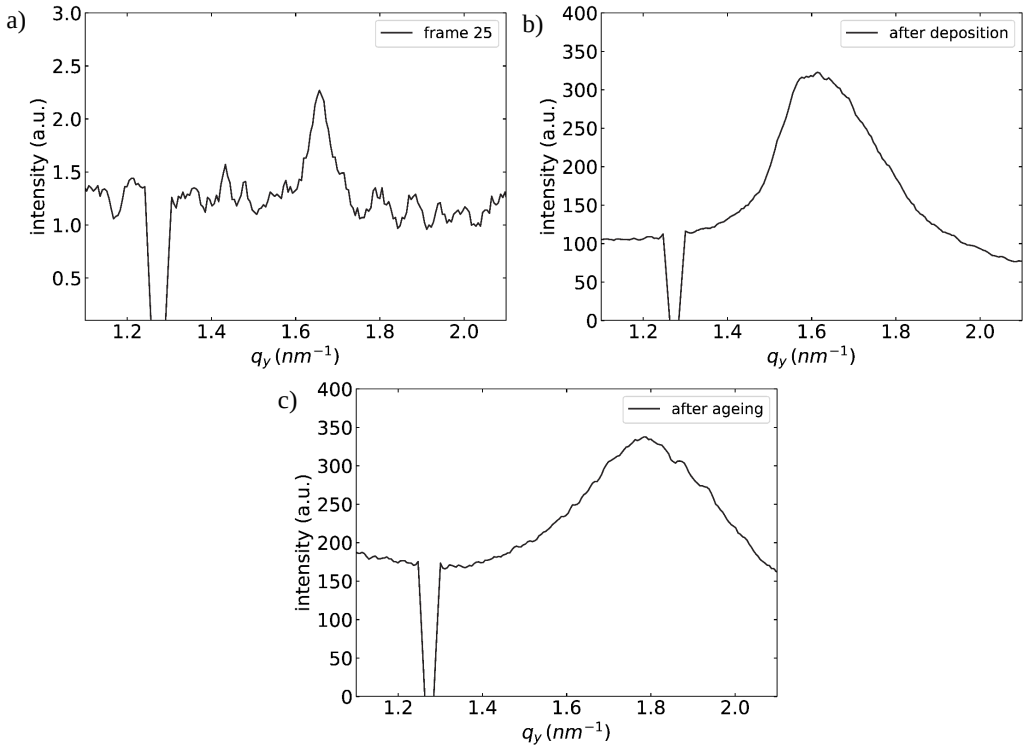

FIGURE 4.4: Comparison of the horizontal peak for a) the first appearance during deposition, b) after deposition and c) after ageing of the samples.

TABLE 4.2: Peak positions (10) corresponding to the signals shown in Figure 4.4.

	First appearance	After deposition	After ageing
q_y	$1.66 \pm 0.03\,nm^{-1}$	$1.63 \pm 0.16\,nm^{-1}$	$1.78 \pm 0.24\,nm^{-1}$
d	$3.78 \pm 0.07\,nm$	$3.86 \pm 0.38\,nm$	$3.53 \pm 0.48\,nm$

SEM After the experiment, the sample was analysed using SEM to get a better idea of its morphology. Top view SEM images of the sample made using solution A1 (A1_2) are shown in Figure 4.5 where a), b) and c) show the film at x20, x110 and x5500 magnification respectively. The images show the appearance of the sample after deposition and overnight ageing at 130°C. No further treatment was done, which means that the surfactant (CTAB) is still present in the film. As expected, the silica film is fully covered in aggregates, ranging up to 1 micron in diameter. As one can see in Figure 4.1 c), the dendritic structures are made up from spherical particles which stick to each other. This is expected from the long deposition time of 60 s, as longer times lead to an increased amount of surface aggregates. The scattering data obtained from the aged sample indicates the presence of a vertical structure. As this is not visible from the top, it must be underneath the thick coat of particles.

For this reason, the sample was cleaved for cross-sectional analysis by SEM, which was done by our project partners at Warwick University. Prior to that, the surfactant was removed from the sample by immersion into 0.2 M HCl in ethanol for 5 minutes. Figure 4.6 a) shows the results of that, in which the very thick layer of particles on top of the

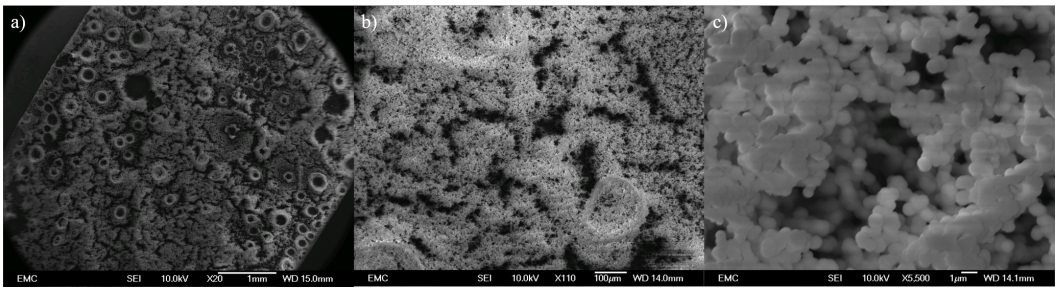

FIGURE 4.5: SEM images of sample A1_2 at magnifications of x20, x110 and x5500. 10 kV acceleration voltage was used. The sample was not coated prior to microscopy.

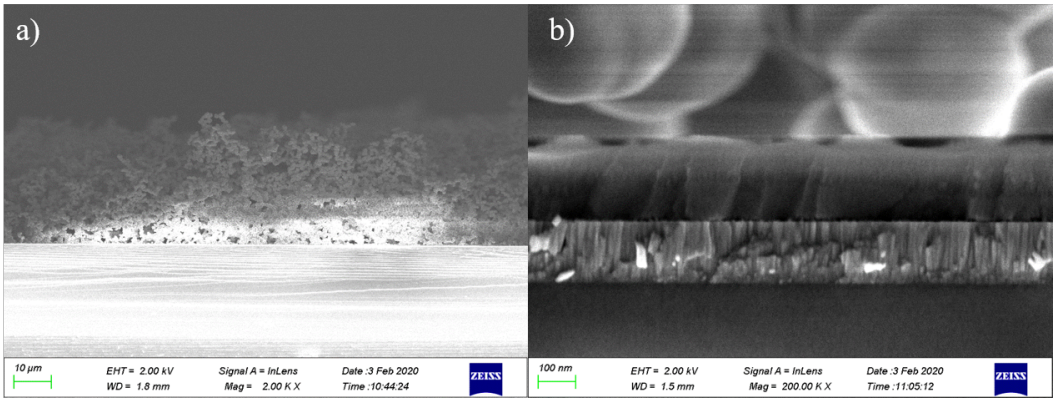

FIGURE 4.6: SEM crosssections taken from sample A1 at magnifications of a) x2000 and b) x200000. The bottom of the images shows the SI substrate, with the 200 nm thick TiN layer on top, which in turn is covered by a layer of mesoporous silica with roughly the same thickness. On the very top, spherical agregates can be seen, which form a layer up to 30 microns thick. Surfactant removed prior to microscopy by immersion into 0.2 M HCl in ethanol for 5 minutes.

film is very obvious, having a thickness of roughly 30 microns. This was expected from the previously shown top down images. Figure 4.6 b) shows a close up of the same crosssection at higher magnification, where one can clearly see the composition of the sample (bottom to top): silicon substrate, TiN layer, compact silica layer, and surface aggregates. The lateral component seen in the scattering image in Figure 4.3 c) must hence come from the silica film underneath the silica particles, which was expected to be vertically aligned.

Structural evolution in time With 60 s deposition time at -2.0 V, the process of electrochemically assisted surfactant assembly leads to the formation of a film with vertically aligned pore channels at the substrate surface, with large spherical particles on top that make up a film of aggregates of tens of microns in thickness. The actual part of the surfactant assembly leading to the vertically aligned pores in a compact film happens mostly at the beginning of the process until reaching a critical thickness, upon which only spherical particles are formed. The time evolution of the scattering signals in lateral direction as well as the ring have to be analysed in detail. Figure 4.7 shows a

contour plot of horizontal scattering profiles extracted from each frame versus deposition time. The blue line below q_y=0 is the shadow of the beam stop that was not used in this experiment but kept close to its working position because it would not move reliably on large distances. The two symmetrical dark lines outside of q_y=$\pm$1.0 nm^{-1} are detector gaps. Integrations were done at the Yoneda position of the TiN/silica sol interface at q_z= 0.5 nm^{-1}. One can see that the features in lateral direction appear in the scattering images after 3 s, which symmetrically move towards smaller q_y values until the shutoff of the potential at 60 s. After this, its q_y values seem to slightly increase again. Once again, a closer look at these scattering profiles is needed, which is why the peak position of the features was extracted using custom-made Python based software.

An inspection of the frames at the beginning of deposition had revealed that two separate signals were present: 1. spots on either side of the reflection plane corresponding to a vertical feature in real space and 2. the ring. Figure 4.8 shows the evolution of the peaks during silica deposition. Peak positions (blue: spot, purple: ring) were extracted from fitting a Gaussian function to the peak in each frame (700). One can see that the first values around 3 s are a bit lower than the 1.66 nm from frame 25 reported above, however, they do fit when taking into account the fit errors of both. The slight discrepancy might arise from the different peak functions used (Lorentzian *vs* Gaussian) and from the fact that the graph above was fitted manually, while the time series was done automatically. When looking at the time evolution of the horizontal peak position, one can observe a decrease of the q-values, which in turn corresponds to an increasing d-spacing during deposition. The decrease seems to be going on until reaching 40 s deposition time, at which the curve reaches a plateau at q_y= 1.56 nm^{-1} that expands up to 60 s, where the potential is switched off. After that, the values slightly increase again until the end of the measurement at 84 s. When comparing this profile to the current transients in Figure 4.1, one can see that the electrochemistry does not reflect any of the features that appear in the scattering data, which is expected as the electrochemical process is indirect.

The "inflation" of the structure shown in Figure 4.8 could arise from hydroxide ions generated at the electrode surface which, as the deposition progresses, have to travel through the network in order to diffuse away. The trend matches the deflation of the structure as soon as the potential is switched off. As the ring signal strongly dominates the entire scattering pattern throughout most of the deposition, one can not directly assume that the compact film expands to the same extent as the surface aggregates. More likely is, that the expansion process is related to the diffusion of ethanol into the micelles, which is produced during the condensation of TEOS.[206] This effect is said to decrease the overall curvature of the micelles formed on the electrode surface, ultimately leading to their elongation into standing pore channels. Figure 4.9 shows the

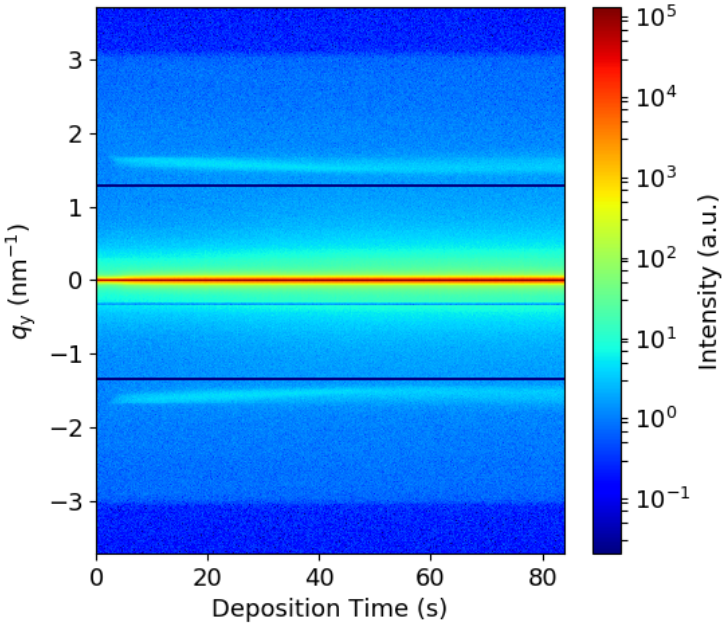

FIGURE 4.7: Contour plot of horizontal scattering profiles extracted from each frame *versus* deposition time. Integrations were done at the Yoneda position of the TiN/silica sol interface at $q_z = 0.5\,nm^{-1}$. CTAB was used as a surfactant in this experiment.

evolution of intensity averaged over the q-range 1.46-1.7 nm^{-1}, showing a sharp increase after a few seconds when silica condensation starts, with a maximum around 22 s that levels off at around 40 s, just about the same time at which the inflation effect reaches its plateau. The formation of SiO_2 increases the contrast between the solid parts of the film and the solution environment, leading to this increase in intensity. At this point, the contrast between silica structure and solution reaches its highest value, which might correspond to crossing a critical condition similar to a percolation threshold. The network solidifies sufficiently for it to retain the pore spacing at this point, followed by only slight shrinkage. After that, the reduction of the TiN area by the growing silica structure limits hydroxide generation and also the condensation process. The consecutive drop in hydroxide concentration might then lead to the partial dissolution of already condensed species until reaching a stable equilibrium which remains even after the potential is switched off. The process including the interpretation of the trends shown in Figure 4.8 & 4.9 are summarised schematically in Figure 4.10, illustrating; i) the formation of hemimicelles an initiation of condensation amongst hydrolised silica species, ii) the emergence of scattering features and their migration towards smaller q values with simultaneous increase in intensity, iii) reaching maximum scattering contrast (intensity) when passing the percolation threshold, iv) inflation limit of the network due to advanced solidification, v) relaxation of the condensed network after removal of hydroxide influx. Further details on the mechanism behind the EASA process are discussed later in this work (see Section 4.1.5).

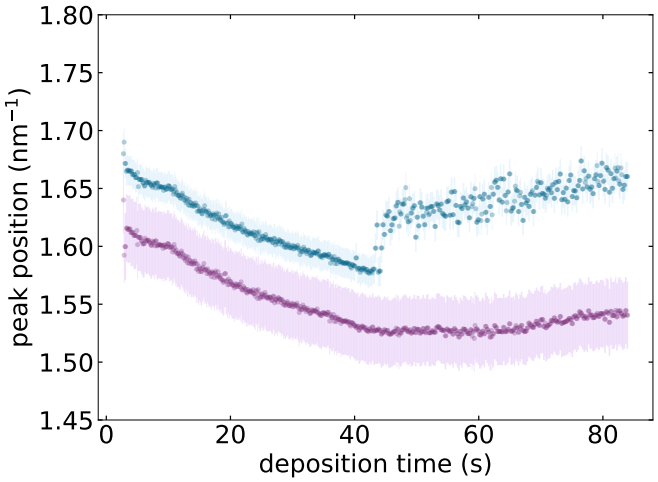

FIGURE 4.8: Position of the horizontal peaks (blue: spot, purple: ring) *vs* deposition time during EASA using CTAB. Peak positions were extracted from individual Gaussian fits of the peaks in each frame (699).

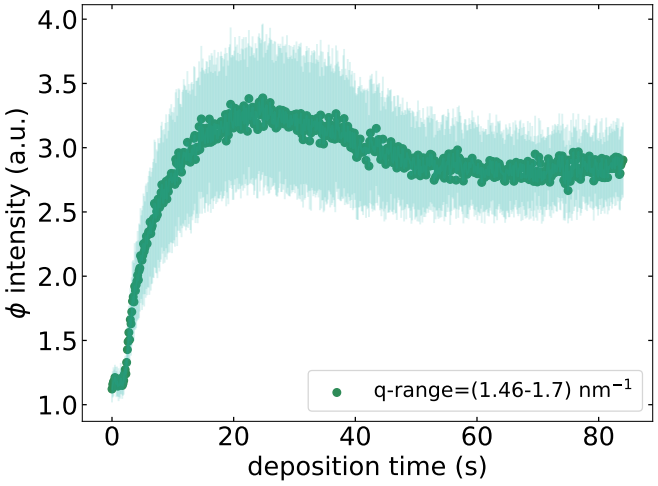

FIGURE 4.9: Intensity of the averaged signal in the q-range between 1.46 and 1.7 nm^{-1} *vs* deposition time during EASA using CTAB.

Superposition of reflection and transmission Concerning the different positions of the signals, it suggests that the pores in the film have slightly smaller spacing than the ones in the surface aggregates. Naively, one would assume the same pore distance and size and both structures would be very similar due to the presence of the same surfactant. However, there is another point to consider regarding the scattering images: when looking back at the full patterns from the detector, one can see that in Figure 4.3 b) the ring attributed to the structure within the surface aggregates does not show the typical distortion one would obtain from the GISAXS geometry, which leads to a distortion of the signal in q_z and would make that ring an ellipse. In addition, the signal of the ring is visible even below the horizon of reflection, which indicates its emergence from a geometry of different nature: a transmission signal. It appears hence, that the GISAXS data shows two things at the same time due to the experiment

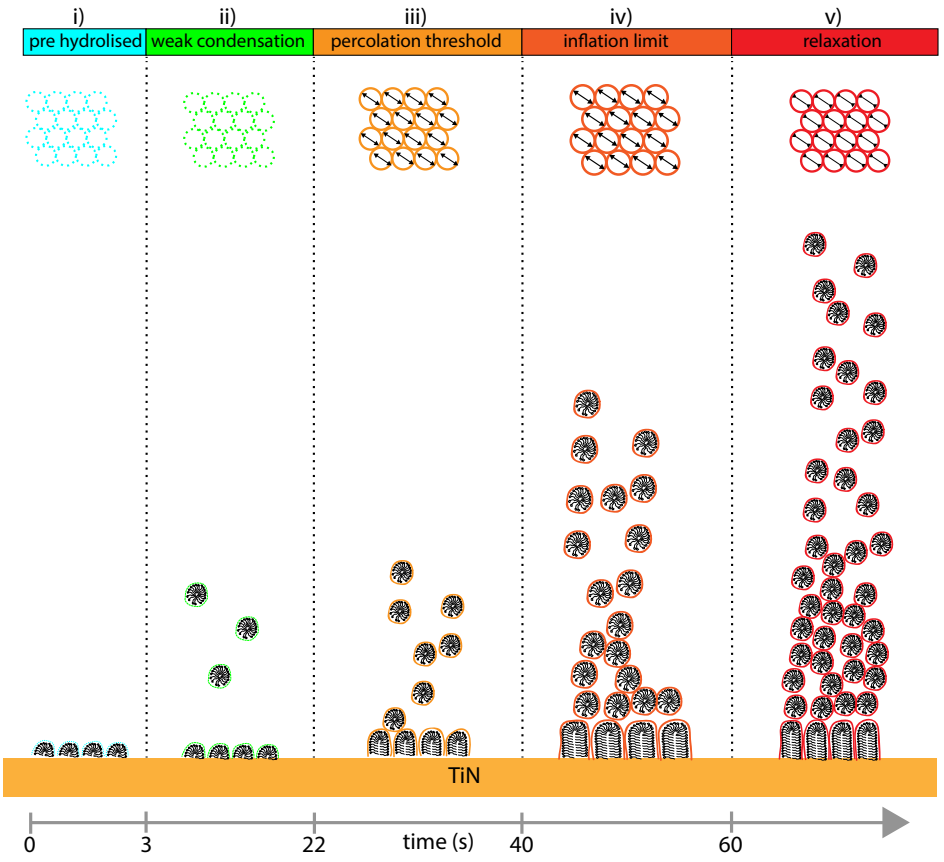

FIGURE 4.10: Schematic drawing of the observations and their interpretations made from the data in Figure 4.8 & 4.9. i) the formation of hemimicelles and initiation of condensation amongst hydrolised silica species, ii) the emergence of scattering features from film/aggregate formation and their migration towards smaller q values with simultaneous increase in intensity, iii) reaching maximum scattering contrast (intensity) when passing the percolation threshold, iv) inflation limit of the network due to advanced solidification, v) relaxation of the condensed network after removal of hydroxide influx. Colours indicate the progression of silica condensation (increasing from blue over green to yellow, orange and red).

being performed *operando*. The reflective part consists of the Yoneda signal, the specular reflection and the two spots in lateral direction coming from the vertically aligned channels on the substrate, while the ring is the result of a convolution of signals coming mainly from the beam travelling through these spherical aggregates on the way to the substrate and back, resulting in a SAXS signal. This means that most of the aggregates contributing to this signal are reasonably far away from the substrate surface. A horizontal projection of the signal at $q_z = 0.5\,\mathrm{nm}^{-1}$ leads therefore to an underestimation of the peak positions, because the ring is symmetrical around the direct beam. Radial integrations of the two-dimensional images around $(q_y, q_z) = (0, 0)$ are shown in Figure 4.11 plotted *versus* deposition time. It visualises that when treated as a transmission signal, the position of the ring corresponding to the surface aggregates resides at an

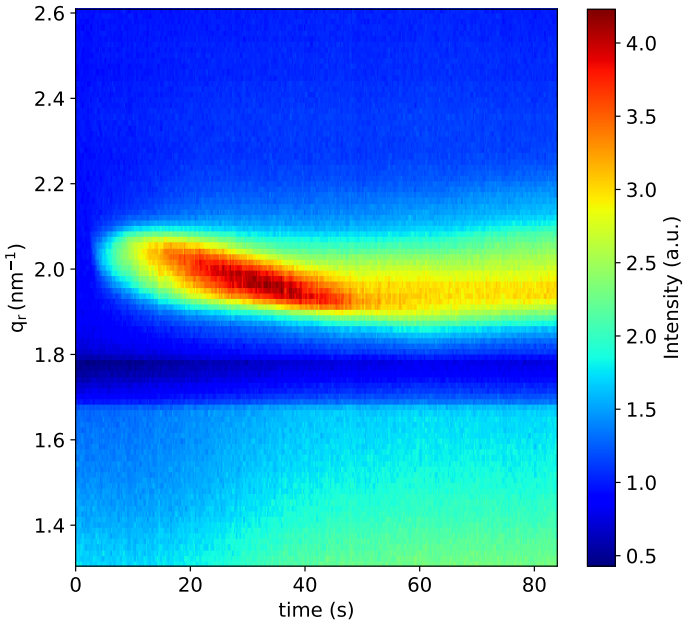

FIGURE 4.11: Radial integrations of GISAXS images around $(q_y, q_z) = (0, 0)$ for all 700 frames taken during the EASA of silica at -2.0 V for 60 s. Intensities along q_r plotted versus deposition time.

increased magnitude - the real space dimensions are hence diminished. While the pore distance in the film has a value of around 4 nm, the surface aggregates would show only roughly 3 nm. The very different conditions of the surfactant assembly (bulk *vs* surface) seem to not only lead to morphological differences between the two regimes, but also to change micellar dimensions.

4.1.3 Silica EASA using OTAB

The same experimental procedure was applied to a sol containing OTAB instead of CTAB (sol B1 in Table 4.1), of which the electrochemical data can be seen in Figure 4.1 b). The transient has the same shape as the one obtained in the CTAB experiment. The elongation of the chain from 16 to 18 carbon atoms was expected to result in a slightly enlarged pore distance. Once again, a contour plot of the horizontal scattering profiles was made, as shown in Figure 4.12. The scattering signal has a very similar appearance to the one shown in the CTAB experiment (see Figure 4.7), with symmetrical peaks appearing after a few seconds after switching on the potential, migrating towards smaller q_y values until 60 s, after which a slight increase is observed. By eye, one can already see that the peak position is generally shifted to smaller q_y values. Note the close association of the randomly appearing lines in the contour plots with a vibration of the beamstop during the experiment, which led to overexposure of the detector in some frames, but did otherwise not have any impact on the data treatment as the signal of interest was always clearly visible. The scattering profiles were once again fitted using a twin peak function consisting of two Gaussian peaks, of which the result is on display in Figure 4.13 (blue: spot, purple: ring). As expected, the peak positions are generally shifted to smaller q-values due to the longer chain length of OTAB, but the inflation effect prevails.

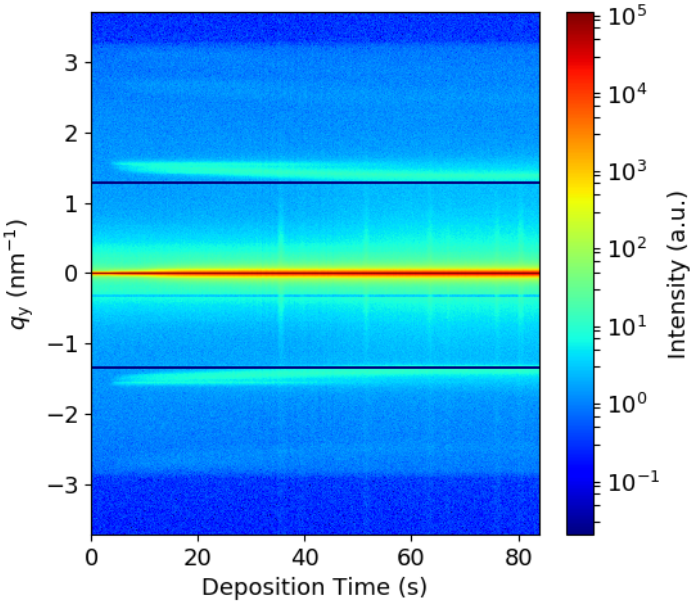

FIGURE 4.12: Contour plot of horizontal scattering profiles extracted from each frame *versus* deposition time. Integrations were done at the Yoneda position of the TiN/silica sol interface at $q_z = 0.5\,nm^{-1}$.

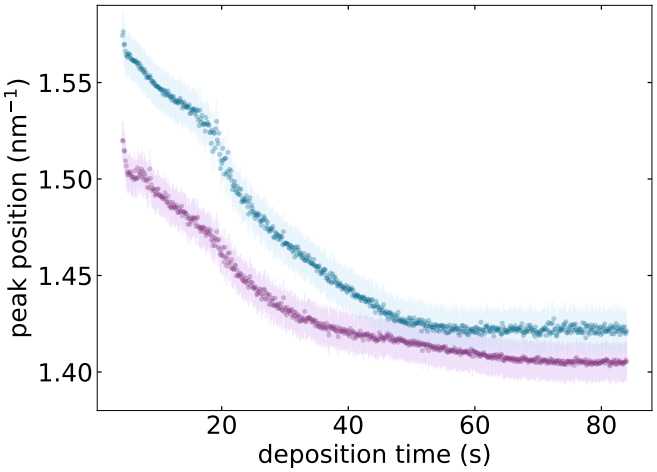

FIGURE 4.13: Position of the horizontal peaks (blue: spot, purple: ring) *vs* deposition time during EASA using OTAB. Peak positions were extracted from individual Gaussian fits of the peaks in each frame (699).

The chain length must be a limiting factor of the process when extended further, which is the focus of work done by a fellow PhD student in the group. Issues when doing that will probably arise from the decreased solubility of longer carbon chains in water, making a modification of the sol composition necessary.

4.1.4 Pore swelling using mesitylene

CTAB&mesitylene In this part of the study, the swelling agent mesitylene was added to the silica sols. The idea is to add a hydrophobic molecule to the system, which would be expected to seek the hydrophobic inside of the CTAB/OTAB micelles and increase the diameter of those, which results in increased pore size and spacing of the silica structure.[196] As shown before in Table 4.1, three different concentrations were used. From previous experiments, it was known that the micelle swelling cannot be done indefinitely,[196] meaning that no vertically aligned channels were formed when exceeding a certain concentration of mesitylene. At equal molar concentrations of CTAB and mesitylene (1:1), a collapse of the vertically aligned pore structure was seen in the microscopy, verified by the lack of a corresponding GISAXS signal. The question arising from this was, whether the surfactant assembly would not happen at all due to the disturbance by the large amount of swelling agent or whether it would still form initially and only collapse during the deposition.
Figures 4.14 a)-d) display GISAXS images taken right after silica deposition with the sample still inside the cell. A strong ring feature can be seen in all images, indicating the formation of spheroid particles in the bulk solution, which totally dominate the scattering signal as long as the substrates reside in solution. For the aged samples shown in Figure 4.14, one can see that the films with ratio of (mesitylene:CTAB) e) 0:1, f) 0.1:1 and g) 0.5:1 show two spots in the horizontal plane in convolution with the strong semicircle, while the one with the maximum amount of mesitylene (Figure 4.14, h) does not show that feature. This could mean that no vertically aligned pores were formed in the latter case.
Figure 4.15 a) shows the horizontal scattering profiles post deposition and b) after ageing in the horizontal plane and c) their corresponding real-space values obtained for increasing amounts of mesitylene concentration. The graphs show that until reaching a ratio 0.5:1, the inter-domain spacing increases slightly, starting from 3.55 nm to 3.63 nm. Surprisingly for the 1:1 ratio, the spacing decreases to a value lower than without the swelling agent. The scattering signals do also become broader when [mesitylene] is increased, indicating an overall loss of order.
The effect of the different amounts of swelling agent on the actual peak positions fitted using the previously introduced twin Gaussian function, is shown in Figure 4.16. The curves gradually shift to lower q_y values with increasing ratio of [mesitylene:CTAB] (Figure 4.16 a)-c)), while the one with a ratio of 1:1 (see Figure 4.14 d),f)) only had the ring as a visible feature. The inflation of the structure does also seem to be a lot weaker in this measurement than in the ones with lower amounts of mesitylene. The best fit with continuous positions of two peaks was obtained for a ratio of 0.1:1 shown in Figure 4.16 b). Figure 4.16 a) and c) show how the algorithm lost track of one of the shapes as they are practically merging, causing the false detection of background noise as a second peak at depositions times larger than 40 s, where the blue curve makes an

abrupt change to higher q values again. In Figure 4.16 one can see that another peak was tracked with a much higher q value than seen previously, as it was not possible to deconvolve two peaks in the main signal around $1.62\,nm^{-1}$. This peak could correspond to a higher order peak of the observed structure, but is most likely the result of false tracking due to the fitting algorithm reaching a local convergence minimum. The presence of mesitylene could inhibit the diffusion of ethanol (mentioned in[207] into the micelles as vital for the vertical pore alignment) and hence the formation of vertically aligned channels as a film. This would fit well with the observation that the amount of inflation in the structure diminished with increasing content of swelling agent.

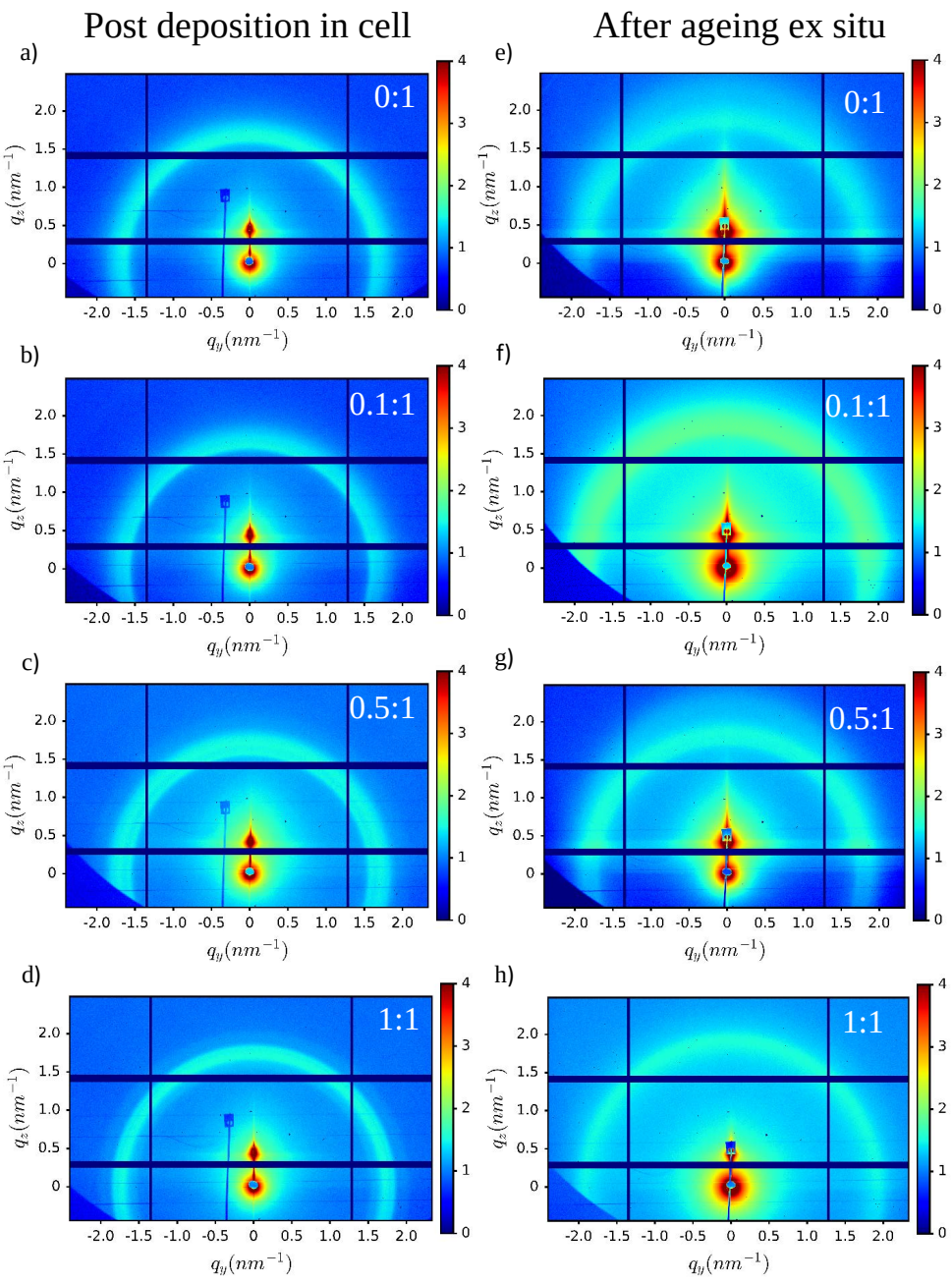

FIGURE 4.14: GISAXS images of silica samples taken a-d) after deposition *ex situ* and e-h) after ageing at 130°C overnight. The mesitylene concentration was varied *versus* [CTAB] as a,e) 0:1, b,f) 0.1:1, c,g) 0.5:1, and d,h) 1:1. Exposure time: 60 s, incident angle: 0.2°.

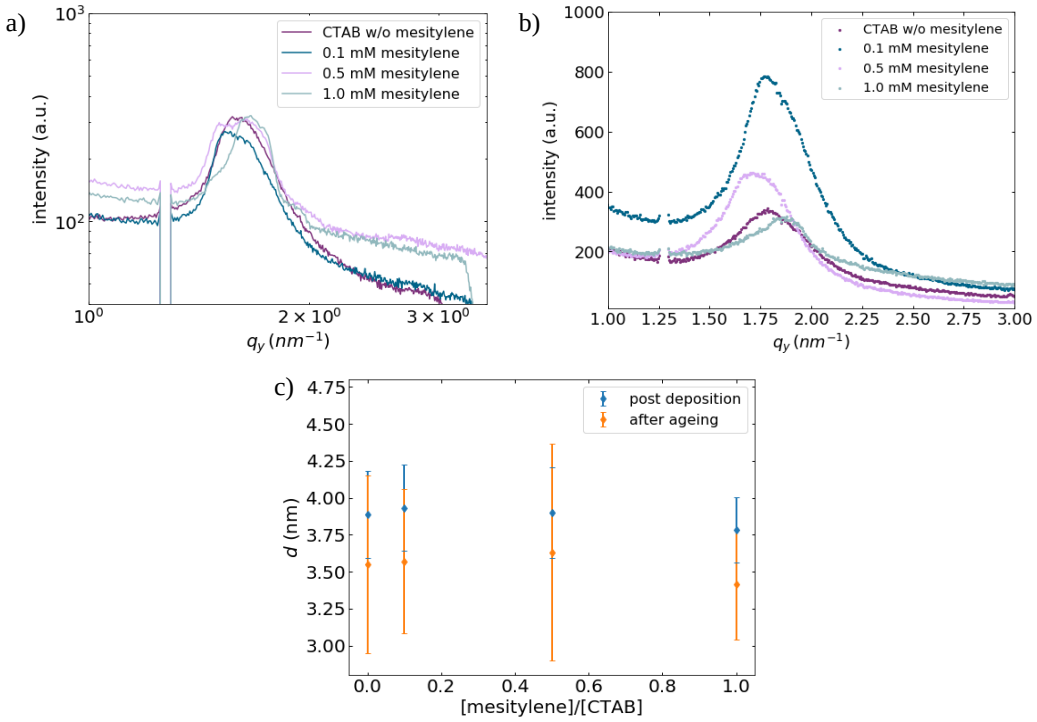

FIGURE 4.15: Horizontal scattering profiles of the silica structures a) post deposition (still in the cell), b) after ageing with increasing amounts of mesitylene concentration using CTAB. c) Real space values corresponding to the peaks shown in a) and b).

OTAB&mesitylene A series of similar experiments involving the swelling agent mesitylene were done using OTAB as the surfactant. Otherwise, all conditions were kept the same as previously, excluding a slight variation of the concentration ratios between mesitylene/OTAB (as shown in Table 4.1). 2D scattering images of the sample after deposition as well as after ageing are summarised in Figure 4.17 a-d) and e-h) respectively. Similarly as for the CTAB experiments, the images taken in the cell after deposition are dominated by the ring features from particles in solution, while the aged samples also possess a horizontal feature. Figure 4.18 shows the lateral peak profiles a) post deposition, b) after ageing and c) their corresponding pore distances d for increasing amounts of mesitylene (0, 0.5, 1.0, 2.0/CTAB). Previously it was shown that the use of OTAB instead of CTAB leads to a larger pore structure (with no swelling agent present). The introduction of mesitylene to this system leads most strikingly to a broadening of the scattering peaks, where the Gaussian curves fitted to those suggest that the pore spacing actually decreases when increasing the amount of added mesitylene up to 1:CTAB, after which it returns to a centre value close to the one at 0 concentration, but with at least double the width. The accuracy of the peak position dramatically decreases with increased amounts of swelling agent, showing that its addition mainly leads to a decrease in the degree of ordering within the film structure, and not to a significant increase in pore size.

As done for the CTAB experiments, the lateral peaks in the two-dimensional images

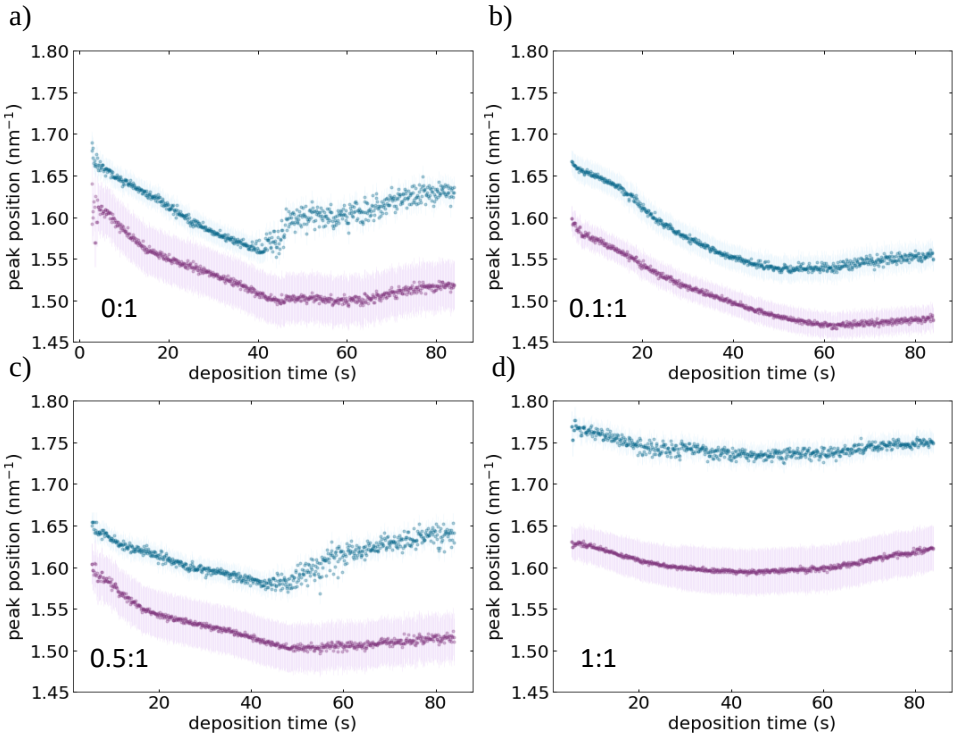

FIGURE 4.16: Lateral peak position fitted from scattering profiles obtained during the depositon of silica using concentrations of mesitylene versus [CTAB] of a) 0:1, b) 0.1:1, c) 0.5:1, and d) 1:1.

were tracked using a twin Gaussian peak function, of which the results are shown in Figure 4.19 for a) 0 mM, b) 0.5 mM, c) 1.0 mM and d) 2.0 mM of mesitylene present in the sol (solutions B1-B4 in Table 4.1). Here, double peaks were successfully tracked for all data sets, except for the first ≈17 s of the experiment done with sol B3 (4.19 c)). The degree of inflation seems to be less and less with increased amount of mesitylene again, as seen in the previous section on CTAB. The persistence of this behaviour indicates its relation to the presence of mesitylene in the sol, with the actual surfactant chain length being of less importance.

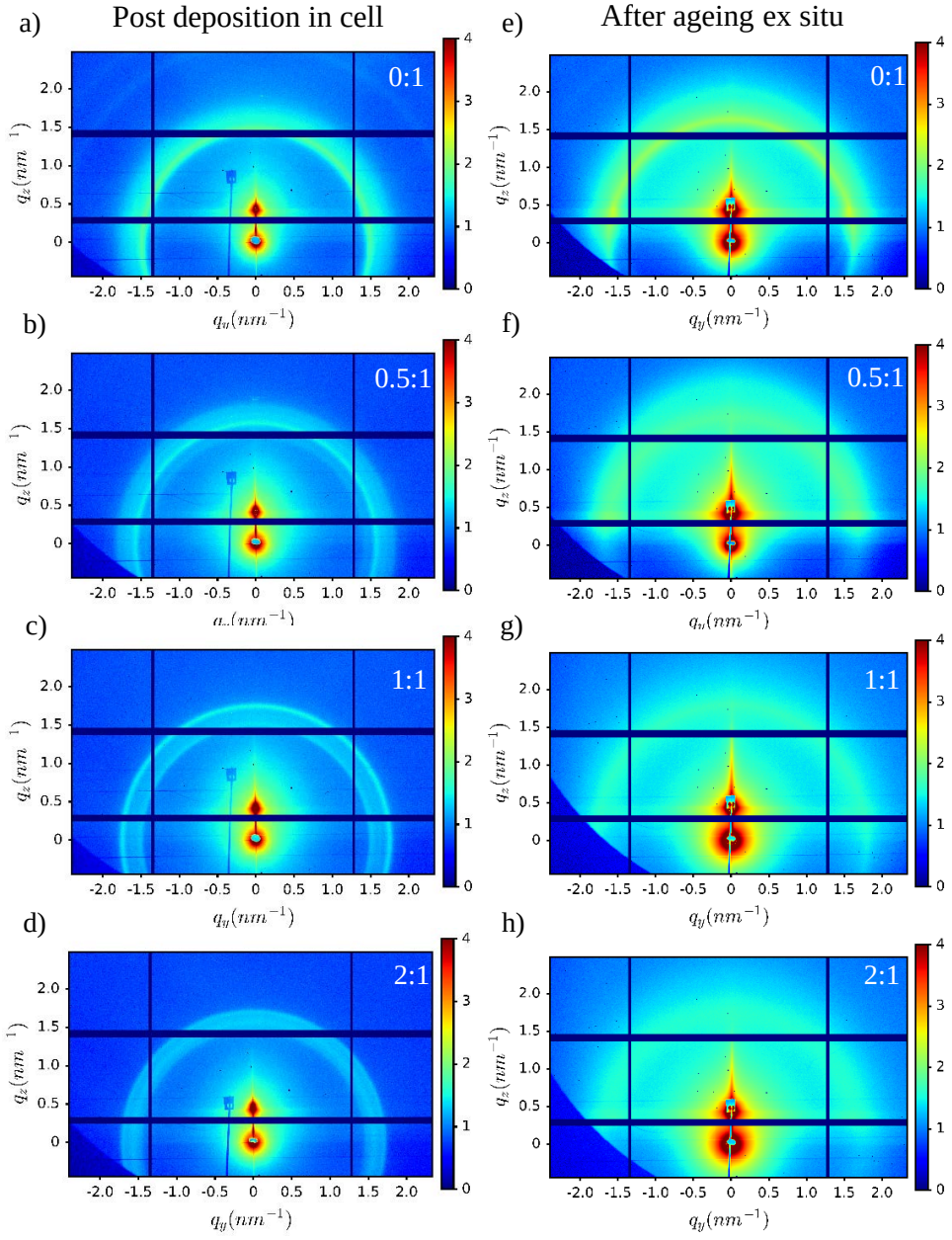

FIGURE 4.17: GISAXS images of silica samples taken a-d) after deposition *ex situ* and e-h) after ageing at 130°C overnight. The mesitylene concentration was varied versus [OTAB] as a,e) 0:1, b,f) 0.5:1, c,g 1:1, and d,h) 2:1. Exposure time: 60 s, incident angle: 0.2°.

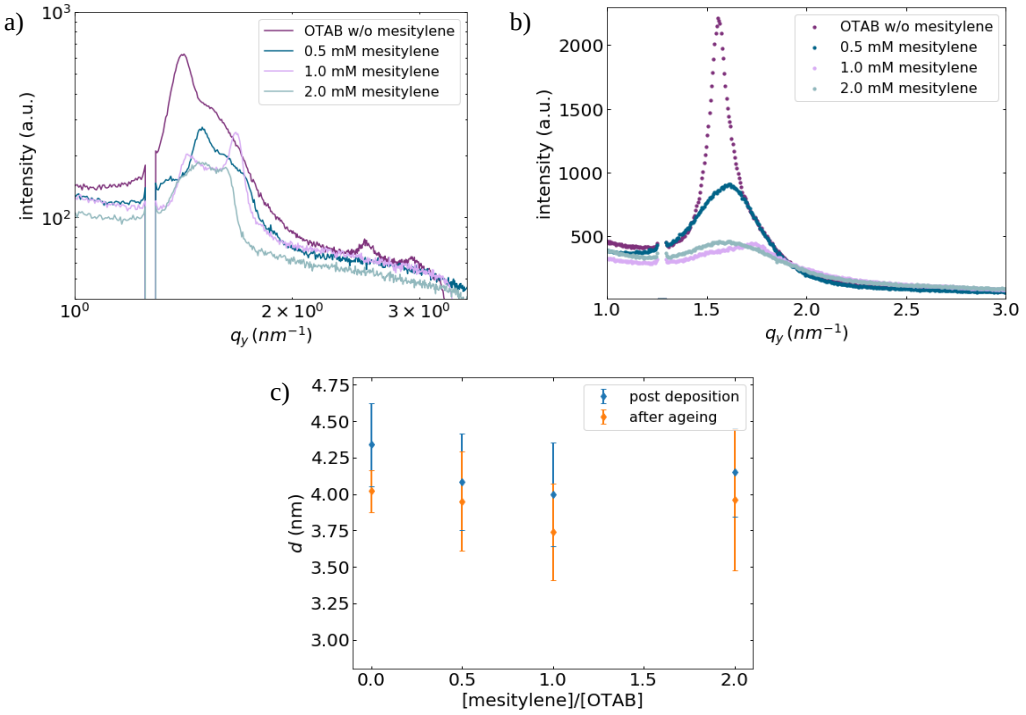

FIGURE 4.18: Horizontal scattering profiles of the silica structures a) post deposition (still in the cell), b) after ageing with increasing amounts of mesitylene concentration using OTAB. c) Real space values corresponding to the peaks shown in a) and b).

4.1.5 The EASA mechanism

The actual mechanism behind EASA was somehow neglected in the scientific literature regarding an in depth study. In the pioneering article by Walcarius *et al.*[110] which firstly introduced the technique, only the pH change induced by the negatively charged electrode was mentioned as the driving force, with no further detail given. A similar explanation was given in an article reporting on the effects of varying a multitude of component ratios of the silica sol,[137] and it was only in a review published a few years later that a first diagram of the mechanism was presented,[138] showing the formation of hemimicelles on the electrode surface, which grow into vertical cylinders. The formation of aggregates on top of the film was shown in the work of Goux *et al.*,[137] where the particles were analysed and it was shown that they were indeed mesoporous too, but their formation was still not included in the overall mechanism.

Before further discussing EASA, it is worthwhile to mention other routes to depositing vertically aligned silica films. The Stoeber process for making mesoporous silica spheres from solution is a well known technique.[208] This approach was adapted for the making of thin films by Teng *et al.*, who also give a quite detailed explanation as to why the pores order vertically and not horizontally to the surface.[207] They postulate that spherical micelles form on the surface of the substrate due to its negatively charged nature (ITO or glass in this case) which attracts the cationic surfactant. Then, the spaces

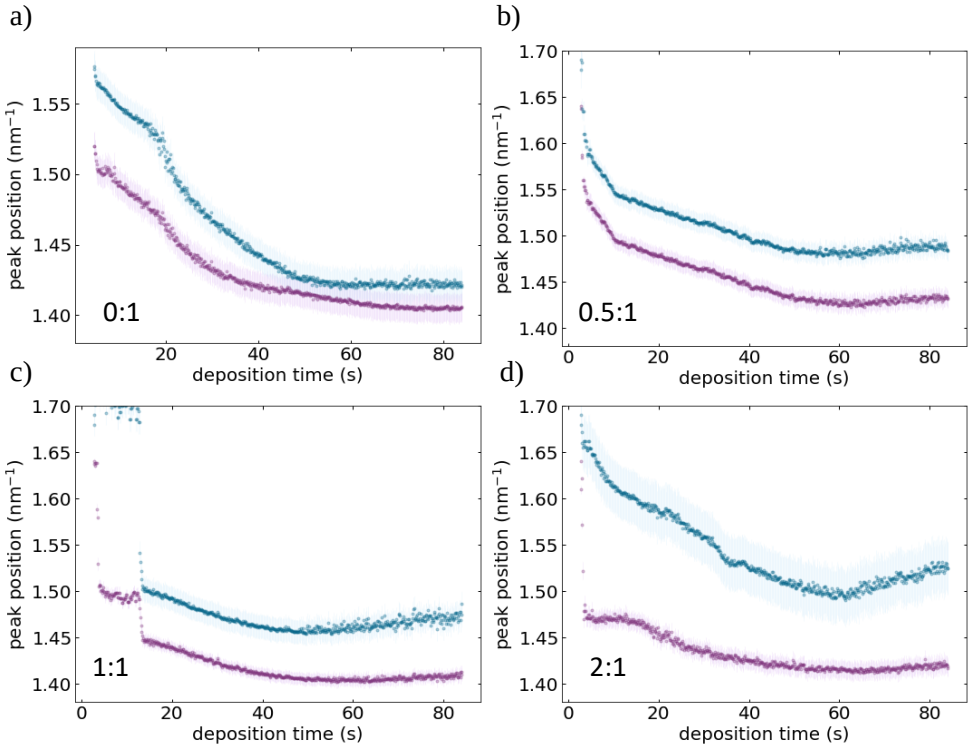

FIGURE 4.19: Lateral peak position fitted from scattering profiles obtained during the depositon of silica using concentrations of mesitylene versus [OTAB] of a) 0:1, b) 0.5:1, c) 1.0:1, and d) 2.0:1.

between micelles are filled with negatively charged oligomeric silicate species formed by the hydrolised TEOS, having an electrostatic screening effect on the micelles. At the same time, ethanol diffuses into the micelles, lowering their curvature and finally resulting in the cylindrical growth of the micelles away from the substrate, where new surfactant/silicate species attach to the "head" of the micelles. The initial formation of spherical micelles is hence essential for the further formation of vertically aligned channels instead of ones aligned parallel to the substrate. The issue of surface aggregates on top of the films are also present when using this route, which dominate when the rate of silica condensation is increased.

The main difference between EASA and the Stoeber route is the dynamic change of pH during EASA *versus* a pre-set alkaline condition in the Stoeber route. Both processes seem to rely on similar effects, but while EASA happens in the range of seconds at room temperature including an electric field, Stoeber derived films are made at typically 60°C over the course of several days. Nevertheless, it does not seem unintuitive to expect a similar process happening in both approaches.

As mentioned in the introduction (see Section 1.6), the critical micelle concentration of the bulk does not seem to determine whether organised films are formed or not, since the vertically aligned hexagonal pore systems have been synthesised below and above the CMC of CTAB for solutions made of 1:1 water/ethanol.[137] The study did not consider the influence of the inorganic salt present in the sol, which is likely to decrease the

CMC of CTAB and would mean that all experiments were carried out above CMC,[209] unless the ethanol in the solution counteracted the effect. In this work, a concentration of 33 mM CTAB was used, which would be above the bulk CMC of 22 mM reported for 1:1 ethanol/water mixtures,[143] which indicates that spherical CTAB micelles should be present in solution from the beginning. Bing Tan *et al.* reported that a sufficiently high concentration of ethanol (above 2.4 m/l) leads to ethanol acting as a co-solvent, decreasing the dielectric constant of the liquid phase (which increases the counterion association), and increasing the CMC of CTAB.[210] They state that high concentrations of ethanol destroy the long range order of CTAB structures and lead to the formation of micellar solutions only, due to the decreased solubility of silicates in the continuous phase leading to the association of shorter silicate oligomers with the CTAB. This would be consistent with the process happening in the bulk solution. The increased counterion association however favours the formation of lower curvature micelles (*e.g.* cylinder-shaped), dominating the process of vertical pore formation at the electrode surface.

In the previous section of this work, none of the scattering images prior to deposition showed any evidence of micelle presence, most likely due to their very weak contrast to the other species present in solution. When applying the potential, both scattering features discussed earlier appear almost simultaneously after a few seconds, meaning that the assembly on the substrate as well as the particle formation in solution happen at the same time. The main question around the first stage of the process on the substrate surface is whether hemimicelles (cylindrical/spherical) or full spherical micelles are formed, and especially whether their formation is the result of crossing a "local" CMC or the attraction of "pre-formed" micelles. The speed of formation hints more towards the local assembly of micelles on the surface either as soon as the electrode is immersed into the sol, or with application of the electric field as opposed to ones migrating from solution to the surface, especially since migration effects should be rather small due to the presence of supporting electrolyte. In the literature there are reports on the assembly of CTAB on silica, which reported that the surfactant either forms a layer of hemimicelles residing on top of a flat layer, or a layer of spherical micelles.[140,141]

Control experiments showed that dipping a blank TiN substrate into a solution of 0.1 M $NaNO_3$/EtOH (1:1) with CTAB (480 mg per 20 ml water) for a couple of minutes results in the formation of a horizontally aligned structure, as to be seen in Figure 4.20. The first order peak around 2.4 nm^{-1} corresponds to a interlayer thickness of 2.6 nm, which lies within the range of the length of CTA^+ molecules.[211] The application of a potential to the blank TiN electrode in the CTAB solution (dummy sol) led to the same kind of structure (see Figure A.2), implying that the potential does not affect the CTAB self-assembly. This is in agreement with previous reports,[140,141] suggesting that CTAB behaves similarly on a TiN surface as on a silica surface. For comparison, another experiment was conducted where a TiN substrate was immersed in the previously mentioned "dummy sol" for a couple of minutes, after which first 905 μl (per 20 ml water)

were added, followed by 12 μl (per 20 ml of water) of 35 w% NH_3 solution. The substrate was left without stirring over night and recovered the next day. A corresponding GISAXS image is shown in Figure 4.21. A vertically aligned structure of typical dimension was obtained (spots), including surface aggregates (ring).
This proves that the replication of the EASA conditions without any electric field lead to a very similar result in terms of the pore alignment. The quality of the film is presumably not as high as from a typical EASA process, but the electric field can be excluded as driving force for the assembly. The presence of the silica precursor leads to the surfactant assembling very differently, meaning that studies of it alone in solution are not sufficient. It is therefore highly likely that the fundamental mechanism responsible for the EASA process is very similar to the one happening during the Stoeber-process. Using the target surface as the source of catalysts needed for the reaction is advantageous to the simple incorporation by stirring, making EASA a faster and more selective route for the making of mesoporous silica films.
The ultimately limited availability of reactive species during the initiation of the silica polycondensation along the length of the hydroxide diffusion layer should lead to a condition at which the next incorporable species is too far away from the upper end of the compact film due to their concentration profile depending on hydroxide diffusion, meaning that their number decreases with increasing distance from the electrode. At a certain film thickness, there should be no more species close enough for them to further condense onto the film, as most other available species had been forming spherical particles since the beginning of deposition since they were not affected by the surface effect at the TiN electrode.
Considering ethanol moving from a co-surfactant to co-solvent when exceeding a critical concentration might also explain the effect of the swelling agent mesitylene on the system: For CTAB, the addition of mesitylene led to (see Figure 4.15 c)) an initial increase in pore spacing up to 0.5 [mesitylene]/[CTAB], followed by a decrease below the initial value at equal concentrations of both. The dielectric constant of mesitylene is almost 10 times smaller than that of ethanol (ethanol: 24.40 , mesitylene: 2.266 at 298.15 K[212]). Mesitylene must hence be acting as a co-surfactant up to 0.5 [mesitylene]/[CTAB], increasing the micelle size and pore spacing. Above that value, it seems to be acting as a co-solvent. For OTAB on the other hand, the structure decreases in size when adding mesitylene until reaching equal concentration, followed by and increase back to initial value at doubled concentration (see Figure 4.18 c)). In this case, only the co-solvent effect could be seen, which must be the result of the increased chain length of OTAB *vs* CTAB.

To successfully resolve this question about the mechanism, an experiment with considerably higher structural and temporal resolution would need to be performed with a similar set of parameters. The *operando* GISAXS experiments shown in this work had high temporal resolution, however the penetration of the entire solution by the X-ray

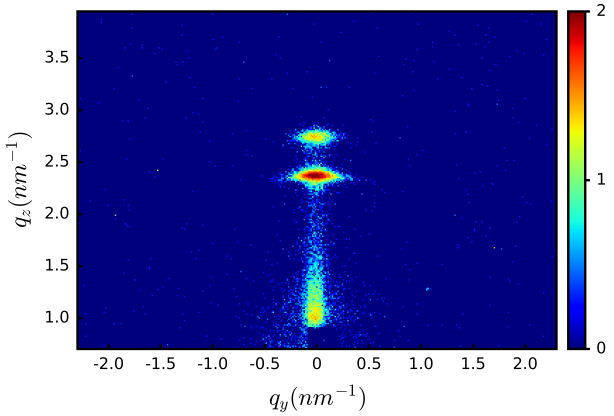

FIGURE 4.20: Scattering image of a TiN substrate dipped into a solution of 0.1 M $NaNO_3$/EtOH (1:1) with CTAB (480 mg per 20 ml water) for a couple of minutes. Incident angle: 0.3°, exposure time: 600 s (In-house measurement).

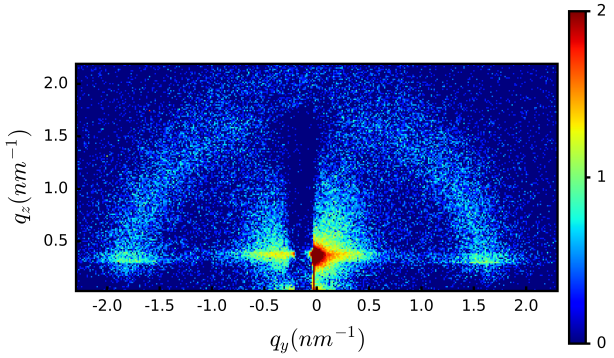

FIGURE 4.21: GISAXS image of a TiN substrate placed overnight into a solution of 0.1 M $NaNO_3$/EtOH (1:1) with CTAB (480 mg per 20 ml water), followed by the addition of 905 μl (per 20 ml water) and 12 μl (per 20 ml of water) of 35 w% NH_3 solution. Incident angle: 0.3°, exposure time: 600 s (In-house measurement).

beam did not allow for a distinct separation of the form factors from bulk and surface structures. A neutron experiment in reverse geometry as shown in Chapter 2.6 would bypass the bulk solution effects, but would be very challenging in its realisation due to the need for a very large electrochemical cell and substrate (10x10 cm^2), and it would be limited in temporal resolution due to the current limitations in neutron flux.

4.2 EASA with sinusoidal potential

The previous section showed that the formation of surface aggregates on top of the desired mesoporous film is not avoidable with the regular experimental procedure, as it is the natural result of applying a potential to drive the catalytic reaction. The expansion of the pH gradient takes place within very short time and on a large scale, so that the bulk reaction can not effectively be inhibited, even when using short deposition times. Changes in the sol composition are considerable, but any change, *e.g.* a reduction of the precursor concentration will always affect both parts of the process.
Ideally, the pH gradient should be limited to just a little bit more than the actual film thickness, in which an aggregate free film would be formed. Such a reduction of the hydroxide diffusion layer thickness can be obtained by using a non-constant potential, *e.g.* a pulsed potential (rectangle) or even a sinusoidal signal. The sinusoidal potential oscillates between two potential values at which hydroxide generation is high/low repectively, resulting in a modulated and almost pulse-like hydroxide influx at the electrode, comparable to switching the current/influx on and off periodically. When doing so, the concentration gradient at the electrode divides into an oscillating region (thickness depending on frequency) and a static gradient of much less strength.[213] In EASA, this should allow for a preferred formation of the compact film at the electrode surface while generating a significantly lower number of surface aggregates, and ideally none at all if the conditions could be tuned to this extreme case. At the same time, the film thickness increases considerably, making higher aspect ratios of the pore channels available. The films would be generated continuously along their whole thickness, as opposed to the stacking of mesoporous layers through the repeated application of the EASA process to the same substrate.[214]
In this section, the results from using a sinusoidal signal will be shown. As for the adaptation of the deposition protocol, the amplitude and offset of the sinusoidal potential are chosen in a way that makes the potential oscillate through the range at which hydroxide generation becomes more and less important.

4.2.1 Electrolyte-free sol

In this experiment, the same electrode configuration as in the previous section was used. The silica sol was modified by omitting the originally used sodium nitrate completely, reducing its composition to 1:1 ethanol/water, CTAB and TEOS at initially pH=3 (using 0.24 M HCl). The applied signal was a sinusoidal signal with a frequency of 100 Hz between -1.0 V and -2.0 V *vs* Ag/AgCl reference electrode. The electrode area was limited to 5 mm x 15 mm using nail polish to mask off the remaining part of the substrate. Deposition time was given by the number of cycles, of which 10000 were the initial smallest number at which a proper film could be seen on the TiN substrate. Deposition was hence done for 10, 15, 20 and 30 thousand cycles respectively after which the samples were rinsed with water. The optical appearance of the silica films immediately after deposition was distinctively different from the usual, as it was of strong iridescence. This indicates the presence of a well ordered film structure. The effect was most prominent for samples deposited at 15- and 20- thousand cycles, while the sample made with 30000 cycles seemed to have a more turbid appearance, indicating the increased presence of surface aggregates. Samples made using the same solution composition and regular constant potential conditions showed thick white aggregate layers and were not further characterised.

Electrochemical data The current resulting from the application of the AC signal at 100 Hz frequency if shown in Figure 4.22 a), where the inset shows a zoomed in part illustrating the oscillating current, which can not be displayed properly otherwise due to the high frequency. The current profiles were Fourier transformed using a custom Python script, as depicted in Figure 4.22 b). Once again the inset shows a zoomed in part, underlining the presence of a sharp peak at 100 Hz and a definitive DC component towards low frequencies. The interesting part of the signal for this experiment is the DC component of the signal, which corresponds to the static diffusion gradient generated by the oscillating potential. Another custom Python script was used to filter out the AC component of the signal around 100 Hz by applying a bandstop notch filter with a Q factor of 30. Figure 4.22 c) shows the resulting current profiles with removed oscillation. These are of roughly the same order of magnitude and shape throughout all samples, with their length being their main difference. In comparison to the application of constant -2.0 V for 60 s, the current magnitude is about 10 times smaller when using the sinusoidal potential. This makes sense as the alternating potential mainly generates non-Faradaic currents from the oscillating double layer. The ”efficiency” of the signal in terms of hydroxide production at the electrode was therefore significantly decreased.

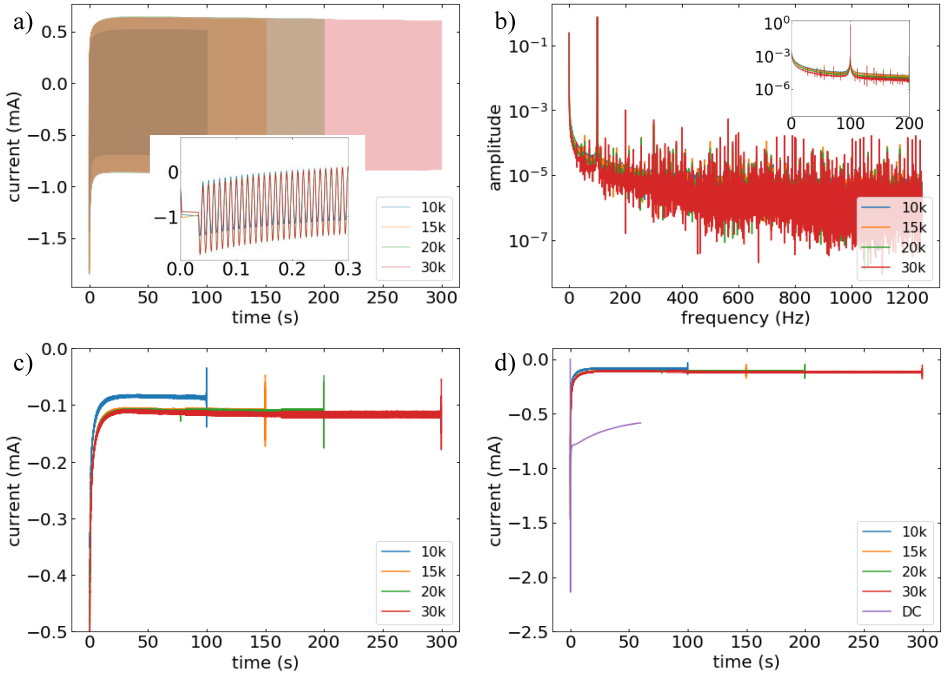

FIGURE 4.22: a) raw data of the currents recorded during the deposition of silica using a sinusoidal signal with a frequency of 100 Hz, between -1.0 V and -2.0 V with deposition times of 10k, 15k, 20k, and 30k cycles (100, 150, 200 and 300 s). Inset: zoomed plot of the same signals for the period between 0 and 0.3 s. b) Fast-Fourier-Transform of the data shown in a) done using a custom made python script. Inset: zoom to the range 0-200 Hz. c) Data from a) filtered using another custom python script which employs a bandstop notch filter at 100 Hz with Q=30. d) Same data as c) plotted in conjunction with a current transient obtained from a deposition at constant potential of -2.0 V (DC) for 60 s.

SEM Our partners at the University of Warwick kindly collected SEM images of the mentioned samples, including top down as well as cross sectional views. These can be seen in Figure 4.23. Images i) and ii) correspond to 10k cycles, iii) and iv) to 15k, v) and vi) to 20k and vii) and viii) to 30k cycles of potential. The odd numbers correspond to top down images, while the even ones indicate cross sections. It can be seen that in Figure 4.23 i), only very few surface aggregates are present on the film. Their number does slightly increase with increasing number of cycles, but it is very obvious that it is significantly smaller than with the traditional approach using chronoamperometry, as even in Figure 4.23 vii) the film is not fully covered in aggregates after a deposition of 300 s. From the cross sections, the tried and tested software ImageJ[158] was used to approximately measure the thickness of the deposited films, as plotted in Figure 4.24. The film thickness increases from almost 150 nm at 10k cycles in a mostly linear fashion to close to 350 nm at 30k cycles.

GISAXS data Once again, GISAXS was used to analyse the structure and arrangement of the silica films. The images shown in Figure 4.25 a-d) were measured on our

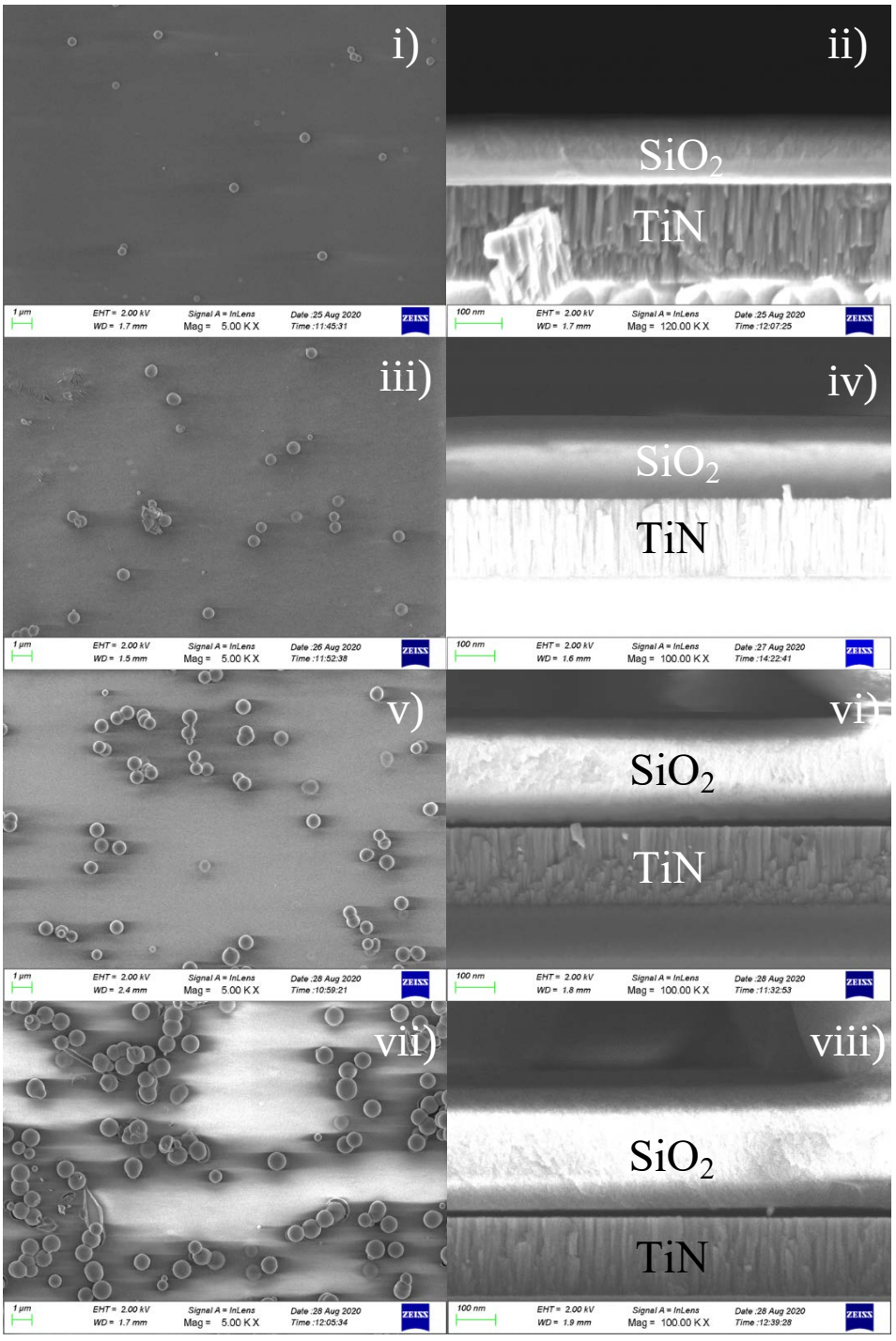

FIGURE 4.23: Images i) and ii) correspond to 10k cycles, iii) and iv) to 15k, v) and vi) to 20k and vii) and viii) to 30k cycles of potential.

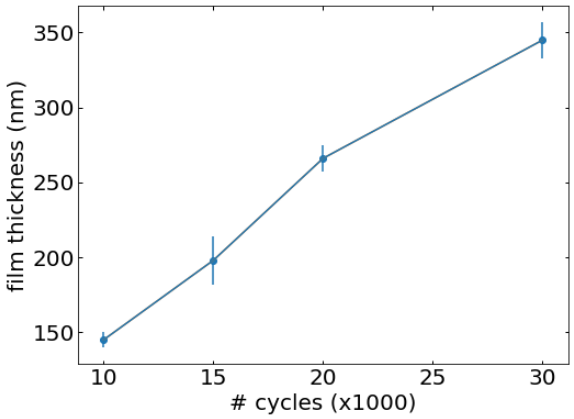

FIGURE 4.24: Film thickness versus number of cycles extracted from the images shown in a) using the software ImageJ.[158]

in-house instrument at an angle of 0.3° for a duration of 15 min for the samples deposited with a) 10k, b) 15k, c) 20k, and d) 30k cycles. The four images look very similar by eye, showing the symmetrical horizontal spots expected for a vertically aligned two-dimensional hexagonal pore structure, including two higher order peaks highlighting the augmented degree of ordering within and low number of surface aggregates on the films.

Characterisation using a redox probe Hexaamine ruthenium chloride $Ru(NH_3)_6Cl_3$ was used in cyclic voltammetry experiments on the newly generated silica films. Measurements were performed for each sample both before and after removal of the surfactant through immersion in 0.2 M HCl in ethanol overnight. The potential was scanned between -0.4 V and 0.2 V vs Ag/AgCl in a solution containing 5 mM $Ru(NH_3)_6Cl_3$ with 0.1 M $NaNO_3$ using a Pt gauze as counter electrode. Results from measurements done at 20 mV/s are shown in Figure 4.26. This cationic probe was chosen because it reliably indicates whether the surfactant was properly removed from the silica film, as it does not penetrate the surfactant within the film (as opposed to other redox probes, which do so[110]). The solid black line in Figure 4.26 shows the current response obtained from using a blank TiN substrate. The current response of the silica films as prepared is significantly smaller than of blank TiN, indicating continuous coverage of the electroactive area. After surfactant removal, the redox peaks become visible again, whereby consistently higher currents were recorded as compared to the blank substrate. This observation is common for highly ordered mesoporous silica films, where cationic probes tend to accumulate in the pores due do their negatively charged silica walls.[215] This confirms the successful generation of vertically aligned silica films through the application of a sinusoidal potential.

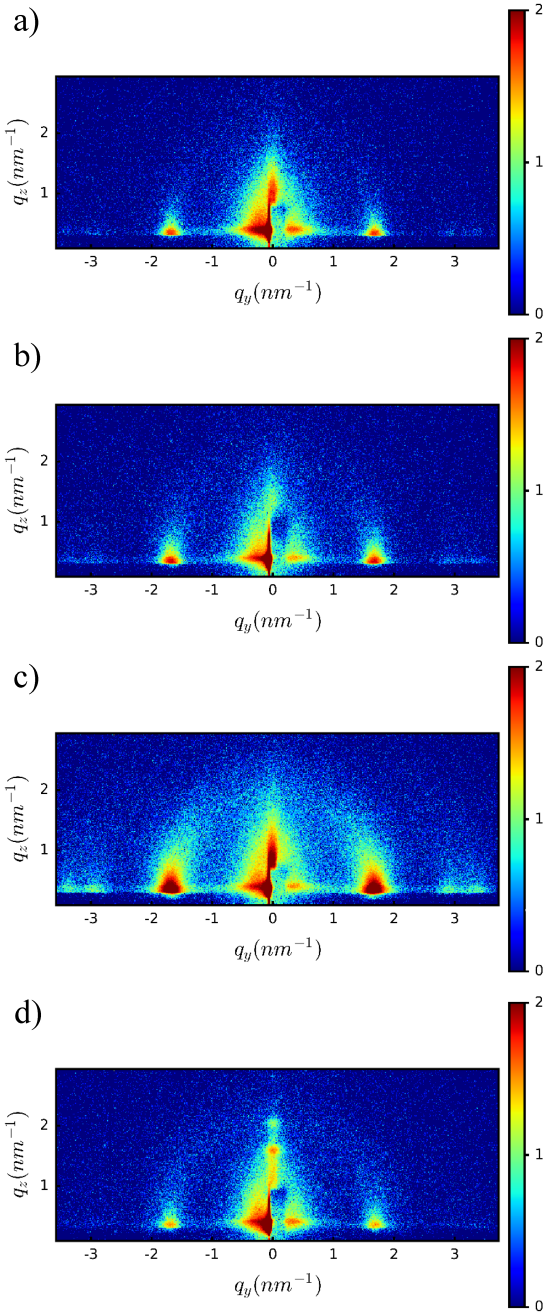

FIGURE 4.25: 2D GISAXS images measured on our in-house instrument at an angle of 0.3° for a duration of 15 min for the samples deposited with a) 10k, b) 15k, c) 20k, and d) 30k cycles.

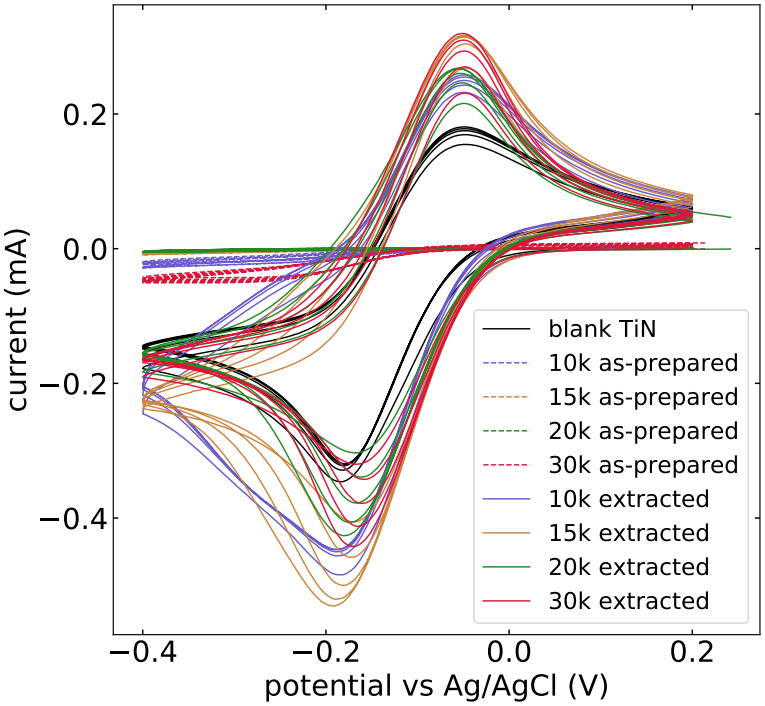

FIGURE 4.26: Cyclic voltammetry of silica films on TiN in 5 mM $Ru(NH_3)_6Cl_3$ with 0.1 M $NaNO_3$ between -0.4 V and 0.2 V vs Ag/AgCl at a scan rate of 20 mV/s, five cycles each. Solid black line shows response of a blank TiN substrate with an electrode area of 5 mm x 15 mm. Coloured dashed lines show the current response before, solid ones after surfactant removal.

4.2.2 Regular sol

The procedure described in Section 4.2.1 was repeated in a control experiment, where a silica sol containing $NaNO_3$ was used (see Section 4.1.1). The same electrochemical setup and conditions were used. After application of the sinusoidal potential, the samples were rinsed with deionised water immediately. No iridescence was visible to the naked eye for these samples - their whitish appearance hinted at the presence of numerous surface aggregates. As displayed in Figure 4.27, the filtered raw data of the current responses consist of a DC signal in similar range to the ones shown in Figure 4.22 c). The transients of the samples with 10 and 15k cycles seem to be slightly lower in magnitude than the other ones. This could be the result of a slight variation in electrode positioning during sample change, but should not affect the general results as the potential was controlled in this experiment.
SEM images of the films are shown in Figure 4.28. They show clusters of surface aggregates in the micron range from 15k cycles onwards (b-d), whereby more than half of the pictured area seems to be covered at 30k cycles. The number of clusters formed during silica EASA is increased significantly when $NaNO_3$ is present in the sol, which is plausible as the generated current is higher. $NaNO_3$ has been suggested to be supporting the formation of hydroxide at the working electrode,[110] accelerating the silica condensation process not only at the electrode surface but also in the bulk solution.

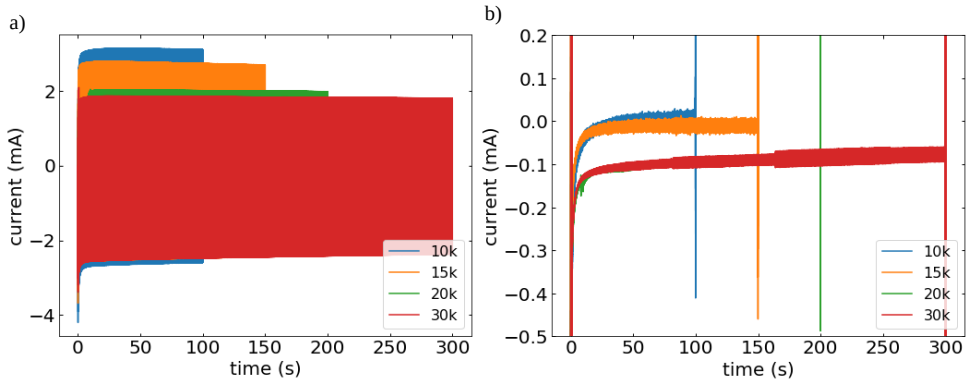

FIGURE 4.27: Filtered current response during silica deposition a regular silica sol using a sinusoidal signal of f=100 Hz, potential, -1 V to -2 V, a) 10k, b) 15k, c) 20k, d) 30k cycles. A custom python script was used to employ a bandstop filter at 100 Hz , Q=30 to the raw data.

The structure of the samples was investigated by GISAXS on our in house instrument. Figure 4.29 displays the raw two-dimensional images of the respective samples made at a) 10, b) 15, c) 20 and d) 30k cycles, measured at an angle of 0.3° with an exposure time of 30 min. An increased exposure time was used for the control samples compared to the main ones (15 min) as their scattering seemed to be generally weaker. The presence of surface aggregates is confirmed in the GISAXS data, showing strong semicircles for the samples made at 15, 20 and 30k cycles (b-d), with only the shortest deposition time (10k, a) not showing such. Horizontal scattering features are seen for all of the control samples, whereby only the first order peak is visible. This indicates the successful formation of a vertically aligned structure below the surface aggregates, but with a much lower degree of ordering than the original samples made using this technique (see Section 4.2.1). This shows that not only the use of a sinusoidal signal, but also the neglect of supporting electrolyte leads to the formation of higher quality films during EASA.

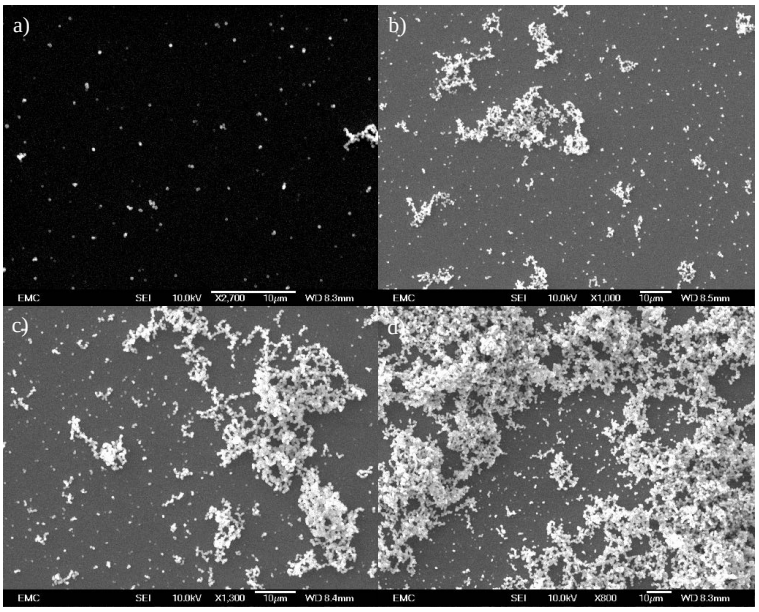

FIGURE 4.28: SEM images of control samples made by applying a sinusoidal potential to a TiN electrode immersed in a regular silica sol as described in Section 4.1.1. f=100 Hz, potential, -1 V to -2 V, a) 10k, b) 15k, c) 20k, d) 30k cycles.

Film structure analysis From the GISAXS images shown in Figures 4.25 and 4.29, horizontal profiles of the intensities were made which are shown in Figure 4.30 a) for the electrolyte free and b) 0.1 M $NaNO_3$ containing sol (in the water part). The first possesses strongly pronounced peaks of up to second order, while the latter only has a first order peak. This shows that the ordering of the films made using the electrolyte free sol have a higher degree of ordering than the ones using the conventional sol. Figure 4.30 c) displays a comparison of the d-spacings corresponding to the peaks shown in Figure 4.30 a) and b) ($d = 2\pi/q$). The blue dots corresponding to the electrolyte free so show a very consistent value of roughly 3.75 nm, while the distances using the conventional sol (orange) appear to slightly decrease with increasing number of AC cycles. This is probably a result of the increased peak width of those points, as the data is still in overall agreement for both conditions within their error bars.

The obtained structures both have dimensions in good agreement with the initially shown silica films made by applying a constant potential to an electrode situated within a regular silica sol containing $NaNO_3$. This novel route hence allows for the generation of high quality silica films with decreased amount of surface aggregates, as required for any application needing a "clean" film surface. Further tuning of the AC protocol and the sol composition might make aggregate free depositions possible, with obtainable films beyond microns in thickness.

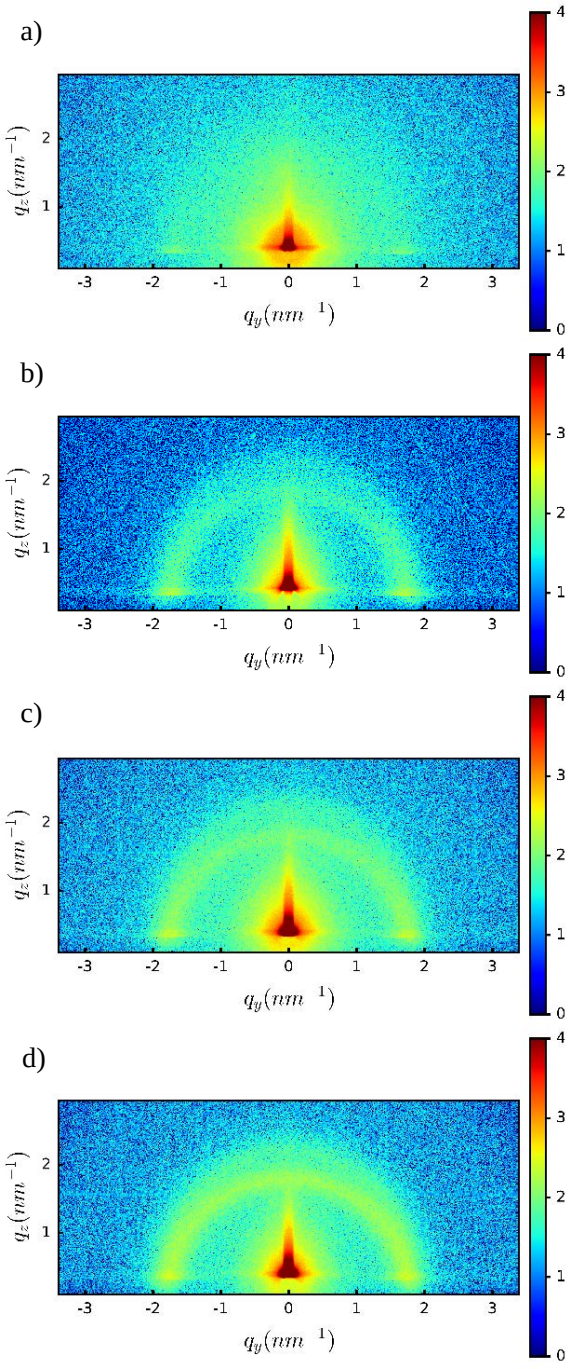

FIGURE 4.29: 2D GISAXS scattering images of the control samples taken on our Rigaku Smartlab at an angle of 0.3° for a duration of 30 min for the samples deposited with a) 10k, b) 15k, c) 20k, and d) 30k cycles.

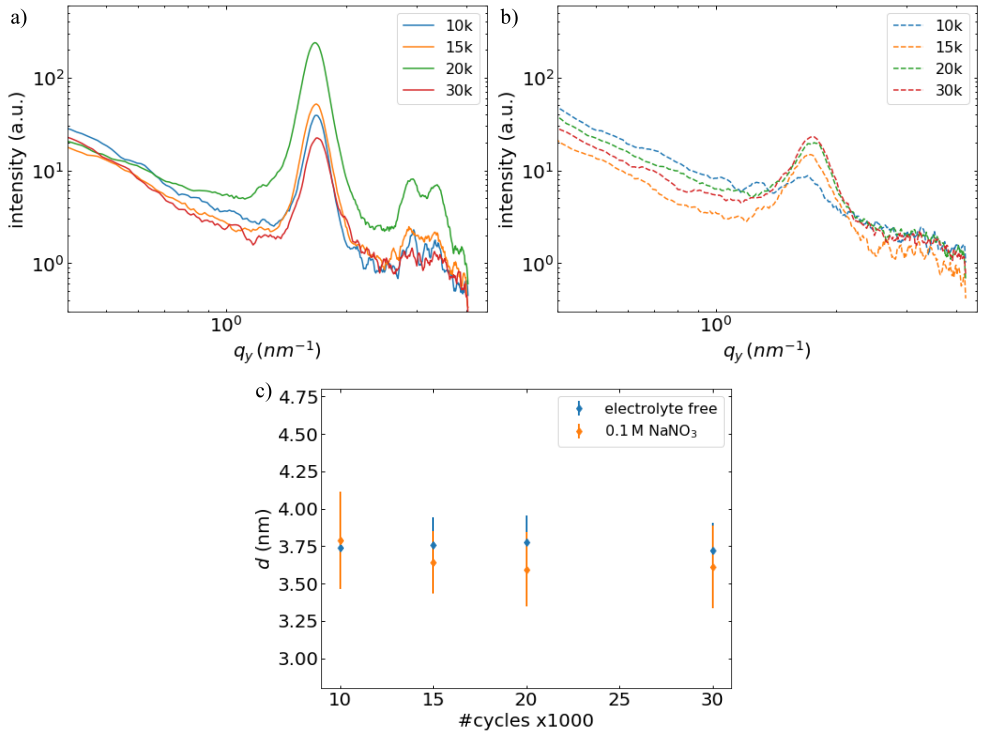

FIGURE 4.30: Horizontal scattering profiles for a(the electrolyte free and b) 0.1 M $NaNO_3$ containing sol. c) Comparison of the d-spacings corresponding to the peaks shown in Figure 4.30 a) and b) calculated using $d = 2\pi/q$.

4.3 Dynamic pH experiments

The following part of this work contains the results obtained from potentiometric pH measurements on a TiN working electrode, as used in the previous chapter for the EASA of mesoporous silica films. Fabrication of Pt microdisk electrodes (Pt-MDE), preparation of the required Pd plating mixture and the characterisation/calibration of the obtained Pd microdisk electrodes (Pd-MDE) are summarised in a previous chapter (Chapter 2, 2.2).

When deemed operational, the pH sensors were used in a series of dynamic pH experiments, for which the composition of the solution was gradually changed, but the electrochemical setup stayed the same. Ultimately, a regular silica sol was used and the results compared to the priorly investigated "idealised" solutions. The experiments presented in the following consist of a five-element series. The silica sol used for EASA is a very complex system of multiple ingredients, of which not all cross-correlations are known. The monitoring of the local pH near an electrode being not a straight forward experiment made it necessary to start from an ideal solution containing only a simple electrolyte. Consecutively, chemicals were added one at a time until reaching the actual sol composition.

The simplest system in this series was chosen to be a solution of 0.1 M KCl, which was

used for an experimental proof of concept. Then, ethanol was added while the concentration of KCl was kept constant. Thirdly, an equal part mixture of ethanol/water was investigated, before adding 0.1 M $NaNO_3$ to its water part and finally, the full sol including surfactant (CTAB) and silica precursor (TEOS). The experimental setup and measuring routine can be consulted in Chapter 2, 2.2. All of the solutions used in this chapter were acidified using 0.24 M HCl until reaching a pH value of 3 on a pH meter (Mettler Toledo FiveEasy). No degassing was done, meaning that all experiments were done in the presence of air in the solutions. Two Pd-MDEs were used in these experiments and they will be identified for each (Pd-MDE5/Pd-MDE6). Both electrodes underwent the same fabrication process and differ mainly in their tip geometry due to their shaping by hand. Cyclic voltammetry was performed on a TiN working electrode in these solutions (except the silica sol) at 100 mV/s, using a Pt gauze counter and Ag/AgCl reference electrode (see Figure 4.31). The data shows features related to hydrogen, water and oxygen reduction reactions[216,217] for all three salt-containing solutions (a,b,d), with the smallest current response from the water/ethanol mixture (c). The magnitude of those features reduces with each cycle, indicating the consumption of oxygen. The purely aqueous solution shown in Figure 4.31 a) possesses the largest current in the hydrogen evolution wave (below -1.5 V), but all salt containing solutions show oxygen reduction waves between -0.5 and -1.5 V (b,d). Only 4.31 c) has an oxidation peak around -0.5 V, but does not seem to show the same reduction features, suggesting that the previously mentioned reactions do not take place with the same magnitude in the electrolyte-free solution. Details on the involved reactions will be discussed later on in this Section.

4.3.1 Proof of concept

The first actual experiment was performed in 0.1 M KCl using Pd-MDE6. The electrode was angled to roughly 45 degrees with respect to the longer axis of the TiN electrode and approached until the glass body touched the TiN surface close to its outer edge. The distance between MDE tip and TiN electrode was hence below 1 mm, but can not be determined more accurately in this case. The pH sensor was loaded before each measurement using a current of -18 nA, where loading took roughly 300 s. Once fully loaded, an OCP measurement was started. Chronoamperometry on the TiN electrode was started as soon as it was visible that the pH sensor had reached its plateau region, which was typically 30-40 s after stopping the loading current. Loading was always done in the bulk solution, at 10 mm distance to the measurement point in order to minimise any changes in chemical environment near the TiN electrode. This was done using the micropositioner, which allowed for quick and precise movement of the MDE away from the target and back. The potential during loading at -18 nA as well as the relaxation of the pH sensor without any disturbance is shown in Figure 4.32. The blue curve displays the typical shape of a galvanostatic loading curve, showing the initial

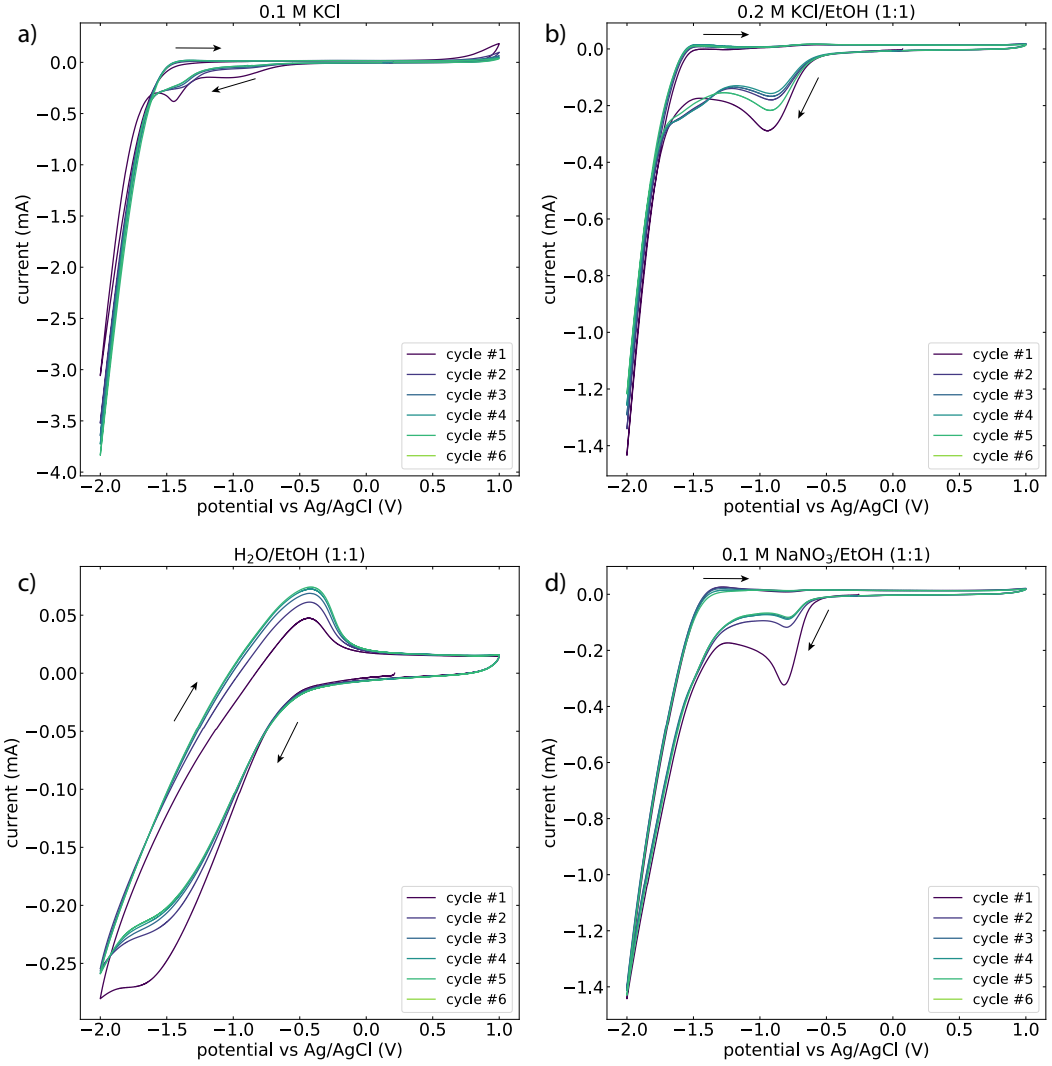

FIGURE 4.31: Cyclic voltammetry (100 mV/s) of a TiN electrode in a) 0.1 M KCl, b) 0.2 M KCl/EtOH (1:1), c) H_2O/EtOH (1:1) and d) 0.1 M $NaNO_3$/EtOH (1:1) at pH=3. Pt gauze counter, Ag/AgCl reference electrode.

loading of hydrogen into the HPd α-phase up until roughly 90 s, after which the potential flattens out, indicating the formation of the HPd β-phase.[153] It shows a feature at 300 s, where the potential suddenly decreases to a lower flat region. This indicates the transition into the hydrogen evolution regime, where the sensor cannot be further loaded. The current was switched off at 400 s. The pH sensor OCP (green curve) then abruptly rises to about -0.25 V vs Ag/AgCl, where it stays on a plateau for slightly more than 150 s until suddenly increasing to over 0.4 V. The shoulder at 600 s corresponds to the unloading of the HPd α-phase.[153] The lifetime of the pH sensor in this case was of around 120 s, which is rather short due to the presence of air in the solution. As the target experiments are shorter than one minute, this was deemed as "good enough".

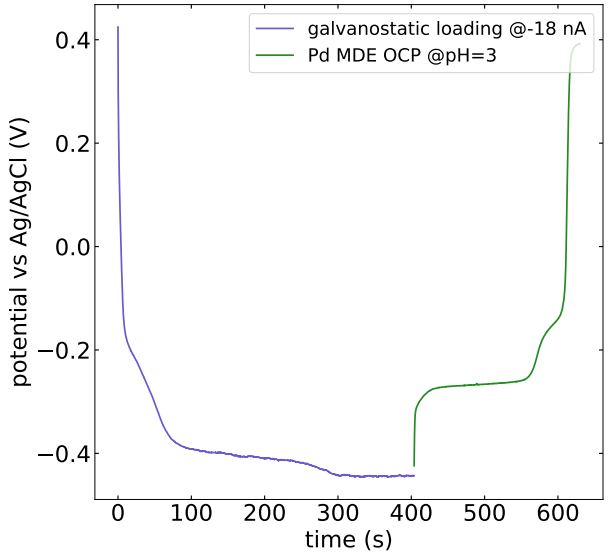

FIGURE 4.32: Galvanostatic loading curve of the HPd pH sensor at -18 nA (blue), showing the initial loading of hydrogen into the HPd α-phase (<90 s), the HPd β-phase (<300 s) and the region of hydrogen evolution (>300 s).[153]

Potential *vs* pH For the first set of measurements, the potential during chronoamperometry was held at -1.25, -1.5, -1.75 and -2.00 V *vs* Ag/AgCl for 10 s each. Figure 4.33 a) shows an exemplary response obtained for -2.0 V. The time axis was set to start at the exact moment at which the chronoamperometry was started. The blue curve shows the raw pH sensor response during chronoamperometry, which is shifted to more negative potentials compared to the response after chronoamperometry (yellow). This is the result of the ohmic drop between MDE and reference electrode due to the electrical current between TiN electrode and the counter electrode. It increases with increasing current. All potentials recorded at the pH sensor hence need to be corrected for the ohmic drop using the interruption of the current to determine the uncompensated resistance. This is done by the equation $U_{corr}(t) = U_{data}(t) - R_u * i_{CA}(t)$, with the corrected potential $U_{corr}(t)$, the raw data $U_{data}(t)$, the uncompensated resistance R_u and the current from chronoamperometry i_{CA}.[218] The difference in the potential profile after correction is shown by the red curve in Figure 4.33 a), where the abrupt change in potential at 10 s is no longer visible. The corrected transients for the previously mentioned potential values are shown in Figure 4.33 b). All transients show a minimum shortly after the respective potential is switched off; the magnitude of the dip increases with increasing overpotential. The time delay between hydroxide generation at the electrode during chronoamperometry and the minimum in potential recorded at the pH sensor arises from the alkaline wave travelling away from the electrode into the bulk, passing the sensor at the time needed to diffuse along the distance between electrode and sensor. This distance δ can be approximated using the diffusion coefficient of hydroxide ($D_{OH} = 5.3 \times 10^{-5}$ cm^{2}s^{-1} [202]) and $\delta = \sqrt{\pi D_{OH} t_{min}} \approx 600$µm (with a t_{min} of approximated 20 s). This fits well with the previously assumed value of less than 1 mm.

Interestingly, the pH sensor lifetime seems to increase dramatically when exposed to the alkaline wave. Its lifetime was previously recorded as in the range of 120 s (see Figure 4.32), however the characteristic features at the end of the plateau region seem to be delayed with decreasing potential during chronoamperometry. While the lifetime of the sensor agrees with its initial measurement after the application of -1.25 V and -1.5 V, the data shows an increase to more than 200 s after applying -1.75 V and 300 s for -2.0 V. The electrolysis reaction happening during chronoamperometry generates the swing into the alkaline region, which partly happens through oxygen reduction and hence increases the sensor lifetime due to the consumption of oxygen in the vicinity of the pH sensor.[216]
Figure 4.34 displays dynamic pH profiles corresponding to the IR drop corrected raw data shown in 4.33 b). *Please Note: from now on, any pH curve shown in this work will have been corrected for ohmic drop, unless stated otherwise*. The top panel shows the pH response obtained from the pH sensor (Pd-MDE6) using the calibration curve shown in Chapter 2, 2.2, while the lower panel displays the corresponding current transients recorded on the TiN electrode. The calibration offset was chosen so that the transients initiate at pH=3. As for the response after the application of the potential, one can observe an increase in pH at about 20 s, which ranges in amplitude from only one or two increments of pH at the higher potentials (-1.25, -1.5 V) to beyond 10 increments for the highest overpotential. The features seem to be rolling in a wave-like manner during which the local pH reaches a maximum, followed by its decay until reaching bulk pH again. Both, amplitude and relaxation time increase with higher overpotential, as more hydroxide is generated at the TiN electrode. This experiment looked rather promising because it clearly visualises the passing of an alkaline wave at the pH sensor, originating at the TiN electrode.

The sensor possibly operates closer to oxygen free conditions when exposed to the alkaline wave, which would mean that the recorded pH values shown in Figure 4.34 are probably overestimated in their magnitude, due to the sensor becoming more Nernstian (closer to -59 mV/pH) during the measurement. As this effect is not possible to gauge at the moment, no strictly quantitative interpretation will be deduced from this. The data does however show the expected qualitative trends.

Control experiments As means of control, an experiment was performed where chronoamperometry was done at the TiN electrode, but where the pH sensor was either 10 mm away and still in the ”beam” of the electrode, or completely out of its way in order to see whether the recorded responses were just effects arising from electrically coupled cables in the setup. The OCP of the sensor did not show even remotely similar

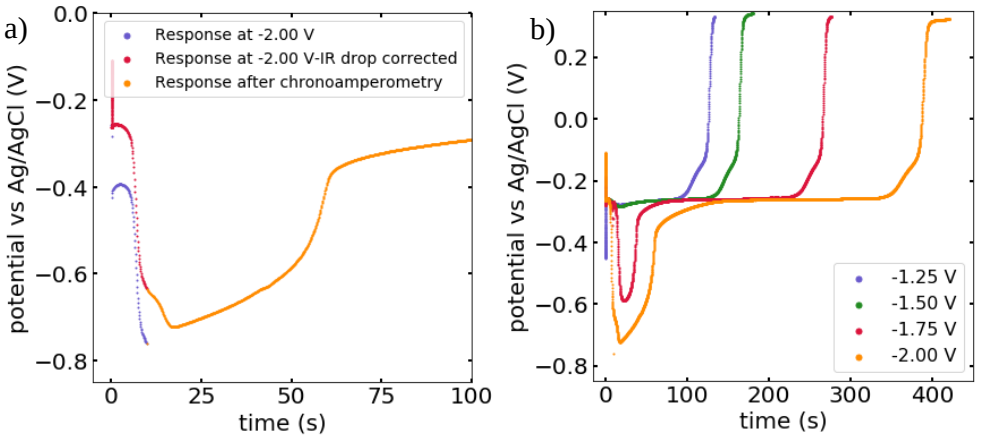

FIGURE 4.33: a) pH sensor response during (blue) and after (yellow) 10 s of chronoamperometry at 2.0 V. The blue curve is shifted to lower potentials due to the IR drop between reference electrode and the pH sensor. The red curve shows the same data corrected for IR drop using $U_{corr}(t) = U_{data}(t) - R_u * i_{CA}(t)$. b) Raw data of the pH measurement of TiN electrode at a potential of -1.25, -1.5, -1.75 and -2.00 V *vs* Ag/AgCl for 10 s using Pd-MDE6 in 0.1 M KCl at bulk pH=3 (0.24 M HCl). Distance between TiN and pH sensor <1 mm.

features, which consisted of only a slight ohmic drop in the first and no response at all in the latter case.

Length of chronoamperometry and pH sensor distance As a second step, the measurements at -1.75 V and -2.00 V were repeated with 30 s of potential application, as shown in Figure 4.35 a). It shows that through longer application of the potential, the alkaline wave has a higher amplitude and relaxation time, while the behaviour regarding the magnitude of the potential is maintained. In addition, measurements were carried out for both, 10 and 30 s of applied potential with the pH sensor at 0.5 mm distance of its original location as close as possible to the electrode, as shown in Figure 4.35 b). The pH response at half a mm further away from the TiN electrode is almost invisible compared to the original signal, and the lifetime of the sensor remains in the range of the initial measurements without chronoamperometry. The location chosen for the measurements seems to be sufficiently close in order to obtain a good signal from the pH change. One issue encountered during this experiments was the formation of bubbles on the TiN electrode whenever the potential was kept at -2.0 V for longer than 5 s. Bubbles of that kind are most probably also responsible for the noise seen in the 30 s measurement at -2.0 V shown in Figure 4.35 a). In order to remove them from the electrode, the beaker containing the solution had to be lowered until the electrode was in air and put back. This was done whenever a previous measurement had led to bubble formation, but as it was not possible to achieve exactly the same configuration as before; variations of the current magnitudes during chronoamperometry were observed due to slight changes of the electrode's active area. These variations are not of great

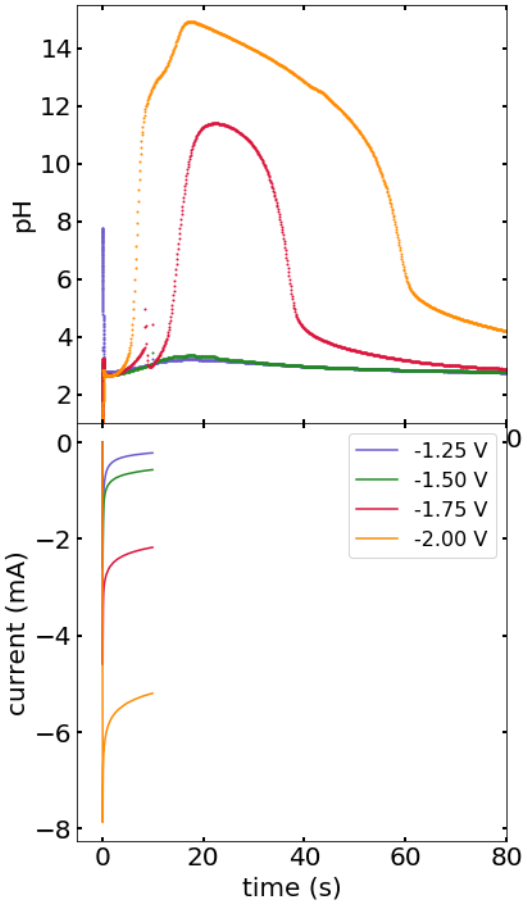

FIGURE 4.34: IR drop corrected dynamic pH responses generated from the raw data shown in Figure 4.33.

concern for this work though, because the TiN electrode was only used to create the alkaline wave and no quantitative information will be deduced from the current transients.

The geometry chosen in this experiment was not ideal due to the pH sensor tip being very close to the edge of the TiN electrode, which is expected to distort the diffusion field if sufficiently close to the surface. Additionally, as the distance between sensor tip and TiN electrode is limited by the glass housing, it would not be possible to move the tip closer to the middle of the TiN electrode without it being much further away than before. For this reason, the working electrode was slightly tilted away from the longitudinal axis of the MDE, so that the tip could be moved as close as possible to the working electrode. Schematic drawings of this setup can be seen in Figure 2.7 in Chapter 2.

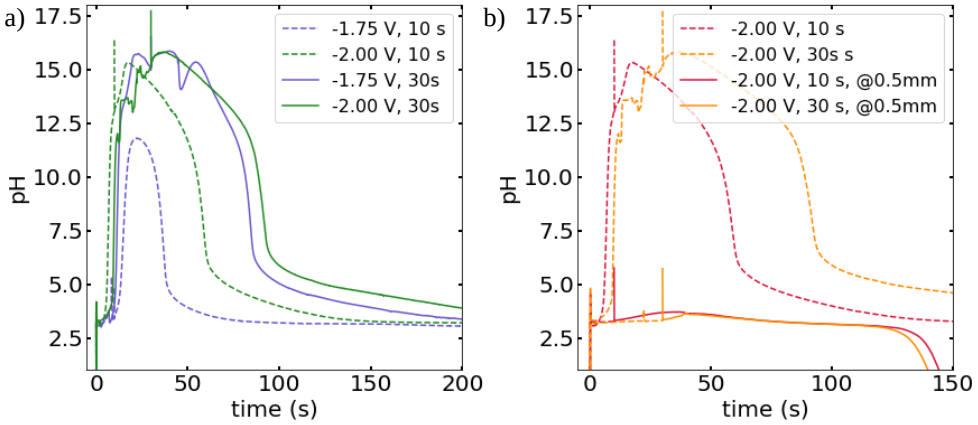

FIGURE 4.35: pH response of Pd-MDE6 recorded a) at -1.75 and -2.00 V applied for 10 and 30 s, and b) -2.00 V for 10 and 30 s each and at the original measurement location as well as 0.5 mm away from it respectively.

4.3.2 0.1 M KCl

The previously shown measurements were partially repeated with a more precise calibration of the distance between MDE tip and TiN electrode. This was done using a USB microscope and the image processing software ImageJ. Figure 4.36 shows the raw microscopy image. The distance was approximated by using the width of the Pt wire within the MDE, which is known as 25 μm. The number of pixels corresponding to this width was taken at the very top of the electrode, where the wire itself is most in focus. As the edge of the TiN electrode is not in focus due to its much larger depth compared to the MDE, there is of course a high uncertainty about the actual numerical value given here. The picture is however useful for illustrating how close the electrodes were in the setup. Electrochemical techniques for determining the distance such as an approach curve or similar were not possible here, because that would have required a vastly different setup which was not realisable at the time. The time of applied constant potential during chronoamperometry will from now on be referred to as t_{CA}, and t_{AC} when an AC potential is used.

Time resolved pH measurements in 0.1 M KCl at pH=3 were repeated for -1.5, -1.75 and -2.0 V *vs* Ag/AgCl. The electrodes used and the measurement procedure was identical to the one in the previous section. Pd-MDE5 was used this time, and the pH responses were calculated using the calibration curve shown in Chapter 2, 2.2 (Pd-MDE5). -18 nA were used as the loading current for a duration of roughly 5 min. The sensor lifetime was observed as similar to the measurements presented previously. The constant potentials during chronoamperometry on the TiN working electrode were applied for durations of t_{CA}=1, 2, 5, 10 and 30 s each. The resulting pH responses are shown in Figure 4.37 for a) -1.5 V, b) -1.75 V and c) -2.0 V. As seen before, the magnitude of the response and also the time needed for the sensor to reach its initial value again increase not only with increasing chronoamperometry time, but also with more cathodic

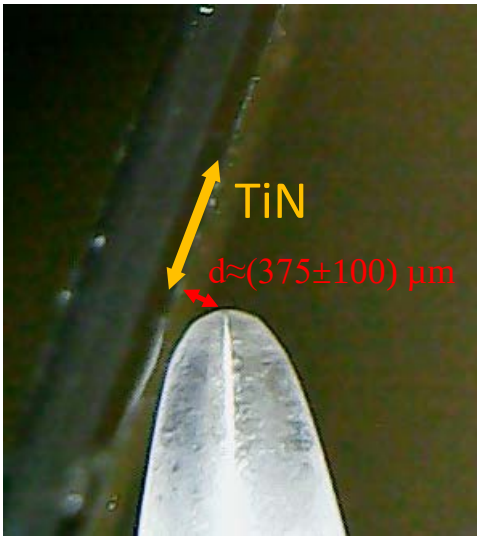

FIGURE 4.36: Calibration image for the distance between Pd-MDE5 and the TiN working electrode. The distance was determined as roughly (375±100) μm using the software ImageJ.

potential values. The responses at -1.5 V stay at most near pH=4 mark for the longest time (t_{CA}=30 s), while they reach values above pH=10 at 10 s for -1.75 V and only 5 s at -2.0 V. The maximum values reached by each of the response curves for a given time of applied potential are gathered in Figure 4.37 d). While the maximum value depends almost linearly on the duration of chronoamperometry at -1.5 V up to t_{CA}=30 s, a massive increase can be seen for the lower potentials, happening at shorter times for -2.0 V. This can be explained by looking at the two main reactions involved at the electrode:

$$2H^+_{(aq)} + 2e^- \rightarrow H_{2(g)}, \tag{4.1}$$

$$2H_2O + 2e^- \rightarrow H_{2(g)} + 2[OH]^-_{(aq)}. \tag{4.2}$$

Equation 4.1 corresponds to the reduction of protons in the solution, which takes place already at small overpotentials. When the overpotential is sufficiently high, the reduction of water as described in Equation 4.2 becomes relevant.[219,220] This leads to a strong increase in hydroxide generation and hence to the observed rise in pH maximum for higher overpotentials. In aerated solutions (as used in this work), oxygen reduction reactions also need to be considered,[216,217] as shown in Equations 4.3&4.4

$$O_2 + 2H_2O + 4e^- \rightarrow 4[OH]^-, \tag{4.3}$$

$$O_2 + 2H_2O + 2e^- \rightarrow H_2O_2 + 2[OH]^-, \tag{4.4}$$

for alkaline and Equations 4.5&4.6

$$O_2 + 2H^+ + 4e^- \rightarrow 2H_2O, \tag{4.5}$$

$$O_2 + 2H^+ + 2e^- \rightarrow H_2O_2, \tag{4.6}$$

for acidic conditions. Putting this into context with the presented experiments, the oxygen reduction reactions near the electrode change from generating water and hydrogen peroxide to mainly hydroxide as the local environment evolves from acidic to alkaline. This means that the alkaline wave might have several ”layers” depending on how much of the chronoamperometric current is converted to hydroxide ions. The rise in pH at the electrode should be leading to an increased hydroxide production due to the contribution from oxygen reduction reactions. This could explain the emergence of multiple maxima in the pH transients (as seen in Figure 4.37 a), 30 s (brown)) if the changes in chemical environment happen sufficiently slowly to be resolved as individual waves. During and after application of the potential, generated species diffuse away from the electrode until bulk pH is restored. In the acidic bulk solution, the main reaction taking place is probably the combination of generated hydroxide and protons to water (Equation 4.7):

$$[OH]^- + H^+ \rightarrow H_2O. \tag{4.7}$$

The overall shape of the pH transients looks very similar to the ones obtained by Critelli *et al.*, which simulated and measured pH transients near a gold electrode in buffered solution.[219] Its comparability to the study in this work is reasonable because even though no buffer was added, a small amount of carbon dioxide/carbonic acid would have been present in all solutions used in this work, as it dissolves in water at ambient conditions.[221,222] The weakly acidic nature of carbonic acid leads to it acting as a buffer for the hydroxide generated at the TiN electrode, leading to the similarity in transients to the work of Critelli *et al.* . For comparison, a set of measurements was done during the application of an AC potential. The conditions were the ones used in the previous chapter, meaning f=100 Hz with the potential oscillating between -1 and -2 V. The corresponding pH responses from the sensor as well as the maximum pH values are shown in Figure 4.38 a) and b) respectively. The total time of applied potential was generally extended for these measurements because the effective generation of hydroxide is expected to be a lot less effective when using this electrochemical protocol. A longer time would then be needed at this tip-working electrode distance until a change in pH would be seen. Figure 4.38 a) shows the obtained pH curves and b) their maximum values. The data was not corrected for ohmic drop because no reliable estimation could be made regarding the actual current contributing to the potential shift, especially as it seemed to arbitrarily change polarity within consecutive measurements. Only the data after switching off the chronoamperometry will therefore be discussed in this case. As expected, the maximum values are considerably smaller than for the constant potentials, where even for the longest time of 200 s the local pH does not exceed a value of 5. The lifetime of the sensor is also not increased as much, especially when comparing the application of 30 s at -2 V to the longest time of AC potential, which allows for the conclusion that the application of an AC potential does indeed lead to a smaller pH gradient. The absence of an actual peak in the curve at t_{AC}=200 s indicates that the

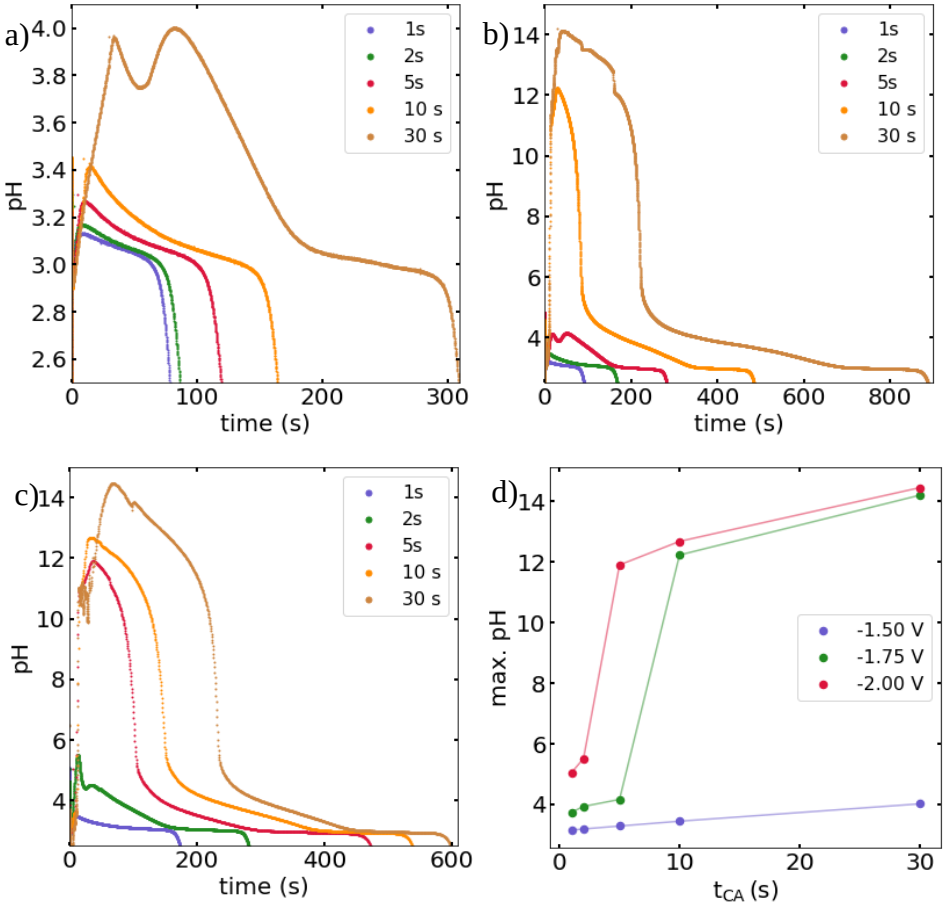

FIGURE 4.37: pH responses of Pt-MDE5 at (375±100) μm from the TiN working electrode in 0.1 M KCl at pH=3 for t_{CA}=1, 2, 5, 10, and 30 s of chronoamperometry at a) -1.5 V, b) -1.75 V and c) -2.0 V. d) Maximum pH values reached by the response curves shown in a)-c) versus chronoamperometry time for each of the applied potentials.

maximum concentration was reached before 200 s, until which the pH gradient resided in a steady state until the potential was switched off and observed decay began. This means that the alkaline wave travelled to the sensor in a shorter time than the potential was applied for, which is reasonable if compared to the previously calculated distance of 600 µm in 20 s.

4.3.3 0.2 M KCl/EtOH 1:1

Using the same configuration as in the previous subsection, the solution was changed to a mixture of 0.2 M KCl with ethanol at a ratio of 1:1 at pH=3. This solution was chosen in order to keep the overall KCl concentration similar to the previous one, but to introduce a large amount of ethanol, as would be in the original silica sol. During the experiment, it was quickly visible that the overpotentials needed to obtain similar response curves were slightly higher than before, as *e.g.* at -1.5 V no response was visible in the range of times used until then. In addition, the galvanostatic loading current

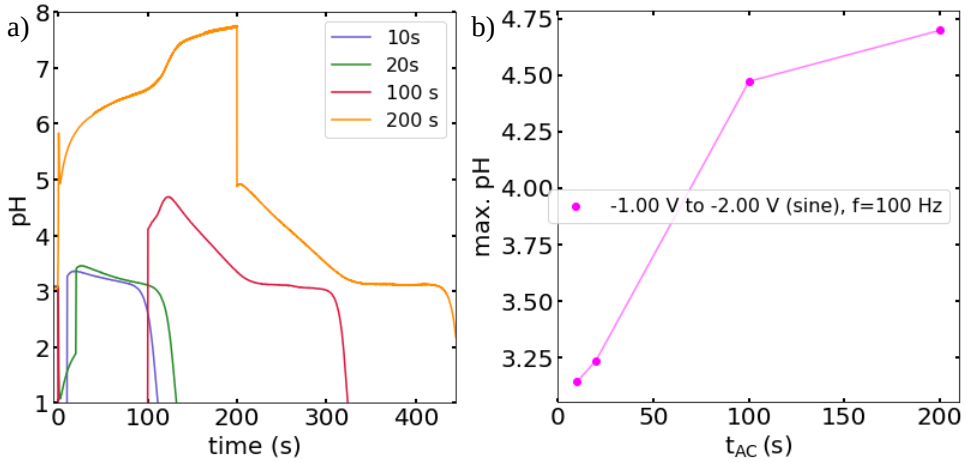

FIGURE 4.38: a) pH responses (not corrected for ohmic drop) recorded using Pd-MDE5 at (375±100) μm from the TiN working electrode in 0.1 M KCl at pH=3 with an applied sinusoidal potential between -1 V and -2 V, f=100 Hz, for the total duration of t_{AC}=10, 20, 100, and 200 s. b) Maximum pH values from (a) *vs* the time of applied potential. Values taken from pH transients after the period of chronoamperometry.

also had to be increased to -48 nA, as otherwise the point of full charge was not visible. This did also decrease the loading time to just under three min. This highlights already a major difference of the system compared to the purely aqueous one, in which the efficiency of the electrode regarding the generation of hydroxide seems to be decreased through the presence of ethanol in the solution. pH response curves were recorded for the applications of -1.75, -1.875 and -2.0 V for varying times between 5 and 60 s, in-between which the sensor was reloaded every time. The corresponding data plots of the measurements are shown in Figure 4.39 for a) -1.75 V, b) -1.875 V, and c) -2.0 V. The data shows, that the response at -1.75 V (a) does in this case resemble more the ones obtained at -1.5 V (see Figure 4.37 a) in the aqueous solution, or slightly weaker in amplitude for the shorter times. The responses at -1.875 V (b) are of intermediary height, whereas the ones at -2.0 V (c) are rather similar to their aqueous references (Figure 4.37 c). At t_{CA}=60 s and -2.0 V (Figure 4.39 c)), the transient has an unexpected dip at approximately 70 s after having passed pH=12. This could be related to bubble formation between electrode and sensor, which was not observed for this solution composition but cannot be totally excluded. Figure 4.39 d) summarises the maxima of the pH responses, showing again that lower potentials lead to an extreme pH swing even at short periods of applied potential. It can be seen that while the overall trends regarding lower potentials are similar to the ones seen before (see Figure 4.37 d)), the maximum values are slightly lower for the same times of applied potential at -2.0 V and dramatically lower at -1.75 V. The conclusion can be made that the introduction of ethanol into the system decreases the amount of generated hydroxide species at the TiN electrode (which fits well with the CV in Figure 4.31 b) showing lower currents than in Figure 4.31 a)). This makes sense as there are only half as many water molecules available. Complementary experiments using the previously introduced sinusoidal protocol did

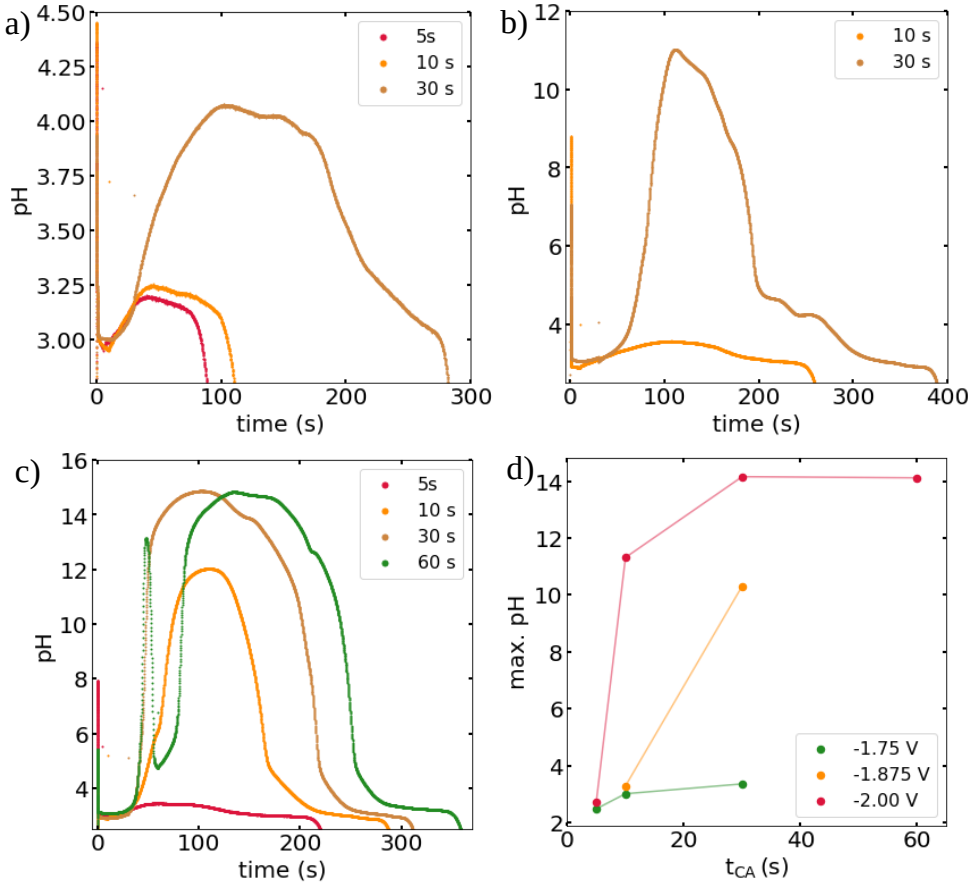

FIGURE 4.39: pH responses recorded using Pd-MDE5 at (375±100) μm from the TiN working electrode in 0.2 M KCl/EtOH (1:1) at pH=3 for the applications of a) -1.75, b) -1.875 and c) -2.0 V for t_{CA} of (not b) 5, 10, 30 and (only c) 60 s. d) Maximum pH values from a) vs time of applied potential. At -1.75 V (a), the maximum pH does not go far beyond pH=4, while a value above pH=10 is obtained when applying -1.875 V for 30 s (b). At -2.0 V, even a t_{CA} of 10 s is sufficient for reaching a maximum pH above pH=10.

show only very little response at times of applied potential of more than t_{AC}=100 s, and will hence only be included in the Appendix of this work (see Figure A.3). They do however still show that the AC protocol leads to significantly lower pH responses at the given distance between MDE tip and TiN working electrode.

4.3.4 H_2O/EtOH 1:1

During the same experimental run, the solution was changed again, keeping the electrode configuration intact as before. The solution now used consisted of only water and ethanol in a ratio of 1:1, at pH=3. This time, only -2.0 V were applied during chronoamperometry as a strong decrease in signal response was observed in this solution. A loading current of -48 nA was used. Figure 4.40 a) shows the obtained pH response curves for times of applied potential of t_{CA}=10, 30, 60 and 200 s, with the corresponding max. pH values shown in Figure 4.40 b). The parts of the transients during

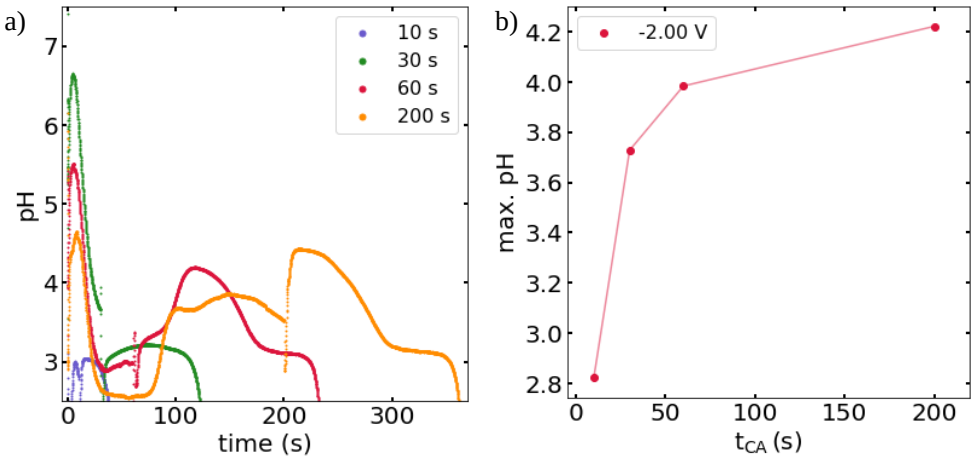

FIGURE 4.40: a) pH responses recorded using Pd-MDE5 at (375±100) μm from the TiN working electrode in H_2O/EtOH (1:1) at pH=3 during the application of -2.0 V for times between 10 and 200 s. b) Maximum pH values (taken from the transient after the end of chronoamperometry) from a) vs the time of applied potential. The massive IR drop caused by the absence of supporting electrolyte makes the interpretation of the signal during applied potential complicated. The corrected transients are not consistent with previous measurements, especially with the one at t_{CA}=200 s (yellow) dropping beneath the bulk value of pH=3 from 30-90 s (not reasonable). This implies that the correction using a constant uncompensated resistance is not sufficient in this case and that the transients should only be analysed in their parts after the application of the potential.

chronoamperometry are in this case not consistent, especially with the one at t_{CA}=200 s (yellow) dropping beneath the bulk value of pH=3 from 30-90 s, which is not reasonable. The curves show an unexpected feature right at the beginning of chronoamperometry, which could be related to a concentration overpotential arising from the absence of supporting electrolyte. This causes a massive IR drop which is apparently not sufficiently taken into account by a constant uncompensated resistance. Even after applying -2.0 V for t_{CA}=200 s on the TiN electrode, the maximum pH values recorded at the sensor after application of potential do not exceed values of pH=5. This fits well with the absence of oxygen reduction features and the very small current in the hydrogen evolution wave seen in 4.31 c). Only one AC measurement was done in this experiment, where the peak obtained for a total of 200 s had roughly the same height as the one from constant -2.0 V for t_{CA}=60 s, confirming the previously observed trend (see Figure A.4).

4.3.5 0.1 M $NaNO_3$/EtOH 1:1

The closest solution composition to the original sol is the one used in this experiment, consisting of 0.1 M $NaNO_3$+EtOH (1:1) at pH=3. It has the exact same components except for the surfactant and silica precursor, so should be similar in its hydroxide generation environment. The loading current was increased to -80 nA in order to properly

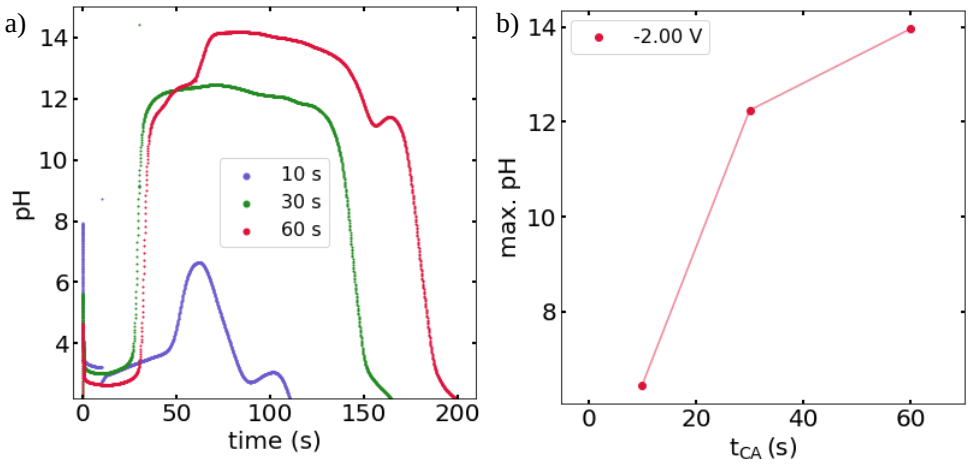

FIGURE 4.41: a) pH responses recorded using Pd-MDE5 at (375±100) μm from the TiN working electrode in 0.1 M $NaNO_3$+EtOH (1:1) at pH=3 during the application of -2.0 V for times between t_{CA}=10, 30 and 60 s. b) Maximum pH values from a) vs the time of applied potential. The decreased amount of supporting electrolyte (compared to the first two solutions presented in this series) leads to lower maximum pH values at comparable times of applied potential. A t_{CA} of 10 s is however still sufficient to surpass a maximum pH value of pH=10.

see the transition of the sensor to its fully charged state. The curves recorded on the sensor are shown in Figure 4.41 a), with their maxima shown in b). Due to the globally reduced amount of supporting electrolyte compared to the first two solutions used in this series, the maximum pH values are generally lower than those for the shorter times, but significantly higher than the one containing no supporting electrolyte. Two measurements using AC potentials were done for times of t_{AC}=100 and 200 s, showing reasonable responses of both over pH=10 at their maximum. These can be seen in Figure A.5.

4.3.6 Regular Silica Sol

The final experiment of this series was a pH measurement with the electrodes immersed in an actual silica sol consisting of 0.1 M $NaNO_3$ and ethanol at pH=3, including CTAB and TEOS (see composition A1 in Chapter 4, 4.1.1). Prior to the experiment, Pd-MDE6 was newly plated with nanostructured Pd (Pd-MDE6.2). Since no recalibration was done, previous values of Pd-MDE6 will be used as the geometry of the tip was not changed in the process. The loading current was -48 nA. Only two measurements were performed successfully due to the fact that the TiN working electrode had to be replaced after each chronoamperometry as the sol gel reaction would irreversibly change its surface. As the experimental setup was only of temporary nature, it as not possible to reliably change the TiN electrode without moving any of the electrodes and hence destroying the distance calibration. One issue expected beforehand was the generation

of a silica gel around the pH sensor during the experiment, possibly rendering it useless right from the start or considerably changing the signal in a way that would have made it impossible to interpret any of the data. Luckily, this was not the case, as even the "empty" run of loading the sensor and just leaving it to relax in the sol did not show any unusual behaviour in the potential. It did seem that the sensor needed a slightly longer time (roughly 2x) to reach its plateau region after turning off the loading current, but the potential seemed to be generally comparable to the ones seen previously. Figure 4.42 shows the calibration image for this experiment, where the electrode can be seen aligned very closely to the TiN electrode. The distance was estimated again using ImageJ as (100±50) μm, significantly smaller than in the previous series due to the thinner tip of this microelectrode. A constant potential of -2.0 V was applied for 10 and 30 s respectively. The resulting pH curves can be seen in Figure 4.43 a), with the maximum values plotted in b). Both measurements lead to similar maxima in pH of just below 6, whereby the longer t_{CA} leads to a longer relaxation time. The general shape of the curves shown in 4.43 a) is very similar to the ones seen in the previous experiments. The maximum value for the 30 s measurement is lower than for comparable a measurement in the solution containing 0.1 M $NaNO_3$+EtOH (1:1), which is closest to the original sol, even though the distance between electrode and tip of the sensor is smaller in this experiment. This indicates that the hydroxide species either are used up in the silica poly-condensation reactions taking place at the electrode or that the gelation process leads to a severe decrease of their diffusion. Silica hydrolysis (see Equation 4.8) and its reverse reactions consume hydroxide, but the sol being kept at pH=3 should contain mainly hydrolysed species due to the high reaction rate at low pH.[223] Reverse reactions and further hydrolysis are however still possible.[206] At the same time, the main condensation reactions as shown in Equations 4.9&4.10 are catalytically driven, so the reduction in pH transient is most likely the result of the reduced diffusion rate in the gel area. The calibration distance can only be guaranteed as accurate for the measurement with t_{CA}=10 s, as the TiN working electrode was manually changed after that to obtain a clean substrate. This means that a slight increase of the distance could be the reason for the measurement at t_{CA}=30 s to not be significantly higher.

$$-SiOR + H_2O \rightarrow -SiOH + ROH \tag{4.8}$$

$$-SiOH + HOSi \rightarrow -Si - O - Si - + H_2O \tag{4.9}$$

$$-SiOH + HO-_{surface} \rightarrow -Si - O -_{surface} + H_2O \tag{4.10}$$

A reduction of the efficiency of the TiN electrode regarding its generation of hydroxide species to its coverage by the formation of the silica gel is also possible. In Figure 4.6 it had been shown that the dry film thickness of the film and aggregates deposited at -2.0 V a for 60 s lies at around 30 μm. The pH response measured at 100 μm -2.0 V/30 s

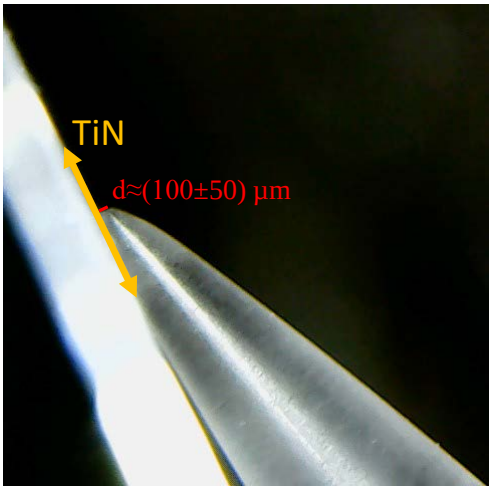

FIGURE 4.42: Calibration image for the distance between Pd-MDE6.2 and the TiN working electrode. The distance was determined as roughly (100±50) μm using the software ImageJ.

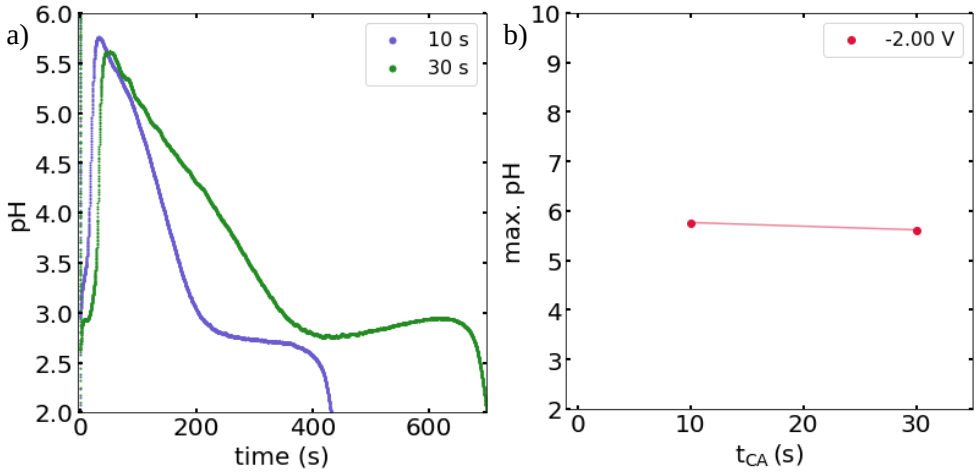

FIGURE 4.43: a) pH responses recorded using Pd-MDE6.2 at (100±50) μm from the TiN working electrode in an original silica sol at pH=3 during the application of -2.0 V for t_{CA}=10, 30 s .b) Maximum pH values from (a) vs the time of applied potential.

shows that at this distance, only little silica condensation would occur, which corresponds to the dry film being thinner than 100 µm. The pH profile hence potentially allows for an indirect measurement of the film thickness in solution.

4.3.7 Implications for EASA experiments

The discussion of the results obtained from pH measurements in the vicinity of a TiN electrode indicate that the alkaline wave produced by the redox reactions (at the electrode) reaches substantial thickness at the shorter end of typically used time periods during EASA experiments. The amount of hydroxide produced for a given time decreases with the addition of ethanol to the solution, as does any reduction of supporting electrolyte concentration due to the reduced current for a given potential. The maximum values indicate the high degree of alkalinity expected on the electrode surface (as the pH sensor is relatively ”far” away from the electrode surface), which is needed for the successful formation of the silica structure. The most important effect to note for experimental practice is the time needed to revert back to bulk pH, which is generally considerably longer than the actual experimental time itself. Even with the application of only 10 s of -2 V in the real sol (see Figure 4.43 a)), the solution returns to bulk pH only 3 minutes later. As this was measured ”far” away from the electrode, the reaction near the surface must continue long after the external input is removed. The time between the end of chronoamperometry and sample removal from solution/rinsing is therefore a crucial value, which should be recorded along with other experimental parameters. Variations of this time should strongly affect the number of aggregates formed on top of the films. Regarding the AC deposition protocol, the pH measurements showed that the alkaline wave is significantly reduced by the application of the AC potential, which in turn leads to a decrease in the number of surface aggregates vs the formation of the compact film (as shown in Section 4.2). The ”inflation” effect seen in Section 4.1.2 was initially attributed to the either hydroxide or ethanol going through/entering the network during electrochemically induced poly-condensation of silica. The results from the pH measurements in the real silica sol do show that a significant amount of hydroxide is consumed in this reaction, since the alkaline wave is much weaker under the original experimental conditions that in the absence of the silica precursor. It therefore is unlikely that a strong stream of hydroxide across the silica network would lead to the inflation, especially since its decay back to bulk pH is of longer duration than the relaxation of the structural inflation after the application of the potential. It seems as if the application of the potential leads to one of the species behaving as a co-surfactant for the micelles, leading to their expansion during chronoamperometry.

Chapter 5

Conclusions

The practical execution of most electrochemical processes is simple, but their investigation to gain a fundamental understanding remains challenging. Chemical reactions taking place in solution limit any kind of real-time study to techniques that are applicable within the environment of a liquid substance. With most of these processes taking place at or below the nano-scale, photon-based optical tools remain one of the few possibilities for such. In this work, small angle (X-ray/neutron) scattering was chosen as the main technique alongside electron microscopy to resolve the structural arrangement of metals/semiconductors during electrodeposition and the Electrochemically Assisted Surfactant Assembly of mesoporous silica films. Its minimal influence on the experimental environment and inherent suitability for the monitoring of liquid/solid interfaces make it a valuable tool, although it is still not widely used on electrochemical systems due to the frequent requirement of dedicated experimental equipment, large scale facilities and the not trivial interpretation of the acquired data.[184,224–227]

In the initial phase of this work, GISAXS was used to probe the arrangement of Au nanoparticles electrodeposited on a TiN electrode. The average particle distance as well as information on their size and number density were analysed and compared to findings obtained from electron microscopy, showing that the trends regarding the effect of potential and deposition time are present in both techniques. While electron microscopy allows for more detailed quantitative analysis of particles outside their conditions of formation, GISAXS gives qualitative information and would be applicable to tracing the properties of particles forming in solution. Emphasis was also put on the importance of the scattering image quality, which mainly depends on the available instrument. The most useful results where obtained when using a dedicated facility like a synchrotron beamline, as the quality and brilliance of the beam as well as the typically larger measurable range of structure sizes improves data quality and its interpretation simultaneously. Finally, that the electrodeposition of Au on blank TiN leads to non-randomly arranged nanoparticles despite the surface not being constrained by *e.g.* a

template. This could decrease the degree of filling of a sufficiently small porous host on the electrode. It emphasizes the need for further attention to the complicated dynamics present during electrodeposition.[228] So far, electron microscopy has been used to track individual particles in order to reveal their arrangement and size over time, which limits the analysis to a low number of particles.[15,22] The addition of GISAXS to this kind of study would allow for a comparison of the observations made with individual particles to structural data averaged over a significantly larger area.
Consecutively, small angle scattering was applied to a completely novel system: the non-aqueous deposition of Bismuth Telluride. Template electrodeposition being the required step to a new functional material, its deposition from a single plating bath on non-templated TiN electrode was studied. The previous approach of SEM and GISAXS applied to this system resulted in no clear evidence on the formation of singular/binary composed particles or their transition from one to the other with increasing deposition time. The data indicated that the particle arrangement depended strongly on the distribution of available species in solution, rather than the momentary particle arrangement on the electrode. After that, neutrons were employed instead of photons in order to minimise absorption effects from the solvent DCM, allowing for an exotic experimental geometry, which made probing the electrode surface accessible from outside the electrochemical cell. Once again, no evidence of binary composed phases could be seen, indicating that they might be forming at timescales below 1 s of deposition time. As opposed to Au deposition, no correlation distance was visible in the data, indicating the growth of rough layers as opposed to individual islands. This is in agreement with previous studies.[75]

The other major point of interest in this work was the formation of mesoporous silica films through EASA. The process was monitored in real-time using GISAXS, showing that a compact film with vertically aligned pores as well as mesoporous surface spherical aggregates form almost simultaneously (film before aggregates) on top of it. During application of the potential, the whole structure inflates slightly in size. This effect was present regardless of the employed surfactant/amount of swelling agent, although its degree varied depending on the conditions to no extractable trend. A maximum in scattering contrast was seen on a similar time scale and was interpreted as an indication for passing the percolation threshold of the system, after which the gel became too rigid to undergo any further changes in pore spacing. Limitations of pore swelling were seen with increasing amount of swelling agent for both employed surfactants, indicating that it undergoes a transition from co-surfactant to co-solvent, the critical concentration of which seems to depend on the chain length of the surfactant. In control experiments, the importance of the electric field regarding the pore alignment could be relativised, as vertically ordered structures could be generated in its absence using similar conditions. For future studies, GISAXS could be used to very accurately optimise deposition protocols in solution, and to determine critical parameters of the

system as *e.g.* surface/bulk CMC of the surfactant in presence of the silica precursor. The addition of an infra-red technique to also determine the chemical composition of species near the electrode would also be beneficial. Using a reverse GISANS geometry on this system would allow for the separate monitoring of the surface process only, due to the bypassing of the bulk electrolyte in the beam path.

In order to reduce the number of surface aggregates on the silica films, a new approach using a sinusoidal potential and an electrolyte-free sol composition was tried and tested. The film thickness was increased while significantly decreasing the number of surface aggregates when using an electrolyte-free sol and an oscillating potential. This reduced the magnitude of the alkaline layer away from the electrode, slowing down aggregate formation in the bulk solution, making this the first and closest route to aggregate-free EASA silica films using a single deposition step. Using the original sol composition increased the number of aggregates, but still led to the formation of vertically aligned structures. The fact that highly ordered silica pores could be formed using a non-constant potential indicates further that itself is not responsible for the surfactant assembly, as opposed to the commonly used description of the process.[223] Further development of the technique could involve the use of an asymmetrical square wave, with the duty cycle being only $1/10^{th}$ of the period to further reduce the flux of hydroxide.

Finally, a home-made pH sensor made from a Pd nanostructure was used to measure the evolution of hydroxide generation near a TiN electrode during the application of a cathodic potential. The sensor was calibrated and then used to perform experiments in a variety of solutions, starting from a simple aqueous solution of a potassium salt and finishing with an actual silica sol. The pH sensor life time increased significantly with the time used for potential application, indicating the consumption of dissolved oxygen in the solution as previously reported.[216] The sensor provided consistent results throughout a multitude of experiments in differently composed solutions, showing for the first time its applicability to not purely aqueous environments. So far, similar sensors have been used only in aqueous environments to monitor pH near working electrode.[219] Higher overpotentials at the TiN electrode led to increased hydroxide production, although the respective magnitude declined with the addition of ethanol to the solution and was lowest for a solution consisting of water and ethanol only (no supporting electrolyte). The application of a sinusoidal potential resulted in lower magnitudes of the pH transients. The relaxation time back to bulk pH was seen to be significantly longer than typical experiments, showing the importance of exactly timing the period between switching off the potential and removing the sample from the silica sol, during which the reaction proceeds and therefore affects the properties of the obtained silica films. The measurements also showed that hydroxide species are unlikely to cause the swelling effect described earlier, as the relaxation time of the structure is considerably shorter than the one of the alkaline wave. Its is more likely that hydrogen gas travelling through the gel is causing this, even though no bubbles were observed.

Regarding future work, the studies of nucleation during electrodeposition would certainly benefit from an increased use of combined structurally and chemically sensitive techniques, as for example X-ray absorption with X-ray/neutron scattering. The resulting link between the evolution of the chemical environment and its structure from the atomic to the macro-scale would give a more accurate understanding of the involved processes. A reverse neutron experiment on the formation of silica through EASA might be very interesting, as the contribution from the solution would be omitted completely. X-ray reflectivity performed in real-time on this system would give vital information on the evolution of film thickness during deposition, an important quantity which has not been measurable so far. Similarly, pH sensors similar to the used HPd electrode shown in this work might be useful for tracking proton/hydroxide environments during any kind of electrodeposition process in aqueous solution, as these charged and highly mobile species should be expected have a significant impact on the behaviour of any other electrochemically active species involved.

Appendix A

Appendix

A.1 Additional Figures Instrumental methods

In order to follow the morphology of electrodeposited materials in real time, a cell was designed to make such experiments possible. On the one hand it had to be sufficiently transparent to X-rays to obtain good time-resolution, on the other it had to allow for enough scattering volume to obtain reasonable statistics for the data. The cell as shown in Figure A.1 was designed for substrates with a width of 3 mm, which results in a probed area of still a few hundreds of μm^2. The beam energy was chosen as 18 keV, at which the transmission through the electrolyte resides in the range of 0.7 and hence gives a very good signal. The SDD in that setup was 3034 mm, using a Dectris Pilatus 2M for the measurements. Depending on the time resolution one wants to achieve, the beam energy could be decreased down to 12 keV, as the experiment at 18 keV caused visible beam damage to a silica template TiN substrate.

A.2 Additional Figures EASA

A.3 Additional graphs: ”Potentiometric pH measurements in the vicinity of a TiN electrode”

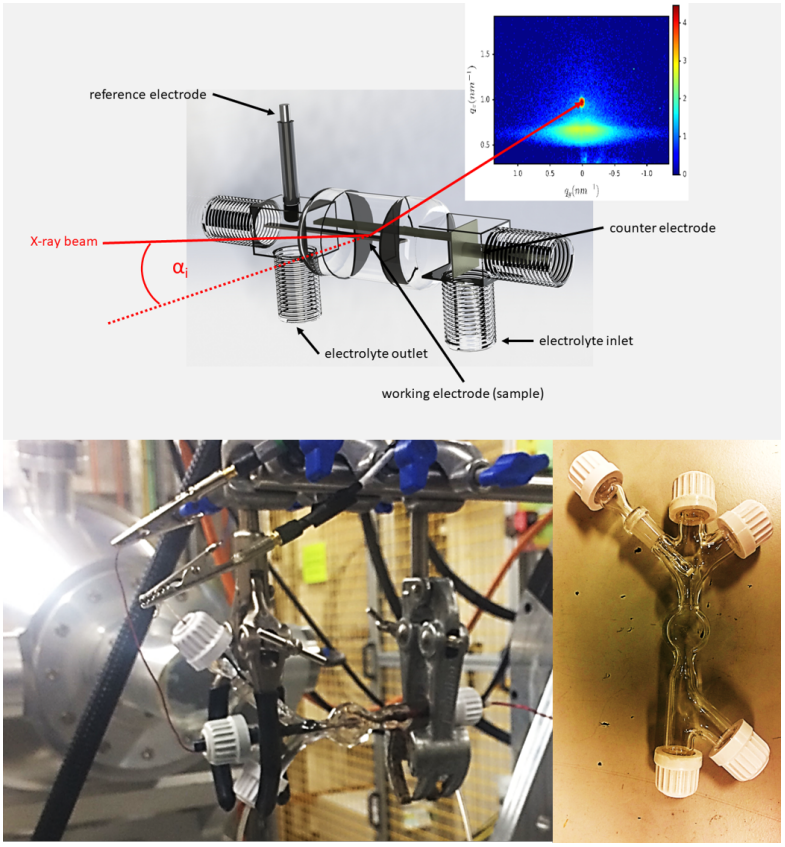

FIGURE A.1: (top) Schematic drawing of the cell designed for *in operando* GISAXS experiments. (bottom, left) Cell mounted on the hexapod of the I07 beamline at Diamond Light Source. (bottom, right) Close-up of the empty cell.

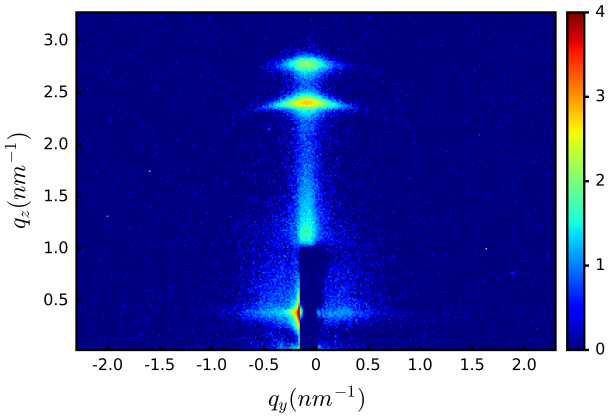

FIGURE A.2: Scattering image of a TiN substrate to which -2.0 V were applied for 3 s in a solution of 0.1 M $NaNO_3$/EtOH (1:1) with CTAB (480 mg per 20 ml water). Incident angle: 0.3°, exposure time: 1800 s (In-house measurement).

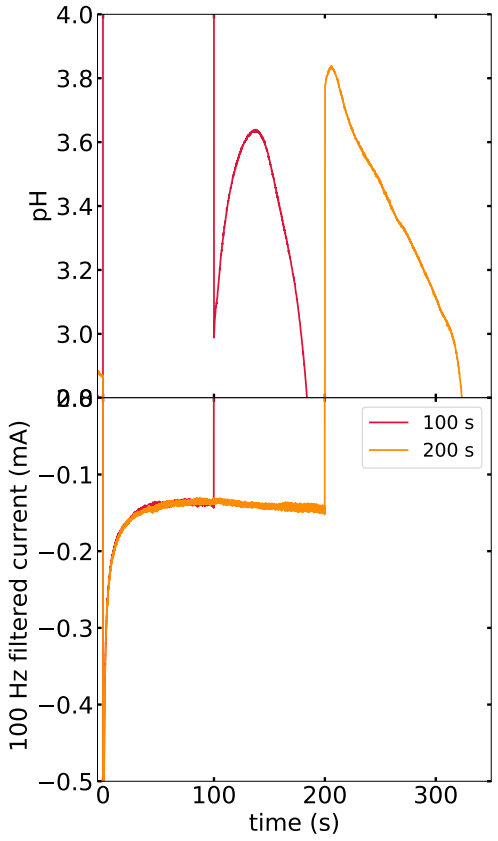

FIGURE A.3: pH responses (not corrected for ohmic drop) recorded using Pd-MDE5 at (375±100) μm from the TiN working electrode in 0.2 M KCl + EtOH (1:1) at pH=3 with an applied sinusoidal potential between -1 V and -2 V, f=100 Hz, for the total duration of t_{AC}=100, and 200 s (not IR drop corrected).

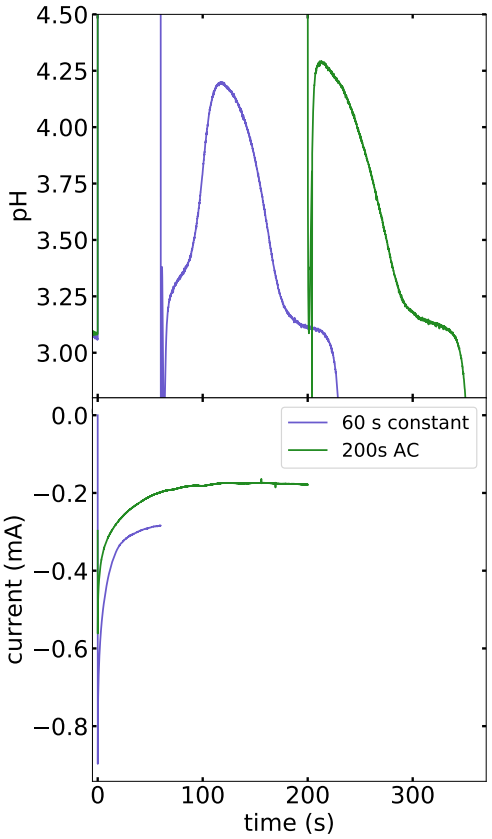

FIGURE A.4: pH responses recorded using Pd-MDE5 at (375±100) μm from the TiN working electrode in H_2O/EtOH (1:1) at pH=3 during the application ofsinusoidal potential between -1 V and -2 V, f=100 Hz, for the total duration of t_{AC}=200 s (not IR drop corrected). Response for 60 s at -2 V constant potential shown for comparison (not IR drop corrected).

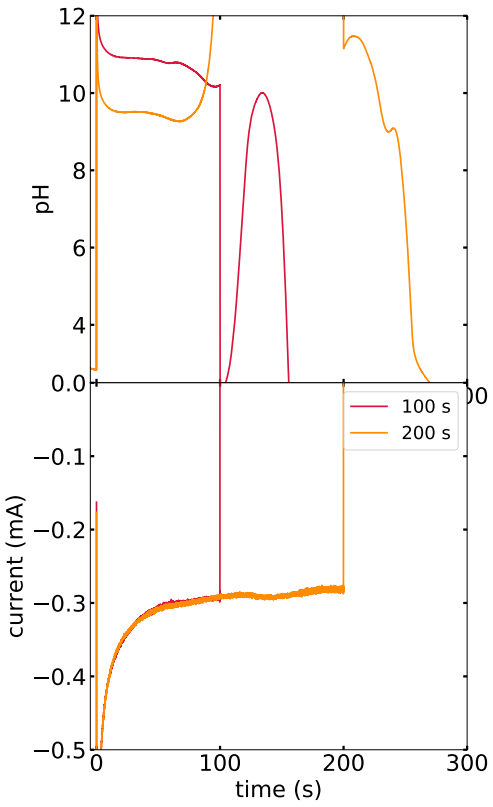

FIGURE A.5: pH responses recorded using Pd-MDE5 at (375±100) μm from the TiN working electrode in 0.1 M $NaNO_3$+EtOH (1:1) at pH=3 during the application of a sinusoidal potential between -1 V and -2 V, f=100 Hz, for the total duration of t_{AC}=100, and 200 s (not IR drop corrected).

References

[1] A. Brenner, *Electrodeposition of alloys: principles and practice*, Elsevier, New York, 2013.

[2] W. Schwarzacher, *Electrochemical Society Interface*, 2006, **15**, 32–33.

[3] G. A. Di Bari, *Modern Electroplating*, 2000, **5**, 79–114.

[4] J. K. Dennis and T. E. Such, *Nickel and Chromium Plating*, Woodhead Publishing Ltd, Cambridge, 1993.

[5] E. Budevski, G. Staikov and W. Lorenz, *Electrochimica Acta*, 2000, **45**, 2559–2574.

[6] B. Scharifker and G. Hills, *Electrochemica Acta*, 1983, **28**, 879–889.

[7] M. Sluyters-Rehbach, J. H. Wijenberg, E. Bosco and J. H. Sluyters, *Journal of Electroanalytical Chemistry*, 1987, **236**, 1–20.

[8] L. Heerman and A. Tarallo, *Journal of Electroanalytical Chemistry*, 1999, **470**, 70–76.

[9] L. Heerman and A. Tarallo, *Journal of Electroanalytical Chemistry*, 1998, **451**, 101–109.

[10] H. Liu, F. Favier, K. Ng, M. P. Zach and R. M. Penner, *Electrochimica Acta*, 2001, **47**, 671–677.

[11] H. Liu and R. M. Penner, *The Journal of Physical Chemistry B*, 2000, **104**, 9131–9139.

[12] B. Scharifker and J. Mostany, *Journal of Electroanalytical Chemistry and Interfacial Electrochemistry*, 1984, **177**, 13–23.

[13] J. Mostany, J. Mozota and B. Scharifker, *Journal of Electroanalytical Chemistry and Interfacial Electrochemistry*, 1984, **177**, 25–37.

[14] M. E. Hyde and R. G. Compton, *Journal of Electroanalytical Chemistry*, 2003, **549**, 1–12.

[15] H. E. Hussein, R. J. Maurer, H. Amari, J. J. Peters, L. Meng, R. Beanland, M. E. Newton and J. V. Macpherson, *ACS Nano*, 2018, **12**, 7388–7396.

[16] J. Ustarroz, J. A. Hammons, T. Altantzis, A. Hubin, S. Bals and H. Terryn, *Journal of the American Chemical Society*, 2013, **135**, 11550–11561.

[17] A. Milchev, W. S. Kruijt, M. Sluyters-Rehbach and J. H. Sluyters, *Journal of Electroanalytical Chemistry*, 1993, **362**, 21–31.

[18] W. S. Kruijt, J. H. Sluyters and A. Milchev, *Journal of Electroanalytical Chemistry*, 1994, **371**, 13–26.

[19] T. Arzhanova and A. Golikov, *Journal of Electroanalytical Chemistry*, 2003, **558**, 109–117.

[20] A. Serruya, J. Mostany and B. R. Scharifker, *Journal of the Chemical Society, Faraday Transactions*, 1993, **89**, 255–261.

[21] M. Tomellini, *Physica A: Statistical Mechanics and its Applications*, 2018, **496**, 481–494.

[22] J. Ustarroz, J. A. Hammons, T. Altantzis, A. Hubin, S. Bals and H. Terryn, *Journal of the American Chemical Society*, 2013, **135**, 11550–11561.

[23] M. H. Mamme, C. Köhn, J. Deconinck and J. Ustarroz, *Nanoscale*, 2018, **10**, 7194–7209.

[24] J. Bockris, *Electrochemical Phase Formation and Growth VCH*, VCH Verlagsgesellschaft, Weinheim, 2003, vol. 433, pp. 227–228.

[25] R. Armstrong, M. Fleischmann and H. Thirsk, *Journal of Electroanalytical Chemistry (1959)*, 1966, **11**, 208–223.

[26] M. Abyaneh, *Electrochimica Acta*, 1982, **27**, 1329–1334.

[27] M. Abyaneh and M. Fleischmann, *Electrochimica Acta*, 1982, **27**, 1513–1518.

[28] E. Bosco and S. Rangarajan, *Journal of Electroanalytical Chemistry and Interfacial Electrochemistry*, 1982, **134**, 213–224.

[29] M. Abyaneh and M. Fleischmann, *Journal of The Electrochemical Society*, 1991, **138**, 2491–2496.

[30] M. Abyaneh, *Journal of Electroanalytical Chemistry*, 1995, **387**, 29–34.

[31] Y. Li, W. Chrzanowski and A. Lasia, *Journal of Applied Electrochemistry*, 1996, **26**, 843–852.

[32] G. Gunawardena, G. Hills, I. Montenegro and B. Scharifker, *Journal of Electroanalytical Chemistry and Interfacial Electrochemistry*, 1982, **138**, 255–271.

[33] B. Scharifker and G. Hills, *Electrochimica Acta*, 1983, **28**, 879–889.

[34] M. Sluyters-Rehbach, J. Wijenberg, E. Bosco and J. Sluyters, *Journal of Electroanalytical chemistry*, 1987, **236**, 1–20.

[35] L. Heerman and A. Tarallo, *Journal of Electroanalytical Chemistry*, 1998, **451**, 101–109.

[36] L. Hunt, *Gold Bulletin*, 1973, **6**, 16–27.

[37] C. Raub, in *Metal Plating and Patination*, Elsevier, Oxford, 1993, pp. 284–290.

[38] M. C. M. Daniel and D. Astruc, *Chemical Reviews*, 2004, **104**, 293–346.

[39] P. Ghosh, G. Han, M. De, C. K. Kim and V. M. Rotello, *Advanced Drug Delivery Reviews*, 2008, **60**, 1307–1315.

[40] S. Eustis and M. A. El-Sayed, *Chemical Society Reviews*, 2006, **35**, 209–217.

[41] L. P. Kreuzer, M. J. Männel, J. Schubert, R. P. Höller and M. Chanana, *ACS Omega*, 2017, **2**, 7305–7312.

[42] Y. Li, F. El Gabaly, T. R. Ferguson, R. B. Smith, N. C. Bartelt, J. D. Sugar, K. R. Fenton, D. A. Cogswell, A. L. D. Kilcoyne, T. Tyliszczak, M. Z. Bazant and W. C. Chueh, *Nature Materials*, 2014, **13**, 1149–1156.

[43] X. Dai and R. G. Compton, *Analytical Sciences*, 2006, **22**, 567–570.

[44] L. Wang, W. Mao, D. Ni, J. Di, Y. Wu and Y. Tu, *Electrochemistry Communications*, 2008, **10**, 673–676.

[45] J. Zhang and M. Oyama, *Analytica Chimica Acta*, 2005, **540**, 299–306.

[46] E. Sheridan, J. Hjelm and R. J. Forster, *Journal of Electroanalytical Chemistry*, 2007, **608**, 1–7.

[47] O. Shulga and J. R. Kirchhoff, *Electrochemistry Communications*, 2007, **9**, 935–940.

[48] M. O. Finot, G. D. Braybrook and M. T. McDermott, *Journal of Electroanalytical Chemistry*, 1999, **466**, 234–241.

[49] L. Komsiyska and G. Staikov, *Electrochimica Acta*, 2008, **54**, 168–172.

[50] P. V. Dudin, P. R. Unwin and J. V. Macpherson, *The Journal of Physical Chemistry C*, 2010, **114**, 13241–13248.

[51] a. D. Goolsby and D. T. Sawyer, *Analytical Chemistry*, 1968, **40**, 1978–1983.

[52] J. E. Anderson and S. M. Sawtelle, *Inorganica Chimica Acta*, 1992, **194**, 171–177.

[53] G. Oskam and P. C. Searson, *Surface Science*, 2000, **446**, 103–111.

[54] A. Bulusu and D. Walker, *Superlattices and Microstructures*, 2008, **44**, 1–36.

[55] H. Goldsmid, *Proceedings of the Physical Society. Section B*, 1954, **67**, 360.

[56] J. Bardeen and W. Shockley, *Physical Review*, 1950, **80**, 72.

[57] R. Peierls, *Annalen der Physik*, 1929, **395**, 1055–1101.

[58] H. Goldsmid and R. Douglas, *British Journal of Applied Physics*, 1954, **5**, 386.

[59] J. George and B. Pradeep, *Solid State Communications*, 1985, **56**, 117–120.

[60] A. Boulouz, A. Giani, F. Pascal-Delannoy, M. Boulouz, A. Foucaran and A. Boyer, *Journal of Crystal Growth*, 1998, **194**, 336–341.

[61] D. G. Ebling, A. Jacquot, M. Jägle, H. Böttner, U. Kühn and L. Kirste, *Physica Status Solidi (RRL)–Rapid Research Letters*, 2007, **1**, 238–240.

[62] J. Yang, R. Chen, X. Fan, S. Bao and W. Zhu, *Journal of Alloys and Compounds*, 2006, **407**, 330–333.

[63] J. W. R. Harding and A. S. Gelb, *Thermoelectric Materials and their Production by Powdered Metallurgy Techniques*, 1964, US Patent 3,129,117.

[64] J. Yang, X. Fan, R. Chen, W. Zhu, S. Bao and X. Duan, *Journal of Alloys and Compounds*, 2006, **416**, 270–273.

[65] P. Magri, C. Boulanger and J.-M. Lecuire, *Journal of Materials Chemistry*, 1996, **6**, 773–779.

[66] V. Richoux, S. Diliberto, C. Boulanger and J. Lecuire, *Electrochimica Acta*, 2007, **52**, 3053–3060.

[67] Y. Miyazaki and T. Kajitani, *Journal of Crystal Growth*, 2001, **229**, 542–546.

[68] S. Li, M. S. Toprak, H. M. Soliman, J. Zhou, M. Muhammed, D. Platzek and E. Müller, *Chemistry of Materials*, 2006, **18**, 3627–3633.

[69] H. J. Goldsmid, *Materials*, 2014, **7**, 2577–2592.

[70] H. J. Goldsmid, in *Introduction to Thermoelectricity*, Springer, Berlin, Heidelberg, 2016, pp. 153–195.

[71] C. Boulanger, *Journal of Electronic Materials*, 2010, **39**, 1818–1827.

[72] A. J. Naylor, E. Koukharenko, I. S. Nandhakumar and N. M. White, *Langmuir*, 2012, **28**, 8296–8299.

[73] J. Recatala-Gomez, P. Kumar, A. Suwardi, A. Abutaha, I. Nandhakumar and K. Hippalgaonkar, *Scientific Reports*, 2020, **10**, 1–10.

[74] W.-J. Li, *Electrochimica Acta*, 2009, **54**, 7167–7172.

[75] L. Meng, K. Cicvarić, A. L. Hector, C. de Groot and P. N. Bartlett, *Journal of Electroanalytical Chemistry*, 2019, **839**, 134–140.

[76] P. N. Bartlett, R. Beanland, J. Burt, M. M. Hasan, A. L. Hector, R. J. Kashtiban, W. Levason, A. W. Lodge, S. Marks, J. Naik, A. Rind, G. Reid, P. W. Richardson, J. Sloan and D. C. Smith, *Nano Letters*, 2018, **18**, 941–947.

[77] A. W. Lodge, M. M. Hasan, P. N. Bartlett, R. Beanland, A. L. Hector, R. J. Kashtiban, W. Levason, G. Reid, J. Sloan, D. C. Smith and W. Zhang, *RSC advances*, 2018, **8**, 24013–24020.

[78] J. D. Klein, R. D. Herrick, D. Palmer, M. J. Sailor, C. J. Brumlik and C. R. Martin, *Chemistry of Materials*, 1993, **5**, 902–904.

[79] R. O. Loutfy and D. S. Ng, *Solar Energy Materials*, 1984, **11**, 319–328.

[80] P. N. Bartlett, S. L. Benjamin, C. H. (Kees) de Groot, A. L. Hector, R. Huang, A. Jolleys, G. P. Kissling, W. Levason, S. J. Pearce, G. Reid and Y. Wang, *Materials Horizons*, 2015, **2**, 420–426.

[81] C. L. Colyer and M. Cocivera, *Journal of The Electrochemical Society*, 1992, **139**, 406.

[82] R. Huang, G. P. Kissling, R. Kashtiban, Y. J. Noori, K. Cicvari, W. Zhang, A. L. Hector, R. Beanland, D. C. Smith, G. Reid, P. N. Bartlett and C. H. K. de Groot, *Faraday Discussions*, 2019, **213**, 339–355.

[83] I. Nandhakumar, J. M. Elliott and G. S. Attard, in *Thin Films: Preparation, Characterization, Applications*, Springer, Boston, 2002, pp. 113–120.

[84] F. Xiao, C. Hangarter, B. Yoo, Y. Rheem, K.-H. Lee and N. V. Myung, *Electrochimica Acta*, 2008, **53**, 8103–8117.

[85] M. S. Dresselhaus, G. Chen, M. Y. Tang, R. Yang, H. Lee, D. Wang, Z. Ren, J.-P. Fleurial and P. Gogna, *Advanced Materials*, 2007, **19**, 1043–1053.

[86] M. Dresselhaus, G. Dresselhaus, X. Sun, Z. Zhang, S. Cronin and T. Koga, *Physics of the Solid State*, 1999, **41**, 679–682.

[87] L. Hicks and M. S. Dresselhaus, *Physical Review B*, 1993, **47**, 16631.

[88] I. Ng, K. Kok, C. C. A. Rahman, T. Choo and N. Saidin, *Materials Today: Proceedings*, 2016, **3**, 533–537.

[89] C. J. W. Smith, J. S. Cahill and A. Nuhoglu, *PAM Review: Energy Science & Technology*, 2016, **3**, 86–99.

[90] H. Yu, P. C. Gibbons and W. E. Buhro, *Journal of Materials Chemistry*, 2004, **14**, 595–602.

[91] S. A. Sapp, B. B. Lakshmi and C. R. Martin, *Advanced Materials*, 1999, **11**, 402–404.

[92] A. Huczko, *Applied Physics A*, 2000, **70**, 365–376.

[93] S. Shingubara, *Journal of Nanoparticle Research*, 2003, **5**, 17–30.

[94] D.-A. Borca-Tasciuc, G. Chen, A. Prieto, M. Martín-González, A. Stacy, T. Sands, M. Ryan and J. Fleurial, *Applied Physics Letters*, 2004, **85**, 6001–6003.

[95] A. Mavrokefalos, A. L. Moore, M. T. Pettes, L. Shi, W. Wang and X. Li, *Journal of Applied Physics*, 2009, **105**, 104318.

[96] E. Koukharenko, X. Li, I. Nandhakumar, N. Fréty, S. Beeby, D. Cox, M. Tudor, B. Schiedt, C. Trautmann, A. Bertsch and N. M. White, *Journal of Micromechanics and Microengineering*, 2008, **18**, 104015.

[97] M. Sander, R. Gronsky, T. Sands and A. Stacy, *Chemistry of Materials*, 2003, **15**, 335–339.

[98] A. L. Prieto, M. S. Sander, M. S. Martín-González, R. Gronsky, T. Sands and A. M. Stacy, *Journal of the American Chemical Society*, 2001, **123**, 7160–7161.

[99] M. S. Sander, A. L. Prieto, R. Gronsky, T. Sands and A. M. Stacy, *Advanced Materials*, 2002, **14**, 665–667.

[100] L. Trahey, C. R. Becker and A. M. Stacy, *Nano Letters*, 2007, **7**, 2535–2539.

[101] E. Menke, M. Brown, Q. Li, J. Hemminger and R. Penner, *Langmuir*, 2006, **22**, 10564–10574.

[102] C.-L. Chen, Y.-Y. Chen, S.-J. Lin, J. C. Ho, P.-C. Lee, C.-D. Chen and S. R. Harutyunyan, *The Journal of Physical Chemistry C*, 2010, **114**, 3385–3389.

[103] W. Lu, Y. Ding, Y. Chen, Z. L. Wang and J. Fang, *Journal of the American Chemical Society*, 2005, **127**, 10112–10116.

[104] H. Mamur, M. R. A. Bhuiyan, F. Korkmaz and M. Nil, *Renewable and Sustainable Energy Reviews*, 2018, **82**, 4159–4169.

[105] C. Frantz, N. Stein, L. Gravier, S. Granville and C. Boulanger, *Journal of Electronic Materials*, 2010, **39**, 2043–2048.

[106] A. Davydov and V. Volgin, *Russian Journal of Electrochemistry*, 2016, **52**, 806–831.

[107] W. Lee, R. Ji, U. Gösele and K. Nielsch, *Nature Materials*, 2006, **5**, 741–747.

[108] A. Li, F. Müller, A. Birner, K. Nielsch and U. Gösele, *Journal of Applied Physics*, 1998, **84**, 6023–6026.

[109] F. Li, L. Zhang and R. M. Metzger, *Chemistry of Materials*, 1998, **10**, 2470–2480.

[110] A. Walcarius, E. Sibottier, M. Etienne and J. Ghanbaja, *Nature Materials*, 2007, **6**, 602–608.

[111] G. Riveros, H. Gómez, A. Cortes, R. Marotti and E. Dalchiele, *Applied Physics A*, 2005, **81**, 17–24.

[112] M. Skupinski, M. Toulemonde, M. Lindeberg and K. Hjort, *Nuclear Instruments and Methods in Physics Research Section B: Beam Interactions with Materials and Atoms*, 2005, **240**, 681–689.

[113] P. Apel, *Radiation Measurements*, 2001, **34**, 559–566.

[114] C. Trautmann, W. Brüchle, R. Spohr, J. Vetter and N. Angert, *Nuclear Instruments and Methods in Physics Research Section B: Beam Interactions with Materials and Atoms*, 1996, **111**, 70–74.

[115] R. Lv, C. Cao, H. Zhai, D. Wang, S. Liu and H. Zhu, *Solid State Communications*, 2004, **130**, 241–245.

[116] L. Martins, M. A. A. Rosa, S. H. Pulcinelli and C. V. Santilli, *Microporous and Mesoporous Materials*, 2010, **132**, 268–275.

[117] M. A. Rosa, E. Santos, C. V. Santilli and S. Pulcinelli, *Journal of Non-crystalline Solids*, 2008, **354**, 4786–4789.

[118] R. H. Au and R. J. Puddephatt, *Chemical Vapor Deposition*, 2007, **13**, 20–22.

[119] J. E. Wijnhoven, S. J. Zevenhuizen, M. A. Hendriks, D. Vanmaekelbergh, J. J. Kelly and W. L. Vos, *Advanced Materials*, 2000, **12**, 888–890.

[120] P. N. Bartlett, P. R. Birkin, M. A. Ghanem and C.-S. Toh, *Journal of Materials Chemistry*, 2001, **11**, 849–853.

[121] R. Ojani, Z. Abkar, E. Hasheminejad and J.-B. Raoof, *International journal of hydrogen energy*, 2014, **39**, 7788–7797.

[122] S. Cherevko and C.-H. Chung, *Electrochemistry Communications*, 2011, **13**, 16–19.

[123] A. Ott, L. A. Jones and S. K. Bhargava, *Electrochemistry Communications*, 2011, **13**, 1248–1251.

[124] S. Cherevko and C.-H. Chung, *Electrochimica Acta*, 2010, **55**, 6383–6390.

[125] G. E. Possin, *Review of Scientific Instruments*, 1970, **41**, 772–774.

[126] S. Valizadeh, J. George, P. Leisner and L. Hultman, *Thin Solid Films*, 2002, **402**, 262–271.

[127] K. Kim, M. Kim and S. M. Cho, *Materials Chemistry and Physics*, 2006, **96**, 278–282.

[128] J. Azevedo, C. Sousa, J. Ventura, A. Apolinario, A. Mendes and J. Araujo, *Materials Research Express*, 2014, **1**, 015028.

[129] P. N. Bartlett, J. Burt, D. A. Cook, C. Y. Cummings, M. W. George, A. L. Hector, M. M. Hasan, J. Ke, W. Levason, D. Pugh, G. Reid, P. W. Richardson, D. C. Smith, J. Spencer, N. Suleiman and W. Zhang, *Chemistry–A European Journal*, 2016, **22**, 302–309.

[130] P. N. Bartlett, D. A. Cook, M. Hasan, A. L. Hector, S. Marks, J. Naik, G. Reid, J. Sloan, D. C. Smith, J. Spencer and Z. Webber, *RSC Advances*, 2017, **7**, 40720–40726.

[131] L. Vieira, J. Burt, P. W. Richardson, D. Schloffer, D. Fuchs, A. Moser, P. N. Bartlett, G. Reid and B. Gollas, *ChemistryOpen*, 2017, **6**, 393–401.

[132] W. Linpé, G. S. Harlow, J. Evertsson, U. Hejral, G. Abbondanza, F. Lenrick, S. Seifert, R. Felici, N. A. Vinogradov and E. Lundgren, *ACS Applied Nano Materials*, 2019, **2**, 3031–3038.

[133] G. S. Harlow, J. Drnec, T. Wiegmann, W. Lipé, J. Evertsson, A. R. Persson, R. Wallenberg, E. Lundgren and N. A. Vinogradov, *Nanoscale Advances*, 2019, **1**, 4764–4771.

[134] L. Nicole, C. Boissière, D. Grosso, A. Quach and C. Sanchez, *Journal of Materials Chemistry*, 2005, **15**, 3598–3627.

[135] Y. Lu, R. Ganguli, C. A. Drewien, M. T. Anderson, C. J. Brinker, W. Gong, Y. Guo, H. Soyez, B. Dunn, M. H. Huang and J. I. Zink, *Nature*, 1997, **389**, 364.

[136] C. J. Brinker, Y. Lu, A. Sellinger and H. Fan, *Advanced Materials*, 1999, **11**, 579–585.

[137] A. Walcarius, J. Ghanbaja, M. Etienne, E. Aubert, C. Lecomte and A. Goux, *Chemistry of Materials*, 2009, **21**, 731–741.

[138] A. Walcarius, *Chemical Society Reviews*, 2013, **42**, 4098–4140.

[139] A. E. Sánchez-Rivera, M. Romero-Romo, M. T. Ramirez-Silva, M. Palomar-Pardavé and V. Vital-Vaquier, *Journal of the Electrochemical Society*, 2004, **151**, C666.

[140] J.-F. Liu and W. A. Ducker, *The Journal of Physical Chemistry B*, 1999, **103**, 8558–8567.

[141] A. Rennie, E. Lee, E. Simister and R. Thomas, *Langmuir*, 1990, **6**, 1031–1034.

[142] S. Besson, C. Ricolleau, T. Gacoin, C. Jacquiod and J.-P. Boilot, *Microporous and Mesoporous Materials*, 2003, **60**, 43–49.

[143] W. Li, M. Zhang, J. Zhang and Y. Han, *Frontiers of Chemistry in China*, 2006, **1**, 438–442.

[144] E. Sibottier, S. Sayen, F. Gaboriaud and A. Walcarius, *Langmuir*, 2006, **22**, 8366–8373.

[145] Y. Guillemin, J. Ghanbaja, E. Aubert, M. Etienne and A. Walcarius, *Chemistry of Materials*, 2014, **26**, 1848–1858.

[146] C. Nunes Kirchner, K. H. Hallmeier, R. Szargan, T. Raschke, C. Radehaus and G. Wittstock, *Electroanalysis: An International Journal Devoted to Fundamental and Practical Aspects of Electroanalysis*, 2007, **19**, 1023–1031.

[147] P. Caldwell, *The Journal of Physiology*, 1954, **126**, 169–180.

[148] F. Haber and Z. Hlemensiewicz, *Zeitschrift für Physikalische Chemie*, 1909, **67**, 385–431.

[149] M. I. Khan, K. Mukherjee, R. Shoukat and H. Dong, *Microsystem Technologies*, 2017, **23**, 4391–4404.

[150] J. C. Dutta, 2012 2nd National Conference on Computational Intelligence and Signal Processing (CISP), 2012, pp. 185–191.

[151] P. Bartlett, B. Gollas, S. Guerin and J. Marwan, *Physical Chemistry Chemical Physics*, 2002, **4**, 3835–3842.

[152] M. Serrapede, G. L. Pesce, R. J. Ball and G. Denuault, *Analytical Chemistry*, 2014, **86**, 5758–5765.

[153] M. Serrapede, *Ph.D. thesis*, University of Southampton, 2014.

[154] T. Graham, *Proceedings of the Royal Society of London*, 1869, 212–220.

[155] T. B. Flanagan and W. Oates, *Annual Review of Materials Science*, 1991, **21**, 269–304.

[156] M. Vasile and C. Enke, *Journal of the Electrochemical Society*, 1965, **112**, 865.

[157] T. Imokawa, K.-J. Williams and G. Denuault, *Analytical Chemistry*, 2006, **78**, 265–271.

[158] M. D. Abràmoff, P. J. Magalhães and S. J. Ram, *Biophotonics International*, 2004, **11**, 36–42.

[159] L. De Broglie, *Foundations of Physics*, 1970, **1**, 5–15.

[160] K. Vernon-Parry, *III-Vs Review*, 2000, **13**, 40–44.

[161] H. Hasegawa, T. Hashimoto, H. Kawai, T. P. Lodge, E. J. Amis, C. J. Glinka and C. C. Han, *Macromolecules*, 1985, **18**, 67–78.

[162] C. Williams, M. Nierlich, J. Cotton, G. Jannink, F. Boue, M. Daoud, B. Farnoux, C. Picot, P. DeGennes, M. Rinaudo, M. Moan and C. Wolff, *Journal of Polymer Science Part C: Polymer Letters*, 1979, **17**, 379–384.

[163] S. Rosenfeldt, N. Dingenouts, M. Ballauff, N. Werner, F. Vögtle and P. Lindner, *Macromolecules*, 2002, **35**, 8098–8105.

[164] M. J. Hore, J. Ford, K. Ohno, R. J. Composto and B. Hammouda, *Macromolecules*, 2013, **46**, 9341–9348.

[165] A.-J. Petrescu, V. Receveur, P. Calmettes, D. Durand, M. Desmadril, B. Roux and J. C. Smith, *Biophysical Journal*, 1997, **72**, 335–342.

[166] H. Pessen, T. F. Kumosinski and H. M. Farrell, *Journal of Dairy Research*, 1989, **56**, 443–451.

[167] A. Dupuis, G. Zaccai and M. Satre, *Biochemistry*, 1983, **22**, 5951–5956.

[168] D. Vivares and F. Bonneté, *Acta Crystallographica Section D: Biological Crystallography*, 2002, **58**, 472–479.

[169] P. Müller-Buschbaum, *Advanced Materials*, 2014, **26**, 7692–7709.

[170] L. Feigin and D. I. Svergun, *Structure Analysis by Small-Angle X-ray and Neutron Scattering*, Springer, Boston, 1987, vol. 1.

[171] G. R. Strobl and G. R. Strobl, *The Physics of Polymers*, Springer, Berlin, Heidelberg, 1997, vol. 2.

[172] M. Ballauff, *Current Opinion in Colloid & Interface Science*, 2001, **6**, 132–139.

[173] A. Guinier, G. Fournet and K. L. Yudowitch, *Small-angle scattering of X-rays*, Wiley, New York, 1955.

[174] F. S. Varley, *Neutron News*, 1992, **3**, 29–37.

[175] Â. Lazzari, *Interfaces*, 2002, 406–421.

[176] M. Rauscher, T. Salditt and H. Spohn, *Physical Review B*, 1995, **52**, 16855.

[177] Y. Yoneda, *Physical Review*, 1963, **131**, 2010.

[178] J. Daillant and A. Gibaud, *X-ray and Neutron Reflectivity: Principles and Applications*, Springer, Berlin, Heidelberg, 2008, vol. 770.

[179] G. Pospelov, W. Van Herck, J. Burle, J. M. Carmona Loaiza, C. Durniak, J. M. Fisher, M. Ganeva, D. Yurov and J. Wuttke, *Journal of Applied Crystallography*, 2020, **53**, 262–276.

[180] M. Schwartzkopf, A. Buffet, V. Körstgens, E. Metwalli, K. Schlage, G. Benecke, J. Perlich, M. Rawolle, A. Rothkirch, B. Heidmann, G. Herzog, P. Müller-Buschbaum, R. Röhlsberger, R. Gehrke, N. Stribeck and S. V. Roth, *Nanoscale*, 2013, **5**, 5053.

[181] G. Kaune, M. A. Ruderer, E. Metwalli, W. Wang, S. Couet, K. Schlage, R. Röhlsberger, S. V. Roth and P. Müller-Buschbaum, *ACS Applied Materials & Interfaces*, 2009, **1**, 353–360.

[182] M. Ruge, F. Golks, J. Zegenhagen, O. M. Magnussen and J. Stettner, *Physical Review Letters*, 2014, **112**, 1–5.

[183] M. Ruge, J. Drnec, B. Rahn, F. Reikowski, D. A. Harrington, F. Carlà, R. Felici, J. Stettner and O. M. Magnussen, *Journal of the American Chemical Society*, 2017, **139**, 4532–4539.

[184] O. Magnussen, K. Krug, A. Ayyad and J. Stettner, *Electrochimica Acta*, 2008, **53**, 3449–3458.

[185] A. R. Hillman, R. Barker, R. M. Dalgliesh, V. C. Ferreira, E. J. R. Palin, R. M. Sapstead, E. L. Smith, N.-J. Steinke, K. S. Ryder and A. D. Ballantyne, *Faraday Discussions*, 2018, 429–449.

[186] G. S. Harlow, I. M. Aldous, P. Thompson, Y. Gründer, L. J. Hardwick and C. A. Lucas, *Physical Chemistry Chemical Physics*, 2019, **21**, 8654–8662.

[187] F. Renner, Y. Gründer, P. Lyman and J. Zegenhagen, *Thin Solid Films*, 2007, **515**, 5574–5580.

[188] Y. Gründer and C. A. Lucas, *Nano Energy*, 2016, **29**, 378–393.

[189] L. Komsiyska and G. Staikov, *Electrochimica Acta*, 2008, **54**, 168–172.

[190] M. D. Abràmoff, P. J. Magalhães and S. J. Ram, *Biophotonics International*, 2004, **11**, 36–41.

[191] J. Potton, G. Daniell and B. Rainford, *Journal of Applied Crystallography*, 1988, **21**, 663–668.

[192] J. Ilavsky and P. R. Jemian, *Journal of Applied Crystallography*, 2009, **42**, 347–353.

[193] G. E. Moehl, P. N. Bartlett and A. L. Hector, *Langmuir*, 2020, **36**, 4432–4438.

[194] E. Budevski, G. Staikov, W. Lorenz and K. Keusler, *Angewandte Chemie-German Edition*, 1997, **109**, 1418–1418.

[195] G. Benecke, W. Wagermaier, C. Li, M. Schwartzkopf, G. Flucke, R. Hoerth, I. Zizak, M. Burghammer, E. Metwalli, P. Müller-Buschbaum, M. Trebbin, S. Förster, O. Paris, S. V. Roth and P. Fratzl, *Journal of Applied Crystallography*, 2014, **47**, 1797–1803.

[196] C. Robertson, R. Beanland, S. A. Boden, A. L. Hector, R. J. Kashtiban, J. Sloan, D. C. Smith and A. Walcarius, *Physical Chemistry Chemical Physics*, 2015, **17**, 4763–4770.

[197] N. Godino, X. Borrise, F. X. Munoz, F. J. Del Campo and R. G. Compton, *The Journal of Physical Chemistry C*, 2009, **113**, 11119–11125.

[198] M. Atighilorestani and A. G. Brolo, *Analytical Chemistry*, 2017, **89**, 6129–6135.

[199] G. E. Moehl, R. Cubitt, S. D. S. Fitch and A. Hector, *In situ GISANS Study on the Electrodeposition of Bismuth Telluride on Titanium Nitride from Non-Aqueous Solution. doi:10.5291/ILL-DATA.1-04-145*, 2018.

[200] A. E. Whitten, S. Cai and J. Trewhella, *Journal of Applied Crystallography*, 2008, **41**, 222–226.

[201] K. L. Sarachan, J. E. Curtis and S. Krueger, *Journal of Applied Crystallography*, 2013, **46**, 1889–1893.

[202] D. R. Lide, *CRC Handbook of Chemistry and Physics*, CRC press, Boca Raton, 2004, vol. 85.

[203] *https://www.eurisotop.com/methylene-chloride-d2-0?c=D023, 2021-05-06*.

[204] B. Hammouda, *Journal of Applied Crystallography*, 2010, **43**, 716–719.

[205] L. Liu and A. Walcarius, *Physical Chemistry Chemical Physics*, 2017, **19**, 14972–14983.

[206] C. J. Brinker and G. W. Scherer, *Sol-gel science: The Physics and Chemistry of Sol-Gel Processing*, Academic press, San Diego, 2013.

[207] Z. Teng, G. Zheng, Y. Dou, W. Li, C.-Y. Mou, X. Zhang, A. M. Asiri and D. Zhao, *Angewandte Chemie International Edition*, 2012, **51**, 2173–2177.

[208] M. Grün, I. Lauer and K. K. Unger, *Advanced Materials*, 1997, **9**, 254–257.

[209] K. Kuperkar, L. Abezgauz, K. Prasad and P. Bahadur, *Journal of Surfactants and Detergents*, 2010, **13**, 293–303.

[210] B. Tan and S. E. Rankin, *The Journal of Physical Chemistry B*, 2004, **108**, 20122–20129.

[211] N. Venkataraman and S. Vasudevan, *Journal of Chemical Sciences*, 2001, **113**, 539–558.

[212] C. Wohlfarth, *Static Dielectric Constants of Pure Liquids and Binary Liquid Mixtures: Supplement to IV/6*, Springer Science & Business Media, Berlin, Heidelberg, 2008, vol. 17.

[213] N. Ibl, J. C. Puippe and H. Angerer, *Surface Technology*, 1978, **6**, 287–300.

[214] G. Giordano, N. Vilà, E. Aubert, J. Ghanbaja and A. Walcarius, *Electrochimica Acta*, 2017, **237**, 227–236.

[215] D. Basnig, N. Vilá, G. Herzog and A. Walcarius, *Journal of Electroanalytical Chemistry*, 2020, 113993.

[216] P. Deepa, M. Kanungo, G. Claycomb, P. M. Sherwood and M. M. Collinson, *Analytical Chemistry*, 2003, **75**, 5399–5405.

[217] D.-W. Wang and D. Su, *Energy & Environmental Science*, 2014, **7**, 576–591.

[218] G. Denuault, M. T. Frank and L. Peter, *Faraday Discussions*, 1992, **94**, 23–35.

[219] R. A. Critelli, M. Bertotti and R. M. Torresi, *Electrochimica Acta*, 2018, **292**, 511–521.

[220] R. A. Critelli, P. T. Sumodjo, M. Bertotti and R. M. Torresi, *Electrochimica Acta*, 2018, **260**, 762–771.

[221] W. Mook, *Environmental Isotopes in the Hydrological Cycleprinciples and Applications*, 2001, **1**, 143–166.

[222] K. G. Schulz, U. Riebesell, B. Rost, S. Thoms and R. Zeebe, *Marine Chemistry*, 2006, **100**, 53–65.

[223] D. Levy and M. Zayat, *The Sol-Gel Handbook, 3 Volume Set: Synthesis, Characterization, and Applications*, John Wiley & Sons, Weinheim, 2015, vol. 2.

[224] M. Bogar, I. Khalakhan, A. Gambitta, Y. Yakovlev and H. Amenitsch, *Journal of Power Sources*, 2020, **477**, 229030.

[225] S. Richardson, M. Burton, X. Luo, P. A. Staniec, I. Nandhakumar, N. J. Terrill, J. M. Elliott and A. Squires, *Nanoscale*, 2017, **9**, 10227–10232.

[226] J. Tillier, T. Binninger, M. Garganourakis, A. Patru, E. Fabbri, T. J. Schmidt and O. Sereda, *Journal of The Electrochemical Society*, 2016, **163**, H913.

[227] J. Liu and K. G. Yager, *IUCrJ*, 2018, **5**, 737–752.

[228] J. Ustarroz, *Current Opinion in Electrochemistry*, 2020, **19**, 144–152.